The Interpretation of Motionally Induced Electric Fields in Oceans of Complex Geometry

by Zoltan B. Szuts

Technical Report
APL-UW TR 0803
October 2008

Applied Physics Laboratory   University of Washington
1013 NE 40th Street   Seattle, Washington 98105-6698

The Interpretation of Motionally Induced Electric Fields in Oceans of Complex Geometry

Zoltan B. Szuts

A dissertation submitted in partial fulfillment
of the requirements for the degree of

Doctor of Philosophy

University of Washington

2008

Program Authorized to Offer Degree:
School of Oceanography

University of Washington
Graduate School

This is to certify that I have examined this copy of a doctoral dissertation by

Zoltan B. Szuts

and have found that it is complete and satisfactory in all respects,
and that any and all revisions required by the final
examining committee have been made.

Chair of the Supervisory Committee:

_____

Thomas B. Sanford

Reading Committee:

_____

Thomas B. Sanford

_____

Eric A. D'Asaro

_____

James B. Girton

Date: _____

University of Washington

Abstract

The Interpretation of Motionally Induced Electric Fields
in Oceans of Complex Geometry

Zoltan B. Szuts

Chair of the Supervisory Committee:
Professor Thomas B. Sanford
School of Oceanography

Sea water moving through the earth's magnetic field induces electric currents in the ocean, and in general their distribution depends on the 3D structure of the ocean and its surroundings. Although velocity is traditionally calculated from measurements of the electric field with a one-dimensional relationship in the vertical, higher dimension processes are expected near steep topography or in energetic and variable flows. The observational capabilities of recently developed electric field instruments highlight the need for a qualitative and quantitative assessment of higher dimensional processes.

The first part of this dissertation analyzes electric field solutions for 2D effects caused by horizontal gradients of either velocity or topography. Magnetostatic solutions are calculated for simple geometries that are described by a few non-dimensional spatial scales. The solution depends most strongly on the aspect ratio of the flow, that is the ratio of water depth H to velocity width-scale L or topographic width-scale L_t. Aspect ratios are expected to be less than 0.1 for a variety of realistic flows and topography. For aspect ratios less than 0.1 and sediment less thick than the water column, the velocity errors caused by velocity gradients are $< 2\%$ of the 1D approximation, while velocity errors caused by sloping topography are $< 0.5\%$.

The second part analyzes measurements collected across the Gulf Stream where it separates from the continental margin, where the oceanic flow is fast and meandering,

topographic is steep, and sediment is thick. Geophysical data are compiled to estimate the sediment electrical properties. The observations of electric field at the 500 m isobath are not fully described by the 1D approximation, therefor higher dimension effects were investigated with a numerical model initialized with the observations. The discrepancy at 500 m is explained by a maximum of the vertically averaged velocity on the upper continental slope caused by meanders. Errors in the depth-varying velocity are less than 0.02 m s^{-1} and are corrected with an iterative method. The depth-uniform errors are less than 0.005 m s^{-1} over most of the Gulf Stream, with larger errors on the upper continental shelf cause by jets meandering over topography.

TABLE OF CONTENTS

Page

LIST OF FIGURES

LIST OF TABLES

ACKNOWLEDGMENTS

I owe a large amount of gratitude to my committee members Eric D'Asaro, James Girton, Chuck Nittrouer and Tom Sanford for their willingness to push and support me towards reaching this milestone on the tight schedule I set. The frequent discussions I've had with them, aside from focusing and expanding how I make sense of my research, have been a very pleasant introduction to the scientific process.

I could not have asked for anything more of Tom as an advisor and mentor — he has consistently supported me through all aspects of my graduate career, and his high expectations have forced me to extend myself and my work beyond the initial goals. It is impressive how he always kept the larger picture in mind and made sure I did not lose sight of it. I will be striving to live up to his example.

My time would have been much less enjoyable without the companionship (and commiseration) of my fellow graduate students, especially my past and present office-mates Marlene Jeffries, Abdullah BaMasoud, Beth Curry, and Kim Martini.

I thank my parents for their enthusiasm for science in all forms that have shaped the course of my education, and also for showing me that there is much more of interest in life than science. I am especially grateful to my mom for starting me on the path that eventually led to oceanography.

Lastly, I can't imagine having spent the last 6+ years without Kathleen. Beyond providing encouragement, distractions, and baked goods, most importantly she has put this whole process into perspective for me.

Chapter 1

INTRODUCTION

The horizontal electric fields (HEF) that arise from the motion of seawater through the earth's magnetic field are a convenient way to indirectly measure ocean velocity. High quality velocity observations have been collected during the past few decades that take advantage of the benefits of HEF-based methods. The technique is ideal for rapid and high-vertical resolution of the relative velocity from profiling floats, while stationary sensors measure a quantity that is proportional to the vertically-averaged velocity and is dynamically similar to oceanic transport. Theoretical understanding of electric fields is based on nearly horizontal oceans, however, and potential higher order influences near steep topography and ocean flows with small length-scales have not yet been examined. This dissertation quantifies higher order influences on ocean electric fields through numerical and analytical calculations and through a detailed interpretation of observations.

The first order theory that relates ocean velocity to the resulting electric fields depends only on the vertical dimension. Stationary sensors measure a quantity proportional to the vertically-averaged velocity, while profiling instruments measure a relative velocity profile. As these quantities involve vertical variations and vertical averages of the velocity, this first order approximation is considered one-dimensional.

Observations can be made from submarine cables, bottom-mounted sensors, vertical profilers, and drifting or floating platforms, many of which are commercially available to the oceanographic community. In many cases the electric field observations are the only practical means for measuring the currents. For example, expendable current profilers (XCP, *Sanford et al.*, 1982, 1987) or HEF-equipped APEX floats (EM-APEX, *Sanford et al.*, 2007) are the only current profilers suitable for deployment by aircraft and can also be deployed from ships under harsh conditions (e.g. *Girton et al.*, 2001). Seafloor cables can be used to monitor transport, an essential property for understanding ocean

circulation. For instance, cable measurements of the Florida Current transport over 20 years (*Larsen and Sanford*, 1985; *Baringer and Larsen*, 2001) are important constraints on models and observations of the North Atlantic meridional overturning circulation (*Kanzow et al.*, 2007). Two instruments have recently been developed as part of large-scale distributed sensor observing networks: the EM-APEX float, which adds velocity-measuring capabilities to the ARGO network (*Chen et al.*, 2007; *Gille et al.*, 2007; Joyce et al., 2008, manuscript submitted to Bull. Amer. Meteor. Soc.); and the bottom lander HPIES (Horizontal electric field, Pressure and and Inverted Echo Sounder, Sanford, pers. comm.), which is ideal for deployment with cabled seafloor observatories. With distributed sensors there is higher likelihood for measuring in locations that are less than ideal from a theoretical perspective. Extending the theoretical understanding is essential for more accurate analysis of observations and for improved experiment planning.

Though the theory of motional induction includes temporal and small spatial perturbations of the flow field and topography (*Sanford*, 1971; *Chave and Luther*, 1990), the higher order terms (HOT) have not been investigated in regions outside of where the theoretical assumption of small aspect ratio flows (the ratio of water depth to flow width) is strictly valid. Larger HOT are expected for small velocity length-scales, steep topography, thick sediments, or flow over topography. This dissertation investigates two-dimensional and three dimensional HOT to gain a better understanding of the physical basis for higher dimension effects in the electric field, with the ultimate goal of a more accurate conversion from the measured electric field to the desired velocity.

Oceanographic Electromagnetics Initial development in oceanography occurred in the mid 20th century with theoretical advances by *Stommel* (1948) and *Longuet-Higgins et al.* (1954). Early interpretation of electric field observations was inexact (*von Arx*, 1950; *Wertheim*, 1954). More sophisticated theories were developed later by *Sanford* (1971) for a general and 3D interpretation of ocean velocity, and also by *Filloux* (1967) and *Larsen* (1968) for tidal signals that are influenced by deep earth structure. Although there was a greater theoretical basis for interpreting observations, the number of observations was still very limited. Cable studies (*Bowden*, 1956; *Hughes*, 1969; *Robinson*, 1976) showed a

strong ocean signal, but discrepancies with oceanic parameters could not be explained in a satisfactory manner.

With increased effort measuring oceanic electromagnetic signals, there was increased accuracy with cables (*Larsen and Sanford*, 1985; *Baringer and Larsen*, 2001; *Kim et al.*, 2004; *Nilsson et al.*, 2007), profiling instruments (XCP, *Sanford et al.*, 1982; AVP, *Sanford et al.*, 1985; HRP, *Montgomery et al.*, in prep.), bottom electrodes and magnetometers (*Chave et al.*, 1989; *Luther et al.*, 1991; *Chave et al.*, 1997; *Meinen et al.*, 2002, 2003), and Lagrangian drifting instruments (*Szuts*, 2004; *Sanford et al.*, 2007). Various aspects of the theory has been further refined: *Chave and Luther* (1990) for a decomposition with spherical functions, showing that 1D oceanic EFs are averaged horizontally in space; *Tyler and Mysak* (1995a,b) for application to a global reference frame. The development of sufficiently powerful computers has allowed to numerical modelling of the oceanic electric and magnetic fields, either for oceanographic (*Stephenson and Bryan*, 1992; *Flosadóttir et al.*, 1997; *Vivier et al.*, 2004) or geomagnetic studies (*Tyler et al.*, 2003; *Manoj et al.*, 2006). For interpreting observations in terms of oceanic velocity, however, the formulation based on a 1D approximation for oceans with large length scales is typically used.

Geophysical Electromagnetics   In tandem with the development of the physical oceanographic understanding of oceanic electric fields, there has been concurrent developments in geophysics that use variable frequency electromagnetic signals to probe the earth's conductivity structure or the upper atmosphere's electromagnetic structures. The non-stationary solar wind hitting the earth's magnetosphere and ionosphere generates time-varying electromagnetic signals. Planetary researchers are interested in these fields in and of themselves, for they can create hazardous electric environments for satellites and for ground-based communication and power networks. The fluctuating signals propagate downward into the earth (and ocean) and are attenuated and distorted by geologic features. Geologists can calculate the electric structure of the earth by inverting measurements of the electric and magnetic fields. In the ocean high frequency ionospheric signals are greatly reduced, but similar techniques using active electromagnetic sources have gained wide-spread acceptance (*Constable and Weiss*, 2006).

In recent years there is growing recognition that the ocean can generate magnetic signals that are detectable by satellite or land-based magnetometers and that can obscure the weak signals of interest to geophysicists (*Heinson and Constable*, 1992; *Tyler et al.*, 2003; *Maus et al.*, 2006). The same electromagnetic signals that contain information about ocean velocity also contain information about geologic and ionospheric processes. The oceanic electric fields also depend on the seafloor electrical properties.

The overlap of oceanographic and geophysical electromagnetics can be utilized to obtain a better estimate of the signal of interest, whether oceanic, geological, or magnetospheric. Techniques, results and data from these other fields are used in this study, and demonstrate to the physical oceanographer interested in measuring ocean velocity techniques less well known in oceanography.

Organization of Dissertation   This dissertation investigates broadly the structure and magnitude of oceanic electric fields in the presence of complexities of geometry. Horizontal gradients of velocity and topography are examined in detail, and other higher order and non-oceanic processes are also discussed.

The second chapter investigates HOT in simple geometries that are schematically representative of oceanic flow. The roles of 2D velocity gradients and topographic gradients are separated into different models that are then solved analytically and numerically. This approach facilitates a non-dimensional analysis of the parameter space for the models.

The third chapter investigates observations collected off of Cape Hatteras across the Gulf Stream. This region is an excellent test location because of the presence of a strong and variable (meandering) Gulf Stream, steep topography, thick sediment, and non-uniform sediment electric properties. Geophysical data are compiled to constrain the electrical properties of the sediment, and a magnetotelluric analysis is done to estimate the role of externally-induced signals. The observations are inconsistent with the standard 1D approximation that relates oceanic electric fields to velocity on the upper continental shelf. To investigate this effect a numerical model calculates the electric fields at a higher spatial resolution. In addition to describing the 2D effects in a plane perpendicular to the Gulf Stream, 3D effects are estimated with a vertically integrated form for quantifying

the effect of Gulf Stream transport crossing isobaths.

The overall results are discussed in the conclusion in the last chapter.

Chapter 2

ELECTRIC FIELDS GENERATED BY HORIZONTAL GRADIENTS

2.1 Introduction

This chapter investigates electric fields and electric currents generated in two-dimensional geometries that contain horizontal gradients of velocity and topography. The three geometries are representative of the realistic situations, of which two include horizontal gradients of velocity and the third contains sloping topography. The small number of spatial scales necessary to describe each geometry makes it feasible to find solutions over the full parameter space. The electric field and electric current solutions are evaluated based on the velocity error relative to a 1D interpretation of the 2D electric fields.

The first order theory is discussed in section 2.2, as is the general form of higher dimension terms. The solution for each geometry is calculated with a different technique (section 2.3). The criteria for evaluating the solutions are the same for all geometries (section 2.4.1), based on how much the solution differs from the first order (1D) theory. Immediately following (sections 2.4.2–2.4.4) the differences in velocity between the exact (2D) solution and the 1D approximation are discussed over the parameter space of the geometries. In the discussion (section 2.5) the general perturbations from the 1D approximation are summarized (section 2.5.1), the results are extended for geometries not directly evaluated with the three cases (section 2.5.3), and general geophysical limits on the scalings for oceanic flow and topography are used to proscribe the unrealistic part of the parameter space (section 2.5.4). The chapter finishes in section 2.6 with a summary of the results.

2.2 Theory

Electric fields occur in the ocean because of the motion of conductive salt-water through the earth's magnetic field — this is generally called motional induction. The theory of

motionally induced electric fields in the ocean for time-dependent and 3–D currents and bathymetry was developed by *Sanford* (1971), where the thin aspect ratio of the ocean allows for great simplification from the 3D governing equations. The theory of motional induction is also treated by *Larsen* (1968, 1971), *Chave and Luther* (1990) and *Tyler and Mysak* (1995b).

The principal electric currents generated by ocean currents fall into two modes. The traditional and generally more important mode restricts currents to the vertical plane. This is a toroidal mode that describes, for instance, electric currents in the surface layer forced by surface flow with weaker electric currents returning in the motionless deep ocean. For unidirectional velocity electric currents flow in the perpendicular plane. The second mode, called poloidal, is characterized by electric fields that uniformly fill the water column and are directed in the horizontal plane. This mode only exists in situations where there are gradients in the downstream direction and thus is a 3D effect.

2.2.1 General Solution

Sanford (1971) solves for a general solution that makes use of a number of assumptions. Although the analytic form of his solution is specific to the assumptions made, it suggests the underlying physical factors that all formulations will contain. The assumptions he made are: a horizontal ocean bottom (H) with small topographic perturbations (h, where $h/H \ll 1$), width scales (L) much larger than bottom depth ($H/L \ll 1$), predominantly horizontal oceanic velocity (v), distant lateral boundaries, a layer of underlying sediment that has a uniform electrical conductivity, and small time variations so that magnetic self-induction and mutual induction are negligible.

Although it is readily shown that time variations of the electric field generate induced magnetic fields that are negligible compared to the earth's magnetic field (*Sanford*, 1971; *Chave and Luther*, 1990), a less evident process is inductive coupling between the ocean and the conductive mantle. If large-scale water motion changes quickly in time (e.g. tidal flow), the time variations induce electric currents in the mantle that act to reduce and delay the oceanic electric field. Scaling Maxwell's governing equations finds that the induction

8

parameter $\mu\sigma\omega\mathcal{L}^2$ must be much less than 1 for mutual induction to be negligible (μ is magnetic permeability and σ is electrical conductivity) (*Sanford*, 1971). Although the appropriate length scales $\mathcal{L}^2$ for this problem are unclear, they can range from the water depth H to the velocity width-scale L to the depth of deep conductors in the earth. The induction parameter depends on a combination of time-scales (frequency ω) and length scales ($\mathcal{L}^2$). Generally, this condition is satisfied if the phase speed $\omega/\mathcal{L} < 10$ m s^{-1}. Analysis of a simplified earth geometry constrains large scale flow ($H/L \leq 1$) to have time-scales larger than 6 hours (*Sanford*, 1971). Inclusion of realistic earth conductivity profiles (*Chave and Luther*, 1990) shows that mutual induction is minimal for periods longer than 10 hours. To avoid complications caused by quickly varying large-scale flow, we shall limit the analysis to oceanic flows with sub-tidal frequencies.

In general form, the quasi-static horizontal electric field $\boldsymbol{E}_h$ is

$$-\boldsymbol{E}_h = \nabla_h \phi = \boldsymbol{v} \times \hat{\boldsymbol{k}} F_z - \boldsymbol{J}_h/\sigma \qquad , \qquad (2.1)$$

where ∇_h is the horizontal gradient operator, ϕ is electric potential, $\boldsymbol{v}$ is oceanic velocity, F_z is the vertical component of earth's magnetic field, $\hat{\boldsymbol{k}}$ is the vertical unit vector (pointing upward), σ is electrical conductivity, and $\boldsymbol{J}_h$ is horizontal electric current density. The electromotive driving force is due to $\boldsymbol{v} \times \hat{\boldsymbol{k}} F_z$, which sets up an electric field and electric currents.

For the purposes of this study, the form for horizontal electric current density divided by conductivity is (*Sanford*, 1971)

$$
\frac{\boldsymbol{J}_h}{\sigma} = \overbrace{(\boldsymbol{v} - \overline{\boldsymbol{v}}^*) \times F_z \hat{\boldsymbol{k}}}^{\text{term 1, 1D}} +
$$
$$
\underbrace{- \nabla_h \left\{ \frac{1}{H(1+\lambda)} \int_{-H}^{0} \hat{\boldsymbol{k}} \cdot (\boldsymbol{v} \times \boldsymbol{F}) z'\, \mathrm{d}z' + \overbrace{\int_{-H}^{z} \hat{\boldsymbol{k}} \cdot (\boldsymbol{v} \times \boldsymbol{F})\, \mathrm{d}z'}^{\text{depth-varying}} \right\}}_{\text{term 2, } \boldsymbol{J}_{\nabla_h}}
$$

(2.2)

where the arrow under term 1 is labeled "depth-varying".

with

$$r = \sqrt{(x - x')^2 + (y - y')^2}$$

$$D = H + \zeta - h + \frac{\sigma_s}{\sigma}(H_s - H + h)$$

$$\overline{\boldsymbol{v}}^* = \int_{-H+h}^{\zeta} \sigma \boldsymbol{v} \, \mathrm{d}z' \Big/ \int_{-H_s}^{\zeta} \sigma \, \mathrm{d}z' \quad , \tag{2.3}$$

where ζ is the sea surface, $-H$ is the mean depth of the seafloor, h is the perturbation of the seafloor, $-H_s$ is the bottom of conductive sediment, D is a scaled water depth, σ_s is sediment conductivity, λ is the sediment conductance factor ($D/H = 1 + \lambda$), and $\overline{\boldsymbol{v}}^*$ is the conductivity-weighted vertically-averaged velocity. Terms that vary vertically have been denoted so, and all other terms are depth-uniform. The scaled bottom depth D is the depth of the water column plus a thickness of seawater that has the same vertical conductance as the sediments. Another term that is the same order as term 2 (H/L) is not included in (2.2) (see below and section 3.11), but otherwise the equation is accurate to order H^2/L^2.

First Order Term

The first term of $\boldsymbol{J}_h/\sigma$ is the principal toroidal mode. For baroclinic flows the fastest part of the water column generates the largest electromotive force through $\boldsymbol{v}(z) \times \hat{\boldsymbol{k}}F_z$. Due to geophysical scaling, that the width L of the current is much larger than the depth H, the resulting horizontal electric field is vertically uniform and is equal to $\overline{\boldsymbol{v}}^* F_z$. The electric current density divided by σ is the difference between that driven by the vertically uniform electric field and that generated by local horizontal water motion, $(\boldsymbol{v}(z) - \overline{\boldsymbol{v}}^*) \times \hat{\boldsymbol{k}}F_z$. The toroidal term is considered one-dimensional because it only depends on the vertical dimension: vertical variations of $\sigma(\boldsymbol{v}(z) - \overline{\boldsymbol{v}}^*)$ determine the electric current density, while a vertical integral of velocity (2.3) defining $\overline{\boldsymbol{v}}^*$ determines the horizontal electric field $\overline{\boldsymbol{v}}^* F_z$. In the limiting situation where the flow field is entirely barotropic and there is no sediment layer, there will be no electric currents.

The quantity $\overline{\boldsymbol{v}}^*$ corresponds physically to the vertically-uniform horizontal electric field divided by F_z and is called the vertically-averaged conductivity-weighted velocity.

$\overline{\boldsymbol{v}}^*$ is linearly related to the vertically averaged velocity. If conductive sediment beneath the ocean can support electric currents that act to reduce the oceanic electric potential. In the 1D approximation, where only the toroidal term contributes to $\boldsymbol{J}_h/\sigma$ in (2.2), the horizontal electric current integrated from the bottom of conductive sediment $(-H_s)$ to the top of the water column needs to be zero to conserve charge. This constraint yields the equation that defines $\overline{\boldsymbol{v}}^*$, (2.3).

A simpler form of $\overline{\boldsymbol{v}}^*$ is obtained by reducing the numerator and denominator of (2.3) to factors that describe physical processes. A Reynolds decomposition of the numerator defines the vertical correlation factor γ

$$\frac{1}{H - h + \zeta} \int_{-H+h}^{\zeta} \sigma\boldsymbol{v}\,\mathrm{d}z = \overline{\sigma\boldsymbol{v}} = \overline{\sigma}\,\overline{\boldsymbol{v}} + \overline{\sigma'\boldsymbol{v}'} = \overline{\sigma}\,\overline{\boldsymbol{v}}(1+\gamma) \qquad , \tag{2.4}$$

where $\overline{x}$ indicates a vertical average in the water column and x' indicates the perturbations about the vertical mean. Rearranging the denominator gives the bottom conductance factor λ

$$\lambda = \int_{-H_s}^{-H+h} \sigma(z)\,\mathrm{d}z \Big/ \int_{-H+h}^{\zeta} \sigma(z)\,\mathrm{d}z \qquad , \tag{2.5}$$

the ratio of the sediment conductance to the water column conductance. Combining 2.4 and 2.5 yields a simplified form of $\overline{\boldsymbol{v}}^*$:

$$\overline{\boldsymbol{v}}^* = \overline{\boldsymbol{v}}\left(\frac{1+\gamma}{1+\lambda}\right) \qquad . \tag{2.6}$$

Another form of $\overline{\boldsymbol{v}}^*$ can obtained by defining the denominator of (2.3) as the total vertical conductance $\Sigma = \int_{-H_s}^{\zeta} \sigma\,\mathrm{d}z$, as is often used when the ocean is approximated as a thin-shell (e.g., *Vivier et al.*, 2004).

The strongest factor is λ which describes the amount of shorting through the bottom sediment. The form that is consistent with (2.2) is $\lambda = \sigma_s(H_s - H + h)/\sigma(H + \zeta - h)$, which parameterizes the sediment layer as having a uniform apparent conductivity σ_s and includes the small perturbations of the seafloor h and the surface ζ. For the thin aspect ratio assumption, a vertically uniform electric field drives electric currents through the sediment. In the presence of vertically-varying sediment conductivity, the total conductance of the sediment (the numerator of (2.5)) is simply the vertical integral

of conductivity. Sediment is electrically conductive mainly because the pores are filled with seawater, making its bulk conductivity closely related to porosity. Porosity decreases approximately exponentially with depth into the sediment. Despite these general trends, sediment conductivity is a poorly characterized variable outside of commercial exploration geophysics. Total sediment conductance, for our purposes, can be estimated on a basin scale based on the sediment thickness (*Flosadóttir et al.*, 1997; *Tyler et al.*, 1997) or from more detailed local geophysical data as done in chapter 3.

The vertical correlation factor $\gamma = \overline{\sigma' \boldsymbol{v}'} / \overline{\sigma}\, \overline{\boldsymbol{v}}$ describes return electric currents that flow more readily through more conductive parts of the water column. Measurements of temperature and salinity simultaneous with the apparent electric field ($\boldsymbol{J}_h/\sigma$) allow direct calculation of the vertical correlation. Corrections are also possible from hydrographic data or from data archives (*Luther and Chave*, 1993) by computing representative profiles of geostrophic velocity and electrical conductivity. Prior calculations of γ found it to have less than a 10% influence (*Chave and Luther*, 1990) for open ocean baroclinic modes, with large values only occurring in strong baroclinic flows (e.g., *Szuts*, 2004).

Higher Order Term: Horizontal Gradients

The second terms can be called a higher order term (HOT) because it scales as H/L in this formulation. This scaling explains why the 1D approximation is sufficiently accurate for the small aspect ratios found in the open ocean. This chapter focuses on the effects that the second term describes, using analytic and numerical techniques to calculate electric fields and electric currents for smaller length scales than the assumptions of *Sanford* (1971) allow. The assumption of small horizontal gradients is often invalid in parts of the ocean that are dynamically interesting to physical oceanographers.

The second term of (2.2) depends on horizontal gradients of topography and of the velocity field. In this form, horizontal gradients of H, λ, and $\overline{\boldsymbol{v}}$ can all make this term non-zero. The expression for vertical electric currents (*Sanford*, 1971) includes analogous terms, except horizontal gradient operators are in front of them and they have a vertical dependence on z.

Both the first and the second terms contain depth-varying and depth-uniform components. The first terms depend on local effects in the vertical, at most within a distance a few times the water depth. *Chave and Luther* (1990) showed that the vertical averages of the dominant mode (the first term in (2.2)) have a horizontal weighting function that has a width of a few times the water depth. Similar horizontal dependencies are expected for the second term, that the second term responds to a region within a few water depths.

Other Sources of Oceanic Electric Fields

The theoretical form of (2.2) contains another higher order term that describes horizontally flowing electric currents that are called non-local electric currents (*Sanford*, 1971; *Tyler and Mysak*, 1995a; *Vivier et al.*, 2004) Such currents arise if there are downstream gradients in $F_z \overline{\boldsymbol{v}}^*$ and add a depth-uniform electric field offset. By assumption non-local currents are zero in the 2D geometries considered later.

Periodic ocean circulation such as tides or Kelvin waves can generate further complexities due to the introduction of time-variable flow. Changing surface elevation is another source for generating non-local currents, while there is the potential for large-scale tidal flow to inductively couple with deep conductive layers in the mantle. If the length-scale of the flow is as large as the depth of conductive layers, generally > 500 km (*Kuvshinov and Olsen*, 2006), then mutual induction can occur. The only oceanic flow that meets these criteria of short time-scale and basin-wide extent is tidal flow.

Such phenomena are briefly mentioned for completeness, but they are tangential to the goal of this chapter.

2.2.2   Observation Methods

Practically, electric field measurements are made from platforms that are either stationary of freely drifting in the horizontal. These two platforms measure respectively a depth-uniform electric field $\boldsymbol{E}_h = \overline{\boldsymbol{v}}^* F_z$ and the depth-varying electric current density divided by conductivity $\boldsymbol{J}_h/\sigma = (\boldsymbol{v} - \overline{\boldsymbol{v}}^*) \times \hat{\boldsymbol{z}} F_z$. As the goal of this work is to determine how accurately measured electric fields can be inverted to velocity, the electric field solutions presented

in the next section will be evaluated for depth-uniform and depth-varying perturbations from the 1D approximation.

Absolute electric fields are measured from stationary platforms such as cables or bottom electrometers. For a stationary instrument the local velocity in (2.1) ($\boldsymbol{v} \times \boldsymbol{F}$) cancels that in the first term of $\boldsymbol{J}_h/\sigma$, leaving only the electric fields caused by $\overline{\boldsymbol{v}}^*$ and HOT.

Free-falling platforms move horizontally at the local unknown water velocity, and the resulting electric field across the instrument body comes from the electric current density divided by σ (see *Sanford et al.*, 1978), which is proportional to the relative velocity $\boldsymbol{v}(z) - \overline{\boldsymbol{v}}^*$.

If the instrument's motion is measured independently, then the absolute velocity profile and the absolute electric field ($\overline{\boldsymbol{v}}^* F_z$) can be recovered. Some instruments include a secondary velocity sensor, such as a bottom-reflecting acoustic Doppler velocity sensor on the Absolute Velocity Profiler (AVP, *Sanford et al.*, 1985) or the RAFOS tracking for an electrode-equipped RAFOS float (Electric Field Float, *Szuts*, 2004). Shipboard ADCP or GPS surface fixes can also be used to give coincident water velocities. Generally, any absolute velocity can be used to to make the relative velocity absolute provided that $\overline{\boldsymbol{v}}^*$ is indeed depth-uniform, in so doing also calculating the offset $\overline{\boldsymbol{v}}^*$.

Thus, the two parts of the magnetostatic solution that will be evaluated below are the depth-uniform and depth-varying components. They are equivalent to barotropic and baroclinic velocity modes.

2.3 Analytic and Numerical Techniques

Solutions for 2D representative cases are found using two methods: an analytic solution and a numerical model for electromagnetics (*Tyler et al.*, 2004). The former isolates 2D effects due to horizontal velocity gradients and is evaluated for two different geometries, while the latter isolates the influence of bottom topography for one geometry. The use of simple geometries described by a few non-dimensional scales allows for evaluating the solutions over a wide range of scales. Both techniques solve for the electric field and electric current (that is, the magnetostatic solution) generated by prescribed velocities

and topographies.

All models use mid-latitude northern hemisphere values for the earth's magnetic field, $F_z = -40,000$ nT and $F_h = 20,000$ nT (the field at 35°N). The relative magnitude of the horizontal and vertical components determines by how much F_z dominates the response: the ratio $|F_h/F_z|$ is greater than 1 at latitudes greater than 30° N or S. Close to the geomagnetic equator where F_z approaches 0 the 1D approximation breaks down, although there have been successful measurements up to 2° in latitude from the geomagnetic equator (*Kennelly et al.*, 1986). For the horizontal magnetic field to induce electric fields it must be perpendicular to the direction of water motion, that is only the east-west velocity in magnetic coordinates has a component due to F_h.

The magnitude of the velocity v_0 is set at 1 m s^{-1} in all , which is an appropriate value for energetic flows in the ocean. The equations are linear, so this choice is without loss of generality. Most of the ocean is characterized by velocity that is an order of magnitude smaller (0.1 m s^{-1}), for which our results can be extended by considering relative errors. Relative errors are calculated by normalizing with the maximum velocity for depth-varying velocity errors, and with the barotropic velocity for depth-uniform errors.

2.3.1 Analytic Model, Infinite Sinusoidal Velocity

The analytic solution describes the electric fields that arise in an idealized ocean. The electromagnetic solution for a geometry consisting of three horizontal layers (Figure 2.1) can be solved analytically if the velocity varies as a sinusoid. The top layer is a surface jet over $-H' \leq z \leq 0$ with a vertically uniform velocity $\boldsymbol{v}(x) = v_0 \cos(\alpha x)\hat{\boldsymbol{y}}$, the underlying water is motionless over $-H < z \leq -H'$, and there is a conductive sediment layer beneath $(-H_s < z \leq -H)$. The wave number is $\alpha = 2\pi/L$, where L is the wavelength of the velocity forcing. The velocity forcing extends to infinity in the x-direction. The ocean and sediment each have uniform conductivities of σ and σ_s. The magnetic field has vertical and horizontal components (F_z, F_h). The x, y coordinates are not aligned with east and north. The angle θ between the ocean velocity $\hat{\boldsymbol{y}}$ and magnetic north for a particular region determines the magnitude of $F_x = F_h \sin(\theta)$. Induction due to F_h only

influences the geomagnetic east-west velocity.

Three non-dimensional scales can be formed from the four spatial scales L, H', H, H_s. The solution below shows that the natural way to obtain non-dimensional parameters is by normalizing with L, because of the scales combine as $\alpha H'$, αH, and αH_s. Evaluation of the solution shows, however, that there is practically no dependence on H either. The scale H can also be used to normalize the scales, and is the more intuitive choice for non-dimensionalizing the vertical scales. Thus, there are 4 non-dimensional scales for this geometry that represent the aspect ratio H/L, the relative depth of the jet H'/H, the relative thickness of the sediment $(H_s - H)/H$, and the relative conductivity $\sigma_r = \sigma_s/\sigma$. The depth of the jet H'/H and the relative conductivity σ_r are both strictly ≤ 1, the former because of geometry and the latter because sediment is conductive because of seawater filling its pores and porosity must be less than 100%.

The problem is solved for the electric potential ϕ, from which it is straightforward to calculate all fields of the electromagnetic solution (see Appendix A.1). The solution for the horizontal electrical field E_x is shown here, as it is most relevant for this analysis. The three regions correspond to those in Figure 2.1.

The terms induced by F_z are

$$
\begin{aligned}
E_{x,1} &= -v_0 F_z \cos(\alpha x) \left[1 - \frac{\mathrm{scrcs}(\alpha(H - H'))}{\mathrm{scrcs}(\alpha H)} \cosh(\alpha z) \right] \\
E_{x,2} &= -v_0 F_z \cos(\alpha x) \frac{\sinh(\alpha H')}{\mathrm{scrcs}(\alpha H)} \mathrm{ccrss}(\alpha(z + H)) \\
E_{x,3} &= -v_0 F_z \cos(\alpha x) \frac{\sinh(\alpha H')}{\mathrm{scrcs}(\alpha H)} \cosh(\alpha(z + H_s)) \qquad ,
\end{aligned}
\tag{2.7}
$$

where for notational simplicity I define

$$
\begin{aligned}
\mathrm{scrcs}(C) &\equiv \sinh(C) \cosh(\alpha(H_s - H)) + \sigma_r \cosh(C) \sinh(\alpha(H_s - H)) \\
\mathrm{ccrss}(C) &\equiv \cosh(C) \cosh(\alpha(H_s - H)) + \sigma_r \sinh(C) \sinh(\alpha(H_s - H)) \qquad .
\end{aligned}
$$

There is also a contribution from the horizontal magnetic fields (F_h). The electromotive force generated by F_h is directed upwards, so when the flow is thin as described by $H/L \ll 1$ the electric field induced by F_h scales as H/L. At the small width-scales
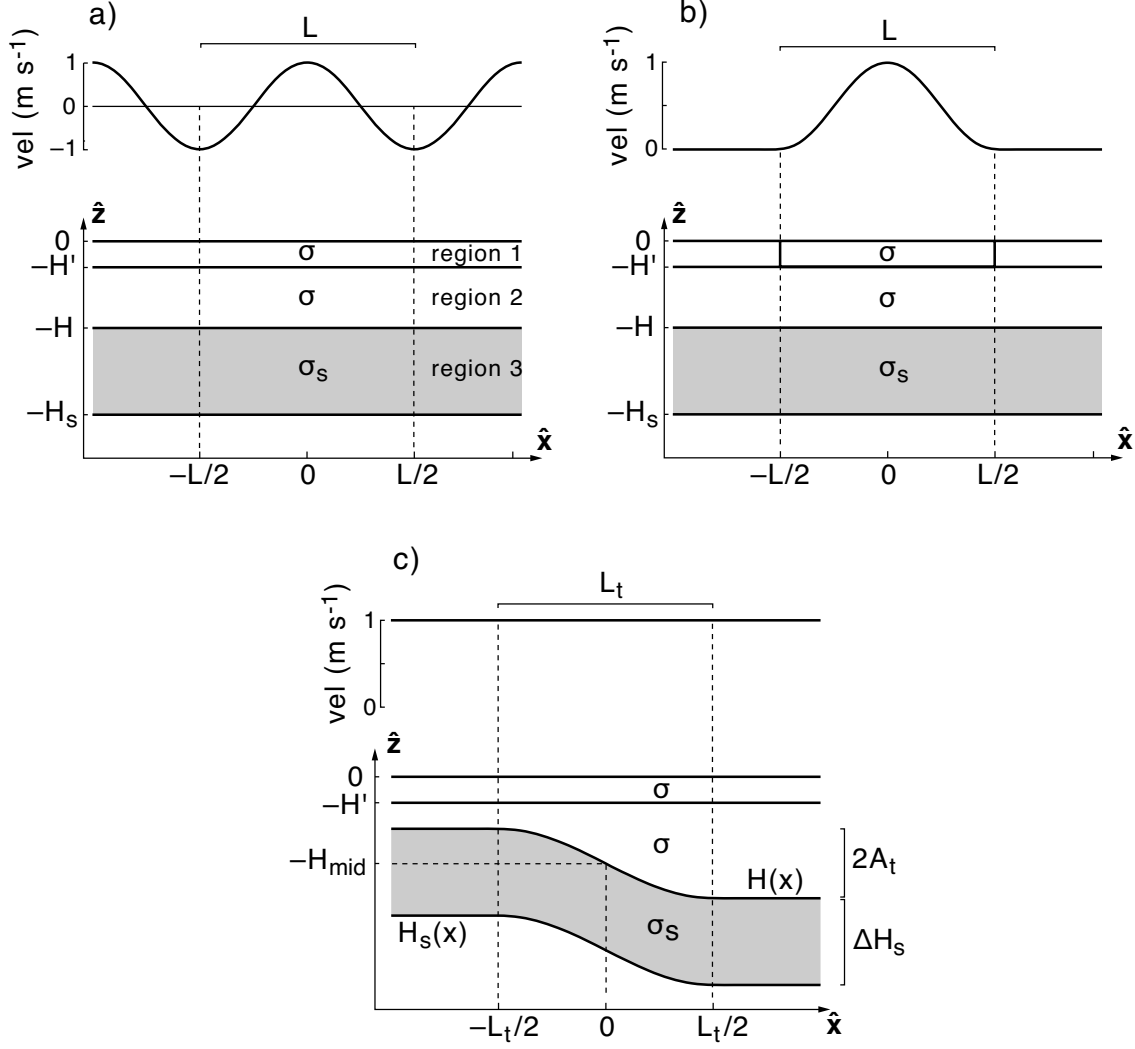
Figure 2.1: Ocean geometries for which magnetostatic solutions are calculated. (a) Infinite forcing solved with an analytic solution (see section 2.3.1), with a sinusoidal velocity of form $\cos(2\pi x/L)$ (top) and 3 horizontal layers (bottom). (b) Numerical Fourier expansion of the analytic solution obtains a finite velocity forcing in the shape of a cosine jet (see section 2.3.2), velocity (top) and the same 3 horizontal layers (bottom). (c) Sloping topography solved with the numerical model MOED (see section 2.3.3), with a constant velocity in the surface layer (top) and topography of shape $-H_{\mathrm{mid}} - A_t \sin(\pi x/L_t)$ for $|x| < L_t/2$ (bottom).

considered here, however, this contribution can be significant and so will be considered below. The electric field solution is

$$E_{x,1,F_h} = v_0 F_h \sin(\alpha x) \left[\frac{\mathrm{ccrss}(\alpha(H - H')) - \mathrm{ccrss}(\alpha H)}{\mathrm{scrcs}(\alpha H)} \cosh(\alpha z) - \sinh(\alpha z) \right]$$

$$E_{x,2,F_h} = v_0 F_h \sin(\alpha x) \frac{\cosh(\alpha H') - 1}{\mathrm{scrcs}(\alpha H)} \mathrm{ccrss}(\alpha(z + H))$$

$$E_{x,3,F_h} = v_0 F_h \sin(\alpha x) \frac{\cosh(\alpha H') - 1}{\mathrm{scrcs}(\alpha H)} \cosh(\alpha(z + H_s)) \qquad . \tag{2.8}$$

These quantities have a super-script F_h to distinguish them from the dominant 1D contribution from F_z.

2.3.2 Finite Velocity

Although analytically simple, the solution above has the unphysical property of representing a forcing field that extends to infinity in the $\hat{x}$ direction. To be able to apply this solution to realistic ocean currents that are bounded, we form a finite forcing by linear combinations of the above solution. *Longuet-Higgins et al.* (1954) performed an analytic inverse Fourier transform to represent a square jet of constant velocity v_0 for $-L/2 < x < L/2$ in the surface layer, but, due to the constraints of contour integration, they only solved for $z = 0$. Work by *Fristedt and Sigray* (2005) extended this solution for all z in the ocean, but their use of an infinitely thick sediment layer limits their analysis to shallow coastal waters where the sediment can be much thicker than the ocean. Another way to obtain a finite forcing function is to cast the problem in an elliptical coordinate system, and then letting the velocity be constant out to a given elliptical radius. Elliptical geometry, however, is most applicable for flow in channels and doesn't describe the first-order effect of finite sediments via the shorting factor λ.

The approach taken here is to perform a finite Fourier expansion numerically to evaluate the solution for any given finite forcing function. The forcing is taken to be

$$v(x) = \begin{cases} \frac{1}{2} \left[1 + \cos\left(\frac{2\pi x}{L} \right) \right] & |x| < L/2 \\ 0 & |x| \geq L/2 \end{cases}, \tag{2.9}$$

as this form goes to 0 smoothly at the edges of the jet (Figure 2.1b).

The solution becomes

$$E_{x,i}(x,z) = \sum_{n=0}^{\infty} a_{n,M} \left[A_i(z)\,cos(k_{n,M}x) + B_i(z)\,sin(k_{n,M}x) \right] \qquad , \qquad (2.10)$$

where $a_{n,M}$ is the Fourier coefficient for the (n,M)th wave number $k_{n,M} = 2\pi n/(ML)$, where $n = \{0, 1, \ldots, N\}$, M is an integer greater than 1 that determines the wave-number resolution, and $A_i(z)$ and $B_i(z)$ are the depth-dependent coefficients for $cos(\alpha x)$ and $sin(\alpha x)$ for the regions $i = 1, 2, 3$ as described by (2.7) and (2.8).

Although (2.10) is exact in the limit of $M \to \infty$ and $\sum_n \to \int dk$, in practice the summation has to be truncated. The value of $a_{n,M}$ decays to 0 for $N \gg M$ (see appendix A.2), so there is little loss of accuracy by ending the sum at a very large wave number $k_{N,M} \gg 1$. Numerical issues arise from the small wave-number end due to the requirement of a finite M. In order for the electric potential to be continuous and repeating, as is characteristic of all finite Fourier expansions, the large decrease in electric potential across the jet must be balanced by a small increase in potential outside of the jet. This results in a non-zero electric field outside of the jet that is physically unrealistic and depends on the repeat period $1/M$ (see appendix A.2 for details)

The background E_x is removed as follows. First, a large value of M is chosen so that the background E_x is much smaller than $E_x(x = 0)$. A uniform E_x is added to the entire domain to obtain a zero background field, and the result is then scaled to maintain the initial maximum value of E_x. Addition and scaling of solutions is possible because the Laplace equation is linear. The final corrected solution using this method is the same within numerical accuracy for all values of M, substantiating the accuracy of this correction.

2.3.3 Numerical Model, Sloping Topography

The analytic solution is computationally inexpensive to evaluate for its geometry of horizontal layers, but the most convenient way to evaluate cases with changing bottom topography is to use a numerical model. The Model for Ocean Electrodynamics (MOED *Tyler et al.*, 2004) is used. It is a 3D model that solves Maxwell's governing electromagnetic

equations in the frequency domain by finite-difference for the electric and magnetic gauge potentials, given prescribed conductivity and velocity fields.

The same three layer case presented above is investigated with MOED, except that the sediment/water interface is allowed to be non-horizontal (Figure 2.1c). A constant sediment thickness is maintained, so that the bottom of the sediment layer has the same shape as the water depth. There are 4 length scales in addition to the relative sediment conductance σ_r: L_t, A_t, H_{mid} and ΔH_s. The depth H_{mid} is used to make 3 non-dimensional scales. A bottom depth is chosen of the form

$$H(x) = \begin{cases} H_{\text{mid}} - A_t & x < -L_t \\ H_{\text{mid}} + A_t \sin\left(\frac{\pi x}{2L_t}\right) & -L_t \leq x \geq L_t \\ H_{\text{mid}} + A_t & L_t < x \end{cases} \qquad (2.11)$$

Note that H_{mid} is the water depth at the center of the slope, with the two uniform water depths on either side being $H_{\text{mid}} - A_t$ and $H_{\text{mid}} + A_t$. The total topographic relief is $2A_t$. As the sediment has a uniform thickness, this yields $H_s(x) = H(x) + \Delta H_s$. The grid spacing in x is smallest over $-1.3L < x < 1.3L$ to fully resolve the slope ($\Delta x = L_t/80$), beyond which the grid-spacing increases by 10% with each successive grid point.

The surface jet is uniform in x of magnitude $v_0 = 1$ m s^{-1} and has a uniform depth H', but because of topography $\overline{v} = v_0 H'/H$ changes across the slope. As the parameter H' is already investigated in the analytic model, for this solution it is set to a constant value of half the smallest water depth, $(H_{\text{mid}} - A_t)/2$ to reduce the number of non-dimensional parameters.

The velocity jet extends from $x = -21(H_{\text{mid}} - A_t)$ to $x = 21(H_{\text{mid}} + A_t)$, that is 20 times the water depth beyond the edges of the slope. This factor is large enough so that 2D effects due to the edges of the jet do not interact with the slope region, based on the results of the analytical models.

The conductivity interfaces in the model domain need to be smoothed for numerical stability. For the water/sediment and sediment/crust interfaces the conductivity over 4 grid-points in the vertical was smoothed based on the exact interface depth according to

$$\sigma(z_i) = \frac{1}{2}\left[1 + \sin\left(\frac{2\pi(z_i - z_{\text{interface}})}{4\Delta z}\right)\right](\sigma_{\text{upper}} - \sigma_{\text{lower}}) + \sigma_{\text{lower}} \qquad (2.12)$$

where z_i is within 2 grid points of the depth of the interface $z_\text{interface}$, Δz is the vertical grid-spacing (Δz depends on A_t, H_mid and ΔH_s), and σ_upper and σ_lower are the conductivities of the upper and lower layers. A non-conductive crust underlies the sediment, for the purposes of limiting the model domain. Realistically, the crust has conductivities of $0.0001 - 0.03$ S m^{-1} (*Chave et al.*, 1992; *Simpson and Bahr*, 2005), which is at least an order of magnitude smaller that sediment conductivity and will not support a flow of electric current that significantly alters the solution.

Validation of MOED is demonstrated in *Tyler et al.* (2004) for 1D, 2D, and 3D cases that have analytical solutions. The particular implementation used here is cross-validated with the analytical solution evaluated with a Fourier summation (appendix A.3). The rms difference between E_x generated by MOED and by the analytic finite-velocity case is 0.37% of the maximum electric field, calculated for the region $-1/2 < x/L < 1/2$ and for all z.

2.4 Results

2.4.1 Analysis of Solutions

For each of the three geometries, the 2D magnetostatic solution can be solved for any combination of the non-dimensional parameters. To understand how the solution depends on each of the parameters, multiple solutions are calculated by varying each parameter over a range of values.

The 2D solutions show the electric fields and electric currents in a vertical plane that corresponds to the toroidal mode. The shape of electric fields and electric currents gives insight into where the largest perturbations are relative to the 1D approximation. To be able to present the results over the full parameter space, however, each set of non-dimensional parameters needs to be summarized with a number that evaluates one particular aspect of the solution. The solutions for all geometries are evaluated with a common approach that is presented first in this section.

There are two modes of electric fields that will be analyzed, depth-uniform and depth-varying modes. In terms of electromagnetic fields, these evaluation modes correspond

to the two ways of performing electric field measurements, from stationary or moving electrodes. In terms of velocity, these modes correspond to barotropic and baroclinic velocity modes.

Depth-uniform Electric Field Mode

The depth-uniform mode is the vertically uniform electric field $(\overline{\boldsymbol{v}}^* F_z)$ defined in (2.6). In the 1D approximation it is driven by the vertically averaged velocity with proportionality factors due to sediment conductance and vertical correlations of conductivity and velocity.

For the 2D situation discussed here E_x is not vertically uniform. A 2D $\overline{\boldsymbol{v}}^*$, $\overline{\boldsymbol{v}}^*_{2\mathrm{D}}$, is calculated by averaging E_x in the water column. The relative error of the depth-uniform velocity error is found by normalizing by $\overline{\boldsymbol{v}}$.

To convert $\overline{\boldsymbol{v}}^*_{2\mathrm{D}}$ to $\overline{\boldsymbol{v}}$ the shorting of the sediment needs to be removed by multiplying $\overline{\boldsymbol{v}}^*_{2\mathrm{D}}$ by $1 + \lambda$. The factor λ is calculated in two ways that are described below.

In general, the baroclinic correlation of σ and v would need to be removed from $\overline{\boldsymbol{v}}^*$ by dividing by $1+\gamma$, but this term is 0 in all three geometries because the ocean conductivity is uniform.

Velocity error from $\lambda_{\mathbf{1D}}$ The most direct method is to use λ calculated from the 1D theory (2.5), denoted $\lambda_{1\mathrm{D}}$, to correct the $\overline{\boldsymbol{v}}^*$ to a physical velocity. For all of the models, $\lambda_{1\mathrm{D}} = (H_s - H)\sigma_r/H$. This leads to an error of

$$\bar{\epsilon}_{\lambda_{1\mathrm{D}}} = \overline{\boldsymbol{v}} - \overline{\boldsymbol{v}}^*(1 + \lambda_{1\mathrm{D}}) \tag{2.13}$$

Though this method is straightforward to use for the prescribed geometries presented here, it presupposes knowledge of the sediment thickness and electrical conductivity for calculating $\lambda_{1\mathrm{D}}$ (see *Flosadóttir et al.*, 1997; *Vivier et al.*, 2004). As geophysical observations of these properties are limited, this approach is not always feasible.

Velocity error from λ calculated over space A method more analogous to observation methods is to use an empirically-derived λ to correct $\overline{\boldsymbol{v}}^*$. Profiling electric-field instruments that use a referencing velocity calculate both an absolute velocity profile that

yields $\overline{v}$ and γ with conductivity measurements (see section 2.2.2) and the vertically-averaged electric field that yields $\overline{v}^*$.

If there is no knowledge of the sediment thickness or conductivity, $1 + \lambda$ can be calculated heuristically from the ratio $\overline{v}/\overline{v}^*$. From an observational perspective, multiple measurements are necessary to accurately calculate λ. Typically $\overline{v}$ changes over time due to horizontal meanders of the ocean current.

For meandering jets, temporal changes in velocity at one location result from sampling different parts of the velocity structure. As the solution does not change with horizontal velocity shifts for the geometries considered here, sampling in space across the velocity shape is equivalent to meandering velocity. The value of λ at any location x_0, denoted $\lambda_{\mathrm{d}x}$, is the average ratio over a horizontal range $x_0 - \Delta x < x < x_0 + \Delta x$

$$1 + \lambda_{\mathrm{d}x} = < \overline{v}/\overline{v}^* >_{\mathrm{d}x} \tag{2.14}$$

The value used for Δx is 100 m. The resulting barotropic error is

$$\overline{\epsilon}_{\mathrm{d}x} = \overline{v} - \overline{v}^*(1 + \lambda_{\mathrm{d}x}) \tag{2.15}$$

Depth-varying Electric Field Mode

The depth-varying mode is the second way to evaluate the results. The depth-varying velocity error ϵ' is calculated by

$$\epsilon'(x, z) = v(x, z) - \frac{J_x(x, z)}{\sigma(z)F_z} - \overline{\epsilon'}(x)$$

$$\overline{\epsilon'}(x) = \frac{1}{H} \int_{-H}^{0} \left[v(x, z) - \frac{J_x(x, z)}{\sigma F_z} \right] \mathrm{d}z \quad , \tag{2.16}$$

where H varies horizontally for the geometry with sloping topography. Subtracting a vertical mean $\overline{\epsilon'}$ decouples the depth-varying velocity error from the depth-uniform velocity error, suitable for profiling floats. These errors will be displayed as absolute values, but relative errors are obtained by scaling with the maximum velocity $v_0 = 1$ m s^{-1}.

Stationary sensors that measure $\overline{\epsilon}$ at a fixed depth z_0 are also in error by $\epsilon'(z_0)$, which is the amount by which E_x is not vertically uniform at that depth. The complete error for a stationary sensor is thus $\overline{\epsilon} + \epsilon'(z_0)$.

The vertical dimension of ϵ' can be summarized in two ways: by calculating a vertical maximum $\epsilon'_{\max}$ or by calculating the vertical second moment ϵ'_{std}. The vertical second moment is the continuous equivalent of a standard deviation:

$$\epsilon'_{\text{std}} = \left(\frac{1}{H} \int_{-H}^{0} \epsilon'^2 \, \mathrm{d}z \right)^{1/2} \qquad . \tag{2.17}$$

where the vertical mean $(\overline{\epsilon'})$ has already been removed (2.16).

In practice, the correction to absolute velocity $\overline{\epsilon'}$ is usually calculated from reference velocities collected over less than the full water column, adding a potential mean offset $\overline{\epsilon'}$ to the depth-varying velocity error. For instance, shipboard ADCP velocities used to reference XCPs are only obtained in the upper 250 m of the water column, so this is the range over which velocity profiles are made absolute. The second moment and maximum velocities are recalculated for this situation using the alternative form

$$\overline{\epsilon'}_{\text{bias}} = \frac{1}{H_2 - H_1} \int_{-H_1}^{-H_2} \left[v(x, z) - \frac{J_x(x, z)}{\sigma(z) F_z} \right] \mathrm{d}z \qquad ,$$

$$\epsilon'_{\text{bias}}(x, z) = v(x, z) - \frac{J_x(x, z)}{\sigma(z) F_z} - \overline{\epsilon'_{\text{bias}}}(x)$$

$$\epsilon'_{\text{std,bias}} = \left(\frac{1}{H} \int_{-H}^{0} \epsilon'^2_{\text{bias}} \, \mathrm{d}z \right)^{1/2} \qquad . \tag{2.18}$$

where the integration limits are typically $H_1 = -300$ m and $H_2 = -50$ m. Some instruments use absolute velocities obtained in the water column for referencing: the Absolute Velocity Profiler when within 250 m of the seafloor (*Sanford et al.*, 1985), or the Electric Field Float at it's floating depth (*Szuts*, 2004). Such referencing gives similar errors for ϵ'_{bias} and $\epsilon'_{\text{std,bias}}$ as the surface referencing performed here

Velocity errors induced by F_h

The full signal from F_h is considered an error, because the 1D approximation includes no contribution from F_h. E_x is normalized to velocity by dividing by F_z (as is J_x), since the contribution from F_h is inseparable from that of F_z in measurements. The errors induced

by F_h increase linearly with F_h/F_z, thus case must be taken near the geomagnetic equator where F_z goes to 0.

To calculate the velocity errors caused by F_h the above equations (2.13), (2.16) and (2.4.1) need to be modified by removing the expected velocities $\overline{v}$ and $v(x,z)$ from the equations. The forms that are evaluated later are:

$$\overline{\epsilon}_{\lambda_{1D},F_h} = \overline{v}^*_{F_h}(1+\lambda_{1D}) \tag{2.19}$$

$$\epsilon'_{F_h}(x,z) = \frac{J_x(x,z)}{\sigma(z)F_z} - \overline{\epsilon}'(x)$$

$$\overline{\epsilon}'_{F_h}(x) = \frac{1}{H}\int_{-H}^{0}\left[\frac{J_x(x,z)}{\sigma F_z}\right]\,\mathrm{d}z \quad, \tag{2.20}$$

$$\epsilon'_{\mathrm{bias}F_h}(x,z) = v(x,z) - \frac{J_x(x,z)}{\sigma(z)F_z} - \overline{\epsilon}'_{\mathrm{bias},F_h}(x)$$

$$\overline{\epsilon}'_{\mathrm{bias},F_h} = \frac{1}{H_2-H_1}\int_{-H_1}^{-H_2}\left[\frac{J_x(x,z)}{\sigma(z)F_z}\right]\,\mathrm{d}z \quad, \tag{2.21}$$

The quantities λ_{1D} and F_z are used for normalizing, because any electric fields or electric currents induced by F_h will be initially considered part of the first order signal. The quantity λ has no physical meaning for the contribution from F_h, so (2.14) and (2.15) are not calculated.

2.4.2 Analytical solution: sinusoidal velocity

The simplest case is considered first with a horizontal 3-layer geometry. From the solution presented earlier (2.7), a 2-dimensional λ is defined as

$$1 + \lambda_{2D} = \frac{\overline{v}}{\overline{v}^*_{2D}} = \frac{\overline{v}F_z}{\overline{E}_x} \tag{2.22}$$

Calculated exactly from 2.7, this is

$$1 + \lambda_{2D} = \left(1 + \frac{\frac{1}{\alpha H'}\sinh(\alpha H')\sinh(\alpha(H_s-H))\,(-\sigma_r)}{\sinh(\alpha H)\cosh(\alpha(H_s-H)) + \sigma_r\cosh(\alpha H)\sinh(\alpha(H_s-H))}\right)^{-1} . \tag{2.23}$$

The sinusoidal forcing causes the electric field to be in phase with velocity, such that this λ_{2D} is valid at all x, even though $\overline{\boldsymbol{v}}$ or $\overline{\boldsymbol{v}}^*$ may be small or even 0.

The small wave-number limit of this solution should converge to the 1D theory when $1/\alpha = L/2\pi$ is much greater than H', H, and H_s. For comparison, the 1D vertically uniform electric field would be

$$\overline{\boldsymbol{E}}_x^{1D} = -\,\overline{\boldsymbol{v}}^* F_z = -\overline{\boldsymbol{v}}\frac{F_z}{1 + \lambda_{1D}} \tag{2.24}$$

$$= -\,\frac{H' v_0 \cos(\alpha x)}{H}\frac{F_z}{1 + \lambda_{1D}} \qquad , \tag{2.25}$$

where $\lambda_{1D} = (H_s - H)\sigma_r/H$ from (2.5).

The small wave-number limit is obtained from (2.3) by keeping the first term of the Taylor expansions for the hyperbolic trig functions. It is straightforward to show that (2.23) reduces to the 1D form. When taking the small wavenumber limit of λ_{2D}, the term in the denominator

$$\mathrm{scrcs}(\alpha H) = \sinh(\alpha H)\cosh(\alpha(H_s - H)) + \sigma_r \cosh(\alpha H)\sinh(\alpha(H_s - H)) \tag{2.26}$$

reduces to αD. The vertical scale D is the governing vertical scale for the solution — it is the water depth that is equivalent to the vertical conductance of the water column plus sediments. For this geometry it is defined as $D = H(1 + \lambda)$. In the 2D approximation the equivalent quantity becomes $(1/\alpha)\,\mathrm{scrcs}(\alpha H)$ and includes a dependence on L.

A second limiting case results from removing the sediment layer by letting $H_s \to H$ or $\sigma_r \to 0$. The numerator of the fraction in (2.23) becomes 0, and so $1 + \lambda_{2D} \to 1$ as expected — there is no longer any shorting of the oceanic electric field through the sediment.

Now we turn to evaluating the magnitude of the 2D electric fields. Detailed analysis that focuses on inverting the electric field to velocity will be postponed for the later cases that are closer approximations to realistic flow fields.

For the analytic solution we only seek general dependencies of the velocity errors on the 4 non-dimensional parameters. The depth uniform error (2.27) is simplified by noting that $\overline{\boldsymbol{v}}/\overline{\boldsymbol{v}}^* = \lambda_{2D}$ is uniform for all x. Substituting $\overline{\boldsymbol{v}}/(1 + \lambda_{2D})$ for $\overline{\boldsymbol{v}}^*$ and dividing by $\overline{\boldsymbol{v}}$
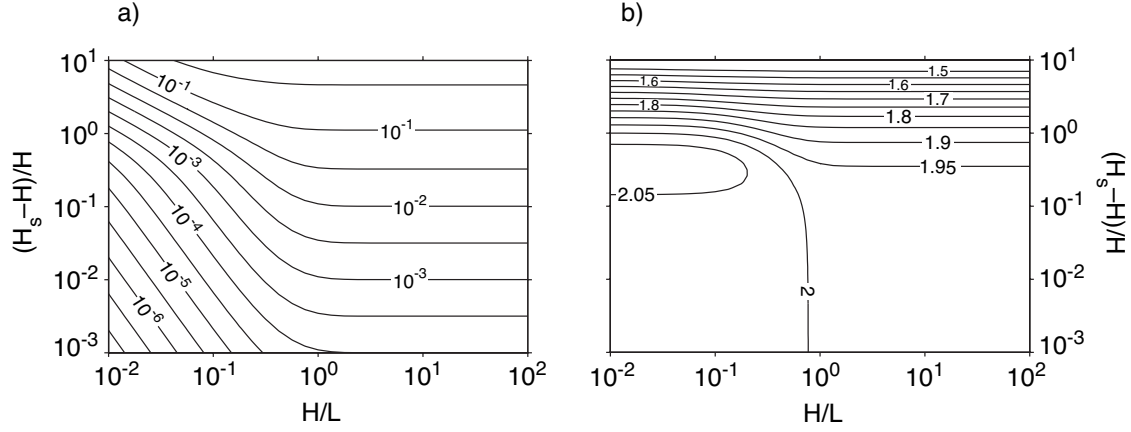
Figure 2.2: The depth-uniform relative velocity error $|\bar{\epsilon}_{\sin}/\bar{v}|$ from (2.27). (a) The relative error plotted for $(H_s - H)/H$ against H/L, with $\sigma_r = 0.1$. (b) The proportional change in $|\bar{\epsilon}_{\sin}\bar{v}|$ if σ_r varies by a factor of 2 centered on $\sigma_r = 0.1$ (see text). Both panels have the common value $H'/H = 0.5$.

gives

$$\frac{\bar{\epsilon}_{\sin}}{\bar{v}} = 1 - \frac{1 + \lambda_{1D}}{1 + \lambda_{2D}} \qquad . \tag{2.27}$$

Because the magnitude of λ_{2D} is greater than λ_{1D}, the absolute value is taken to obtain a positive error. The relative depth-uniform velocity error is the same as

$$|1 - (1 + \lambda_{2D})/(1 + \lambda_{1D})| \qquad . \tag{2.28}$$

For instance, if λ_{2D} and λ_{1D} are equal the relative error $\bar{\epsilon}_{\sin}/\bar{v}$ is 0, and if their ratio is 1.1 the relative error is 10%.

The depth-uniform relative error $|\bar{\epsilon}_{\sin}/\bar{v}|$ is plotted in Figure 2.2. There is a strong dependence of the error on H/L, $(H_s - H)/H$, and σ_r. The shape of the error is controlled by H/L (Figure 2.2a), for if H/L is less than 0.8 the error decreases exponentially with H/L. Above this transition point the error is constant with H/L in the high wave-number limit, although this region is not realistic because ocean currents are never as wide as they are deep. Below the transition point the error increases more rapidly with sediment thickness $(H_s - H)/H$.

The transition point below which the relative error decreases exponentially with H/L

is entirely dependent on the aspect ratio. This result makes sense by noting that the 1D approximation requires a small vertical domain to compress $\boldsymbol{E}$ to one dimension (horizontal). Since electric fields tend to spread equally in all dimensions, thick sediments allow E_x to vary vertically by being weaker at the bottom of the sediment layer. A thin but conductive sediment can support the same amount of electric current as a thick but resistive sediment layer, and the 2D perturbation will be the same. Thus it is the normalized vertical conductance of the sediment $(H_s - H)\sigma_r/H$ that determines the magnitude of error when H/L is held constant. This quantity is the definition of λ_{1D}, so in addition to describing the first order shorting of oceanic electric fields it also determines the magnitude of the 2D error.

The sensitivity of $\bar{\epsilon}_{\mathrm{sin}}$ to sediment conductivity σ_r (Figure 2.2b) is shown by the relative change in the error caused by a factor 2 change in σ_r centered at $\sigma_r = 0.1$. The graphed quantity is the ratio between $\bar{\epsilon}_{\mathrm{sin}}$ calculated for $\sigma_r = 0.1/\sqrt{2}$ and for $\sigma_r = 0.1\sqrt{2}$. For thin sediments the factor approaches 2, as expected from the 1D definition of λ, but if the sediments are very thick the relative change is smaller. This demonstrates that if the electric field reaches to the bottom of the sediments then the sensitivity to σ_r is linear, according to the 1D approximation.

The depth-varying velocity error ϵ'_{std} is not realistic for this geometry, because the infinite sinusoidal velocity prevents J_x from approaching the 1D approximation at small aspect ratios. $\boldsymbol{J}$ flows in elliptical cells that are strongest at $z = -H'$ even for $H/L \ll 1$, instead of becoming nearly horizontal and evenly distributed in the two ocean layers as expected. Analysis of the depth-varying error is performed for the more realistic later two geometries.

The contribution from F_h only occurs for water motion that is perpendicular to magnetic north. That these terms scale as H/L implies that their contribution to E_x and J_x may be significant at large wave-numbers. The form for the vertically averaged electric

field is

$$
\begin{aligned}
\overline{E}_{x,F_h} = &F_h\, v_0 \sin(\alpha x)\, \frac{1}{H_s \alpha \operatorname{scrcs}(\alpha H)} \left\{ \left[\cosh(\alpha H') - 1\right] \cdot \right. \\
&\left[\operatorname{scrcs}(\alpha H) + \operatorname{scrcs}(\alpha(H - H')) + \sinh(\alpha(H_s - H))(1 - \sigma_r)\right] \\
&\left. + \sin(\alpha H')\left[\operatorname{ccrss}(\alpha(H - H')) - \operatorname{ccrss}(\alpha H)\right] \right\}
\end{aligned}
\tag{2.29}
$$

In the small wavenumber limit this becomes

$$
\lim_{\alpha \to 0} \overline{E}_{x,F_h} \; \to \; \frac{H'}{H} v_0 \sin(\alpha x) F_h (1 - \frac{H}{H_s}) \sigma_r
\tag{2.30}
$$

The importance of F_h-induced terms is due to their magnitude relative to the dominant signal induced by F_z. In the small wavenumber limit, the ratio of the depth-uniform E_x from F_h compared to that from F_z is

$$
\frac{F_h}{F_z} \frac{\sin(\alpha x)}{\cos(\alpha x)} (1 - H/H_s)\sigma_r(1 + \lambda)
\tag{2.31}
$$

Three of the factors are less than 1 over most of the globe: $F_h/F_z < 1$ at mid-latitudes and higher, seafloor sediment is typically thin in the open ocean, with a typical maximum scaling of $H_s \le H/2$ and thus $1 - H/H_s \le 0.5$ is of order 0.1, and the effective sediment conductivity σ_s is less conductive than seawater by a factor of 4–10. The remaining factor $1 + \lambda_{1D}$ is slightly greater than 1 in the open ocean, usually < 1.2, although it can reach values of 2 or larger.

The F_h contribution is out of phase with the velocity forcing ($\sin(\alpha x)/\cos(\alpha x)$), the electric field in energetic regions will be almost entirely due to F_z. Near the center of the jet there is a $1/L$ dependence in agreement with the scaling of (2.29), because $\sin(\alpha x) \sim \alpha x$ in the small wave-number limit. On the edges the contribution from F_h will be relatively larger, even though the magnitude remains small relative to v_0 due to the scaling of the other factors. In fact, at $x = \pm L$ the relative contribution from F_h is infinite. Because F_h is expected to be most significant near the edges of velocity jets, it is more physically meaningful to evaluate this effect for a bounded velocity feature, which is done so below in section 2.4.3

To summarize the results, the velocity errors for a sinusoidal velocity and the dominant magnetic component F_z depend most strongly on the aspect ratio H/L, with further exponential dependence on sediment thickness and conductivity through their combination in $\lambda_{1D} = (H_s - H)\sigma_r/H$. Errors are less than 3% for sediment as thick as the water column and typical sediment conductivities ($\sigma_r = 0.1$). The velocity error in the east velocity component cause by induction with F_x generates the largest deviations from the 1D approximation near the edges of velocity jets.

2.4.3   Analytical solution: velocity jet

A finite velocity forcing is a better representation of realistic flows in the ocean than the sinusoidal shape used above. Such a form is obtained by performing a Fourier summation of the analytical solution (2.10). The 4 non-dimensional parameters are the same as in the analytic solution above, except that now L refers to the full width of a bounded velocity field.

The solution for one set of parameters is presented first to provide a physical basis for the 2D solution and to present the methods of calculating depth-uniform and depth-varying velocity errors.

Representative Example

Figure 2.3 shows the solution for width $L = 10$ km, jet depth $H' = 500$ m, water depth $H = 1000$ m, sediment depth $H_s = 2000$ m, and relative sediment conductivity $\sigma_r = 0.1$. The width of 10 km is smaller than could be expected realistically, as it requires an aspect ratio of 0.1, but it shows how the electromagnetic solution deviates from the 1D case. The horizontal electric field is not vertically uniform due to spreading of E_x in the sediment. There are also small regions of negative E_x at the edges of the jet (not visible with this choice of contours). Although the dominant component of electric current density is J_x, the aspect ratio is large enough to see that J_z has a dipole structure and completes the circuit in the vertical plane. For this example the only induction is due to the vertical magnetic field. A horizontal magnetic field F_x would predominantly generate vertical

electric currents, but because of the large aspect ratio the horizontal electric current density may be significant.
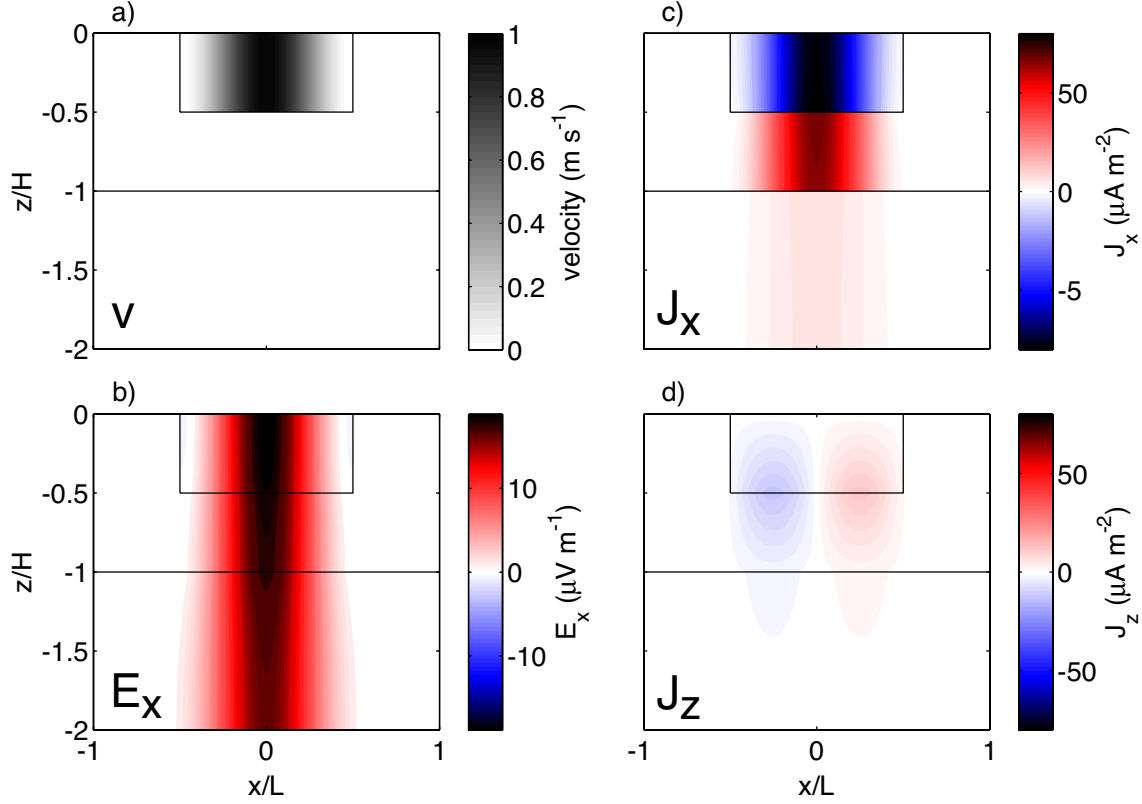
Figure 2.3: Solution for a representative case with a cosine jet forcing: (a) velocity, (b) E_x, (c) J_x, and (d) J_z. The solution is for a small-width jet, with $L = 10$ km, $H' = 500$ m, $H = 1000$ m, $H_s = 2000$ m, and $\sigma_r = 0.1$.

The depth-uniform components and their errors are shown in Figure 2.4. The $\overline{\boldsymbol{v}}^*$ (red solid line) calculated from the vertically averaged electric field does not differ much from the 1D $\overline{\boldsymbol{v}}^*$ (blue dashed line). With $\lambda_{1D} = 0.1$ for this case $\overline{\boldsymbol{v}}^*$ is only 10% smaller than $\overline{\boldsymbol{v}}$ (black). Panel (b) shows depth-uniform velocity errors $\overline{\epsilon}$ from two ways of calculating λ. The error that results from applying the 1D theory with knowledge of the sediment $\overline{\epsilon}_{1D}$ (solid line) has amplitudes of 0.002–0.004 m s^{-1}. Spreading of electric field outside of the jet is shown by non-zero $\overline{\epsilon}_{1D}$ for $|x| > L/2$. Even if this electric field is incorrectly interpreted as due to a local velocity, the magnitude is less than 1 mm s^{-1} ($< 2\%$ relative
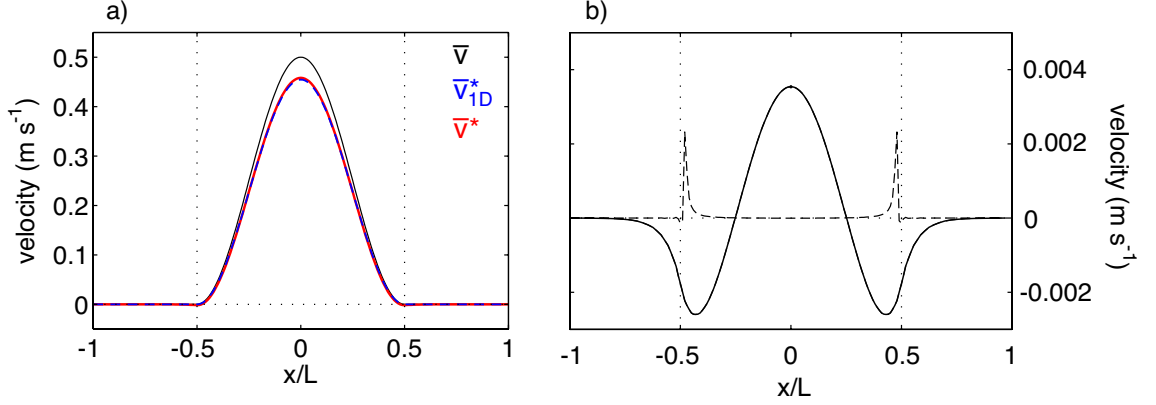
Figure 2.4: (a) Depth-uniform velocities $\overline{v}$ (black solid), $\overline{v}_{1D}^*$ (blue dashed), and $\overline{v}^*$ (red solid). (b) Depth-uniform velocity error, $\overline{\epsilon}_{1D}$ (solid) and $\overline{\epsilon}_{dx}$ (dashed). The dashed vertical lines show the edge of the cosine jet, and the parameters are the same as in Figure 2.3.

error compared with $\overline{v}$).

If there is no independent knowledge of the sediment, then λ must be calculated heuristically from changes in the velocity forcing. The use of λ_{dx} assumes that the cross-stream structure of the jet is sampled, such as due to horizontal meandering of the jet during repeat sampling. The depth-uniform error from λ_{dx} (dashed line) is near zero in the center of the jet, with maximum errors of 2 mm s^{-1} in a small region near the edge of the jet.

To summarize the depth-uniform error for this set of parameters $(L, H', H, H_s, \sigma_r)$ the value of $\overline{\epsilon}_{1D}$ at $x = 0$ is taken, shown by the dot in Figure 2.4 and notated ϵ_{BT}.

The second type of error is the depth-varying errors, shown in Figure 2.5. Unlike the multiple ways to calculate the depth-uniform error, the depth-varying error is simply the difference between $v(z)$ and $J_x(z)/(\sigma F_z)$ with the vertical mean removed. In the water column, the errors are surface- and bottom-intensified (Figure 2.5a). The vertical second moment is at most 1 cm s^{-1} (Figure 2.5b, solid thin blue line), and the maximum error reaches 1.5 cm s^{-1} (blue dashed line). The bias introduced by referencing the relative velocity profile near the surface has a 60% larger second moment and a twice as large maximum error.

32
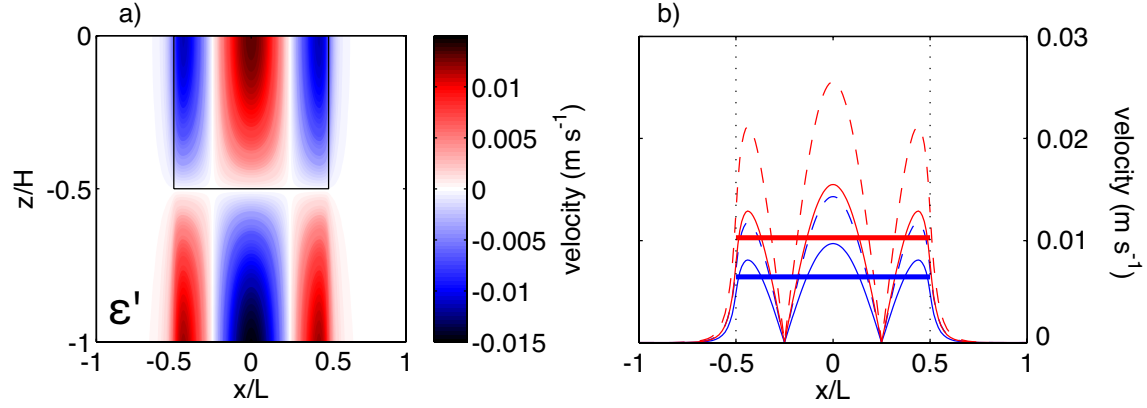
Figure 2.5: The depth-varying velocity errors induced by F_z for a cosine jet geometry. (a) The error ϵ', calculated using (2.16). (b) The vertical second moment $\epsilon'_{\text{std}}(x)$ (thin solid blue line), the vertical maximum $\epsilon'_{\text{max}}(x)$ (blue dashed line), and the second moment over the area of the jet ϵ'_{BC} (thick solid blue line). The biased errors as expected for a surface-referenced profiling float (e.g. an XCP) are shown in red: vertical second moment $\epsilon'_{\text{std,bias}}(x)$ (thin solid red line), the vertical maximum $\epsilon'_{\text{max,bias}}$ (red dashed line), and the second moment over the area of the jet $\epsilon'_{\text{BC,bias}}$ (thick solid red line) (see text for details). The dashed vertical lines show the edge of the cosine jet, and the parameters are the same as in Figure 2.3.

To summarize the depth-varying error the second moment of ϵ'_{std} is calculated over $|x| < L/2$, which is shown by the thick blue line (0.006 m s^{-1}) and notated ϵ_{BC}. For comparison, the biased quantity is shown in red and is 60% larger (0.01 m s^{-1}).

For the large aspect ratio limit we have to be careful that the induced electric from F_h doesn't unduly alter the horizontal electric field at the edges of the jet. F_h directly induces vertical electric currents, but it can generate E_x as the vertical currents form a complete circuit by connecting in the horizontal. Contributions from F_h only arise from the east component of velocity, so this discussion only applies to flows with a zonal component. The E_x that is induced by F_h is treated as an error term, since it is not expected in the 1D approximation. The depth-uniform quantity $\bar{\epsilon}_{\text{1D},F_h}$ is less than 0.002 m s^{-1} (Figure 2.6a), the same magnitude but slightly smaller than the depth-uniform error generated by F_z. The depth-varying error ϵ'_{std} resulting from F_h in the east component of velocity is roughly 2 times larger than that from F_z, with vertical second moments of 0.025 m s^{-1}, a maximum of 0.06 m s^{-1}, and a second moment across the jet of 0.02 m s^{-1} (0.03 m s^{-1}, 0.08 m s^{-1}, and 0.02 m s^{-1} for the biased quantities).

Parameter Space Analysis

To see how errors depend on the full parameter space, it is necessary to summarize each solution for one set of parameters with a single number. For the depth-uniform velocity error, this is chosen as $\bar{\epsilon}_{\text{1D}}$ evaluated at $x = 0$ and denoted ϵ_{BT}. This is the largest error shown in Figure 2.4b. The depth-varying error is summarized by the second moment of ϵ'_{std} over $|x| < L/2$ and is called ϵ_{BC}.

The parameter space for the terms induced by F_z is shown in Figure 2.7, where the contoured quantity is in m s^{-1}. The shape of lines of constant error ϵ_{BT} are similar to the sinusoidal velocity forcing (Figure 2.2) but do not have as sharp a transition between the small and large regimes of H/L — in comparison this plot looks like it has been spatially smoothed. The depth-uniform velocity error decreases exponentially for H/L less than 0.5–1, the same value as found in Figure 2.2. For sediment as thick as the water, an error smaller than 0.01 m s^{-1} occurs if $H/L \leq 0.01\,\lambda_{\text{1D}}^{-4/3}$, as found by an approximate
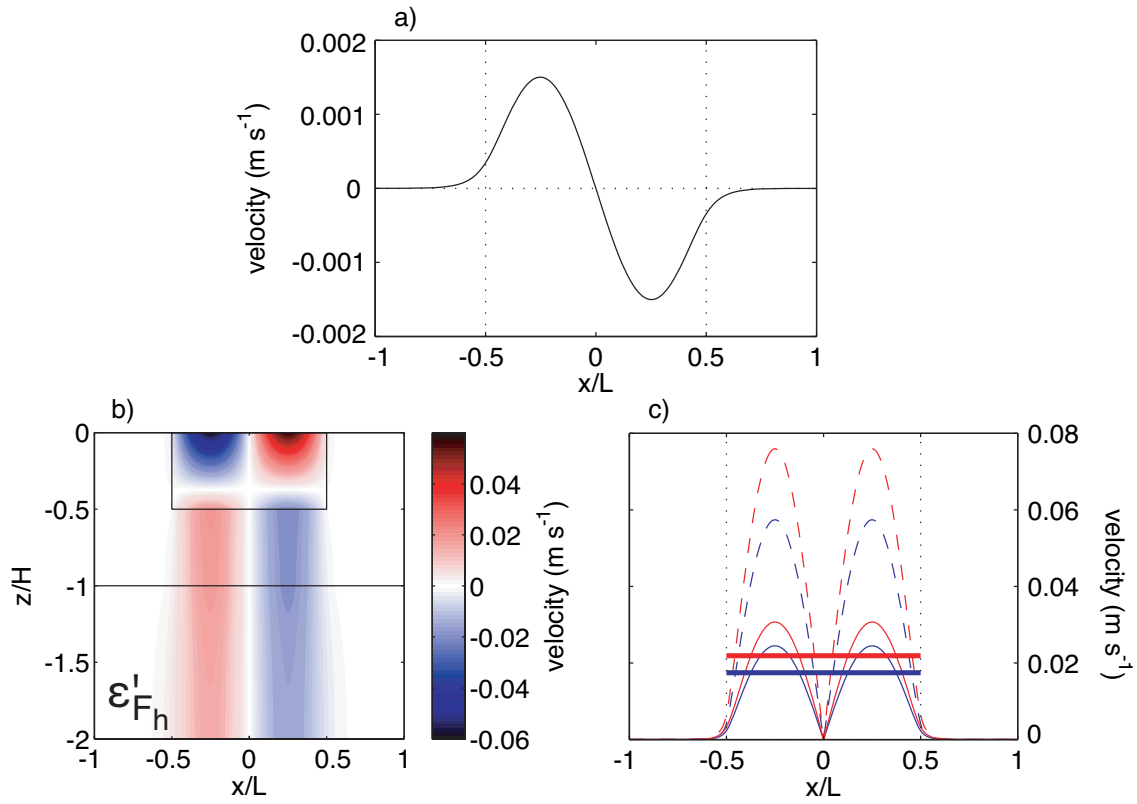
Figure 2.6: The velocity errors that arise from terms induced by F_h if they are interpreted as generated by F_z (see text). (a) $\bar{\epsilon}_{1D,F_h}$. (b) The depth-varying velocity error ϵ'_{F_h}. (c) The depth-varying errors, same as Figure 2.5b. The dashed vertical lines show the edge of the cosine jet, $F_h/F_z = 0.5$, and the parameters are the same as in Figure 2.3.

fit of the 10^{-2} contour. The depth-varying velocity error ϵ_{BC} has no dependence on the sediment thickness, and the magnitude of the error increases exponentially for H/L less than 0.5. A 0.01 m s^{-1} errors occurs if $H/L \geq 0.2$. The dependence on σ_r is slight for the depth-varying error.

A factor 5 change in H' (from $H'/H = 0.5$ to 0.1) reduces the depth-uniform and depth-varying errors by factors of 3–5, where the larger reduction occurs for thick sediment and large H/L.

The velocity errors that arise in the east component of velocity due to F_h are shown in Figure 2.8 for the same parameter space. The depth-uniform errors are smaller than those cause by F_z and depend mostly on the sediment thickness. For any aspect ratio, errors are below 0.003 m s^{-1} if the sediment is less than 3 times as thick as the water column. By contrast, the depth-varying errors due to F_h are larger than those due to F_z: a 0.01 m s^{-1} error occurs if $H/L \geq 0.06$. The transition region to uniform error with H/L still occurs at $H/L = 0.5$, although the maximum uniform error is around 0.05 m s^{-1}.

The influence of H' is much stronger for the F_h contribution: the depth-uniform error is reduced by 2–10 if H'/H changes from 0.5 to 0.1, while the depth-varying error is reduced by 25–30 for the same change. This is expected, as F_h generates a vertical electric potential, of which the magnitude depends on a vertical integral of the forced potential that is close to H'/H.

2.4.4 Sloping Bottom

To extend the analysis to include sloping topography, a second set of solutions are solved with the electromagnetic numerical model MOED (*Tyler et al.*, 2004). The schematic geometry (Figure 2.1c) has 4 spatial scales: the width of topographic slope L_t, the amplitude of topography A_t, the water depth at the center of the slope H_{mid}, the thickness of sediment ΔH_s, and the depth of the jet H'. Normalizing by L_t yields 4 non-dimensional spatial parameters, and the fifth non-dimensional parameter is σ_r.
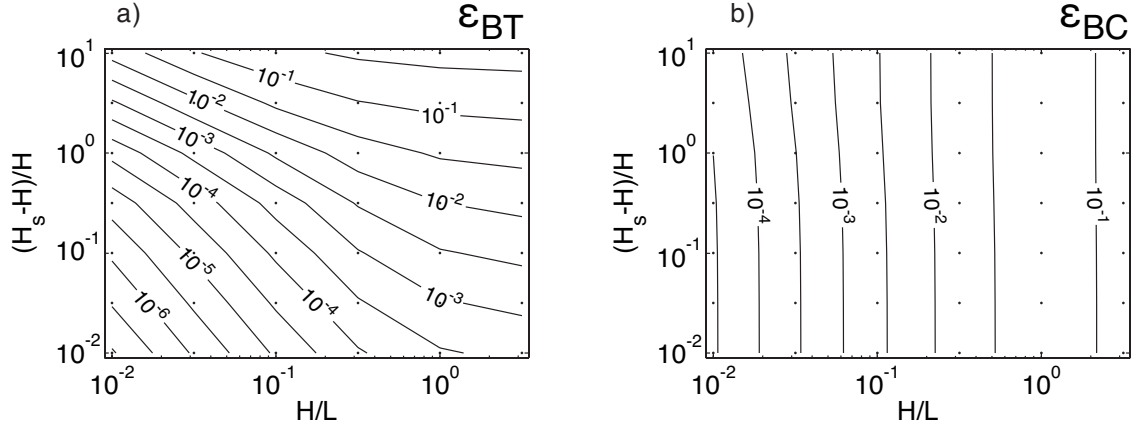
Figure 2.7: Velocity errors from the analytical model for finite forcing, induced by F_z. (a) Depth-uniform velocity error ϵ_{BT}. (b) Depth-varying velocity error ϵ_{BC}. The remaining parameters are $H'/H = 0.5$ and $\sigma_r = 0.1$.
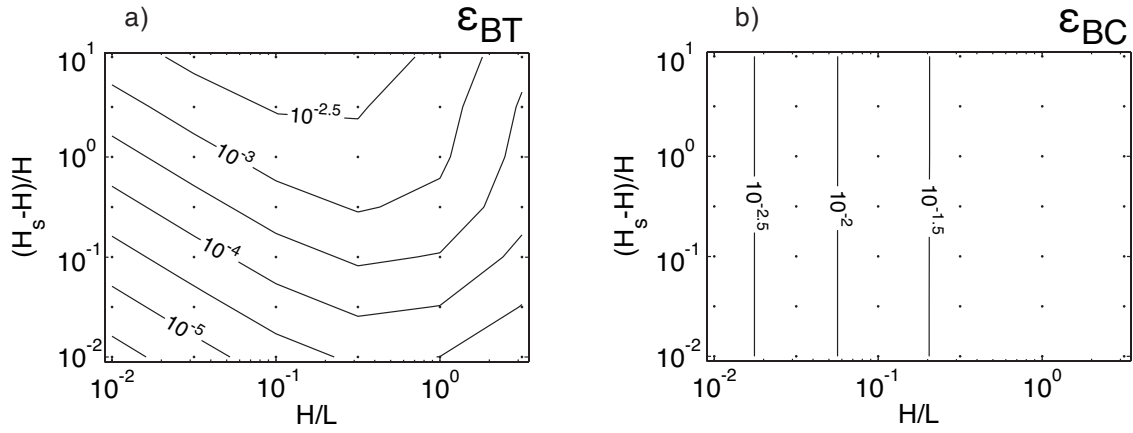
Figure 2.8: Velocity errors from the analytical model for finite forcing, induced by F_h. (a) The maximum depth-uniform velocity error $\bar{\epsilon}_{F_h}$ within $|x| < L/2$. (b) The second moment of ϵ'_{F_h} over $|x| < L/2$ and $-H < z < 0$. The remaining parameters are $H'/H = 0.5$ and $\sigma_r = 0.1$.

Representative Example

The solution for one set of parameters is presented first, before we generalize the results over the parameter space. Figure 2.9 shows the results for the parameters $L_t = 3.2$ km, $A_t = 350$ m, $H_{\mathrm{mid}} = 1000$ m, $H' = 325$ m, $\Delta H_s = 1000$ m, and $\sigma_r = 0.1$. This is equivalent to an average bottom slope of $9°$. The main influence of the topography is to allow an electric current to flow down the slope, both in the water and in the sediment. If the slope were to become shallower, the 1D approximation would hold better at each point along the slope and the vertical electric current density would decrease towards 0.

The depth-uniform component is presented in Figure 2.10. The depth-averaged velocity (black) varies in tandem with topography, and λ is larger on the shallower side because the sediment layer is thicker relative to water depth. The 1D $\overline{\boldsymbol{v}}^*$ (blue) is calculated according to 1D theory and is corrected to asymptote to the value of $\overline{\boldsymbol{v}}^*_{\mathrm{2D}}$ far from the slope. Smoothing σ across the seafloor/water interface introduces imprecision as to the vertical limits of the integrals that define $\overline{\boldsymbol{v}}^*$ and derived quantities. The physical requirement that $\overline{\boldsymbol{v}}^*$ attain a constant value far from topography is met on either side of the slope, however, so the numerical solution meets the physical expectation.

The quantities $\overline{\boldsymbol{v}}^*_{\mathrm{2D}}$ and $\overline{\boldsymbol{v}}^*_{\mathrm{1D}}$ (Figure 2.10a) are very close — their difference (Figure 2.10b, solid line) is at most 0.001 m s^{-1}. The 2D $\overline{\boldsymbol{v}}^*$ is larger (smaller) than $\overline{\boldsymbol{v}}^*_{\mathrm{1D}}$ on the upper (lower) part of the slope. To summarize this depth-uniform error the second moment is calculated over $|x| < L_t$, ϵ_{BT}. The error that results from using an empirical calculation of $\lambda_{\mathrm{d}x}$ (dashed line) is an order of magnitude smaller.

The depth-varying errors are shown in Figure 2.11. As with the analytical model with finite velocity, the errors are intensified near the water surface and near the seafloor (Figure 2.11a). There is a little spreading of the velocity error beyond the slope. The magnitude of ϵ'_{std} is below 0.004 m s^{-1} (solid thin blue line), with a second moment over $|x| < L_t$ of 0.0025 m s^{-1} (solid thick blue line). The biased quantities for surface-referenced profiling floats are 50% larger, but still well below instrumental accuracy. The depth-varying error is summarized by the second moment of ϵ'_{std} (0.002 m s^{-1}), ϵ_{BC}.
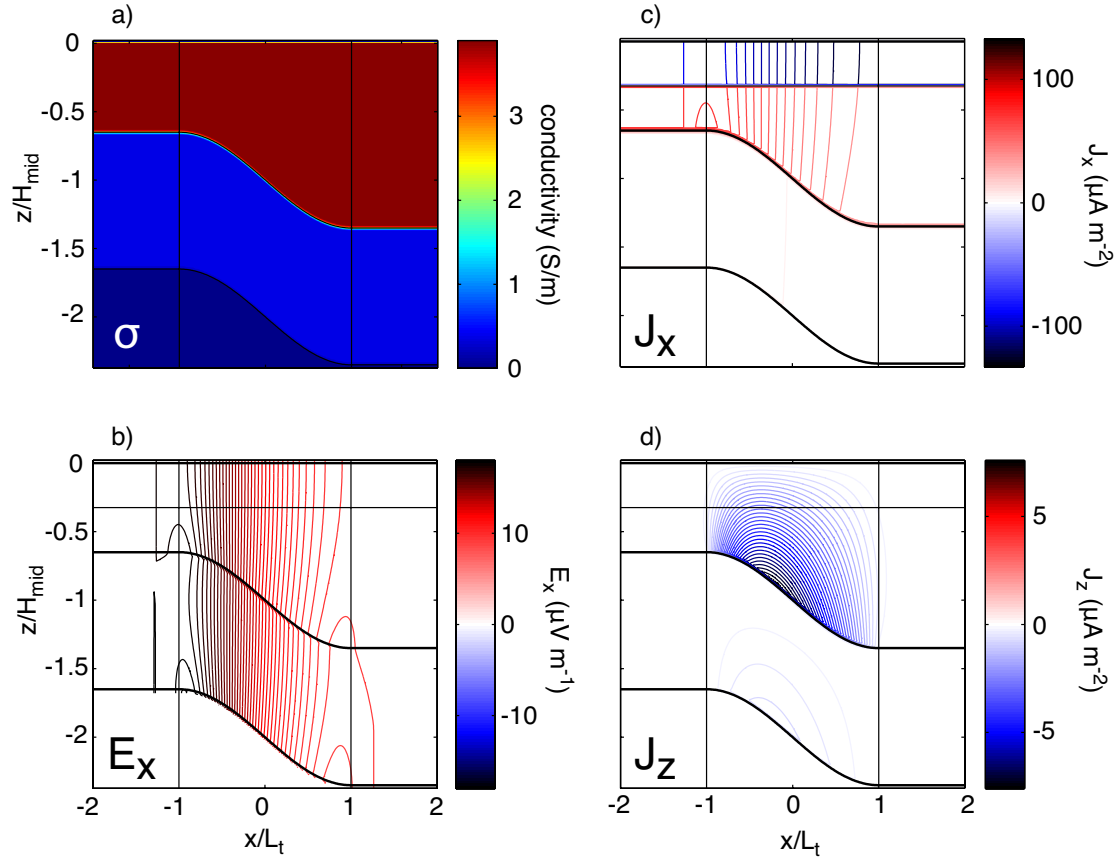
Figure 2.9: Solution for a representative case with sloping topography: (a) conductivity, (b) E_x, (c) J_x, and (d) J_z. Note that the color scales for the vertical component of $\boldsymbol{J}$ is a factor of 20 smaller than the horizontal color scales. The parameters used are $L_t = 3.2$ km, $A_t = 350$ m, $H_{\mathrm{mid}} = 1000$ m, $H' = 325$ m, $\Delta H_s = 1000$ m, and $\sigma_r = 0.1$. The maximum bottom slope is $3°$.
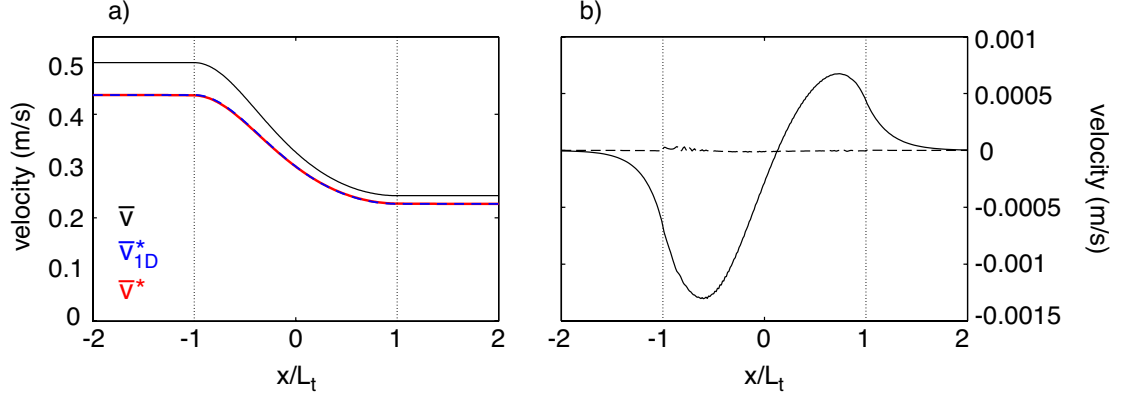
Figure 2.10: Vertically averaged parameters, MOED with bottom slope. (a) $\overline{\boldsymbol{v}}$ (black solid), $\overline{\boldsymbol{v}}(1 + \lambda_{1D})$ (blue dashed), and $\overline{\boldsymbol{v}}^*$ (red solid). (b) Depth-uniform velocity error $\bar{\epsilon}_{1D}$ (solid) and $\bar{\epsilon}_{dx}$ (dashed). The same parameter set is used as in Figure 2.9.
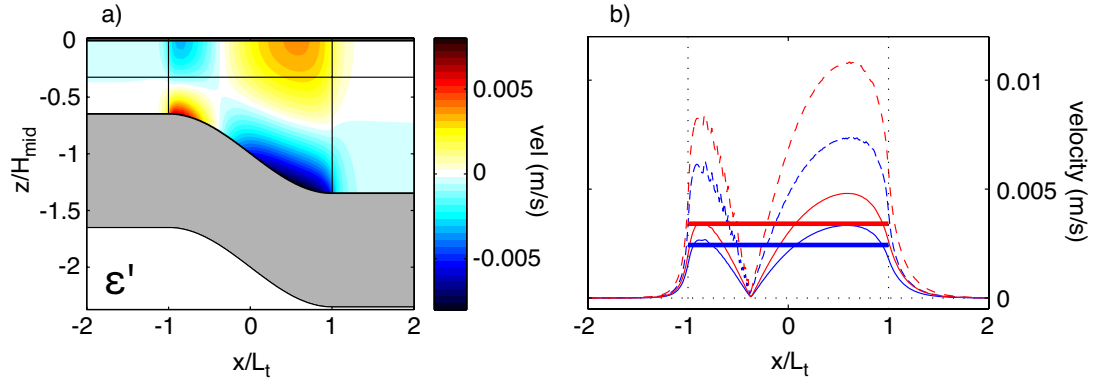
Figure 2.11: The depth-varying velocity error. (a) ϵ' in the water, calculated using (2.16). (b) the vertical second moment ϵ'std (blue solid), the maximum in the vertical $\epsilon'_{\max}$ (blue dotted), and the second moment of ϵ'_{std} across the jet ($|x| < L/2$), or ϵ_{BC}. The same biased quantities are in red. The same parameter set is used as in Figure 2.9.

Parameter Space Analysis

The parameter space for velocity errors are presented in Figure 2.12. At small topographic aspect ratios H_{mid}/L_t the depth-uniform error ϵ_{BT} depends on $\Delta H_s/H$, but for larger aspect ratios the error loses its dependence on sediment thickness. The sensitivity of the error is proportional to σ_r. The combined dependence is roughly proportional to λ_{1D}. If the topographic relief A_t/H_{mid} is small (< 0.35) the depth-uniform error is similarly small, but for values greater than 0.4 the error is most correlated with H_{mid}/L_t. Generally, errors are less than 0.01 m s^{-1} if $H_{\mathrm{mid}}/L_t < 1$, or less than 0.003 m s^{-1} if $H_{\mathrm{mid}}/L_t < 0.3$ if the remaining non-dimensional parameters are not at the extreme end of their ranges.

In contrast, the depth-varying velocity error ϵ_{BC}, the standard deviation of ϵ'_{std} over $-L_t < x < L_t$, depends mostly on H_{mid}/L_t. The error is largest if the topographic relief and the jet depth are near-equal amplitude ($A_t/H_{\mathrm{mid}} = 0.5$). As A_t increases the depth of the jet decreases because $\overline{v}$ is forced to be constant on the shallow side of the slope, which leads to a large reduction in $\overline{v}$ over the slope and on the deep side. On the other hand, it is more obvious that a small topographic relief leads to smaller depth-varying errors. There is a counter-intuitive decrease in the error with increases in $\Delta H_s/H_{\mathrm{mid}}$ and σ_r. The reduction is small: a factor 100 increase in $\Delta H_s/H_{\mathrm{mid}}$ reduces ϵ_{BC} by a factor of 3, and a factor 4 increase in σ_r leads to a factor 1.5–2 reduction. The lines of constant error are nearly vertical when the parameter space is viewed with $\Delta H_s/H_{\mathrm{mid}}$ or σ_r on the ordinate (not shown).

2.5   Discussion

The general question this study addresses is to what extent does the electric field at one location depend on the surrounding velocity and conductivity (seafloor and sediment) structure? The approach taken isolates the effect of gradients in velocity and topography for independent analysis on the basis of non-dimensional scales. Having presented solutions for three geometries earlier, we now discuss generally how the magnetostatic solutions are perturbed from the 1D situation. Although the simple nature of the geometries are applicable to many realistic situations, not every type of flow has been explicitly
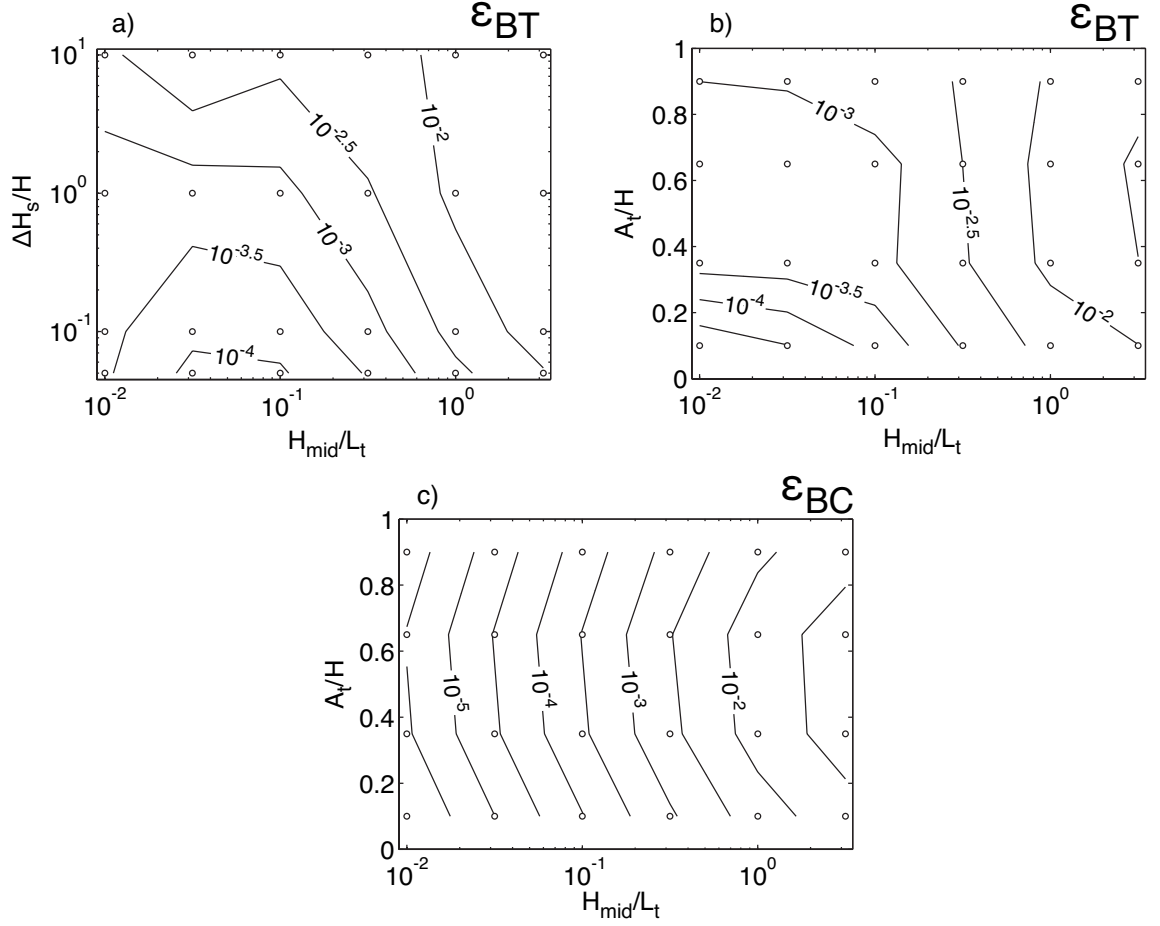
Figure 2.12: Parameter space representation of velocity errors from the geometry with sloping topography, terms induced by F_z. The depth-varying error ϵ_{BT} plotted for (a) A_t/H_{mid} and H_{mid}/L_t, with $\Delta H_s/H_{\mathrm{mid}} = 1$, and for (b) $\Delta H_s/H_{\mathrm{mid}}$ and H_{mid}/L_t, with $A_t/H_{\mathrm{mid}} = 0.35$. (c) The depth-uniform error ϵ_{BT}. The common parameters are $H_{\mathrm{mid}} = 1000$ m and $\sigma_r = 0.1$.

modelled and so the extension of our results to other geometries is discussed. The non-dimensional parameters were prescribed without recourse to dynamic constraints, so it remains to proscribe the regions of parameter space that are not realistic.

2.5.1 General Structure of 2D Perturbations

To present how the 2D solutions are perturbed from that expected by the 1D approximation, unrealistically narrow width-scales are used so that the 2D effects are obvious. The 1D approximation assumes that electric currents flow horizontally and that all points in the vertical are at the same electric potential.

The perturbations that arise from velocity gradients are shown (Figure 2.13) by a stream function for $\boldsymbol{J}$, ψ_J (top row) and by the electric potential ϕ (bottom row). The solutions are from the analytic model with a finite cosine jet for the parameters $L = 500$ km (left column) and $L = 1$ km (right column), with common values of $H = 1$ km, $H' = 500$ m, and $\sigma_r = 0.1$. The vertical exaggeration for $L = 500$ km is 500, whereas for $L = 1$ km it is 1. The electric current stream function shows the paths along which electric currents flow. It is defined by $\nabla_h \times \hat{\boldsymbol{k}}\psi_J = \boldsymbol{J}$ and is calculated directly with the same Fourier summation as used to calculate $\boldsymbol{E}$ and $\boldsymbol{J}$.

When $L = 500$ km, electric currents are confined within the jet (Figure 2.13a) and they flow horizontally, as demonstrated by vertical lines of electric potential (Figure 2.13c). When the velocity scale decreases ($L = 1$ km), these currents develop a vertical component. If L is small enough, the electric currents no longer fully reach to the bottom of the sediment column (Figure 2.13b) and the electric field is weaker in the sediment and is no longer vertically uniform (Figure 2.13d). This has the effect of reducing the effective sediment shorting: E_x averaged in the water column is larger than predicted by the 1D theory. This effect is independent of H and H', and the parameter space analysis shows that the error is less than 0.01 m s^{-1} if $H/L \leq 0.01\,(\lambda_{1\text{D}})^{-4/3}$. Weak electric fields extend beyond $|x| < L/2$ to regions where there is no velocity forcing, but the magnitudes are less than a few percent of the maximum $\overline{\boldsymbol{v}}$ at the center of the jet.

Perturbations caused by sloping topography are presented in Figure 2.14. The solu-
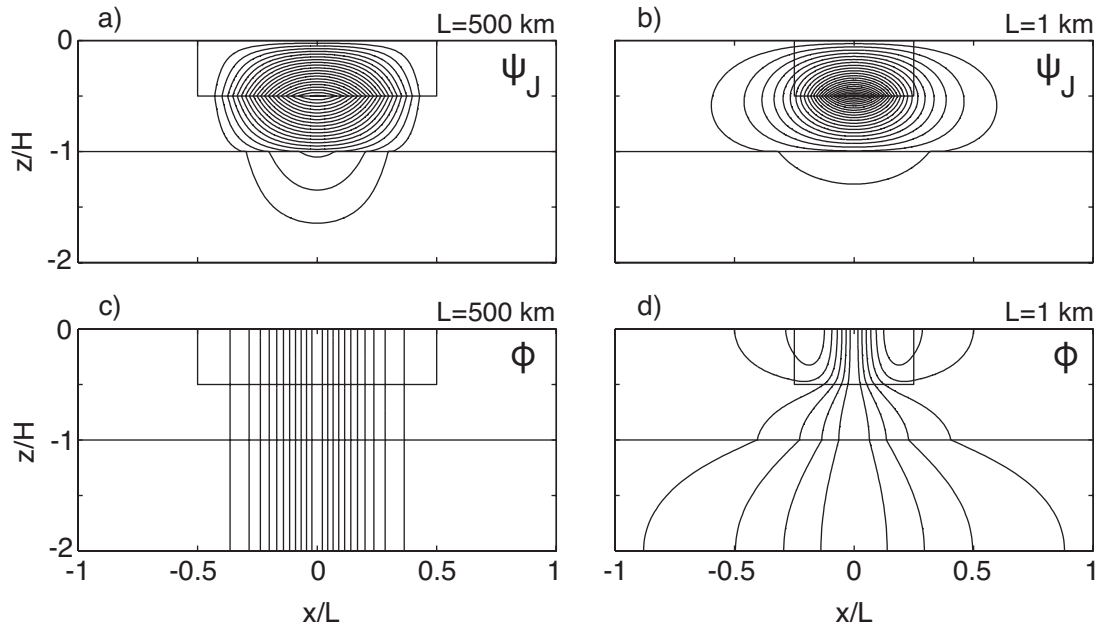
Figure 2.13: The changes in the electric current stream function ψ_J and the electric potential ϕ as L decreases and velocity gradients increase. A geometry that is nearly 1D ($L = 500$ km) is shown in the left column with a vertical exaggeration of 500. A geometry that is fully 2D ($L = 1$ km) is shown in the right column with no vertical exaggeration. ψ_J calculated by Fourier summation is in the top row, with contours (a) every 0.002 A m^{-1} and (b) every 0.001 A m^{-1}. ϕ calculated by Fourier summation is in the bottom row, with contours (c) every 0.2 V and (d) every 0.001 V. The other parameters are the same, $H = 1$ km, $H' = 500$ m, $H_s = 2$ km and $\sigma_r = 0.1$.

tions are from MOED for $L_t = 100$ km and $L_t = 1$ km, with common values of $A_t = 333$ m, $H_{\mathrm{mid}} = 1$ km, $H' = 500$ m, and $\sigma_r = 0.1$. The vertical exaggeration is 100 and 1 for L_t of 100 km and 1 km. The stream function ψ_J is calculated numerically in Matlab. The stream lines are chosen to be visually evenly spaced in the water column, but the separation between adjacent lines is smaller in the sediment.

When the sea floor is no longer horizontal but the slope (or H_{mid}/L_t) is small, the electric currents follow the slope smoothly (Figure 2.14a). Streamlines enter the sediment in close relation to how $\overline{v}$ increases as the bottom shoals, via the 1D approximation. Isopotentials are vertical, demonstrating that electric currents are almost entirely horizontal (Figure 2.14c). As the slope steepens, the electric currents refract when they enter the sediment and they don't uniformly fill the bottom of the sediment near $x/L_t = 0.5$ (Figure 2.14b). This effect can be seen more clearly in Figure 2.11a, where negative (positive) velocity errors ϵ' at the seafloor corresponds to positive (negative) depth-uniform error $\overline{\epsilon}_{\mathrm{1D}}$. The electric potential changes from vertically uniform to tilted perpendicular to the bottom (Figure 2.14d). Extrema in $\overline{E}_x$ occur at the upper and lower parts of the slope.

2.5.2 Velocity Errors for 2D perturbations

The deviations of the electric current stream function ψ_J and the electric potential ϕ discussed above are slight, even for the unrealistic cases of velocity jets and bottom slopes that have a 1:1 aspect ratio (Figures 2.13b,d and 2.14b,d). Although a case of 1:10 aspect ratio (0.1) is more realistic, the 2D perturbations are practically indistinguishable from the 1D approximation. The calculation of velocity errors $\overline{\epsilon}$ and ϵ' shows more precisely the errors that would arise from a 1D interpretation of E_x and J_x generated by 2D features.

The parameter space analyses show that there is a common transition point below which the depth-uniform errors decrease exponentially with H/L, which occurs at H/L or H_{mid}/L_t of 0.5–1. The error $\overline{\epsilon}$ depends exponentially on both $(H_s - H)/H$ and σ_r, in particular, $\overline{\epsilon}_{\mathrm{1D}}$ varies closely with λ_{1D}. The dependence of depth-uniform errors on H'/H is close to linear. The depth-varying errors depend most strongly on H/L or H_{mid}/L_t, with secondary dependence on H'/H and A_t/H_{mid}. The largest ϵ' errors occur when the
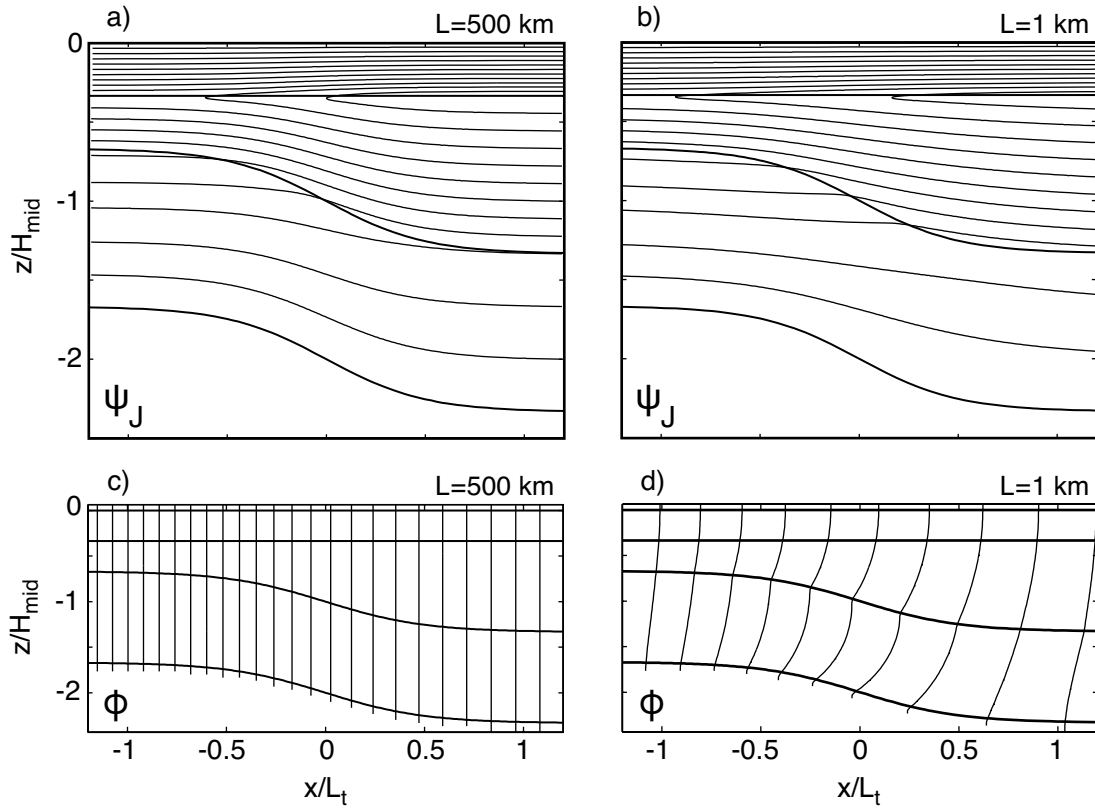
Figure 2.14: The change in $\boldsymbol{J}$ and $\boldsymbol{E}$ as L_t decreases and topographic gradients increase. (left column) A geometry that is close to 1D, $L_t = 100$ km, with a vertical exaggeration of 100. (right column) A geometry that is fully 2D, $L_t = 1$ km, with no vertical exaggeration (top row) Stream lines of ψ_J calculated numerically (not evenly spaced). (bottom row) The electric potential ϕ, with contours every 0.1 V (c) and every 0.0025 V (d). The other parameters are the same, $A_t = 333$ m, $H_{\mathrm{mid}} = 1$ km, $H' = 500$ m, and $\sigma_r = 0.1$.

jet depth or the slope height fills an equal fraction of the water column, with decreasing error for larger or smaller values of these two parameters. The depth-varying error is only weakly dependent on the sediment thickness ΔH_s or the sediment conductivity σ_r. Roughly, depth-varying errors generated by F_h are largest for a given aspect ratio, values of < 0.01 m s^{-1} for $H/L \leq 0.2$; followed by those due to $F_z < 0.01$ m s^{-1} for $H/L \leq 0.06$; and the smallest arise from sloping topography, < 0.01 m s^{-1} for $H_{\mathrm{mid}}/L_t \leq 1$.

When velocity gradients are large, perturbations from the 1D approximation result from electric currents not reaching the bottom of the sediment layer (for the depth-uniform errors) and not exactly following the velocity forcing (for the depth-varying errors). The breakdown is related to the increase of the vertical component J_z, which implies a scaling of H/L because it is proportional to $\partial v/\partial x$ in the small aspect ratio approximation (*Sanford*, 1971).

The definition of the velocity errors as either depth-uniform $\bar{\epsilon}$ and depth-varying ϵ' decouples these two modes from each other for the analyses performed here. These errors were used because measurements are either of the nearly depth-uniform electric field (using stationary electrodes) or of the depth-varying signal from J_x (electrodes on vertically profiling floats).

Full water column averaging was used to calculate $\overline{\boldsymbol{v}}^*$ and $\overline{\epsilon'}$ from the model solutions, but in practice the use of averages over the full water column is not logistically practical. Stationary electrodes measure E_x at one point in the vertical, or vertical profiling floats are referenced to absolute velocity over some fraction of the water column (e.g. XCPs are typically referenced with shipboard ADCPs within the upper 300 m). Thus, the 2D perturbation of the E_x measured on the seafloor is not exactly the same as $\bar{\epsilon}$, but rather to $\bar{\epsilon}_{\mathrm{bias}} = \bar{\epsilon} + \epsilon'(z = -H)$. Referencing vertical profilers over a fraction of the water column can bias the velocities slightly, which was explicitly calculated by the biased quantity $\epsilon'_{\mathrm{bias}}$. The errors are smallest if the referencing occurs outside of the velocity jet, either for $\bar{\epsilon}_{\mathrm{bias}}$ or $\epsilon'_{\mathrm{bias}}$. For surface-intensified flow, instrumental errors are smaller if the reference velocity or velocities are close to the seafloor.

2.5.3   Extension to Baroclinic Flow

The velocity geometries used in the three cases all contain surface intensified oceanic flow. Many oceanic flows are either surface or bottom intensified, with both barotropic and baroclinic velocity components, so the two-layer geometry can be broadly applied. Purely baroclinic flows are not directly analogous to these cases since they lack a barotropic component.

For baroclinic flows the bottom sediment has less of an influence on the electric field, for the electric currents are able to form closed circuits in the ocean. This is substantiated by the lack of dependence on sediment thickness or sediment conductivity. The maximum errors were found when the velocity occupies half of the water column, that is when the vertical second moment of velocity is the largest. Higher modal structure, because it has a smaller velocity second moment, may lead to smaller depth-varying velocity errors.

Internal tidal beams are the extreme case of purely baroclinic velocity, for they contain high modes and can propagate at relatively steep angles but have no $\overline{v}$. Internal waves at near-inertial frequencies have nearly horizontal velocities, and the most common frequencies that are less than $\sqrt{2}N$ (N is the buoyancy frequency) propagate at angles less than $45°$ in the vertical. The high mode structure makes it likely that most electric currents form closed circuits in the water column. The E_x induced by F_h will be most likely to influence the 1D approximation, although the magnitude of the contribution from F_z is expected to the same order but smaller.

The vertical scale of the barotropic mode H is always equal to or greater than the vertical scale H' for baroclinic modes. Thus, the barotropic mode will always have a larger aspect ratio. As the aspect ratio is found to govern the deviations from the 1D approximation, baroclinic modes are necessarily flatter than barotropic scales and thus are expected to be closer to the 1D approximation. Further study is needed to definitively resolve the depth-varying velocity errors associated with high-mode baroclinic flow.

2.5.4   Geophysical Constraints on Width Scales L and L_t

The model geometries were solved for a wide range of parameters, but realistically certain scales will not be encountered in the ocean. Because the geometries of ocean velocity and sediment were prescribed initially without recourse to their geophysical constraints, now the realistic range of scales must be discussed.

Velocity Aspect Ratios   The starting assumption of the theory developed by *Sanford* (1971) was that ocean flow is much wider than it is deep, $H/L \ll 1$. The governing vertical scale is the effective water depth D, which is often close to H for thin sediments, whereas ocean flow can be as wide as ocean basins. As small aspect ratios are governed by the 1D approximation, we only seek an upper limit for aspect ratios. For comparison with observations, the quantity L is the full-width of the cosine jet, whereas the half-width is more practical in observations. This discussion cannot account for all situations, but gives guidelines that are generally applicable.

In the open oceans, the geostrophic balance is the primary dynamic equilibrium. The barotropic Rossby radius $R_{\mathrm{BT}} = \sqrt{gH}/|f|$ is the distance over which flow adjusts to geostrophy (g is gravity, $f = 2\Omega \sin(\text{latitude})$ is the Coriolis parameter, and Ω is the angular rotation rate of the earth). Even at high latitudes and in shallow water this scale is greater than 200 km ($H \geq 100m$, all latitudes), and so $H/R_{\mathrm{BT}} \ll 1$.

The shape of velocity for the finite-forcing analytic geometry remains idealized due to the two-layer geometry and the vertically uniform velocity in the top layer. Although large-scale open-ocean flow doesn't typically have a step change in velocity, the shape is representative of a broad range of surface- or bottom-intensified flows. One example in the open ocean is how the Gulf Stream remains surface intensified when it enters the open ocean, taking 100s of km before the velocity in the deep ocean gains appreciable transport (*Johns et al.*, 1995; *Meinen et al.*, 2007) despite the seafloor deepening over 100 km along its path. Other situations that resemble a step change in velocity are flows over sills, in which case the bottom ocean layer is moving and the top is stationary, or two-layer exchange flow (e.g. through the Straits of Gibraltar).

The scale for baroclinic flow is $R_{\mathrm{BC}} = c_n/|f|$ where c_n is the wave speed of the nth baroclinic mode. This width scale is 10–30 km at high latitudes, and increases towards the equator ($Gill$, 1982), so H/L can potentially reach a maximum of order 0.1 at high latitudes although smaller values of 0.03 will typically be encountered. High mode structure or beams of internal waves are included in these phenomena, which have not been directly addressed by the geometries considered. Baroclinic eddies formed by instability often have a barotropic component. One example with small scales are eddies along the shelf-break front north of Cape Hatteras ($Churchill$ and $Gawarkiewicz$, 2008), which has aspect ratios of $\Delta z/\Delta x = 250$ m / 20–30 km $= 8 \times 10^{-3} - 1.25 \times 10^{-2}$.

Another way of considering baroclinic aspect ratios is through the Burger number $S^{1/2} = NH/(fL)$, which is the ratio of water depth H to Taylor column height fL/N (N is the buoyancy frequency). The value of S is typically less than 1, which implies that for typical stratification $N \leq 3 \times 10^{-3}$ s^{-1} and latitudes equatorward of 60°, H/L is less than 3×10^{-3} for baroclinic flow. For the near-shelf ocean off of Cape Hatteras values for S are found to range from 2–100 ($Savidge$ et $al.$, 2007), although these assume that H is the depth of the deep ocean (3 km) and that L is the width of the continental shelf (40–80 km) or that H/L is $4 \times 10^{-2} - 8 \times 10^{-2}$.

A second class of scales can occur in situations where the velocity jet is bottom trapped: this happens for dense flow over sills or through constrictions, such as the Denmark Strait, the Strait of Gibraltar, or through sills that separate ocean basins. These scales apply to both barotropic and baroclinic velocity components. The geometry of the sill and hydraulic constraints give rise to different dynamical scalings at the topographic restriction. Some examples of such conditions are: the Denmark Strait overflow with $\Delta z/\Delta x = 600$ m / 50 km $= 1.2 \times 10^{-2}$, the Mediterranean outflow/Strait of Gibraltar with 200–400 m / 20 km $= 1 - -2 \times 10^{-2}$, the Indonesian sills connecting the Pacific and Indian Oceans with 200 m / 30–60 $= 0.3 - -7 \times 10^{-3}$ ($Hautala$ et $al.$, 2001), Windward Passages into the Caribbean of 1000 m / 30 km $= 3 \times 10^{-2}$ ($Wilson$ and $Johns$, 1997). The maximum aspect ratio for these overflow regions is 0.03.

From these considerations an upper limit for the aspect ratio H/L is order 0.1 for

baroclinic flows, with barotropic flows occurring below 0.03.

Topographic Aspect Ratios and Geological Scales   A second set of geophysical constraints are necessary to limit the realistic topographic slopes. The geometry used for investigating topographic effects used independent scales for the width and height of the seafloor, L_t and A_t (the width and half-height), instead of the more standard geologic use of the slope angle $\theta = \tan^{-1}(\Delta z/\Delta x)$. A small region of steep slope will not effect the EM solution, however, the slope has to have a significant vertical extent compared to the water depth to appreciably change the EM response. The average slope angle of the sinusoidal topography over $-L_t/2 < x < L_t/2$ is shown in Figure 2.15a for the parameter space used for sloping topography.

Large-scale sloping topography are associated with continental margins (continental slopes), submarine ridges, escarpments and island-arc chains. *Pratson and Haxby* (1996) studied high-resolution bathymetry from 5 regions of the US continental margins. Typical slopes at a scale of 0.1 km ranged from 5° for unstable margins (tectonically active or salt-tectonized) to 8° for passive margins, although there are many small-scale features with steeper slopes. Topography from *Smith and Sandwell* (1997) at a resolution of 3 km shows the steepest part of the continental slope at these same locations to be 5–10°. Although slope stability in the instantaneous sense for sedimented regions is larger than these slopes (*Pratson et al.*, 2007), these smaller angles are maintained by numerous types of instabilities: spatially heterogeneous processes such as elevated pore pressure or water outflow through sediments or by temporally infrequent events such as turbidity currents (*Lee et al.*, 2007) or earthquakes (*Pratson and Haxby*, 1996). Another hypothesis for setting the slope of continental margins is the vertical propagation angle of the M_2 internal tide (*Cacchione et al.*, 2002), because critical reflection of internal waves generates high turbulence at the seafloor that prevents slopes from growing steeper. This angle is determined by the dispersion relation for internal waves and is close to the topographic slope for 2 of the regions considered by *Pratson and Haxby* (1996).

Igneous topographic features will have different controls on their slope than sedimented features. Examples of these are mid-ocean island chains, mid-ocean ridges, or escarpments

at transform boundaries. The slope of topography around Hawaii has maxima of 8–12° and median values of 4-5° (*Smith and Sandwell*, 1997). A second example is the Mendocino Escarpment, a transform fault extending off the coast of California that has slopes of up to 15° (*Smith and Sandwell*, 1997). The escarpment is nearly 2 km high and 10 km wide on one side, with a mean slope of 11°. For basaltic landforms there will be very thin or non-existent sediment layers, so the parameter space reduces to that for thin ΔH_s with little shorting through the sediment.

The two other geologic parameters, sediment thickness and relative sediment electrical conductivity, can be constrained by their observed global values. Total sediment depths range from 0 over newly formed oceanic crust to up to 10 km deep in old sedimentary basins. Passive sedimented margins typically have sediment thicknesses of 4–8 km within 100 km of the continental slope, while subducting margins have thicknesses of 1–4 km (*Laske and Masters*, 1997).

Sediment conductivity is largely constrained by porosity, as most oceanic sediments contain saltwater in their pores. The simplification of the sediment column into a homogeneous region of uniform conductivity σ_s means that the apparent conductivity is vertically weighted over the entire sediment column. In 1D cases the apparent conductivity is the vertical average of the sediment conductivity, but for 2D solutions the surficial sediments support strong J_x and are weighted more than the deep sediments in determining the apparent conductivity. For 2D situations the sediment influence on $\overline{v}$ loses the physical interpretation of the 1D approximation, as λ_{2D} depends on horizontal length scales in addition to the sediment properties.

Conductivities of specific sediment types and layers can vary from $\sigma_r \sim 0.05$ ($\sigma_s = 0.2$ S m^{-1}) for low-porosity consolidated silt to $\sigma_r \sim 0.5$ ($\sigma_s = 1.5$ S m^{-1}) for sandy unconsolidated sediments. In general porosity and conductivity decreases with depth in the sediment column because deeper sediments are more consolidated and undergo chemical changes as they lithify into a more solid state. Thus, unless a sediment column is unusually homogeneous its influence on the electric field through λ is through an apparent conductivity that is a vertical weighting of the depth-varying conductivity. Unusually

resistive sediment occurs if saltwater is displaced from interstitial pores by fresh water, hydrocarbons, gas hydrates, or solid salt/evaporites. These alternative pore fluids all act to make the sediment less conductive. Most of these features have a very heterogeneous distribution in oceanic sediment, so their existence or lack thereof in a region of interest will need to be independently verified.

2.5.5 Combined effect of velocity and topographic gradients

The geophysical constraints on scales of velocity and of topography are summarized in Figure 2.15b. The boxes show the realistic parameter space assuming no interactions between topography and velocity.

The analyses only extend the theory along each axis and don't cover how gradients in velocity and topography can interact. For small gradients the errors may be described by linear addition, but in general topographic and velocity gradients will interact non-linearly in terms of the 2D velocity errors. The errors from the two axes don't add linearly. A region with strong gradients of velocity and topography and thick sediment (Cape Hatteras) is investigated in detail in the next chapter.

There are two limitations with the chosen geometries. The geometry of the finite cosine jet, although close to the instantaneous shape of numerous ocean currents, will not accurately represent broader ocean currents that have sharper edges. A central region of uniform velocity will drive larger 2D perturbations at the edges than seen in the finite cosine jet. A case in point is J_x from the sinusoidal velocity: even with very small aspect ratios ψ_J still retains an elliptical shape instead of becoming horizontal. It is not just the immediate velocity gradient that influence J_x, but also the presence of neighboring strong velocity jets.

The second limitation is that the constant velocity layer used in the geometry of sloping topography is overly simplified. Not only does topography impose strong constraints on geostrophic flow, but it also separates regimes of different dynamics (e.g. shelf circulation and ocean-basin boundary currents). This choice of geometry was chosen to allow the general investigation done here over a feasible number of parameters, but more realistically

steep slopes tend to act as boundaries between different velocity regimes. Although it is expected that small-scale flows over topography will have larger 2D perturbations than resolved here, the dependence of errors on the non-dimensional scales will be similar.

The two processes that give rise to 2D electric field perturbations are summarized in Figure 2.15b. The second and third geometries resolve velocity errors along the two axes, along which rough velocity errors (both for $\bar{\epsilon}$ and ϵ') are summarized from the previous discussion. The realistic region of geophysical scales is shown by the red, blue, and black lines for barotropic, baroclinic, and topographic aspect ratios. The lower left corner is where the 1D approximation is strictly valid.

Although the combined effect of gradients in velocity and topography has not been investigated in this chapter, in the following chapter data from an extreme corner of the parameter space is investigated in detail. This data was collected across the Gulf Stream at Cape Hatteras, where velocity is strong and subject to sharp fronts and the continental slope is unusually steep. The depth-varying velocity error is a few cm s^{-1} while the depth-uniform velocity error is 0.1 m s^{-1}. This implies that there are not strong non-linear combination of perturbations caused by velocity gradients and sloping topography.

2.6   Conclusion

The influence of horizontal velocity gradients and sloping topography on motionally induced electric fields is investigated with schematic geometries. In regions where there are strong velocity gradients or steep topography, the calculation of velocity from measured electric fields is subject to errors if the standard 1D approximation is used. The magnitude and structure of these errors are quantified for three schematic ocean geometries that are solved by analytic and numerical methods. All geometries are in a vertical plane perpendicular to flow and describe a 2 layer ocean and a layer of sediment beneath.

The 1D approximation describes electric fields that are vertically uniform $(\overline{E}_{x,1\mathrm{D}})$ and electric current densities divided by conductivity $(J_{x,1\mathrm{D}}(z)/\sigma)$ that have the same vertical structure as velocity. This approximation is formally valid when the aspect ratio of height to width H/L is much smaller than 1 and when topographic relief is small relative to to
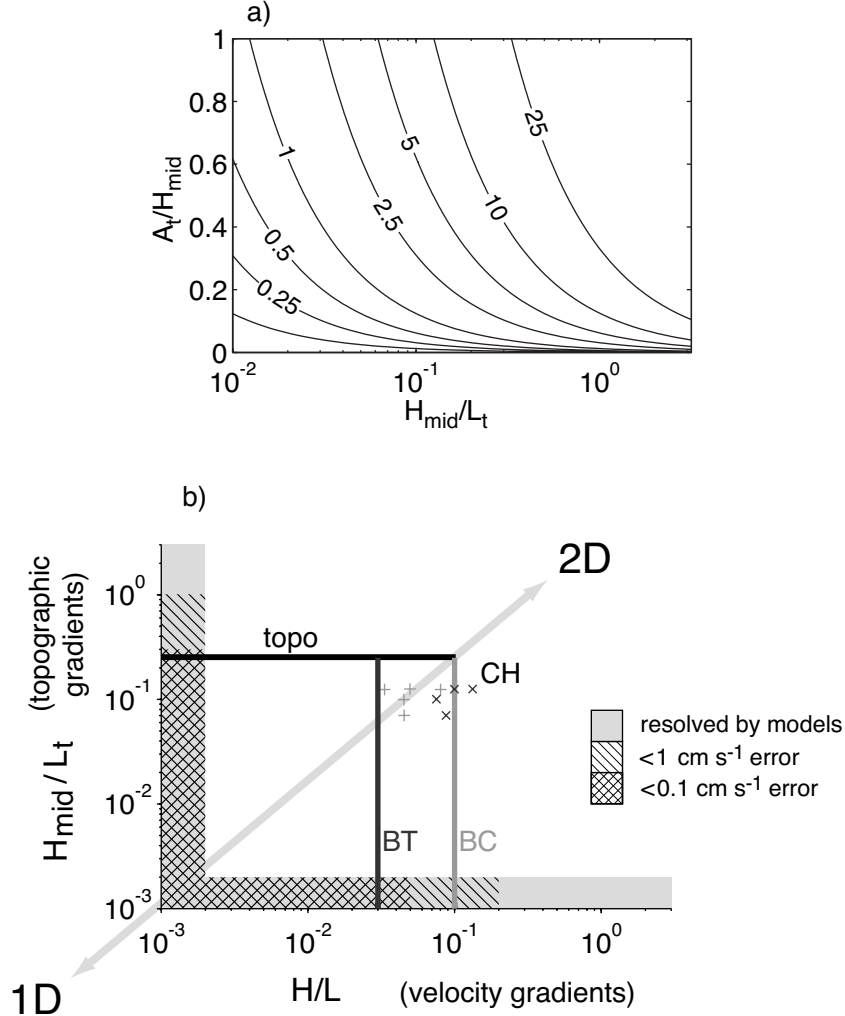
Figure 2.15: Parameter space for velocity scales and topography scales. (a) Mean slope angles in degrees that correspond to Figure 2.12. (b) Schematic representation of the resolved and realistic parameter space. The velocity aspect ratio is on the abscissa and the topographic aspect ratio is on the ordinate, with the regions with velocity errors smaller than indicated shown by hashes (for $(H_s - H)/H \leq 1$ or $\Delta H_s/H < 1$ and $\sigma_r = 0.1$). The region of expected maximum aspect ratios are outlined for the barotropic and the baroclinic velocity modes. For reference, the parameter space location of 5 stations in the Gulf Stream at Cape Hatteras are also plotted (denoted CH), for the baroclinic component (medium gray +) and the barotropic component (dark gray ×, two points are identical) as discussed in chapter 3.

the water depth ($A_t/H \ll 1$). As H/L and the topographic slope increase the electric fields become two-dimensional. Two criteria are used to evaluate the electric field solutions: the difference between the depth-uniform electric field $\overline{E}_x$ and that predicted by the 1D approximation $\overline{E}_{x,\text{1D}}$, and the second moment in the vertical between J_x/σ and the 1D approximation $J_{x,\text{1D}}/\sigma$. The criteria correspond to the two ways of measuring oceanic electric fields, whether from electrodes mounted on stationary or vertically-profiling platforms, and also to the decomposition of velocity into barotropic and baroclinic modes.

For all geometries, the depth-uniform and depth-varying velocity errors depend most strongly on the aspect ratio (H/L for velocity gradients or H_{mid}/L_t for topographic gradients). Depth-uniform errors depend on the relative thickness of ocean and sediment $(H_s - H)/H$ and the electrical conductivity of the sediment relative to seawater σ_r. In particular, their combination as λ_{1D} determines the depth-uniform error, which is less than 0.01 m s^{-1} for $H/L \leq 0.01 \, (\lambda_{\text{1D}})^{-4/3}$. Depth-varying errors, by contrast, depend most on the thickness of the jet H'/H and are insensitive to $(H_s - H)/H$ and σ_r. For aspect ratios smaller than 0.5–1 the magnitude of errors decrease exponentially with H/L.

General limitations on the largest aspect ratios possible comes from geophysical constraints on the velocity field or on topographic slopes. Rossby number and Burger number arguments show that velocity gradients are limited to aspect ratios no greater than 0.1. Barotropic flow generally is in the regime $H/L \leq 0.01$, whereas baroclinic flows can be an order of magnitude larger $H/L \leq 0.1$. Maximum slope angles of large relief topography are generally smaller than 10–15°, which is equivalent to $H_{\text{mid}}/L_t < 0.1$–0.5 (for A_t/H_{mid} of $1 - 0.2$). Realistic values for sediment thicknesses are less than 10 km and more typically 2–4 km for heavily sedimented passive margins, while the apparent relative conductivity of the sediment column has a smaller range of 0.05–0.5.

For realistic constraints on velocity aspect ratios, the maximum errors introduced by a 1D interpretation of the 2D solution are less than 2–5% for sediment that is no thicker than the water column and a relative conductivity of 0.1. Errors are smaller by a factor of 3 for a topographic slope of 10° with the same parameters. These analyses investigate the effect of velocity gradients and topographic slopes independently, but in realistic situations

both these two features may be present and will combine non-linearly.

This analysis has sought general results that are broadly applicable to many types of oceanic electric field measurements. The results lead to specific recommendations for incorporating into field experiments. Practically, a 2D interpretation of observations is too complicated for most field programs, so the focus is on mitigating for 2D perturbations in observations and for providing realistic (if unconfirmed) error estimates. Correcting 2D perturbations is the ideal goal, and though this is shown to be feasible in the next section such procedures are too involved to be of operational utility. The velocity errors that arise from 2D geometries depend on the platform used to collect measurements: stationary sensors will be subject to a depth-uniform error, while horizontally drifting instruments such as vertical profilers will include depth-varying errors.

The maximum velocity in the geometries is 1 m s^{-1}, and in weaker flow regimes the 2D errors will be reduced proportionally. Instrumental errors of electric field instruments have shown to be 1–2 cm s^{-1}, so it is only in locations that have strong 2D perturbations where the 2D velocity errors are the same magnitude or larger than instrument accuracy.

The general dependencies of these two types of errors on the surrounding spatial and electrical scales are the direct result of this study. For a field program, these give a rule of thumb for estimating which locations may have 2D signals. Such locations can be avoided with prior planning, but if they must be sampled due to logistical or scientific reasons then steps can be taken to estimate the 2D errors. With sufficient horizontal resolution of the velocity field 2D errors can be calculated directly and removed in an iterative process. The broad shape of velocity errors into dipole or quadrapole shapes that are surface- and bottom-intensified allow ready identification of which locations are most likely to be biased by 2D influences. For instance, at the center of a jet the depth-varying error is positive in the surface layer and negative beneath.

The general treatment of 2D perturbations allows physical insight into their structure, their magnitude, and their dependence on spatial scales and sediment electrical properties. Although falling short of a general 3D model, this work extends the theory of motionally induced electric fields and applies that insight for improving velocity calculations.

Chapter 3

ELECTRIC FIELDS GENERATED NEAR CAPE HATTERAS

3.1 Introduction

This chapter investigates electric field measurements collected across the Gulf Stream SE of Cape Hatteras, North Carolina, USA. A 1D interpretation of the electric fields shows small but significant inconsistencies with the 1D approximation, which suggests higher order effects may be present. The initial goal is to explain the observations through a detailed study of the study region, which involves a number of varied studies. The use of a high-resolution numerical model for calculating the electric fields and electric currents allows the discussion to extend beyond what is directly observable in the data, including corrections to the observed data that remove the 2D effects.

This chapter is organized as follows. After presenting the first order theory (section 3.2) these data show inconsistencies with the 1D theory (section 3.3). To explain these discrepancies we investigate higher order terms that depend on horizontal gradients of velocity and of topography (section 3.4). A numerical model is used for a higher resolution analysis of a 2D transect across the Gulf Stream (section 3.5). The thickness and electrical properties of the sediment are determined in section 3.6 by a synthesis of existing geological observations. Magnetotelluric signals can generate electric fields in the ocean, but in section 3.7 they are shown to be uncorrelated with the deviations from 1D theory. The electric field is calculated numerically from the Gulf Stream velocity structure in section 3.8. The presence of meanders is shown to result in ambiguity in applying the first order theory, and on the upper continental slope there are significant 2D perturbations of the electric field (sections 3.9 and 3.10). The limitations of our analysis and the extension of our results for regions other than Cape Hatteras are discussed in section 3.12. The last section (3.13) summarizes the results.

3.2   *Motionally Induced Electric Fields*

Electric fields occur in the ocean because of the motion of conductive salt-water through the earth's magnetic field, a process generally called motional induction. The theory of motionally induced electric fields in the ocean for time-dependent and 3–D currents and bathymetry was developed by *Sanford* (1971), where the thin aspect ratio of the ocean allows for great simplification from the 3D governing equations. *Larsen* (1968, 1971), *Chave and Luther* (1990) and *Tyler and Mysak* (1995b) treat additional aspects of the theory of motional induction.

The first order response is presented first, with the discussion of higher order terms postponed until later. The dominant mode restricts electric currents and electric fields to the vertical plane. This is a toroidal mode that describes, for example, electric currents in one direction in the surface intensified oceanic flow with weaker return electric currents in the slower water and sediment beneath.

3.2.1   First Order Theory

Sanford (1971) solved for a general solution that makes use of a number of assumptions, including: a horizontal ocean bottom (H) with small topographic perturbations (h, $h/H \ll 1$), width scales (L) much larger than bottom depth ($H/L \ll 1$), predominantly horizontal oceanic velocity ($\boldsymbol{v}$), distant lateral boundaries, a layer of underlying sediment that has a uniform electrical conductivity, and small time variations.

Although it is readily shown that time variations of the electric field generate induced magnetic fields that are negligible compared to the earth's magnetic field (*Sanford*, 1971; *Chave and Luther*, 1990), a less evident process is inductive coupling between the ocean and the conductive mantle. If large-scale water motion changes quickly in time (e.g. tidal flow), the time variations induce electric currents in the mantle that act to reduce and delay the oceanic electric field. Scaling Maxwell's governing equations finds that the induction parameter $\mu\sigma\omega\mathcal{L}^2$ must be much less than 1 for mutual induction to be negligible (μ is magnetic permeability and σ is electrical conductivity) (*Sanford*, 1971). Although the appropriate length scales $\mathcal{L}^2$ for this problem are unclear, they can range from the water

depth H to the velocity width-scale L to the depth of deep conductors in the earth. The induction parameter depends on a combination of time-scales (frequency ω) and length scales ($\mathcal{L}^2$). Generally, this condition is satisfied if the phase speed $\omega/\mathcal{L} < 10$ m s^{-1}. Analysis of a simplified earth geometry constrains large scale flow ($H/L \leq 1$) to have time-scales larger than 6 hours (*Sanford*, 1971). Inclusion of realistic earth conductivity profiles (*Chave and Luther*, 1990) shows that mutual induction is minimal for periods longer than 10 hours. To avoid complications caused by quickly varying large-scale flow, we shall limit the analysis to oceanic flows with sub-tidal frequencies.

In the quasi-static limit, the horizontal electric field is

$$-\boldsymbol{E}_h = \nabla_h \phi = \boldsymbol{v} \times F_z \hat{\boldsymbol{k}} - \boldsymbol{J}_h/\sigma \qquad , \tag{3.1}$$

where ϕ is electric potential, $\boldsymbol{v}$ is oceanic velocity, F_z is the vertical component of earth's magnetic field, $\hat{\boldsymbol{k}}$ is the vertical unit vector (pointing upward), σ is electrical conductivity, and $\boldsymbol{J}_h$ is horizontal electric current density. The electromotive force $\boldsymbol{v} \times F_z \hat{\boldsymbol{k}}$ generates the electric field and electric currents.

For the 1D approximation, it is assumed that $\boldsymbol{J}_h$ is solely caused by local water motion. Thus the form of $\boldsymbol{J}_h/\sigma$ is (*Sanford*, 1971)

$$\frac{\boldsymbol{J}_h}{\sigma} = (\boldsymbol{v} - \overline{\boldsymbol{v}}^*) \times F_z \hat{\boldsymbol{k}} \; + \; \text{HOT} \quad , \tag{3.2}$$

with

$$\overline{\boldsymbol{v}}^* = \int_{-H}^{0} \sigma \boldsymbol{v} \, \mathrm{d}z' \Big/ \int_{-H_s}^{0} \sigma \, \mathrm{d}z' \quad . \tag{3.3}$$

The seafloor is located at $z = -H$, and the bottom of the sediment layer is at $z = -H_s$. Although the water conductivity σ varies in the vertical, the conductivity of the sediment σ_s is assumed uniform. The quantity $\overline{\boldsymbol{v}}^*$ is the conductivity-weighted vertically-averaged velocity. Higher order terms (HOT) are discussed later.

The equation 3.2 describes the principal toroidal mode. Water motion generates an electric field through $\boldsymbol{v} \times \hat{\boldsymbol{k}} F_z$, which can drive electric currents in the ocean and the sediment. The assumption of $H/L \ll 1$ means that the horizontal return segments for $\boldsymbol{J}$ are much longer than the vertical paths. Because electrical resistance is proportional to

path length, the vertical resistance is negligible and the horizontal resistance dominates. This is the physical reason for vertically uniform electric fields, which is equal to $\overline{\boldsymbol{v}}^* F_z$.

The electric current density is the difference between the vertically uniform electric field and that generated by local horizontal water motion scaled by σ, $\sigma F_z(\boldsymbol{v}(z) - \overline{\boldsymbol{v}}^*)$. First we'll consider cases where there is no bottom sediment, for which $\overline{\boldsymbol{v}}^*$ reduces to $\overline{\boldsymbol{v}}$ (the full reason for this is explained below). In the simple case where the ocean velocity is entirely barotropic, $\boldsymbol{v}(z) = \overline{\boldsymbol{v}}$, no electric currents flow. The potential generated by water motion is exactly balanced by the oceanic electric field 3.1 at all depths. This situation is analogous to the Hall effect, which describes the uniform electric potential across a conductive strip that is moving in a uniform magnetic field. Electric currents arise when a baroclinic velocity component is added, for instance if the ocean has a moving surface layer with a motionless deep layer. In the surface layer the velocity is larger than $\overline{\boldsymbol{v}}$, so $\boldsymbol{v} - \overline{\boldsymbol{v}}$ is greater than 0 and $\boldsymbol{J}$ is driven in one direction. The circuit is completed by return electric currents flowing in the opposite direction in the lower layer, where $\boldsymbol{v} - \overline{\boldsymbol{v}}$ is less than 0.

This first term is considered 1D because it only depends on the vertical dimension: vertical variations of $\sigma(\boldsymbol{v}(z) - \overline{\boldsymbol{v}}^*)$ determine the electric current density, while a vertical integral for $\boldsymbol{v}$ determines the absolute electric field.

The parameter $\overline{\boldsymbol{v}}^*$ corresponds physically to the vertically-uniform electric field. It is linearly related to the vertically averaged velocity and is strongly influenced by subbottom sediment. Conductive sediment beneath the ocean supports return electric currents that reduce the oceanic electric potential. The horizontal electric current density integrated from the bottom of conductive sediment (H_s) to the top of the water column needs to be zero to conserve charge. This constraint yields the equation for $\overline{\boldsymbol{v}}^*$ in (3.3), which can be further be simplified by performing a Reynolds decomposition of the water velocity and conductivity in the vertical (where for the variable c, $\overline{c}$ indicates a vertical average and c' indicates perturbations about the vertical mean). This yields

$$\overline{\boldsymbol{v}}^* = \overline{\boldsymbol{v}} \left(\frac{1 + \gamma}{1 + \lambda} \right) \qquad , \tag{3.4}$$

where

$$\lambda = \int_{-H_s}^{-H} \sigma(z)\,\mathrm{d}z' \Big/ \int_{-H}^{0} \sigma(z)\,\mathrm{d}z' \tag{3.5}$$

is the bottom conductance factor λ, and $\gamma = \overline{\sigma' \boldsymbol{v}'} / \overline{\sigma}\,\overline{\boldsymbol{v}}$ is the vertical correlation of conductivity and velocity.

The stronger factor is λ, which describes the amount of shorting through the bottom sediment. The form that is consistent with (3.2) is

$$\lambda = \frac{(H_s - H)\sigma_s}{H\sigma} \quad, \tag{3.6}$$

which parameterizes the sediment layer as having a uniform conductivity σ_s. For the thin aspect ratio assumption, a vertically uniform electric field drives electric currents through the sediment. In the presence of vertically-varying sediment conductivity, the total conductance of the sediment (the numerator of (3.5)) is simply the vertical integral of conductivity.

The electrical properties of sediment are poorly characterized for calculating λ, although they can be estimated on a basin scale as shown in *Flosadóttir et al.* (1997); *Tyler et al.* (1997). The bottom conductance factor can be understood physically by defining an effective water depth $D = H(1 + \lambda)$ that is the depth of water that has the same vertical conductance as the ocean and sediment column.

The vertical correlation factor $\gamma = \overline{\sigma' \boldsymbol{v}'} / \overline{\sigma}\,\overline{\boldsymbol{v}}$ describes the increase or reduction of $\overline{\boldsymbol{v}}^*$ caused by baroclinic correlations of conductivity and velocity. A layer of large velocity and increased conductivity drives a larger electric current $\sigma(\boldsymbol{v} \times F_z \hat{\boldsymbol{k}})$ than if the water column were uniformly conductive, which leads to a larger $\overline{\boldsymbol{v}}^*$ for the same $\overline{\boldsymbol{v}}$. Measurements of temperature and salinity simultaneous with the apparent electric field $(\boldsymbol{J}_h/\sigma)$ allow direct calculation of the vertical correlation. Corrections are also possible from hydrographic data or from data archives (*Luther and Chave*, 1993) by computing representative profiles of geostrophic velocity and electrical conductivity. Prior calculations of γ found it to have less than a 10% influence (*Chave and Luther*, 1990; *Szuts*, 2004) and to be small outside of strongly baroclinic flows.

3.2.2   Application to Field Measurements

There are two ways to make measurements of the ambient electric field: 1) from a platform at a fixed location or known horizontal velocity or 2) from a free-falling platform.

For a stationary instrument the local velocity in equation (3.1) ($\boldsymbol{v} \times \boldsymbol{F}$) cancels that in the first term of $\boldsymbol{J}_h/\sigma$ (3.2), leaving only the electric field generated by $\overline{\boldsymbol{v}}^*$.

Profiling floats, however, move horizontally at the local and unknown water velocity. The instrument's motion through the earth's magnetic field induces an additional potential in the internal electronics that cancels the external source $\boldsymbol{v} \times \hat{\boldsymbol{k}} F_z$, leaving an apparent electric field that depends on (3.2) $F_z(\boldsymbol{v} - \overline{\boldsymbol{v}}^*)$ and the higher order terms (*Sanford et al.*, 1978). The quantity $\boldsymbol{v} - \overline{\boldsymbol{v}}^*$ is a relative velocity profile, and much like a geostrophic velocity it can be made absolute by any absolute reference velocity. Possible sources for reference velocities include shipboard ADCP (e.g. for XCPs, *Girton et al.*, 2001), surface GPS fixes (e.g. for EM-APEX, *Sanford et al.*, 2007), or subsurface ranging (e.g. electrode-equipped RAFOS floats, *Szuts*, 2004). Referencing with an independent absolute velocity yields a vertical profile of absolute velocity. The offset is equivalent to $\overline{\boldsymbol{v}}^*$ plus higher order terms.

3.3   Observations

During Leg 1 of R/V *Endeavor* cruise 239 a transect SE of Cape Hatteras was occupied during 6 days in July, 1992 (*Sanford et al.*, 1996). Among the data collected were 30 full water column drops of the Absolute Velocity Profiler (AVP) at stations of depths between 500 m to 3500 m. The station positions are shown in Figure 3.1. The inshore 3 stations were repeated 6–7 times each, and the 2 deeper stations 2–3 times each. The station repeats were not exactly in the same location: the standard deviation of position was 200 m along the transect and 500-1000 perpendicular to the transect. Information about each drop is listed in appendix B.1, as are the velocity and CTD profiles from each profile.
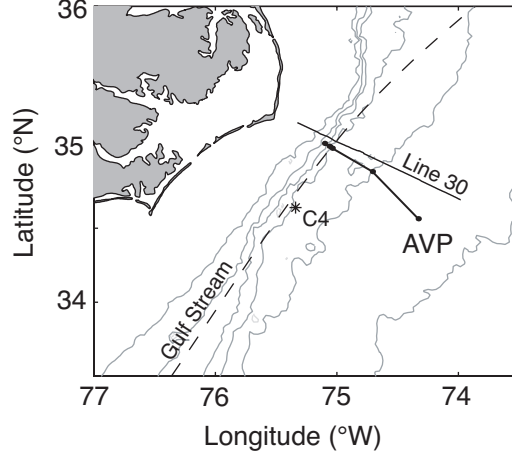
Figure 3.1: Chart showing the study area: AVP stations (black dots), AVP transect (thick solid black line), the Line 30 seismic transect (*Hutchinson et al.*, 1995), the C4 current meter (*Berger et al.*, 1995), and the schematic north wall of the Gulf Stream (*Savidge*, 2004). Bottom depths are at 100, 500, 1000, 2000, 3000, and 4000 m.

3.3.1   Absolute Velocity Profiler (AVP)

The AVP is a free falling vertical profiler that rotates as it descends and ascends. Two pairs of electrodes and an internal magnetometer measure the ambient electric and magnetic fields. The electrodes measure an apparent electric field E_{app} equivalent to $\boldsymbol{J}_h/\sigma$ in (3.2) due to the tall and narrow shape of the instrument (*Sanford et al.*, 1978). The instrument rotation causes the ambient electric field to be sinusoidally modulated, allowing separation of the weak oceanic signal (μV) from the larger but slowly varying electrode offset (mV). The instrument is made negatively buoyant with weights suspended below it that cause it to fall at 1 m s^{-1}. The weights are dropped by a mechanical release when they hit the seafloor, and the then positively buoyant instrument ascends at a velocity similar to its descent.

An acoustic Doppler system measures the instrument's velocity relative to the seafloor when it is within 50–250 m of the bottom. The method is by calculating the Doppler shift of acoustic signals that back-scatter from the seafloor as the instrument rotates. The Doppler sensors are oriented at 30° from the vertical. Acoustic reflections are weak or

non-existent when the bottom slope is steep, such as at the stations above the continental slope. The maximum slope angle is 8–10° (*Smith and Sandwell*, 1997), but high resolution topography (100 m *Pratson and Haxby*, 1996) show a large range of slope angles (4–15°) along similar continental margins due to rugosity of canyons, gullies, slumps, and other small-scale features. The Doppler system ensonifies a circular area of the seafloor within a 150 m radius of the AVPs horizontal location (assuming a flat bottom), so steep slopes at a scales of 150 m or smaller can potentially degrade the Doppler velocities. Most of the velocity in this location is parallel to topography, however, so any errors in the reference velocity are in the velocity component perpendicular to the direction of the Gulf Stream.

Combining electric field measurements and acoustic Doppler velocities, the AVP determines absolute velocities with a vertical resolution of 4 m. Additional sensors include a CTD package and shear probes. The instrument is fully described in *Sanford et al.* (1985).

3.3.2 1D Analysis

Processing of the observations uses 1D theory, that is

$$\boldsymbol{E}_{\text{apparent}} = (\boldsymbol{v}_{\text{EF}}) \times \hat{\boldsymbol{k}} F_z = (\boldsymbol{v} - \overline{\boldsymbol{v}}^*) \times \hat{\boldsymbol{k}} F_z \qquad . \tag{3.7}$$

The vertical average of the offset between the apparent velocity ($\boldsymbol{v}_{\text{EF}}$) and the acoustic Doppler absolute velocity determines $\overline{\boldsymbol{v}}^*$. Electrical conductivity from the CTD and the relative velocity from the electrode-system allow γ to be readily calculated. Magnetic field values are calculated from the IGRF10 field model prepared by the International Association of Geomagnetism and Aeronautics (*Macmillan et al.*, 2003).

The velocities are rotated into stream coordinates, where $\hat{\boldsymbol{y}}$ is directed downstream and $\hat{\boldsymbol{x}}$ is directed offshore. The criterion used for rotating the velocities is that the correlation between the cross-stream velocity u and conductivity be 0 ($\overline{\sigma' u'} = 0$) (see Table B.2).

For each profile, the quantities $\overline{v}$, γ, and $\overline{v}^*$ are calculated from the relative velocity profile, the offset between v_{EF} and the Doppler velocity, and the CTD data (see Table B.2). The remaining factor in the 1D approximation (3.3) is λ, which is the slope between

$\overline{v}(1 + \gamma)$ and $\overline{v}^*$. If the 1D theory is accurate, all profiles should give a similar slope and the best-fit line should go through the origin with no y-intercept.

For calculating λ, data from both up and down profiles are used. The values of $\overline{v}(1+\gamma)$ and $\overline{v}^*$ between up and down profiles are highly correlated, so the 2 data points have an effective degrees of freedom that is between $1 \leq N_{\text{eff}} \leq 2$ and is close to 1. The effective degrees of freedom is calculated at each station by (*Bretherton et al.*, 1999)

$$N_{\text{eff}} = N_{\text{pairs}} + \frac{1 + r_{\Delta t}^2}{1 - r_{\Delta t}^2} N_{\text{profiles}} \tag{3.8}$$

where N_{pairs} is the number of profile pairs, N_{profiles} is the number of profiles, and $r_{\Delta t}^2$ is the correlation of $\overline{v}$ between down and up profiles. There is only a small increase in N_{eff} compared to N_{pairs} (Table 3.3.2). Two profiles were removed from the 500 m station (drops 414 and 427) because they were collected at water depths significantly different from the other drops at that station. Additionally, stations avp424 and avp430 could not be fully processed due to corrupted data.

Linear fits at each station are shown graphically in Figure 3.2 and numerically in Table 3.3.2. Although the 1D theory suggests that a proportionality constant $(1+\lambda)$ is sufficient for a fit, the fit at the 500 m station does not go through the origin ($y_0 = -0.10 \pm 0.02$) despite being highly linear ($r^2 = 0.996$). This result is not fully consistent with the 1D approximation, and an explanation for this non-zero y-intercept is investigated in the remainder of this paper. A fit that is forced to go through the original still recovers most of the relationship, so the 1D approximation explains the majority of the relationship. Note that there are 1 and 0 degrees of freedom in the fits at the 3000 and 3500 m stations, so these stations lack enough statistical confidence for further analysis.

3.4   3D Theory

Before turning to further analyses, the general dependencies of higher order terms can be examined in the analytic forms calculated by *Sanford* (1971) to motivate what may be causing the deviations. These terms come from a perturbation analysis where the seafloor varies slowly in height $h(x)$ such that $h/H \ll 1$, and where the velocity gradients are limited by the prior assumption that $H/L \ll 1$. His results are strictly valid for
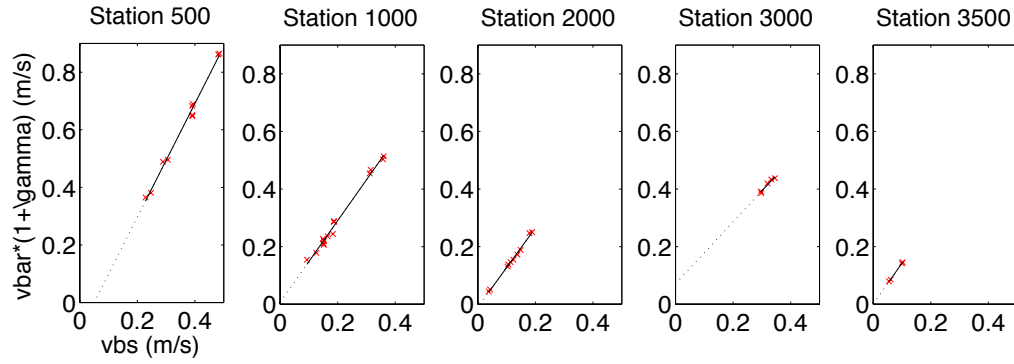
Figure 3.2: AVP observations of $\overline{v}^*$ and $\overline{v}(1+\gamma)$ with the fit at each station.

Table 3.1: Linear fits to the AVP data at each station. N is number of profiles and DOF is the degrees of freedom in a linear fit.

station	N	DOF	λ	y_0 (m s^{-1})	r^2
500	10	3.0	0.97±0.06	-0.10 ± 0.02	0.996
1000	14	5.1	0.42±0.04	0.007 ± 0.010	0.995
2000	12	4.1	0.37±0.04	-0.010± 0.005	0.996
3000	5	1	0.08±0.14	0.071 ±0.0009	0.976
3500	4	0	0.42±0.02	0.0009±0.0014	0.9999

small aspect ratio flows and small topographic perturbations. The underlying physics responsible for 2D effects should be the same when these assumptions are no longer met.

The full form for horizontal electric current density divided by conductivity is (*Sanford*, 1971)

$$\frac{\boldsymbol{J}_h}{\sigma} = \overbrace{(\boldsymbol{v} - \overline{\boldsymbol{v}}^*) \times F_z \hat{\boldsymbol{k}}}^{1} + \overbrace{\frac{H(1+\lambda)}{2\pi D} \nabla \times \hat{\boldsymbol{k}} \iint\limits_{-\infty}^{\infty} \nabla \cdot F_z \overline{\boldsymbol{v}}^* \ln(r) \, \mathrm{d}x' \, \mathrm{d}y'}^{2} \tag{3.9}$$

$$\underbrace{- \nabla_h \left\{ \frac{1}{H(1+\lambda)} \int_{-H}^{0} \hat{\boldsymbol{k}} \cdot (\boldsymbol{v} \times \boldsymbol{F}) z' \, \mathrm{d}z' + \overbrace{\int_{-H}^{z} \hat{\boldsymbol{k}} \cdot (\boldsymbol{v} \times \boldsymbol{F}) \, \mathrm{d}z'}^{\text{depth-varying}} \right\}}_{3} + \mathcal{O}\left(\frac{H^2}{L^2}\right)$$

where the first under-brace at left is labeled "depth-varying".

with

$$r = \sqrt{(x - x')^2 + (y - y')^2}$$

$$D = H + \zeta - h + \frac{\sigma_s}{\sigma}(H_s - H + h) \tag{3.10}$$

$$\overline{\boldsymbol{v}}^* = \int_{-H+h}^{\zeta} \sigma \boldsymbol{v} \, \mathrm{d}z' \Big/ \int_{-H_s}^{\zeta} \sigma \, \mathrm{d}z' \,, \tag{3.11}$$

where ζ is the surface elevation of the ocean, $-H$ is the location of the seafloor, h is the perturbation of water depth with $h/H \ll 1$, and other variables are defined earlier in section 3.2. Unlike the discussion of the first order theory, now the variables H, H_s, σ and σ_s are uniform in space. This change of notation results in different limits for vertical integrals and thus in modified definitions for λ and D. Terms that vary vertically have been denoted so — all other terms are vertically uniform or barotropic. Though there is the vertical components J_z, we do not discuss it here because horizontal components are sufficient for calculating horizontal velocity.

The first term in (3.9) was described earlier. The remaining terms (terms 2 and 3) are called higher order terms (HOT) because they scale as H/L. Vertical electric current density also scales as H/L.

A second mode of electric currents flow in the horizontal plane and are called poloidal. This mode only exists in situations where there are gradients in the downstream direction

and thus is a 3D effect. Term 2 describes a poloidal mode that is non-zero only if the forcing quantity $\nabla \cdot F_z \overline{\boldsymbol{v}}^*$ is non-zero. The integral can be recast as a convolution in wave-number space by taking the curl operator inside the double integral, in which case the Fourier transform of $\nabla \cdot F_z \overline{\boldsymbol{v}}^*$ is convoluted with the Fourier transform of the Green's Function $1/r$. Assuming that gradients of F_z are much smaller than the divergence of $\overline{\boldsymbol{v}}^*$, the forcing quantity can be written

$$\nabla \cdot \overline{\boldsymbol{v}}^* = -\frac{\partial \zeta / \partial t}{D} - \frac{\overline{\boldsymbol{v}}^*}{D} \cdot \nabla D \neq 0 \qquad .$$

Electric currents are generated through this term due to changes in surface height with time ($\partial \zeta / \partial t$), flow across gradients of bathymetry ($\overline{\boldsymbol{v}}^* \cdot \nabla H$), or flow across gradients in bottom conductance ($\overline{\boldsymbol{v}}^* \cdot (1 + \lambda)$). Changing surface elevation is expected to be important for tidal flow and high frequency waves (e.g. Kelvin waves), whereas for mesoscale ocean circulation along-stream gradients of $F_z \overline{\boldsymbol{v}}^*$ predominantly generate horizontal electric currents. These horizontal currents are called non-local currents ($\boldsymbol{J}^*$), because they are formed at a distance from the reference point. This mode generates magnetic fields outside of the ocean that can be observed at inland stations (*Filloux*, 1967) or at satellite altitude (*Tyler et al.*, 2003).

The integrand is a convolution of a Green's function ($\ln r$) with a divergence ($\nabla \cdot \overline{\boldsymbol{v}}^* F_z$), so with increasing distance from where the divergence is non-zero, the curl of the integral diminishes, decaying as $1/r$ for an integrand that is an unit impulse delta function. Numerical modeling of the kernel (not shown) demonstrates that the horizontal structure is a double dipole with two maxima and minima centered around the the location of non-zero divergence, in agreement with the results of *Chave and Luther* (1990). This term depends on the curl of an integral over all horizontal space, which makes it necessary to calculate this term with a 3D approach. Mean ocean circulation is constrained to flow along topography by conservation of vorticity, so $\overline{\boldsymbol{v}}^* \cdot \nabla_h H$ is expected to be small. Vorticity conservation can be broken in extremely energetic cases that are computationally expensive to model, such as the Gulf Stream leaving the continental slope or baroclinic instabilities of surface intensified jets. A secondarily expensive requirement is the high resolution required to accurately resolve steep topography along ocean margins (of order

10 km). Although non-local currents generated by subtidal flows is an interesting question, it is beyond the scope of this article.

The third term of equation (3.9) depends on horizontal gradients of topography and of the velocity field and contains both barotropic and baroclinic components. In this form, horizontal gradients of H, λ, and $\overline{v}$ can all make this term non-zero, although these gradients are already assumed small ($H/L \ll 1$) in the derivation. It is not clear that the stronger gradients will retain the same form as presented here.

Term three describes the physical processes investigated in particular in this article. The geometry at Cape Hatteras of a strong surface intensified jet flowing along steep topography allows an analysis of the joint effect of gradients in velocity and topography, unlike the analysis of Sz08 that separates the two effects.

The only depth-varying components of $\boldsymbol{J}_h/\sigma$ are the left side of the first term (involving $\boldsymbol{v}$) and the right side of the third term (involving $\int_{-H}^{z}$); the remaining terms contribute a depth-uniform offset. The first and third terms depend on local effects in the vertical, at most within a distance a few times the water depth. *Chave and Luther* (1990) showed that the vertical averages of the dominant mode have a horizontal weighting function that has a width of a few times the water depth. Result from Sz08 indicate that velocity gradients generate stronger perturbations from the 1D solution than topographic gradients, though in both cases the 1D solution is accurate for length-scales larger than of 4–7 H.

3.4.1 Time-varying Ocean Velocity

Until now the discussion of theory has focused on quasi-static electric fields that are generated by subtidal ocean velocity. If tidal and super-tidal flow occurs over basin-wide scales the oceanic electromagnetic fields are modified by inductive coupling with deep conductive layers in the earth. This is called mutual induction. Magnetic fields generated by rapidly changing ocean velocities induce electric currents in the conductive mantle (below a depth of 500 km), which in turn generate secondary magnetic fields that induce electric currents in the ocean that diminish and delay the original changing ocean electric fields. The scaling of this process requirements that the flow field be horizontally

coherent over scales that are equivalent to the depth of the conductive mantle, otherwise the magnetic fields do not penetrate to the mantle. This conductive layer is below a depth of 500–1000 km, as indicated by compiled conductivity model (*Kuvshinov et al.*, 2002) and by satellite geomagnetic inversions (*Kuvshinov and Olsen*, 2006).

The deep electrical structure of the upper mantle, a poorly characterized feature, is central for estimating the strength of mutual induction. Simultaneous $\boldsymbol{E}$ and $\boldsymbol{B}$ measurements have indicated that mutual induction has an upper limit of 30% of the velocity variance at tidal frequencies from data in the open North Pacific during project BEMPEX (*Filloux et al.*, 1991). That this region of the Pacific is characterized by weak barotropic oceanic flow and strong large-scale atmospheric forcing suggests that the relative effects of mutual induction would be expected to be larger here than in more energetic regimes with smaller length-scales of variability. Comparison of data collected along the west coast of America with tidal models find mutual induction effects less than 10% of the barotropic tidal velocity (data from EMSLAB, *Filloux et al.*, 1989 compared against the tidal model of *Schwiderski*, 1979; data from *Althaus et al.*, 2003 compared against the TPXO.3 tidal model *Egbert et al.*, 1994).

At Cape Hatteras, there are both tides and meanders of the Gulf Stream. The tidal amplitude is small at Cape Hatteras, with a sea-surface surface height amplitude of 0.3–0.4 m for the M_2 tidal constituent and observed tidal velocities of 2–10 cm s^{-1} below the Gulf Stream (from harmonic analysis of the current meter data described by *Berger et al.*, 1995). Because meanders of the Gulf Stream along the continental margin have relatively small length scales (<100 km) and long periods (>3 days *Savidge*, 2004), mutual induction is expected to be small for these features.

3.5 Model for Ocean Electrodynamics

To investigate the 2D transect with finer horizontal resolution than possible with the data, we turn to numerical modelling. The full-complexity numerical simulation of the region is solved with an an electromagnetic numerical model called the Model for Ocean Electrodynamics (MOED, *Tyler et al.*, 2004). MOED is a 3D, conservative, finite-difference

model that solves Maxwell's equations for electromagnetics in the frequency domain for the electric and magnetic gauge potentials, given prescribed conductivity and velocity fields. Validation of this model is demonstrated in *Tyler et al.* (2004) for 1D, 2D and 3D cases that have analytical solutions. The 2D setup used here is evaluated in Sz08 against a numerically-evaluated analytical solution.

The model is used to calculate electric fields given the detailed structure of the 2D transect across the Gulf Stream and the continental margin. The prescribed oceanic properties (conductivity and velocity) come from the station-averaged profiles of water conductivity and velocity measured by the AVP. The velocities (both cross- and along-stream) and conductivities in the water are based on the station-averaged vertical profiles collected by the AVP, gridded to the model grid with a cubic scheme that makes first and second derivatives continuous. The gridded conductivities and downstream velocities are shown in Figures 3.3 and 3.12.

The model grid has a maximum resolution over the continental slope of $\Delta x = 50$ m (for $0 < x < 20$ km) and over the upper water column of $\Delta z = 10$ m (for $-3000 < z < 0$). The grid spacing increases by 5% for each successive grid point in x and z away from this region to reduce the number of grid points, reaching a maximum of $\Delta x = 200$ m and $\Delta z = 40$ m. The vertical resolution is 5 m in the upper 100 m in order to resolve the continental shelf, which smoothly increases to 10 m beneath $z = -100$ m.

The conductivity interfaces in the model domain need to be smoothed for numerical stability. For the water/sediment and sediment/crust interfaces the conductivity over 5 grid-points in the vertical was smoothed based on the exact interface depth according to

$$\sigma(z_i) = \frac{1}{2}\left[1 + \sin\left(\frac{2\pi(z_i - z_{\text{interface}})}{4\Delta z}\right)\right](\sigma_{\text{upper}} - \sigma_{\text{lower}}) + \sigma_{\text{lower}} \qquad (3.12)$$

where z_i is within 2 grid points of the depth of the interface $z_{\text{interface}}$, Δz is the vertical grid-spacing, and σ_{upper} and σ_{lower} are the conductivities of the upper and lower layers. A non-conductive crust underlies the sediment. Realistically, the crust has conductivities of $0.0001 - 0.03$ S m^{-1} (*Chave et al.*, 1992; *Simpson and Bahr*, 2005), which is at least an order of magnitude smaller than sediment conductivity and will not support a flow of electric current that significantly alters the solution.

The geometry of sediment layers is determined from a seismic transect very close to the AVP transect, called Line 30, while sediment conductivity is determined from geophysical data (see section 3.6). The bottom topography under Line 30, however, does not match that underneath the AVP transect. The primary concern for prescribing geophysical properties is internal consistency with the other inputs. For analysis of the electric fields it is necessary to calculate vertical integrals over the water column, and so the exact value of the water depth becomes important, even though the interface is smoothed. Because the velocity is only constrained at 5 stations, a bottom topography that varies over smaller scales will introduce small scale variability to the vertically-averaged quantities. For this reason a smoothed topography is used instead of that present in the seismic lines or that underneath the AVP transect.

Topography from *Smith and Sandwell* (1997) with a resolution of 3 km is first smoothed with a 3 grid point by 3 grid point Gaussian smoothing kernel. A quadratic function is fit to isobaths every 50 m using weighted least squares. The weights are calculated by $\exp\{-(r/\tau_r)^2\}$, where r is the distance from where the isobath cross the AVP transect and τ_r is a length scale that is the larger of 3 km or 5 times the isobath value. This form of weighting is chosen based on the result from Sz08 that the 1D approximation is accurate when length scales are larger than 5–7 times the water depth. By extension, the oceanic EF is expected to respond to the shape of an isobath over distances no larger than 5–7 times the depth of the isobath.

Both the velocities and the conductivities are further smoothed with a Gaussian filter that is 3 points wide in the horizontal and 5 points wide in the vertical. The final conductivity structure from the geophysical and AVP data, as gridded onto the model domain, is shown in Figure 3.3.

The magnetic field is set to values calculated by the most recent International Geomagnetic Reference Field (IGRF-10, which is definitive prior to 2000), $F_z = -46,860$ and $F_h = 22,290$, with a magnetic declination of -10.2° True. This magnetic field is the dominant signal that comes from the earth's core and mantle. The direction of the Gulf Stream axis (toward 48° True) contains a significant component perpendicular to
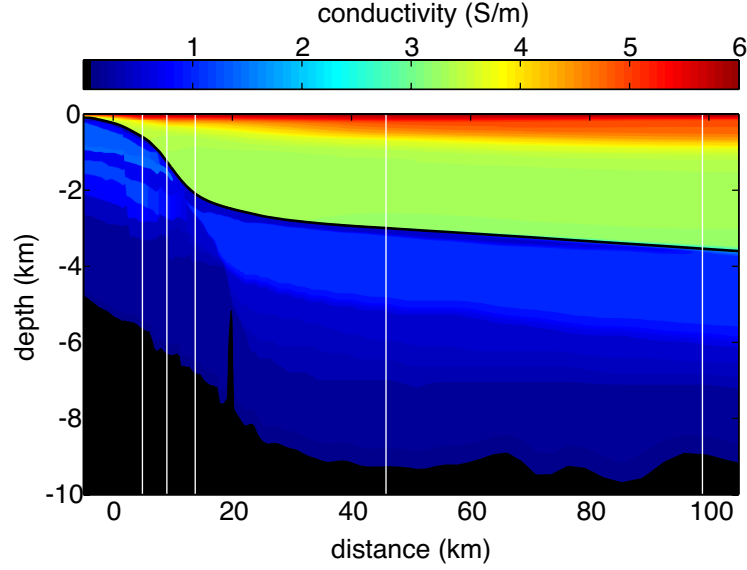
Figure 3.3: Conductivity input into MOED, based on station-averaged conductivity pro-
files and compiled geophysical data. The locations of the stations are shown by white
lines, and the presence of a relatively non-conductive diapir is seen near 20 km.

geomagnetic north, so there is an inductive contribution from the horizontal magnetic
field.

Small scale (< 500 km) perturbations due to lithospheric magnetic anomalies or time-
variable perturbations from ionospheric activity are not included in the geomagnetic field
used in the model. Both these secondary sources have magnitudes less than 1% of the
main field. Ionospheric perturbations are discussed in section 3.7, and the influence of
gradients of lithospheric magnetic anomalies is discussed further in section 3.11.

For the model implementation used for calculating magnetotelluric electric fields in
the ocean, the forcing term is no longer the motion of seawater but instead a downward
propagating plane wave in the atmosphere. Periods range from 10 s to 10^5 s. Unlike the
magnetostatic case where the electric potential ϕ is sufficient for describing the electro-
magnetic response, in these cases MOED also solves for the magnetic vector potential
A.

3.6   Compilation of Geologic Data

The effect of a conductive sediment enters through λ, which physically is the ratio of the sediment to oceanic conductance. This approach reduces the continuously varying electrical properties of the seafloor into a homogeneous layer. While knowledge of the sediment thickness from databases (*Tucholke*, 1986; *Laske and Masters*, 1997) can give an estimate of this effect within 10%–50% (see *Flosadóttir et al.*, 1997), the relation between sediment thickness, layer lithology, and apparent seafloor conductance remains only roughly known.

There is a large amount of geophysical observations collected along the east coast of North America from which a more detailed estimate of the electrical conductivity of the sediment can be constructed. The full sediment-column structure is extracted from deep seismic transects (IPOD, *Grow and Markl*, 1977; Line 30, *Hutchinson et al.*, 1995), whose locations are shown in Figure 3.1. *Hutchinson et al.* (1995) performed a synthesis of geophysical data along this margin and made a consistent database of reflector layers. Their synthesis mapped reflecting surfaces in the sediment column (*Poag and Ward*, 1993), which is called allostratigraphy. Although reflecting units are not defined by age, in practice each layer has a characteristic age found by dating sediment cores.

The stratigraphic mapping only included geoacoustic data, therefore *in situ* electrical conductivity was obtained from borehole resistivity logs in wells located along the margin. This approach assumes that across-margin properties are uniform between the wells and seismic lines. By age-correlating the conductivity in the wells to the layers in the geoacoustic transects (Figure 3.5), an average electrical conductivity is obtained for each layer. Care is taken that the lithology of the seismic layer is similar to that in the seismic well, although only a coarse 4-lithology mapping was performed by *Hutchinson et al.* (1996). Multiple wells are used for obtaining a spatially averaged layer conductivity.

Because of the different depositional environments along the continental margin, ideally wells in diverse locations would serve to constrain electrical properties. Wells that sample the entire sediment column are only found on the shelf or upper slope, however, so the conductivity of deeply buried sediments on the continental rise has to be estimated
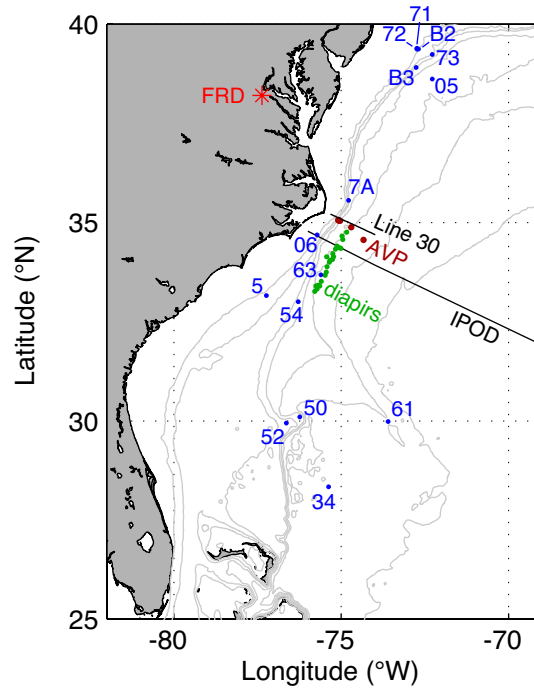
Figure 3.4: Chart showing the wells used for constraining the layer conductivities (using the labels in Table 3.6), the locations of salt diapirs, two seismic transects Line 30 and IPOD, and the Fredericksburg (FRD) magnetic observatory.

from wells in shallower water. The wells are listed in Table 3.6, and their locations are shown in Figure 3.4. The wells are translated to the seismic line by placing them at the appropriate isobath (Figure 3.6). A few seismic layers have different conductivities on the shelf and the rise because of different sedimentary composition. For these layers a linear transition region occurs 20 km seaward of the 200 m isobath, which is $-4 < x < 16$ km in Figure 3.6. The resulting conductivity structure is shown in Figure 3.3 (in which the transition region is $0 < x < 20$ km).

The topography beneath the AVP transect has maximum slopes of 12–16°, with a bimodal distribution centered at 4.5° and 10° (from topography by *Smith and Sandwell*, 1997; *Popenoe*, 1985). This part of the continental slope has been eroded 10–20 of km since the early Miocene, because of scouring by the Deep Western Boundary Current (*Popenoe*, 1985). This history means that there is only a thin layer of recent (Holocene)

Table 3.2: Wells used for the geophysical analysis. The locations are labeled in Figure 3.4 with the characters in parentheses in the first column.

| well name	water depth (m)	— well depth — (m)	(age)	reference
Shelf – mid-Slope Wells				
ASP 5 (5)	250	310	Eocene	*Popenoe* (1985)
ASP 7A (7A)	398	310	upp Pliocene	*Popenoe* (1985)
AMCOR 6006 (06)	56	90	mid Miocene	*Popenoe* (1985)
COST B2 (B2)	159	5704	upp Jurassic	*Mattick and Libby-French* (1988), *Scholle et al.* (1978)
COST B3 (B3)	819	3990	upp Jurassic	*Scholle et al.* (1981)
COST G2 (G2)	83	6584	upp Triassic	*Arthur* (1982)
ODP 1071 (71)	90	514	mid Miocene	ODP Initial Reports, 174A
ODP 1072 (72)	98	457	upp Miocene	ODP Initial Reports, 174A
ODP 1073 (73)	639	1303	Eocene	ODP Initial Reports, 174A
mid-Slope – Rise Wells				
ODP 905A (5A)	2700	910	mid Miocene	ODP Initial Reports, 150
ODP 1050 (50)	2300	606	Albian	ODP Initial Reports, 171B
ODP 1052 (52)	1345	685	Albian	ODP Initial Reports, 171B
ODP 1054 (54)	1294	200	mid Pliocene	ODP Initial Reports, 172
ODP 1061 (61)	4047	361	mid Pliocene	ODP Initial Reports, 172
ODP 1063 (63)	4584	418	mid Pliocene	ODP Initial Reports, 172
DSDP 534 (34)	4973	1667	upp Jurassic	DSDP Initial Reports, 76
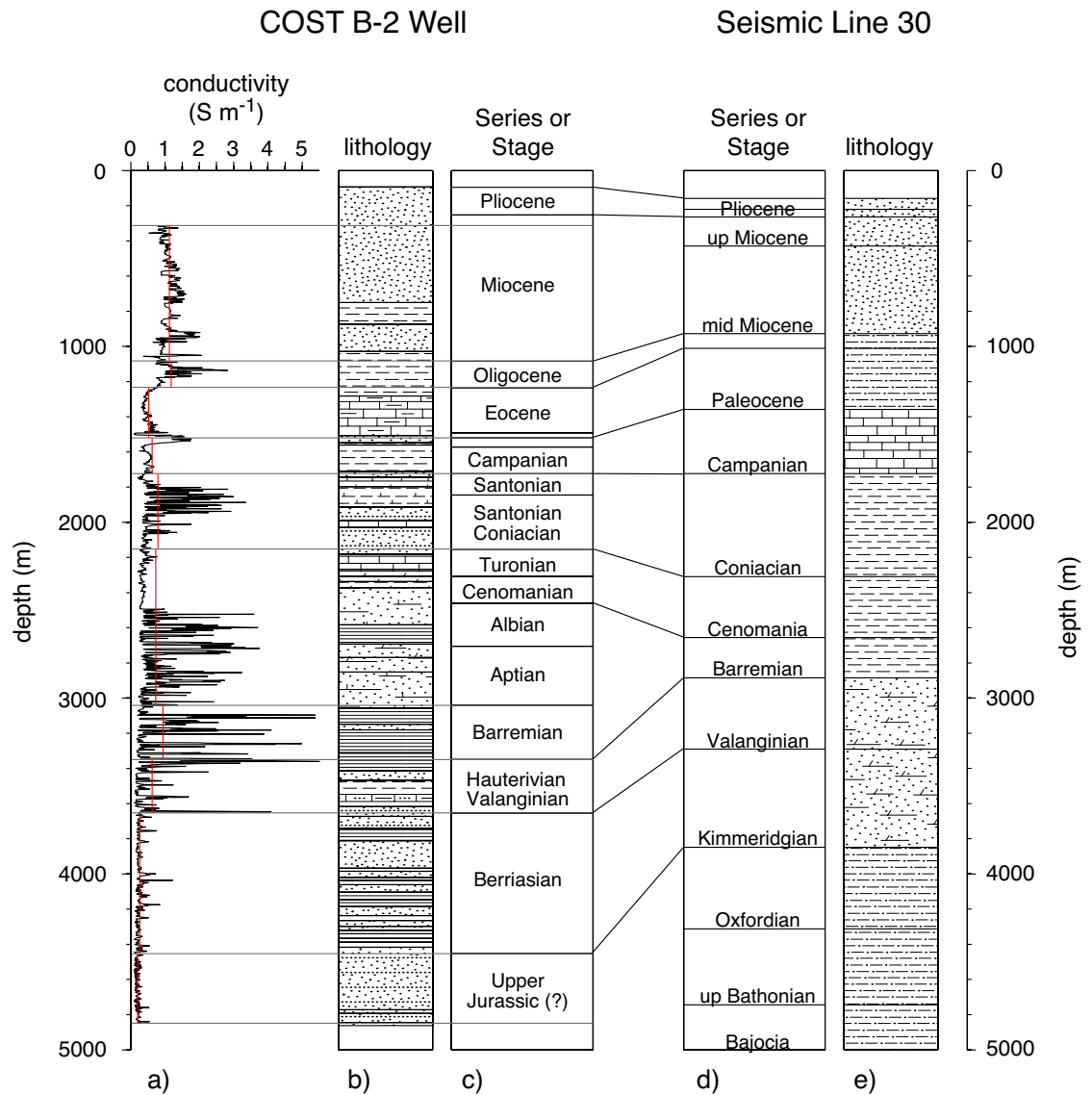
Figure 3.5: The age-correlation used to map layer average conductivity for the COST B-2 well, based on the seismic stratigraphy. (a) Conductivity borehole log for the COST B-2 well, with layer-averaged conductivities show by the vertical lines. (b) Stratigraphic column of the sediment lithology. (c) Age of the layers based on fossil dating. Data from *Scholle et al.* (1978) and *Hutchinson et al.* (1995). (d) Age of the reflector layers from Line 30. (e) Layer lithologies based on a 4 rough classifications. Data from *Hutchinson et al.* (1995) and *Hutchinson et al.* (1996). The vertical structure for Line 30 is taken at a water depth of 110 m, the same water depth as for the COST B-2 well. Strata of the same age are connected with lines, to show how the layer-conductivity is matched from the borehole conductivity to the seismic stratigraphy.

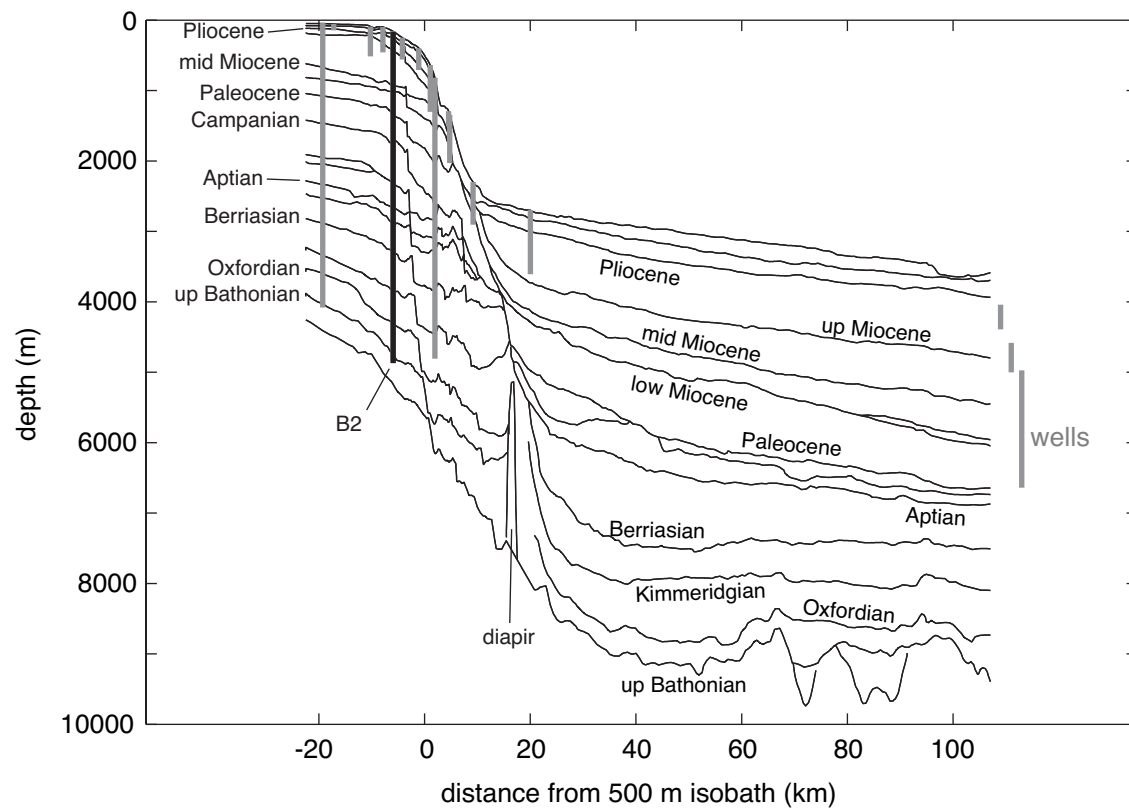Figure 3.6: The seismic structure from the Line 30 acoustic transect is plotted for the major reflectors, with the stage/series ages labeled for comparison with the COST B-2 well (black vertical line) shown in Figure 3.5. Wells with conductivity measurements are translated to the same isobath as their original location (Figure 3.4), to show how much of the sediment column is constrained by *in situ* conductivities.

sediments, and that near-surface sediments are probably more lithified and cemented than their current depth suggests. They are likely less electrically conductive than the near-surface sediments on the shelf.

Two additional geologic features can appreciably influence the sediment's total conductance: gas hydrates and salt diapirs.

Gas hydrates are ice-like complexes of gases and water that can form at high pressures and cold temperature and are generally found within the upper 1000 m of the sediment column. By displacing the conductive seawater that occupies sediment's pore fluids, gas hydrates have much lower electrical conductivity. They can be present in various concentrations in the sediment, however, and even moderate concentrations do not necessarily form a electrically impermeable layer (*Evans*, 2007). Through interpreting existing seismic lines, *Dillon et al.* (1994) calculates the distribution and thickness of hydrates along the east North American margin. They find no evidence of hydrates along the Cape Hatteras transect in water shallower than 3000 m, although there is a bottom simulating reflector 500-700 m below the seafloor at the 3500 m station. More extensive hydrates are found south of Cape Hatteras in the Carolina sedimentary trough.

Deposits of salt in sedimentary layers are electrically resistive. Along the eastern North American margin they formed in the shallow seas of the rift between the Americas and Europe and Africa. As the sedimentary prism grew the salt deposits were unevenly pressurized. Under high pressures salt is plastic, unlike rigid consolidated sediment, and if loaded differentially it can be squeezed out of its original bedding layer into vertical plumes (diapirs) or more complicated structures. A line of diapirs is present along the 3000 m isobath south of Cape Hatteras in the Carolina Trough (Figure 3.4). This line corresponds to the seaward extent of the post-rift salt deposit that was subsequently mobilized by the creation of a sedimentary prism. Relic subsidence faults in the sedimentary prism (*Popenoe*, 1985) indicate that the diapirs are no longer active. The diameters of diapirs are less than 25 km, and most of them in this region do not reach the surface. Diapirs are present in both the IPOD and the Line 30 seismic transects, and the 3000 m AVP station is located along their line of occurrence. Their conductivity and seismic signatures

are seen near $x = 20$ km in Figures 3.3 and 3.6. Unfortunately, there is not enough statistical confidence at the 3000 m AVP station to show whether a reduction of sediment conductance is observed due to the presence of diapirs.

Although diapirs are electrically resistive, they are thermally conductive and can generate fluid flow in surrounding sediment due to thermal gradients. Such mechanisms are observed in diapirs that reach close to the sediment surface (*Hornbach et al.*, 2005). It may also be possible for pore fluids close to diapirs to have elevated salinities. Though these questions are important for determining the electrical conductivity structure of diapirs, they are also questions that are poorly understood in the geophysics community.

In this study high resolution geophysical data are used to obtain a best estimate of the sediment electrical properties, but for researchers at other locations that do not have the necessary geophysical solutions there are other lower resolution sources for this geologic data. *Laske and Masters* (1997) compiled a global database of sediment thickness with a $1° \times 1°$ resolution, such as is useful for modelling electromagnetic fields on a global scale (*Flosadóttir et al.*, 1997; *Tyler et al.*, 2003). In order to calculate the sediment conductance, however, it is also necessary to know the effective sediment conductivity of the entire sediment column. Borehole resistivity traces were used for this purpose here. In other locations that lack nearby wells, this quantity can be estimated in a gross fashion after *Flosadóttir et al.* (1997) or *Everett et al.* (1999).

3.7 Magnetotelluric Analysis

High frequency fluctuations of the earth's magnetic field due to ionospheric disturbances that are globally coherent can also generate electric currents in the ocean. The field of passive magnetotellurics takes advantage of these fields to invert for the deep conductivity structure of the earth. Generally speaking, it is possible to remove ionospheric contamination using magnetotelluric transfer functions from remote observations (*Chave and Thomson*, 1989; *Jones et al.*, 1989). There is increasing recognition that the oceanic signal can obscure the earth or ionospheric signals (*Kuvshinov et al.*, 2002; *Sabaka et al.*, 2004), but in little effort has been made to extract magnetotelluric signals from horizontal

electric field profiles in the ocean.

Electric perturbations in the ionosphere radiate downward and can generate electric currents on land or in the ocean that are called magnetotelluric (MT) signals. Large disturbances are called ionospheric storms and are caused by solar winds. The AVP data was collected during a magnetically quiet time when the global magnetic disturbance index K_p was 1–3 (5–9 are perturbed values). Ionospheric activity is strongest at high latitudes. The magnitude of perturbations is described by the Dst index, which has a maxima of -200 nT during strong ionospheric storms.

There is also a background magnetic field variations due to electric currents in the ionosphere being fixed to the daylight side of the earth — these are called "quiet day" perturbations. In contrast to ionospheric storms, quiet day perturbations are strongest near the ecliptic equator.

An example of the observed magnetic field variations at the Fredericksburg, Virginia, USA (FRD) observatory is shown in Figure 3.7 for data recording during the year 1992. The plotted quantity is the square-root of the energy spectra integrated from the lowest frequency. At the lowest frequency the variance is 0, and at the Nyquist frequency (data is sampled every minute) the square root of the total variance is recovered. The component directed towards magnetic north (red) has the most variance). Most of the variance is at daily frequencies and its sub-harmonics, although 25–50% is broadly spread out over frequencies lower than once per day. There is negligeable variance at periods larger than 5 hours (5×10^{-5} Hz). Electric fields in the ocean can by misinterpreted as due to an oceanic source if they are strong enough.

3.7.1   Transfer Functions

The large-scale coherence of magnetotelluric perturbations suggests that it is possible to estimate the induced electric fields in the ocean from the magnetic field observations at FRD (75 km away from the AVP stations). This approach assumes that: (1) time-variations of the magnetic field at FRD are due to downward propagating waves that are the same as those entering the ocean off-shore of Cape Hatteras, and (2) the geometry of
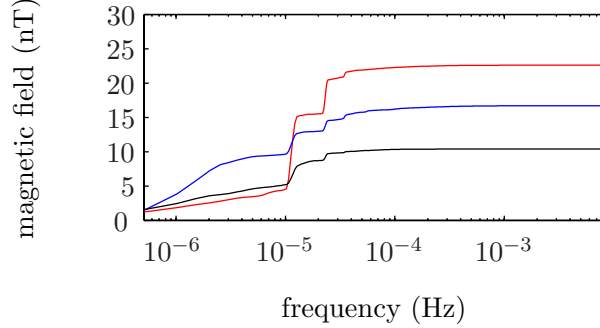
Figure 3.7: Cumulative integral of the magnetic field spectra from $f = 0$. The square-root of the total variance is recovered at the right. The components are north (red), east (blue), and down (black) (in True directions).

the continent/ocean margin can be represented as a 2D structure.

Modeling these disturbances as plane waves propagating downward into a homogeneous semi-infinite ocean (e.g., *Griffiths*, 1999) shows that electric currents equivalent to water velocities of 0.005 m s^{-1} would be generated in the ocean based on observations at FRD (not shown). Close to ocean/continent boundaries, however, there is the potential for significant perturbations of the expected signal due to the large horizontal contrast in electrical properties. Historically this phenomena is called the "coast effect" (*Dosso and Meng*, 1992; *Santos et al.*, 2001).

Electromagnetic waves have a characteristic skin-depth in conductive medium of

$$\delta = \sqrt{2/\mu\sigma\omega} \qquad , \tag{3.13}$$

where μ is the magnetic permeability and $\omega = 2\pi f$ is the frequency in radians s^{-1}. This quantity is how far a wave penetrates into a medium of conductivity σ before being reduced by a factor of e^{-1}. Skin depths in the ocean are greater than 2500 m for periods less than 0.01 Hz, which is close to the observatory sampling frequency (120 s). There is only appreciable variance in $\boldsymbol{B}$ at periods larger than a few hours ($\delta \geq 15$ km for $T \geq 1$ hour), so the ocean magnetotelluric signal is expected to be nearly barotropic at this latitude.

By applying MOED to a two-dimensional transect from FRD to the deep ocean, the magnetic field at FRD and the oceanic electric field at one point in space can be extracted

for a given frequency. Their relative amplitude and phase is a transfer function that varies with frequency

$$E_x = Z_{xy}(f)\, B_y/\mu_0 \qquad \text{B-polarization}$$

$$E_y = Z_{yx}(f)\, B_x/\mu_0 \qquad \text{E-polarization} \quad . \qquad (3.14)$$

The transfer function $Z(f)$ has units of Ω, and here the magnetic field $\boldsymbol{B}(t)$ allows for time variations on top of the main field component $\boldsymbol{F}$. These relationships between $\boldsymbol{E}$ and $\boldsymbol{B}$ are the special case of a 2D earth where $\hat{\boldsymbol{x}}$ and $\hat{\boldsymbol{y}}$ are aligned with the transect (*Simpson and Bahr*, 2005).

The 2D transect is a simplification of the 3D ocean–continent margin that meets at an angle at Cape Hatteras. This reduction to a 2D transect is valid at frequencies for which a spatial averaging of the 3D topography over the horizontal scale of the skin depth corresponds to the 2D geometry. Most of the variance is at periods greater than 6 hours, for which the skin depth in the ocean is greater than 40 km. A transfer function is obtained for estimating the magnetotelluric oceanic electric field by calculating Z over the full frequency band.

3.7.2   Magnetotelluric Results

The 2D geometry for magnetotelluric analysis is presented in Figure 3.8. Near-surface ($z > -10$ km) structure is taken from the IPOD deep seismic line and the geophysical compilation of electric properties discussed earlier, where uniform oceanic and sediment conductivities are used for simplicity. Magnetotelluric studies in the same region are used primarily for the complex lithospheric structure (*Ogawa et al.*, 1996). Deeper electrical properties are compiled from estimates by *Santos et al.* (2001) for the surface to mid-depth continental conductivity and by *Chave and Luther* (1990) for the mid-depth oceanic conductivity, and from global satellite inversions by *Kuvshinov et al.* (2002); *Kuvshinov and Olsen* (2006) for the deep earth conductivity.

MOED is used to calculate electric fields induced in the ocean and earth by downward propagating electromagnetic waves. There are two modes of electric currents: the B-polarization mode denotes magnetic fields that are parallel to the coastline (perpendicular
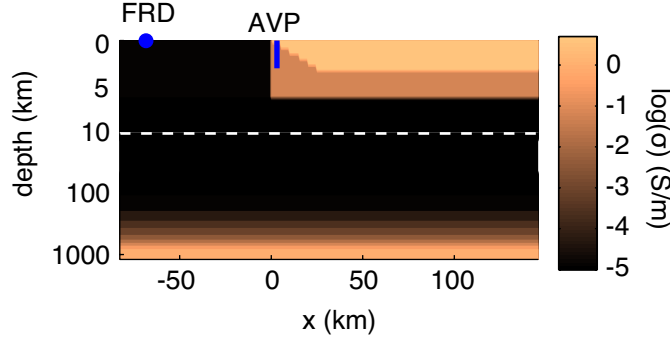
Figure 3.8: 2D Geometry used for calculating transfer functions from the magnetic field at the Fredericksburg, VA magnetic observatory (FRD) to the electric field at an AVP station. The vertical scale changes from linear to logarithmic at a depth of 10 km.

to the transect, B_y) that generate electric currents that flow in the vertical plane of the transect (J_x, J_z); and the E-polarization mode denotes electric fields and electric currents that are oriented parallel to the coastline (perpendicular to the transect, E_y, J_y) with corresponding magnetic fields in the plane of the transect (B_x, B_z). The correlation between F_h and F_z at FRD gives an indication of how much variance is described by a coherent plane-wave. The correlation coefficient is 0.27 for $|r^2|$ calculated between $F_x + iF_y$ and F_z in the time domain, that is 15% of the magnetic field variance is described by a plane wave approximation.

The magnetic field at FRD is readily extracted from the output. The transfer functions converts from the observatory measurements to an oceanic electric field as a function of frequency. In analogy to the analysis of motionally induced horizontal electric fields, two components for the oceanic electric field are considered: a vertically averaged horizontal electric field, and the electric field at one point in the vertical. The vertically-averaged electric field is for comparison with the barotropic velocity, and the point electric field is for comparison with the vertically-varying electric current density. Because MT-induced electric fields decay in amplitude as they propagate into the ocean, a depth of $z = -1000$ m is chosen to be representative of this component. For the low frequencies contained in the spectrum of magnetic field at FRD, the skin-depth is of the order of the water depth.
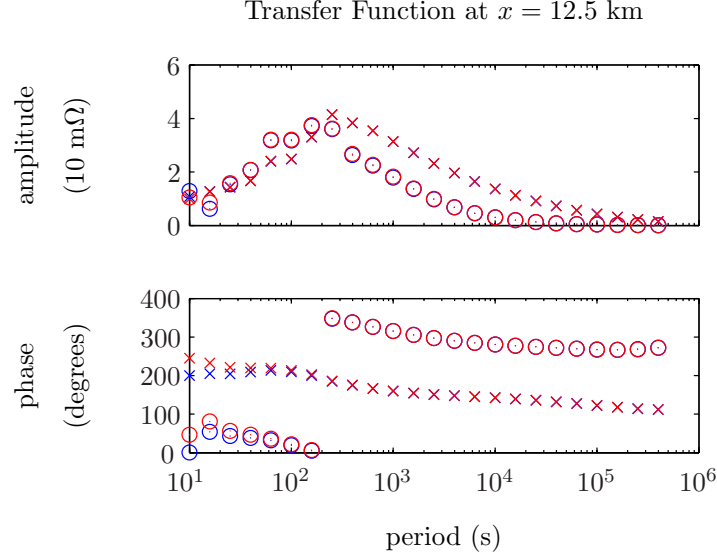
Transfer Function at $x = 12.5$ km

Figure 3.9: Transfer functions between the magnetic field at Fredericksburg, VA and the vertically averaged electric field (blue) or the electric field at a depth of 1000 m (red), both at a distance of 12.5 km from the upper continental slope. (top) The amplitude. (bottom) the phase. The E-polarization mode is shown with $\times$, and the B-polarization mode is shown with o.

Clearly, when there is appreciable high-frequency variance in the magnetic field, such as during an ionospheric storm, this analysis will not resolve the large electric fields induced near the surface of the ocean. The transfer functions obtained are shown in Figure 3.9.

Next the data are tested for noise from magnetotelluric sources. Based on the transfer functions calculated above and the magnetic fields observed at FRD, it is possible to calculate expected electric fields from the magnetic fields measured at the magnetic observatory FRD. Time series of vertically averaged electric field are shown in Figure 3.10 (left panel) as extracted for the AVP stations at the 500 m and 2000 m isobaths. The magnetotelluric-induced $\overline{E}_x/F_z$ is larger in shallower water, with estimated signal strengths of up to 0.3 m s^{-1}.

If there are magnetotellurically induced electric fields in the ocean, then there will be noise in the electric fields measured by the AVP. Because the oceanic motional induction is the dominant signal at Cape Hatteras, the magnetotelluric signal will appear as the
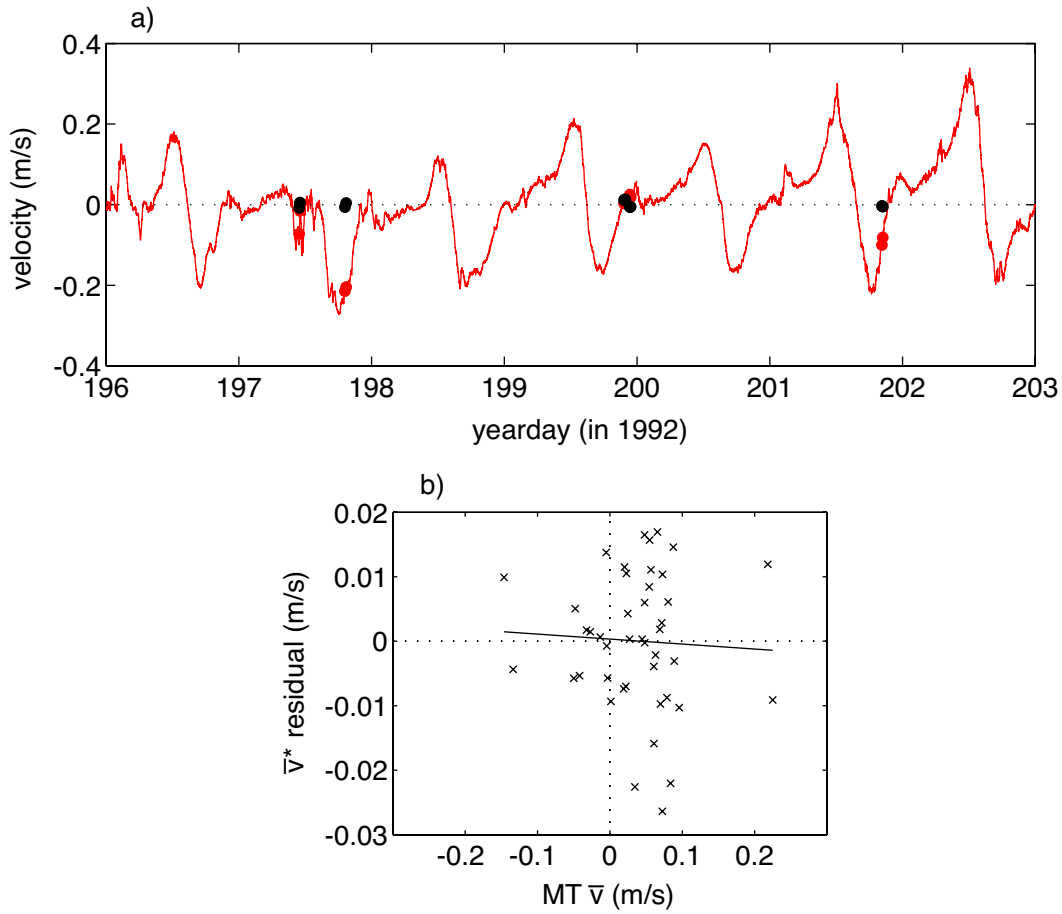
Figure 3.10: (a) Time series of $\overline{E}_{x,\mathrm{MT}}/F_z$ at a water depth of 500 m, calculated with the B-polarization transfer function from the horizontal magnetic fields measured at the Fredericksburg, Virginia magnetic observatory (solid line). The residual of $\overline{v}^*$ (black •) for each profile and the mean value of $\overline{E}_{x,\mathrm{MT}}/F_z$ (red •). (b) Correlation of the residual of $\overline{v}^*$ against $\overline{E}_{x,\mathrm{MT}}/F_z$ for all AVP profiles, for the downstream component v. The least-squares fit is shown (solid line), for which the correlation coefficient r^2 is 0.002.

residual of $\overline{v}^*$ to the 1D linear fits (Figure 3.2). The correlation of AVP residuals with the MT-induced apparent velocity is shown in Figure 3.10b. The magnitude of the residuals is 0.02–0.03 m s^{-1}, whereas the magnitude of the magnetotellurically induced electric fields is 0.05 m s^{-1} at 2000 m and 0.2-0.3 m s^{-1} at 500 m. For both the u and v components of velocity there is no statistical significance between the MT-derived quantity and the residual in $\overline{v}^*$ (right panel, $r^2 < 0.03$).

For comparison with the energy of oceanic velocity, the spectra of MT-induced electric fields are shown (Figure 3.11) against spectra from current meters located nearby as part of a separate study (*Berger et al.*, 1995; *Savidge*, 2004). Only the spectra for the depth-uniform MT-derived velocities is shown. The spectra for MT-derived velocity at $z = -300$ m is nearly the same as the depth-uniform velocity, because there is so little variance in the magnetic field at the high frequencies where the signal's skin depth is less than the water depth. The E-polarization mode (green line) has larger energy at periods larger than a few hours than the B-polarization (black line). The spectrum from a current meter mooring deployed at $z = -1000$ m along the 2000 m isobath 50 km SE of the AVP transect is shown for the along-slope component of velocity (blue) and the across-slope component (red), where tides have been filtered out. Whereas the MT signal is white (during a magnetically quiet period), the oceanic signal is red. At periods longer than a day the oceanic signal dominates: variance is 1.2 m^{2}s^{-2} for ocean velocity and 0.01 m^{2}s^{-2} for MT-derived equivalent velocities. The MT signal dominates by a similar magnitude (a factor of 100) for periods less than a day for these data, but note that tidal signals have been removed from the current meter velocities by low-pass filtering.

3.8 2D Gulf Stream Transect: Results

Having determined the sediment electrical properties and that magnetotelluric signals are relatively small, we now turn to the electric field results based on the 2D transect described in section 3.5. The first question is whether the AVP measurements are reproduced with the numerical model. The model is forced with the average velocity profile at each station, so the question is initially considered in the time-averaged sense.
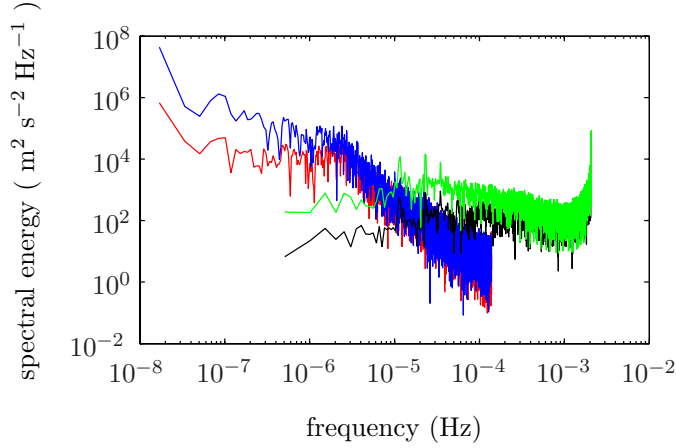
Figure 3.11: Spectra of velocity from MMS current meter C4 located at the 2000 m isobath at a depth of 100 m (*Berger et al.*, 1995) for along-slope (blue) and cross-slope (red) velocities (direction 28° True), and equivalent velocities from MT-derived barotropic transfer functions for the B-polarization mode (black) and the E-polarization mode (green).

The prescribed velocity is shown in Figure 3.12 as gridded to the model grid for the downstream velocity component. The rotation angle is determined so that $\overline{\sigma' u'}/\overline{\sigma}\,\overline{u} = \gamma_x = 0$, where $\hat{\boldsymbol{x}}$ is in the cross stream direction (positive offshore). The rotation angle defined by this method is within a few degrees of the direction of vertically integrated velocity. By definition the model $\overline{v}$ (solid black line) fits the AVP data (*) at the 5 stations (top panel). The 5 AVP stations are indicated by vertical lines, and correspond from left to right to the stations at the 500 m, 1000 m, 2000 m, 3000 m, and 3500 m isobaths. The velocity is gridded with a cubic interpolation technique that maintains a continuous second derivative between stations. Outside of the first and last stations, the velocity is set to go to 0, to define a bounded Gulf Stream.

There is a lack of observations in the literature to constrain the Gulf Stream velocity structure inshore of 500 m, which is seen later to strongly influence the results. The station-averaged velocities show a maximum $\overline{v}$ at the 500 m isobath, and though the 1000 and 2000 m isobath stations resolve the seaward structure of this maximum the landward structure remains unresolved. The depth of the Gulf Stream, defined as the
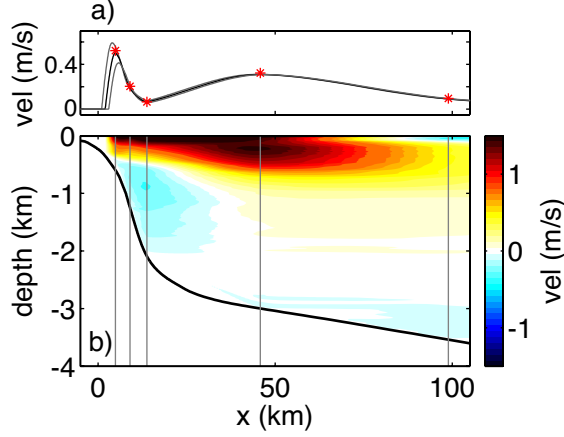
Figure 3.12: Velocity input into MOED. (a) The depth-averaged or barotropic velocity $\overline{v}$ at the central position (black) and shifted by ± 1 km to either side (gray), with the AVP-calculated $\overline{v}$ (red $\ast$). (b) The gridded velocity (color) based on the 5 station-averaged velocity profiles (vertical black lines).

depth where the velocity direction changes from the overlying waters, is 400–500 m along the continental slope and deepens to 1000 m over the continental rise. The Gulf Stream is not expected to be able to extend onto the continental shelf past the shelfbreak (at a depth of 100 m), so the inshore limit of the Gulf Stream is set at the 250 m isobath, 3 km inshore of the 500 m station and 6 km seaward of the shelfbreak. The horizontal velocity structure is only constrained at 7 locations: the 5 AVP stations and the two locations where the velocity goes to 0 (at $x = 2$ km and $x = 150$ km).

The AVP velocity is calculated based on a 1D interpretation of the measured electric field, so it is only as accurate to the extent that the 1D approximation is accurate. The validity of this assumption is returned to in section 3.10.

To be able to compare the calculated electric field with the AVP observations it is necessary to define $\overline{v}^*$ from the model output:

$$\overline{v}^*_{2D} = \frac{1}{F_z(z_2 - z_1)} \int_{z_1}^{z_2} E_x \, dz \quad , \tag{3.15}$$

for a depth range $z_1 \leq z \leq z_2$. This quantity includes 2D effects that arise from gradients in velocity and topography.

The quantity $\overline{v}^*$ is calculated from the AVP data over the depth range for which the acoustic Doppler system provides velocities. The analogous quantity from the model is obtained by setting $z_1(x) = H(x) + 50$ m and $z_2(x) = H(x) + 250$ m, denoted $\overline{v}^*_{\text{2D,AVP}}$. More generally, $\overline{v}^*_{\text{2D}}$ can be calculated over the full water column ($z_1 = H(x)$ and $z_2 = 0$) to obtain a value that is not instrument specific, denoted $\overline{v}^*_{\text{2D}}$. Most instruments determine $\overline{v}^*$ over a limited depth range (e.g. cables are on the seafloor, XCPs are referenced with surface shipboard ADCPs, etc.), however, so the errors discussed for the AVP will not be exactly the same as for different instruments.

A second point of comparison is with the $\overline{v}^*$ expected from the 1D approximation. This uses the 1D form of λ from (3.6), λ_{1D}, to calculate

$$\overline{v}_{\text{1D}} \equiv \overline{v}\frac{1+\gamma}{1+\lambda_{\text{1D}}} \qquad . \tag{3.16}$$

The horizontal electric field E_x (Figure 3.13b) is shown over the whole domain. Along the steep continental slope E_x is not vertically uniform — the strong field in the water doesn't penetrate to the bottom of the sediment — so this is a location where there are perturbations from the 1D approximation. The deviation from the 1D approximation is most readily seen by comparing $\overline{v}^*_{\text{2D,AVP}}$ (red) against $\overline{v}_{\text{1D}}$ (blue) in Figure 3.13a. It is only on the upper continental shelf that differences are significant. The AVP data are within 0.02 m s^{-1} of the calculated results at all stations seaward of the 1000 m isobath, but the shallowest station disagrees by 0.05 m s^{-1} (17%). Although the numerical model resolves any 2D effects, there are two other possible sources of the disagreement. First, the velocity inshore of the 500 m isobath is unknown. If the maximum in $\overline{v}$ is further inshore, then $\overline{v}^*_{\text{2D,AVP}}$ would increase at this station. Second, the station-averaged $\overline{v}(1+\gamma)$ measured by the AVP is not necessarily equal to the average of the two components $\overline{v}$ and $1+\gamma$ used to initialize the model.

MOED is initialized with u, v, F_z, F_h and sediment conductivity structure, each of which is responsible for separate complexities in comparison with the 1D approximation. The dominant 1D signal comes from downstream velocity (v) and the vertical magnetic field (F_z). Secondary signals arise from induction by the horizontal magnetic field ($\boldsymbol{v}_h \times \boldsymbol{F}_h = (uF_y - vF_x)\hat{\boldsymbol{k}}$) and from the detailed sediment structure that contradicts the 1D
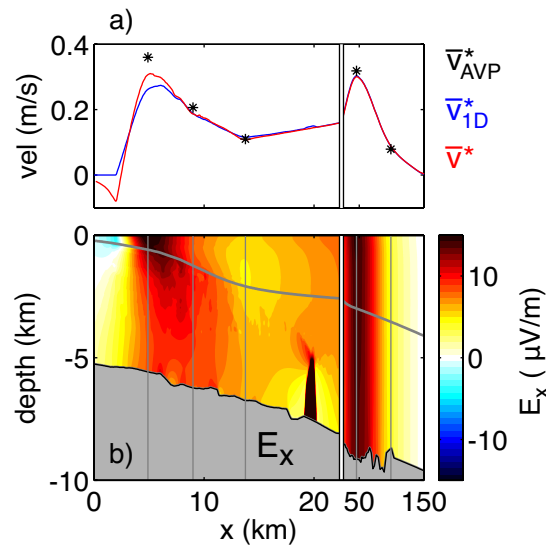
Figure 3.13: MOED results using AVP observations and compiled sediment conductivities. (a) Vertically averaged quantities: $\overline{v}_{1D}$ (blue line), $\overline{v}^*$ from MOED (red line), and station-averaged AVP $\overline{v}^*$ (black *). (b) Horizontal electric field. The full sediment depth is shown, the seafloor (gray line) is in the top half and the non-conductive basement is shown by the gray shading. AVP stations are indicated by vertical lines. Note the break in horizontal scale at $x = 22.5$ km.

assumption of a uniformly conductive sediment column.

How much of E_x comes from each of these source? By removing some of these forcing terms their contribution to the full solution can be quantified. In particular, the solution was calculated for the following cases in addition to the standard case of full forcing: 1) just v and F_z with full sediment structure, 2) just F_h with u and v and full sediment structure, and 3) no sediment structure (uniform $\sigma_s = 0.583$ S m^{-1}) but forcing from u, v, F_z and F_h. The error is considered relative to the 1D approximation for the full initialization, which breaks up the 2D perturbations into the separate components. The 2D error is defined by

$$\epsilon_j = \overline{v}^*_{2\mathrm{D},j} - \overline{v}^*_{1\mathrm{D}} \tag{3.17}$$

This is the magnitude of the correction to the 1D approximation $\overline{v}^*_{1\mathrm{D}}$, where j stands for the 3 cases of reduced forcing complexity. This equation is in terms of $\overline{v}^*$, however, so to obtain equivalent errors in the barotropic velocity it is necessary to multiply by $(1 + \lambda)/(1 + \gamma)$. As this procedure is not necessarily well-defined it is postponed until later.

The quantities $\overline{v}^*2\mathrm{D}$ and ϵ_j for the full forcing and the 3 cases above are presented in Figure 3.14a. The expected $\overline{v}^*_{1\mathrm{D}}$ from the 1D approximation (thick gray line) goes to 0 at the inshore extent of velocity ($x = 2$ km). On the continental slope $\overline{v}^*_{2\mathrm{D}}$ are larger than $\overline{v}^*_{1\mathrm{D}}$ for all cases that include induction due to F_z, with negative electric fields occurring over the upper continental shelf up to the shelfbreak. The negative electric field is cause by vertical spreading of the electric potential in the thick underlying sediments. The signal from v and F_z (case 2, red line) contains almost all of the deviation from the 1D approximation. The magnitude of induction from F_h (blue line) is less than 0.001 m s^{-1}.

The full detail sediment structure results in a few cm s^{-1} correction to the case of homogeneous sediments. The value of the uniform sediment conductivity (0.583 S m^{-1}) was chosen so that the fractional deviation of $\overline{v}^*_{2\mathrm{D},3}$ from the full solution $\overline{v}^*_{2\mathrm{D}}$ integrates to 0 over $60 < x < 120$ km, that is the region over which the 2D perturbations are smallest. This uniform value of σ_s yields a larger $\overline{v}^*$ (green line) on the upper continental slope ($2 < x < 7.5$ km) compared with the full resolution case and a smaller value on the
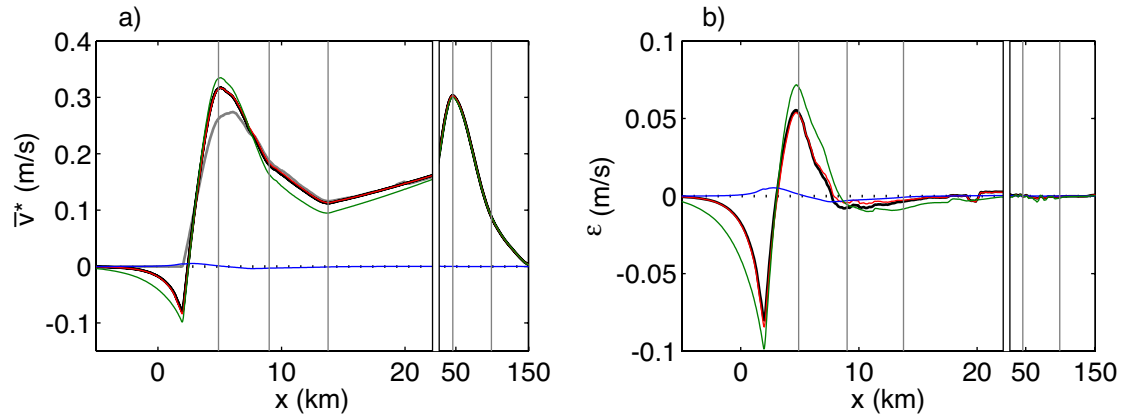
Figure 3.14: (a) $\overline{v}^*$ calculated for the full complexity case (thick black line), the three reduced complexity cases (u and F_z, red; u, v and F_h, blue; uniform conductivity sediment, green), and the 1D approximation $\overline{v}^*_{1D}$ (thick gray line). (b) The difference ϵ_j between the $\overline{v}^*$ shown in (a) and $\overline{v}_{1D}$. The 5 station positions are denoted by vertical gray lines, and there is a scale break at $x = 22.5$ km.

lower continental slope and upper continental rise ($7.5 < x < 25$ km). In other words, uniform sediment conductivity results in decreased sediment shorting of E_x on the upper continental slope and increased shorting on the lower continental slope. The negative $\overline{v}^*$ inshore of $x = 2$ km attenuates exponentially approaching the shelf. The decay is twice as fast when the sediment is fully resolved compared with the uniform conductivity case, because of the presence of conductive layers ($\sigma_s = 1.5$ S m^{-1}) of coarse sand near the top of the sediment column on the upper continental slope and shelf.

The fully initialized run (thick black line) and the less complete runs all deviate from the 1D approximation (Figure 3.14b) on the upper slope ($2.5 < x < 10$), with errors of 0.05 m s^{-1} at the 500 m station ($x = 5$ km). Most of the 2D perturbations are generated by v and F_z (red line). The contribution from F_h is small, it is less than 0.01 m s^{-1} over the continental slope and decreases to less than 0.001 m s^{-1} at and seaward of the 2000 m isobath. All of the cases with reduced forcing deviate by less than 0.01 m s^{-1} from the fully initialized $\overline{v}^*_{2D}$ and from $\overline{v}^*_{1D}$ at locations seaward of the 1000 m isobath. Larger deviations from $\overline{v}^*_{1D}$ occur on the upper continental slope. The velocity structure inshore of the 500 m isobath is unknown, but if the sharp velocity front is realistic, the deviations can reach

0.1 m s^{-1} right where the velocity goes to 0. The case of a uniform sediment conductance introduces the largest differences with the full resolution case, a few cm s^{-1} on the upper slope. The choice of σ_s for the uniform sediment case (green) accurately reproduces the 2D electric field in deep water ($20 < x < 150$), but this uniform value yields an effective sediment conductance that is too small on the upper continental slope compared with the full-resolution sediment. The 5% increase in $\overline{v}^*$ at the 500 m isobath implies that the apparent conductivity of upper continental slope sediment is 20% larger ($\sigma_s = 0.72$ S m^{-1}). The 20% increase in apparent conductance is partly generated by 2D effects, but it is not possible to extract this contribution when the 1D sediment parameterization is applied. The ambiguity of defining an appropriate average sediment conductivity σ_s based on the 1D simplification is reduced by fully resolving the conductivity structure of the sediment.

A comparison of the model output with the AVP data is best performed at the locations where the AVP data constrain the model. Following (3.4), $\overline{v}(1 + \gamma)$ is related to $\overline{v}^*$ in a 1D sense by a slope of $1 + \lambda$ and are plotted in Figure 3.15. The line that describes $\overline{v}^*_{2D,AVP}$ and $\overline{v}(1+\gamma)$ from the model (Figure 3.15a) starts out at the origin at the inshore edge, $\overline{v}^*_{2D,AVP}$ becomes negative while $\overline{v} = 0$, and then both become positive and proceed through the maximum at the 500 m isobath, the local minimum at the 2000 m isobath, and finally the local maximum at the 3000 m isobath. The value from the model at each station is close to the average of the AVP data, but the data have large ranges at each station compared with the model. To perform a more accurate comparison, it is necessary to include time-variations of the Gulf Stream in the model analysis.

3.9 Gulf Stream Meandering

The model results presented in the previous section are based on a time-invariant velocity structure, which is a major simplification of the Gulf Stream.

Along the path of the Gulf Stream, Cape Hatteras is the boundary between the topography-trapped regime to the SW and the freely-meandering regime to the NE. The meander characteristics are quite different in the two regions: to the SW the strongest
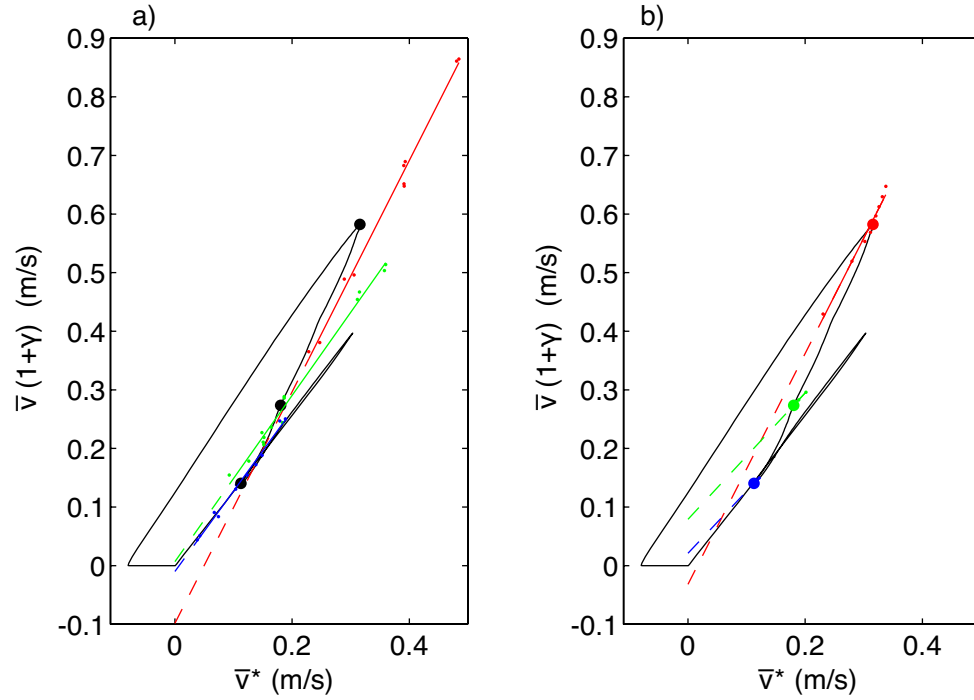
Figure 3.15: Graphs $\overline{v}(1+\gamma)$ against $\overline{v}^*$. (a) The AVP data (dots for individual profiles; solid line, linear fit; dashed line, extension of linear fit to $x = 0$) and the values of $\overline{v}(1+\gamma)$ and $\overline{v}^*_{\mathrm{2D,AVP}}$ from MOED (black line; large black dots at the 500, 1000, and 2000 m stations from top to bottom). AVP Data at the 500 m station is shown in red, at the 1000 m station in green, and at the 2000 m station in blue. (b) Linear fits from the model results at the three stations with schematic meanders: a shift of 0 m (black line, large colored dots), shifts of ± 125, ± 250, ± 500 and ± 1000 m (small colored dots), linear fits at each station (solid line; extension to 0 as dashed line). The color coding is the same as in (a).

meanders have wavelengths of 180–380 km, periods of 3–8 days, and amplitudes of 50 km (*Miller*, 1994; *Savidge*, 2004), while to the NE long period disturbances grow ($T > 10$ days, *Watts et al.*, 1995), meander amplitude increase to 100 km, and the jet's transport becomes increasingly barotropic (*Johns et al.*, 1995; *Meinen et al.*, 2007). The separation region at Cape Hatteras is characterized by a decay of small meanders upstream and the growth of large meanders downstream (*Savidge*, 2004). The meander amplitudes of the north wall decrease to a minimum of 10 km at Cape Hatteras (*Olson et al.*, 1983; *Tracey and Watts*, 1986).

Despite the minimum in meander amplitude, meanders have been observed here and eddies can transit past Cape Hatteras (*Glenn and Ebbesmeyer*, 1994). The AVP stations on the continental slope show a positive correlation between velocity and temperature at constant depth levels. This implies that if the center of the Gulf Stream (near $x = 45$ km) moves inshore and velocity increases that isotherms deepen and temperature rises, which is consistent with a Gulf Stream that shifts from side to side (meanders).

A second oceanographic current at Cape Hatteras is the Deep Western Boundary Current (DWBC) that flows south along the continental slope of the mid-Atlantic Bight. There are few data that directly address the kinematics of how it crosses underneath the Gulf Stream, although chemical tracers show that the upper DWBC (1000–2000 m) joins the North edge of the Gulf Stream while the deeper part (2000–3000 m) continues further south along the margin (*Pickart and Smethie*, 1993; *Pickart*, 1994). The DWBC is a continuous feature from Labrador to the Bahamas, so it clearly retains its strong signature however it crosses the Gulf Stream.

The range of $\bar{v}$ measured by the AVP over the 5 days of measurements shows that the vertically integrated velocity ($H\bar{v}$, transport per unit width) of the Gulf Stream over the continental slope changes direction by 35° and magnitude by a factor of 2. While Gulf Stream meanders downstream of Cape Hatteras can be readily described by translation and rotation of the velocity structure (*Watts et al.*, 1995), meanders at Cape Hatteras and to the south interact with the continental slope. At the 500 m isobath the Gulf Stream is 400 m deep, so the velocity must shoal (and $\bar{v}$ decrease) for shifts greater than

3 km inshore (the distance to the 400 m isobath). There are few studies that resolve the evolution of velocity for an onshore meander. Temperature observations 400 km to the SW (*Bane et al.*, 1981; *Brooks and Bane*, 1983) show a warm filament forming at the leading edge of a meander that wraps around a cold-core eddy behind the meander.

How can this velocity variability be recovered in the model? There are not sufficient data to construct an accurate series of synoptic sections, but schematic modes of variability can be applied.

One of the difficulties in interpreting these data is that the time-averaged velocity structure of the Gulf Stream has large horizontal gradients. With the electric field depending on $\bar{v}$ according to the 1D approximation, small horizontal meanders over steep topography result in large changes in $\bar{v}$ even if the transport per unit width $H\bar{v}$ remains constant. Also, horizontal gradients of velocity are not constant across the Gulf Stream, so meanders also change how velocity gradients align with topography. A secondary issue is that the stations were not repeated exactly: the across-stream distance between station repeats has a standard deviation of 130–220 m. This distance is too small to explain much of the observed velocity variability. The measured variability is thus a mostly due to Gulf Stream meanders, with a small contribution from inexact station repeats.

It is well established that the transport of the Gulf Stream is nearly constant over time. This eliminates a 'pulsing' mode of variability by which the amplitude of the entire velocity structure increases in tandem. It is important to highlight that pulsing is one mode of variability, because this is the mode of variability implied by (3.4): changes in $\bar{v}(1+\gamma)$ and $\bar{v}^*$ are linearly related. In reality, changes in $\bar{v}$ are due to complex meander events, so 2D effects at any one location will not necessarily be the same magnitude as a meander develops.

There are two ways to recover the range of velocity $\bar{v}$ seen in the data at each station. The first method is by sampling on either side of a central x-location when the velocity is fixed to topography, and is denoted by $()_x$. This is analogous to inexact stations repeats and describes horizontal sampling of the time-invariant or instantaneous velocity structure. The second method is by staying at a fixed location relative to topography

while the velocity structure shifts horizontally to either side. This describes meandering and is denoted by $()_v$. The sampling is realistically a combination of these two methods, but the results from combining both methods are very similar to those from just method 2.

The fitting procedures done to obtain λ and y_0 are shown schematically in Figure 3.16. It is easiest to visualize by picking four points on either side of a central point (large dot). Because $\overline{v}(1 + \gamma)$ and $\overline{v}^*$ do not change in tandem, when they are plotted against each other they define a line that does not go through the origin. This is called the tangent line fit (orange). A second method that will be discussed later is a ratio fit (purple), which forces the fit to go through the origin. This constraint causes the line to be defined by the slope to the geometric mean of the data (central large point, Figure 3.16b).
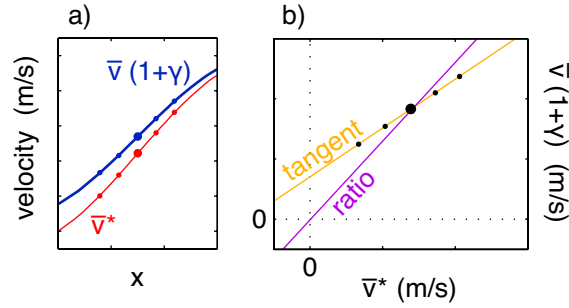

Figure 3.16: Schematic diagram of the fitting procedure. (a) The quantities $\overline{v}$ and $\overline{v}^*$ plotted against distance, with one central point and 2 points on either side. (b) The 5 points from panel (a) plotted for $\overline{v}(1+\gamma)$ against $\overline{v}^*$. A tangent line fit recovers a straight line that does not necessarily go through the origin, whereas a ratio fit connects the origin with the geometric mean of the data.

The fitting procedures done to obtain λ and y_0 from the model is shown in Figure 3.15a. For the first method, a stationary velocity structure, a linear fit extracts the tangent line of the curve of $\overline{v}^*$ against $\overline{v}(1+\gamma)$ (black line) across the transect. The slope and y-intercept calculated by a tangent line for fixed velocity are denoted $1 + \lambda_{\mathrm{d}x}$ and $y_{0,\mathrm{d}x}$ (red dotted line, Figure 3.17 and red solid line, Figure 3.18). At local extrema — the inshore maximum in $\overline{v}$, a local minimum at the 2000 m station, and a local maximum at the 3000 m station — the slope changes rapidly in sign (going through both 0 and ∞)
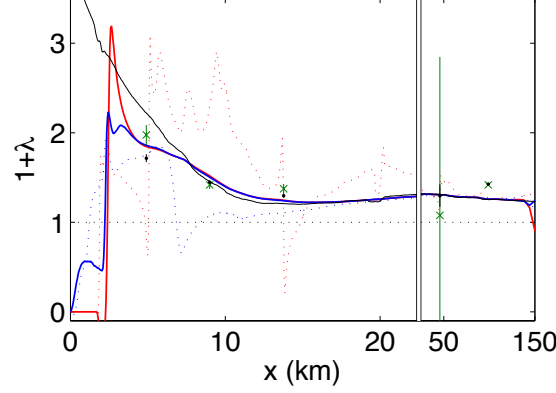
Figure 3.17: The quantity $1 + \lambda$: AVP data, linear fit (green $\times$) and ratio fit (black dot) with vertical lines for error bars, the 1D value $1 + \lambda_{1D}$ (black line), sampling over x with velocity fixed to topography for the ratio method $1 + \lambda_{r,dx}$ (red solid line) and the tangent line method $1 + \lambda_{dx}$ (red dotted line), sampling at one location with velocity shifting relative to topography for the ratio method $1 + \lambda_{r,dv}$ (blue solid line) and the tangent line method $1 + \lambda_{dv}$ (blue dotted line).

and the y-intercept reaches large values. The large variability makes this method unstable for inverting from electric field to velocity.

The second method uses sampling at a fixed location while the velocity structure shifts by $\pm \Delta x$. The changes that occur in $\overline{v}$ for meanders of ± 1 km are shown in Figure 3.12a by the gray lines on either side of the unshifted value (black). A line is fit by least-squares to the values of $\overline{v}^*$ and $\overline{v}(1 + \gamma)$ at each station that result from discreet shifts of the velocity structure. A slope $1 + \lambda_{dv}$ and a y-intercept $y_{0,dv}$ result. The synthetic sampling is performed for an even distribution of meander amplitudes, which are 0, ± 125, ± 250, ± 500 and ± 1000 m (Figure 3.15b).

Schematic meanders add velocity variability at each station in the model analysis (Figure 3.15b), but it is smaller than for the observations (Figure 3.15a), especially at the 1000 and 2000 m stations. The contribution from inexact station repeats is small: it is the horizontal gradient of $\overline{v}$ multiplied by the standard deviation of cross-stream location (200 m), yielding a range of less than 0.02 m s^{-1} for all stations. Meanders are present in the observations with larger velocity variability than can be recovered with schematic
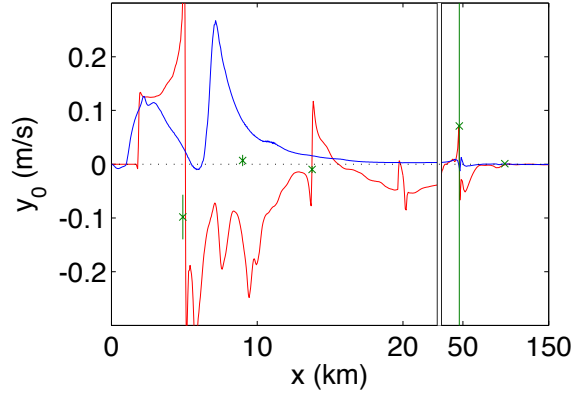
Figure 3.18: The y-intercept y_0: AVP data (green $\times$), tangent line fit with fixed velocity $y_{0,\mathrm{d}x}$ (red line), and tangent line fit with meandering $y_{0,\mathrm{d}v}$ (blue line).

shifting of the time-averaged structure. Lacking additional data there is not a better way to recover the observed variability, however, so this method shall be used below with this caveat.

The linear fit based on schematic meandering is calculated for data points from the 9 meander amplitudes (Figure 3.15b). The y-intercept for the 500 m station is negative (-0.04 m s^{-1}), in general agreement with the AVP data, but the 1000 m station disagrees with the AVP data by having a large positive (0.1 m s^{-1}) y-intercept. Although there is more horizontal averaging and smoothing than by sampling the horizontal structure of velocity fixed to topography, there remains the artifice of the slope going to 0 or ∞ at local extrema.

The tangent line fit with meandering (tangent line with fixed velocity) is shown by the red dotted line (blue dotted line) for the slope $1 + \lambda_{\mathrm{d}v}$ in Figure 3.17 and by the red solid line (blue solid line) for the y-intercept (y_0) in Figure 3.18. Y-intercepts reach values of ± 0.1 m s^{-1}, but neither $y_{0,\mathrm{d}x}$ nor $y_{0,\mathrm{d}v}$ agree with all y_0 calculated at the AVP stations. The tangent line fits do not yield robust values for $1 + \lambda$ or y_0 and so are of little utility for inverting the electric field to velocity.

A simple way to obtain a robust fit is to use a ratio for fixed velocity (denoted $()_{r,dx}$)

between $\overline{v}^*$ and $\overline{v}(1 + \gamma)$

$$1 + \lambda_{\mathrm{r,d}x} = < \frac{\overline{v}(1 + \gamma)}{\overline{v}^*} >_{\mathrm{d}x} \quad . \tag{3.18}$$

This quantity is shown by the red line in Figure 3.17. The use of a ratio forces the y-intercept to be zero.

A similar definition is obtained if the velocity profile shifts relative to topography but the observation point remains fixed in space, where the shifting velocity is denoted by $()_{\mathrm{d}v}$

$$1 + \lambda_{\mathrm{r,d}v} = < \frac{\overline{v}(1 + \gamma)}{\overline{v}^*} >_{\mathrm{d}v} \quad , \tag{3.19}$$

shown by the blue line in Figure 3.17.

Using a ratio for calculating λ from the data affords a more robust calculation of λ that is less influenced by the local extrema or $\overline{v}$ (whether oceanic or due to uneven water depth). Though the relation between $\overline{v}(1 + \gamma)$ and $\overline{v}^*$ may describe a line that doesn't go through the origin with high linearity, these tangent line fits are highly variable. The smoother fit using a ratio is preferred despite its larger misfit. The ratio methods agree with each other very closely except at the inshore edge of the Gulf Stream ($x = 2.5$ km) and reproduce the values of λ calculated from the AVP data the most accurately of any method. The largest misfit is at the 500 m station, where the AVP $\lambda = 0.97 \pm 0.06$ from a linear fit. Using a ratio fit at this station, as this is the only station with a large y-intercept, yields a value for $\lambda_{r,v}$ of 0.72 ± 0.02. Note that there is no statistical confidence for λ calculated at the two deepest AVP stations.

For the time-averaged interpretation of the velocity structure with schematic meanders, the ratio method for calculating λ gives values that are in best agreement with the AVP observations.

3.10 Accuracy of Inverting for Velocity

Now that the relationship between $\overline{v}$ and $\overline{v}^*$ is clearer, we turn to the question of how accurately the electric field can be inverted to velocity.

The depth-uniform error is

$$\epsilon_{\mathrm{BT},i} = \overline{v}_{\mathrm{2D}}(1 + \lambda_i)/(1 + \gamma) - \overline{v} \quad , \tag{3.20}$$

where $\overline{v}_{2D}$ comes from the model output (averaged over the water column). The subscript $()_i$ denotes which λ_i is used from the previous discussion (section 3.9): λ_{1D}, $\lambda_{r,dx}$, or $\lambda_{r,dv}$. The tangent line fits yield large and erratic errors and will not be pursued further.

The depth-uniform errors based on (3.20) are shown in Figure 3.19. In this figure $\epsilon_{BT,1D}$ (black line) indicates that the 1D theory with complete sediment knowledge describes the electric field within a few cm s^{-1} over most of the Gulf Stream. The error is largest on the upper slope where there is a sharp inshore front in velocity and has a maximum of 13 cm s^{-1} ($\sim$25% relative error). All methods for calculating the depth-uniform error give large errors in this region, however. The inversions is most accurate in situations where it is feasible to estimate the sediment conductance independently from geophysical data.

Of the heuristic methods of calculating λ, the smallest barotropic error comes from $\lambda_{r,dx}$ ($\epsilon_{BT,dx}$, red line) based on an instantaneous velocity structure. Errors are less than 2 mm s^{-1} except at the landward edge of the Gulf Stream. The calculations for a shifting velocity structure ($\epsilon_{BT,dv}$, blue line) has significantly larger error that is more variable over the entire width of the Gulf Stream. The values from $\lambda_{r,dv}$ exhibit large barotropic error at the inshore $\overline{v}$ maximum of 0.23 m s^{-1} (50%), but seaward the error is < 2 cm s^{-1} (< 10% of $\overline{v}$). The salt diapir at 19 km creates an error of -5 cm s^{-1} (-50% of $\overline{v}$) when the velocity structure shifts over it. Electric fields tend to spread out relative to velocity gradients, as can be seen in the positive maximum in $\epsilon_{BT,1D}$ at the 500 m isobath with negative extrema on either side. One conclusion is that meanders of velocity fronts over sloping topography lead to a less accurate relationship between $\overline{v}$ and $\overline{v}^*$. Larger errors results from heuristic determination of sediment shorting $\lambda_{r,dv}$ than with independent knowledge of λ_{1D}. Also, $\overline{v}^*$ does not exactly follow the small-scale variations of $\overline{v}$, as can be expected from horizontal averaging arguments (*Chave and Luther*, 1990; chapter 2) .

The second mode of errors are baroclinic errors that arise from $\boldsymbol{J}_h(z)/\sigma$ having different vertical structure from the forcing velocity $\boldsymbol{v}(z)$. Because the electric-field-derived velocity measured by vertically profiling instruments (the AVP in this case) is a relative velocity, the baroclinic error is defined as the difference between these two properties with the
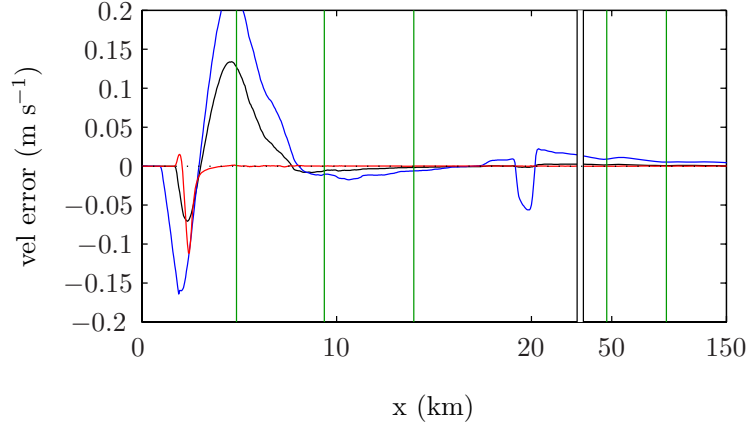
Figure 3.19: Depth-uniform velocity errors: $\epsilon_{\mathrm{BT,1D}}$ (black line), and the rest of the lines follow equation (3.20) for $\epsilon_{\mathrm{BT,d}x}$ (red line) and $\epsilon_{\mathrm{BT,d}x}$ (blue line), see text for details. The error from a linear fit over space $\lambda_{\mathrm{d}x}$ is not shown because it is very erratic. The absolute values are shown in m s^{-1}.

vertical mean removed

$$\epsilon'_{\mathrm{BC}}(x,z) = v(x,z) - \frac{J_x(x,z)}{\sigma(z)F_z} - \overline{\epsilon'}(x) \tag{3.21}$$

$$\overline{\epsilon'} = \frac{1}{z_2 - z_1} \int\limits_{z_1}^{z_2} \left[v(x,z) - \frac{J_x(x,z)}{\sigma(z)F_z} \right] \mathrm{d}z \quad ,$$

This quantity is shown in Figure 3.20 for $z_1 = H(x)$ and $z_2 = 0$ m. The error ϵ'_{BC} (Figure 3.20b) has maximum amplitudes but different signs at the sea surface and bottom. The vertical second moment (similar to a standard deviation) of ϵ'_{BC} is shown in the top graph. On the continental slope the maximum rms errors are ≤ 2 cm s^{-1}, with values of less than 5 mm s^{-1} in deeper water.

The depth-uniform and depth-varying velocity errors discussed above tend to have maximum gradients at the AVP stations where velocity is constrained. The gridding algorithm, despite maintaining a smooth second derivative, generates smaller gradients between the stations. This means that the model is limited to resolving the sampled velocity structure at the 5 stations, and that the true velocity structure is expected to lead to errors of similar magnitude between the AVP stations.
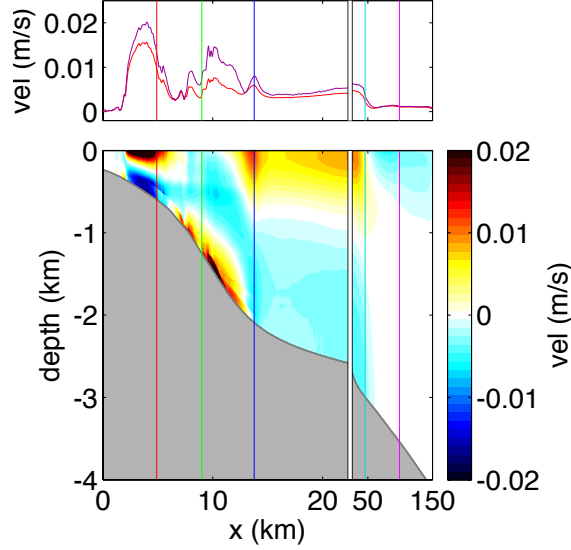
Figure 3.20: Depth-varying velocity errors calculated from the model output. (a) Depth-varying velocity errors based on (3.21). (b) The maximum values in the vertical of these errors (in red) and the maximum value of the biased AVP velocity (in purple, see text for details).

For the AVP data the vertical offset $\overline{\epsilon'}$ from (3.21) is only calculated when the instrument is within 50–250 m of the bottom. In regions where the baroclinic error is significant this will degrade the velocity over the entire water column by 0.01 m s^{-1} rms (purple line, Figure 3.20a). The baroclinic relative error is less than 10% of the barotropic velocity, or given the maximum surface velocities of 1.5–2 m s^{-1} the relative error is 1–2%.

3.10.1 Depth-varying Correction to Observations

Although the AVP data relies on an absolute velocity to remove the influence of $\overline{v}^*$, there can be 2D perturbations of the sampled quantity $\boldsymbol{J}/\sigma$ from the true velocity. The station-averaged velocity profiles can be corrected with the profiles of $\epsilon'_{\mathrm{BC,AVP}}$, where the subscript AVP means that the error integrates to 0 over the depth range that the reference velocity is obtained (3.15). The corrections (Figure 3.21) are mostly less than 2 cm s^{-1} (1–2% of the maximum velocity) and are surface intensified, correlated with the regions of strong flow.
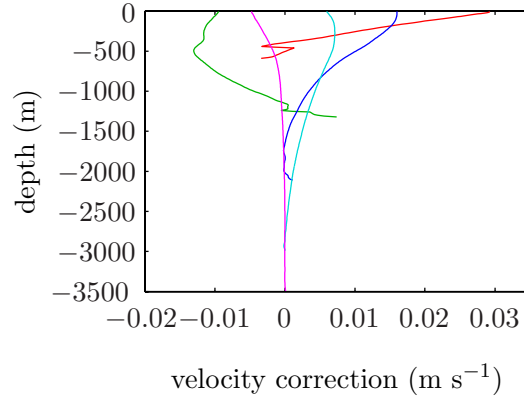
Figure 3.21: Correction to AVP velocities for 2D errors. Profiles of $\epsilon'_{v,AVP}$ at each station. The colors indicate which station (same as in Figure 3.20).

The corrections shown are in error because the velocities they are based on are in error themselves. The velocities used to initialize MOED come from a 1D interpretation of the directly measured electric fields. Assuming that the velocity is accurate to first order, an iterative approach can be used. The iterative correction converges quickly because the correction is only 1–2%: subsequent iterations will be further modified by 1–2%. These corrections are equivalent to the those described by term 3 of (3.9), although this term is not expected to be valid because the assumption of small H/L is inaccurate along the continental slope.

3.11   Non-local Electric Currents

The previous sections assume that electric currents flow exclusively in a vertical plane across the Gulf Stream. By this assumption there can be no non-local currents $\boldsymbol{J}^*$ because there are no downstream gradients, in particular downstream gradients in $F_z\overline{v}^*$ (term 2 of (3.9)). In the vicinity of Cape Hatteras the Gulf Stream flows into deeper water, and although mass transport must be conserved the vertically averaged quantities $\overline{v}$ and $\overline{v}^*$ can diverge in the downstream direction. In this section an equivalent circuit is used to estimate the magnitude of $\boldsymbol{J}^*$.

The equivalent circuit (Figure 3.22) consists of two locations along the path of the
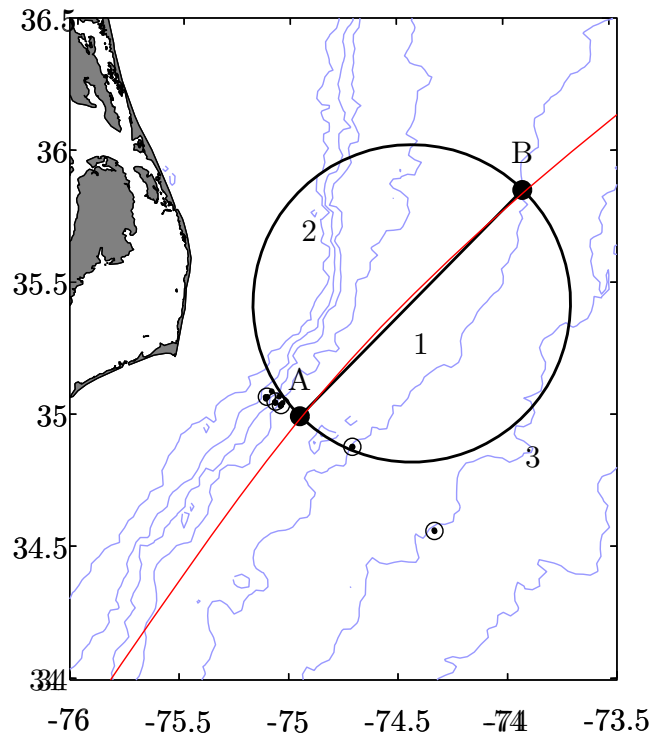
Figure 3.22: The equivalent circuit for calculating the magnitude of $\boldsymbol{J}^*$. AVP stations ($\odot$), the points at which the $\overline{v}^*$ forcing is calculated points A and B ($\bullet$), and the circuit elements 1, 2 and 3 are marked. A schematic Gulf Stream path comes from *Watts et al.* (1995), based on satellite imagery.

Gulf Stream, point A along the AVP transect and point B 130 km downstream. The downstream gradient of $\overline{v}_{2D}$ along line 1 (of distance L) drives electric currents perpendicular to the Gulf Stream, which in this setup is 0.03 m s^{-1}. $\boldsymbol{J}^*$ flow in the horizontal plane in a circular path (segments 2 and 3) that has the same diameter as the separation between points A and B. The voltage difference is $V = \Delta\overline{v}^* L F_z$. Rough estimates of the resistances R_2 and R_3 are taken from mean water depths, sediment thicknesses, and sediment conductivities (see Table 3.3). Resistances of the elements are

$$R_i = \pi L/2W\Sigma_i \tag{3.22}$$

$$\tag{3.23}$$

for a width W and vertical conductance $\Sigma = \sigma H(1+\lambda)$. The apparent velocity generated by non-local currents can be written as

$$R_{\text{total}} = \Sigma_2^{-1} + \Sigma_3^{-1} \qquad\qquad\qquad I = V/R_{\text{total}}$$

$$J_i = I/W\Sigma_i \qquad\qquad\qquad v_{\text{apparent}} = J_i/\sigma F_z \quad . \tag{3.24}$$

The shallow inshore path 2 has an apparent velocity error of 4 mm s^{-1}, while the deeper path 3 has an error of 1 mm s^{-1}. These values are smaller than the 2D errors along the continental slope, and are comparable to 2D errors over the remainder of the Gulf Stream.

3.12   Discussion

As shown in the previous sections, higher-order effects of motional induction are strongly dependent on horizontal gradients, and thus require adequate horizontal resolution for modelling these effects. To gain this resolution the analysis made use of the numerical model MOED. There are two ways in which the numerical model can not represent the observations: 1) the model has higher horizontal resolution in the water depth and sediment than of velocity in the water column, and 2) the AVP observations are time-averaged over a meander event.

   The first incongruity is the higher horizontal constraint of the seafloor and sediment structure compared with velocity structure. The velocity field used to initialize the model

	points		circuit elements	
	A	B	2	3
$\overline{v}$ (m s^{-1})	**0.3**	0.26	-	-
$\overline{v}^*$	0.29	0.26	-	-
H (m)	**2630**	**3010**	**500**	**3250**
$H_s - H$ (m)	**5000**	**5000**	**6000**	**4000**
σ (S m^{-1})			**3.7**	
σ_s (S m^{-1})			$\sigma/5$	
Σ_v (S)	-	-	5550	17760
J (A m^{-2})	-	-	7.3×10^{-7}	2.3×10^{-7}
v_{apparent} (m s^{-1})	-	-	3.9×10^{-3}	1.2×10^{-3}

Table 3.3: Defined values for the equivalent circuit shown in Figure 3.22. Prescribed values based on geometry or AVP data are shown as bold, other values are calculated as described in the text.

is only constrained at a few locations across the Gulf Stream. Using the exact seafloor under tracklines in the model greatly increase the scatter of the analysis, because many of the vertically averaged quantities (e.g. $\overline{v}$, $\overline{v}^*$, etc.) are divided by H and so will respond to the higher wavenumbers inherent in H. For this reason a highly smoothed seafloor is used in the model. Although it is expected that electric fields and electric currents are spatially averaged (*Chave and Luther*, 1990), it is difficult to determine the horizontally averaged spatial scales that electric fields respond to without observations at higher horizontal resolutions.

The second discrepancy is that the model assumes a 'synoptic' (fixed) velocity structure that is not distorted by meanders. This is a necessary simplifying assumption for our analysis, given that there are not sufficient observations to re-create the synoptic development of meanders. Observed fluctuations of $\overline{v}$ by a factor of 2 are not reproduced by schematic meanders in the model. Another way to regard the temporal averaging is that locations of velocity extrema and horizontal velocity gradients are not fixed in stream

coordinates, but rather that any one location in stream coordinates can have a range of velocity or its gradients over the course of a meander event. Thus, the strength of 2D effects will vary with time in stream coordinates. The observations include a broader range of states, and so it is not surprising that the station-averaged response is smoother and gives more robust values than the model results.

The large values in the depth-uniform velocity error found at the 500 m isobath are unexpectedly large. The true error is unknown lacking knowledge of the inshore velocity, but the sensitivity to Gulf Stream meanders and to the width of the inshore velocity front is large. Depth-uniform errors are 0.05–0.15 m s^{-1} for a range of meander amplitudes (shifts of ± 2 km) and widths (1–5 km) over which the velocity decreases to 0 inshore of the 500 m isobath. Errors are minimal with complete sediment knowledge, but they increase when meanders are present over topography and the sediment properties are unknown. The observations sample a larger range of oceanic conditions than are recoverable from the model, which implies that the relation between $\bar{v}(1+\gamma)$ and $\bar{v}^*$ in the data is smoothed over a broader range of velocity states than the model results. Regardless, the instantaneous error will be the same magnitude as described here, with improved accuracy applying in the time-averaged sense to longer time series.

The magnitude of errors found at Cape Hatteras can be put into the context of the results of Chapter 2. At the 500-m station, the velocity aspect ratio is roughly 0.5, the sediment is 10 times thicker than the water column, and the relative sediment conductivity in λ_{1D} is 0.2 ($\sigma_s/\bar{\sigma} = 0.8/4.0 = 0.2$). The linear sensitivity of the depth-uniform error to σ_r is roughly $\Delta\sigma_r/\sigma_r = 0.85$ for very thick sediments, although it approaches 1 if sediments are less thick than the water column. This suggests that the depth-uniform error is 0.4 m s^{-1} (0.03 m s^{-1}) due to F_z (F_h), while the depth-varying error is 0.02 m s^{-1} (0.03 m s^{-1}) due to F_z (F_h). The topographic aspect ratio of 0.5 leads to expected depth-uniform errors of 0.01 m s^{-1} and depth-varying errors of 0.003 m s^{-1}. These parameter space errors agree with or are larger than the errors calculated specifically at Cape Hatteras. The very thick sediment relative to the shallow water depth lead in part to such high errors. In fact, the depth-uniform error at Cape Hatteras is 0.1-0.2 m s^{-1}. Although it is generally not

expected that 2D errors generated by velocity gradients and sloping topography should be additive, that appears to be the case at Cape Hatteras. Unlike the velocity gradient case of a flat bottom, at Cape Hatteras the topography is very steep, with the effect that large relative sediment thicknesses only occur on the upper continental slope. This presumably acts to reduce the depth-uniform errors $(0.1\text{--}0.2 \text{ m s}^{-1})$ from the larger values predicted in Chapter 2.

3.13 Conclusion

This article investigates how the relationship between electric fields and velocity can deviate from the commonly used one-dimensional approximation. The first order 1D approximation describes how oceanic electric fields and electric current densities relate to the forcing velocity using a 1D relation in the vertical: a depth-uniform electric field $(\overline{v}^* F_z)$ is linearly related to the barotropic velocity $\overline{v}$, and the depth-varying electric current density divided by conductivity and F_z is related to $\boldsymbol{v}(z)$ by a depth-uniform offset $(\overline{v}^*)$. These two electric field modes also describe two ways to measure oceanic electric fields, with bottom electrodes/cables or with vertical profilers, and furthermore are analogous to barotropic and baroclinic velocity modes.

In complex regions with strong gradients in depth, velocity, or sediment conductance, however, the 1D approximation can have significant errors. The continental slope near Cape Hatteras is an example of a highly complex location: the continental slope is steep, the Gulf Stream is a strong forcing velocity that supports energetic meanders and sharp velocity fronts, and the bottom sediment is unusually thick with variable conductivity.

Measurements of the electric field across the Gulf Stream were used to test the 1D approximation. At the 500 m isobath the relation between the vertically averaged velocity $\overline{v}$ and the conductivity-weighted depth-averaged velocity $\overline{v}^*$ is not described by a constant ratio, as predicted by the 1D approximation. The highly linear data is best fit with a line that has a non-zero y-intercept. The rest of the article investigates possible reasons why the 1D model is inaccurate at this location.

Initialized with the time-averaged AVP velocities and water conductivities, the nu-

merical model MOED (*Tyler et al.*, 2004) solves for the electric field in a 2D transect across the Gulf Stream. Geophysical data is compiled to constrain the sediment electric properties. The geometry of stratigraphic layers is found from deep seismic surveys, while the conductivity of each layer is estimated from nearby borehole conductivity recordings. A magnetotelluric analysis finds no correlation between the electric field produced by ionospheric fluctuations of the magnetic field and the measured oceanic electric field.

The modelled electric field is in good agreement with the time-averaged AVP data, although the large variability in the measurements is not fully reproduced by schematic meandering. The 1D approximation is in error by $< 0.01 - 0.02$ m s^{-1} ($< 5\%$) for the depth-uniform electric field over most of the Gulf Stream, but the sharp inshore edge in velocity occurring over the upper continental slope gives rise to errors 3–10 cm s^{-1} (10–30% of $\overline{v}$). Meanders over the upper continental slope result in a linear fit between $\overline{v}^*$ and $\overline{v}$ with a negative y-intercept, although the model results do not accurately describe all of the AVP data. Using a ratio to describe the sediment conductivity is found to be more accurate for inverting $\overline{v}^*$ to $\overline{v}$. The schematic meanders invoked by the model yield larger errors than when the velocity structure is fixed to topography, implying that it is more difficult to recover $\overline{v}$ from stationary electrodes when ocean currents meander over steep topography. The inversion is most accurate with knowledge of the sediment thickness and conductivity. Use of heuristic methods for the inversion (the ratio method) in the presence of meanders yields larger errors: 0.01–0.04 m s^{-1} seaward of the 1000 m isobath, and 0.1-0.2 m s^{-1} shoreward. An iterative method corrects the time-averaged velocity profiles by 0.01–0.02 m s^{-1} to remove 2D velocity errors. To be able to calculate 2D perturbations, it is necessary to know the horizontal structure of the flow.

As the Gulf Stream moves into deeper water, the 3D effect due to divergence of $\overline{v}$ generates non-local currents that appear as an additional depth-uniform error. The magnitude of this effect is estimated at 0.5–1 cm s^{-1}.

The higher dimension effects discussed here in great detail may seem too complex to remove for researchers who simply want to measure ocean velocity. The region near Cape Hatteras was chosen specifically because it has a unique confluence of complexities that

distort the electric field from the 1D approximation. Not only is the continental slope unusually steep and the sediment unusually thick, but the Gulf Stream is a very strong forcing constrained by topography and with energetic meanders. Maximum velocities exceed 1.5 m s^{-1} and the barotropic velocity is tens of cm s^{-1}. Instrument accuracy of electric field-based instruments is generally 1–2 cm s^{-1}, so the errors discussed here are the same order as instrumental errors. Less energetic regions will have smaller absolute errors.

Chapter 4

CONCLUSION

Motionally induced electric fields are generated in the ocean by seawater moving through the earth's magnetic field. Physical oceanographers are interested in these fields because they provide a convenient though indirect way to measure ocean velocity. Electric currents and electric fields are straightforward to measure and are closely related to vertical velocity structure and to a spatially averaged quantity $\overline{\boldsymbol{v}}^*$ that is dynamically similar to transport.

Measurements are usually interpreted with a 1D approximation that describes two key modes of the electrical response: the electric field is depth-uniform $\overline{\boldsymbol{v}}^* F_z$, is linearly related to the vertically averaged velocity $\overline{\boldsymbol{v}}$, and includes shorting through conductive sediment; and the electric current density divided by conductivity and F_z has the same vertical structure as velocity with an offset of $\overline{\boldsymbol{v}}^*$. These two aspects correspond to the two ways of measuring oceanic electric fields, from electrodes mounted on stationary or vertically-profiling platforms, and also to the standard decomposition of velocity into barotropic and baroclinic modes.

The 1D approximation is strictly valid in the open ocean when horizontal length scales of velocity and topography are much larger than the water depth. This condition is not met in all parts of the ocean, for instance near continental margins where topography is steep and where energetic and oceanographically important boundary currents generate sharp fronts and baroclinic instabilities. The quasi-static electric response in these regions is not as simple as the 1D approximation. The higher order perturbations are quantified in magnitude and shape, with the ultimate goal of helping oceanographers accurately convert from electric field to velocity.

The influence of higher order perturbations is investigated with two approaches: a theoretical and numerical approach based on simple geometries in which the spatial scales

are varied to resolve the appropriate parameter space, and a detailed analysis of measurements at Cape Hatteras.

The simple geometries presented in the first half of the dissertation resolve electric fields and electric currents generated in the presence of horizontal gradients of velocity and topography. Depth-uniform and depth-varying perturbations from the 1D approximation depend strongly on the aspect ratio of height to width. The aspect ratio used for horizontal velocity gradients is the ratio of water depth to velocity width scale, while that used for sloping topography is the ratio of topographic height to topographic width. Depth-uniform velocity errors decrease exponentially with aspect ratio, normalized sediment thickness, and relative sediment conductivity, while depth-varying errors decrease exponentially with aspect ratio and are only slightly dependent on the other parameters.

Maximum aspect ratios for both velocity and topography are expected to be less than 0.01–0.1 based on observed scales and scaling arguments. The largest realistic aspect ratio for velocity gradients generates velocity errors that are 1–3% of the maximum velocity signal for sediments as thick as the water column and with typical sediment conductivities ($\sigma_r = 0.1$). The depth-uniform errors are proportional to λ_{1D}. The geomagnetic east component of velocity also contains a perturbation induced by F_h, but such perturbations are less sensitive to aspect ratio than those induced by F_z. Depth-varying velocity errors at large aspect ratios are the same magnitude due to F_z and F_h, but for small aspect ratios the F_h contribution dominates (order 0.01 m s^{-1}). Sloping topography generates errors an order of magnitude smaller than velocity gradients for the same aspect ratio. The two source of 2D effects (horizontal gradients of velocity and topography) are not linearly-independent, however, so there may be interactions between higher order processes generated by velocity gradients and sloping topography.

The second part of the dissertation investigates in detail the region near Cape Hatteras where the Gulf Stream separates from the continental margin. This region was chosen to test the 1D approximation because of the unusually complex environment: a fast velocity jet with sharp velocity fronts and meanders, steep topography, and thick sediment with variable conductivity.

The oceanic electric field was measured with a vertically profiling float in a transect across the Gulf Stream. On the upper continental slope the 1D theory doesn't entirely describe the observations, rather the downstream component of velocity $\overline{v}(1+\gamma)$ is related to $\overline{v}^*$ by a multiplicative factor and a y-intercept. To investigate this result a numerical model is used to calculate the electric field at high resolution based on the observed velocity. Sediment thickness and conductivity are estimated from deep seismic lines and from sediment conductivity profiles in nearby boreholes. A magnetotelluric analysis estimates the electric fields induced in the ocean by external (ionospheric) magnetic fluctuations: no significant correlation is found with the AVP data.

The modelled electric field shows that meanders over the upper continental slope can result in a linear fit between $\overline{v}^*$ and $\overline{v}$ with a negative y-intercept. The depth-varying velocity error from a 1D interpretation of the electric fields is 1–2 cm s^{-1} (2–5%). An iterative approach is demonstrated for removing these 2D perturbations from the data. The depth-uniform electric field $\overline{v}^*$, as would be measured by seafloor electrodes or a cable, has an error less than 1 cm s^{-1} ($< 5\%$) for most of the Gulf Stream. A maximum in $\overline{v}$ on the upper continental slope generates a larger depth-uniform error of 5–15 cm s^{-1} (10–40% of $\overline{v}$) in this region. Three dimensional electric currents in the region yield apparent depth-uniform velocity errors that are 0.005 m s^{-1}.

The errors calculated at Cape Hatteras (Chapter 3) agree with the errors estimated from the generalized models (Chapter 2). The Cape Hatteras region has extreme values of velocity and topographic aspect ratios, and it also has very large sediment thickness relative to the water depth. The 500-m station provides a useful demonstration of how to extract expected errors from the general results of Chapter 2.

First, the non-dimensional parameters at the 500 m isobath need to be determined (Table 4). The width-scale is estimated as the width of the velocity maximum on the upper continental shelf (5 km), the effective sediment conductivity comes from section 3.8, and the other scales are evident from the transect geometry (Figure 3.3).

The perturbations expected from velocity gradients are estimated from Figure 2.7. The sediment thickness $(H_s - H)/H$ and the aspect ratio H/L allow values to be obtained for

Table 4.1: Non-dimensional parameters at the 500-m station.

parameter	scales at 500-m station	value	description
$\dfrac{H}{L}$	$\dfrac{500\,\text{m}}{5000\,\text{m}}$	0.1	barotropic aspect ratio
$\dfrac{H'}{L}$	$\dfrac{400\,\text{m}}{5000\,\text{m}}$	0.08	baroclinic aspect ratio
$\dfrac{H_{\text{mid}}}{L_t}$	$\dfrac{1250\,\text{m}}{10{,}000\,\text{m}}$	0.125	topographic aspect ratio
$\dfrac{H_s - H}{H} = \dfrac{\Delta H_s}{H}$	$\dfrac{5000\,\text{m}}{500\,\text{m}}$	10	relative sediment thickness
$\sigma_r = \dfrac{\sigma_s}{\sigma}$	$\dfrac{0.58\,\text{S m}^{-1}}{4.2\,\text{S m}^{-1}}$	0.14	relative sediment conductivity
$\dfrac{A_t}{H_{\text{mid}}}$	$\dfrac{1200\,\text{m}}{1250\,\text{m}}$	0.96	relative topographic relief

the depth-uniform error ϵ_{BT}, 0.2 m s^{-1}, and the depth-varying error ϵ_{BT}, 0.0015 m s^{-1}. There are two corrections to make to these values: the first to correct for the observed $\sigma_{r,}$, and the second because $\overline{v}^*$ is not calculated over the entire water column.

The depth-uniform error needs to be multiplied by the sensitivity to σ_r, because $\sigma_r = \sigma_s/\sigma$ is 1.3 times larger at the 500-m station (0.13) than in the model (0.1). For the given aspect ratio and sediment thickness, the relative change of the error to the change of σ_r is $(1.5-1)/(2-1) = 0.5$ (Figure 2.2b), so a 30% increase in σ_r increases the error by 15% to 0.12 m s^{-1}. The depth-varying error is independent of σ_r.

The second correction is based on where in the water column the velocities are made absolute — for the data at Cape Hatteras this is performed within 250 m of the seafloor. The biased depth-varying error explicitly captures this effect, and is typically 1.25–1.5 times larger than the unbiased error shown in Figure 2.5b. This modifies the depth-varying error to 0.002 m s^{-1}. The instrument-specific depth-uniform error is $\overline{\epsilon}+\epsilon'(z = z_{\text{ref}})$ for some reference depth(s) z_{ref}. Figures 2.4b and 2.5b show that $\overline{\epsilon}_{\text{1D}}$ and ϵ'_{bias} are the opposite sign near the seafloor, so the depth-uniform error is reduced by 0.002 m s^{-1}. If

a surface-referenced XCP is being used, however, the depth-uniform error is increased by the same amount, as the signs of $\bar{\epsilon}_{1D}$ and ϵ' are the same in the surface layer.

Thus, the expected errors induced by F_z at the 500-m station are 0.12 m s^{-1} and 0.002 m s^{-1} for the depth-uniform and depth-varying errors. A similar procedure finds the errors expected from F_h in the geomagnetic east-west velocity component: 0.01 m s^{-1} and 0.015 m s^{-1} for depth-uniform and depth-varying errors. As it is unclear how the errors generated by F_z and F_h combine, we shall simply take the larger value for the depth-uniform and depth-varying components.

The errors expected due to topography are found from Figure 2.12. The depth-uniform errors are 0.003–0.007 m s^{-1} (Figures 2.12a,b), but these values need to be corrected for the proper sediment thickness and topographic relief at the 500-m station. The combined influence of $\Delta H_s/H$, A_t/H_{mid}, and σ_r is estimated from the discussion to increase the error by a factor of 10, giving depth-uniform errors of 0.03–0.07 m s^{-1}. The depth-varying error from Figure 2.12c is 10^{-4} m s^{-1}, which is further reduced by a factor of 2 to 5×10^{-5} m s^{-1} because of the sensitivity to the other parameters.

Table 4.2: Expected and calculated velocity errors at the 500-m station.

	depth-uniform	depth-varying
	(m s^{-1})	(m s^{-1})
Cape Hatteras transect (ch. 2)	0.05–0.15	0.01–0.03
velocity gradient, F_z	0.12	0.002
velocity gradient, F_x	0.01	0.015
topographic gradient F_z	0.03–0.07	5×10^{-5}

The magnitude of estimated velocity errors agrees with the more detailed velocity errors calculated specifically at the 500 m station (summarized in Table 4. This result shows that 2D perturbations generated by both velocity gradients and topographic gradients can be described by the quadrature sum of each process investigated separately ($(0.12^2 + 0.07.^2)^{-1/2} = 0.14$ m s^{-1}). It is not intuitive that the interaction of the two

processes is linear and independent. The comparison of the generalized models and the Cape Hatteras transect is not entirely analogous, however, because the models have uniform non-dimensionalized scales over the entire domain, while at Cape Hatteras the scales change rapidly across the transect. Nevertheless, there do not appear to be non-linear increases in the errors due to the presence of both velocity and topographic gradients.

Generally, there can be significant error in extracting the barotropic velocity $\overline{v}$ from $\overline{v}^*$ for meandering currents over steep topography. The depth-varying velocity errors, which would bias vertically profiling floats, are relatively small in this region given the magnitude of velocity and are the same magnitude as instrument accuracy (typically 0.01–0.02 m s^{-1} for instruments with electrodes).

The higher dimension effects discussed here may seem prohibitively complex for researchers who simply want to measure ocean velocity. The region near Cape Hatteras was chosen specifically because it has a unique confluence of complexities that distort the electric field from the 1D approximation. Not only is the continental slope unusually steep and the sediment unusually thick, but the Gulf Stream is a very fast flow that is constrained by topography and exhibits energetic meanders. Maximum velocities exceed 1.5 m s^{-1} and the barotropic velocity is tens of cm s^{-1}. Less energetic regions will have smaller absolute errors.

For researchers interested in using electric field methods to calculate velocity, these results suggest the following advice. The simple shapes of velocity errors in relation to jet edges or topography allow for errors due to 2D electric fields to be estimated by a perturbation procedure, if the dominant (first order) horizontal velocity structure is known. The accuracy of this procedure depends on sufficient horizontal resolution to resolve the velocity and topography gradients. The largest errors are in the depth-uniform electric fields, so vertical profilers are subject to smaller errors than seafloor cables.

The most benefit comes from being able to plan electric field sampling to either avoid anomalous regions or to include measurements that will allow calculation of 2D perturbations for removal by a perturbation approach. For instance, it may be sufficient to know how the axis of the Gulf Stream meanders with time in regions where its velocity structure

in stream coordinates is nearly constant. Now that there is a basic physical understanding of the geometry and dependencies of these errors, numerical methods can be investigated for heuristically correcting electric-field-derived velocities without the high-resolution numerically modelling performed here.

The detailed analysis of measuring velocity indirectly through electric fields in this dissertation allows researchers to estimate 2D perturbations for a broad range of geometries. The apparent limitations of small errors over most of the realistic parameter space does not diminish the fact that electric field-based methods have unique advantages for measuring velocity — ease of deployment, simple calculation of velocity, high vertical resolution, and a quantity $\overline{\boldsymbol{v}}^*$ that is dynamically consistent with transport. Electric field instruments (e.g. EM-APEX floats in project ARGO, or bottom electrometers on cabled observatories) are easily integrated into large-scale observing networks. The detailed analysis speaks to the ultimate goal for any method of measuring velocity: a better understanding of how the instrument and technique respond to oceanic velocity.

BIBLIOGRAPHY

Althaus, A. M., E. Kunze, and T. B. Sanford (2003), Internal tide radiation from Mendocino Escarpment, *J. Phys. Ocean.*, *33*, 1510–1527.

Arthur, M. A. (1982), Lithology and petrology of the COST nos. G-1 and G-2 wells, in *Geological Studies of the COST Nos. G-1 and G-2 Wells, United States North Atlantic Outer Continental Shelf, Geological Survey Circular*, vol. 861, edited by P. A. Scholle and C. R. Wenkam, pp. 11–29, USGS.

Bane, J. M., Jr, D. A. Brooks, and K. R. Loresnson (1981), Synoptic observations of the three-dimensional structure and propagation of Gulf Stream meanders along the Caroline continental margin, *J. Geophys. Res.*, *86*(C7), 6411–6425.

Baringer, M. O., and J. C. Larsen (2001), Sixteen years of Florida Current transport at 27°N, *Geophys. Res. Lett.*, *28*, 3179–3182.

Berger, T. J., P. Hamilton, R. J. Wayland, J. O. Blanton, W. C. Boicourt, J. H. Churchill, and D. R. Watts (1995), A physical oceanographic field program offshore North Carolina, final synthesis report, *Tech. Rep. OCS Study MMS 94-0047*, Minerals Management Service, Gulf of Mexico OCS Region, New Orleans, LA, 345 pp.

Bowden, K. F. (1956), The flow of water through the Straits of Dover related to wind and differences in sea level, *Philos. Trans. Roy. Soc. Lond. A*, *248*, 517–551.

Bretherton, C. S., M. Widmann, V. P. Dymnikov, J. M. Wallace, and I. Bladé (1999), The effective number of spatial degrees of freedom of a time-varying field, *J. Climate*, *12*, 1990–2009.

Brooks, D. A., and J. M. Bane, Jr (1983), Gulf Stream meanders off North Carolina during winter and summer 1979, *J. Geophys. Res.*, *88*(C8), 4633–4650.

Cacchione, D. A., L. F. Pratson, and A. S. Ogston (2002), The shaping of continental slopes by internal tides, *Science*, *296*(5568), 724–727.

Chave, A. D., and D. S. Luther (1990), Low-frequency, motionally induced electromagnetic fields in the ocean: 1. Theory, *J. Geophys. Res.*, *95*(C5), 7185–7200.

Chave, A. D., and D. J. Thomson (1989), Some comments on magnetotelluric response function estimation, *J. Geophys. Res.*, *94*, 13,215–14,226.

Chave, A. D., J. H. Filloux, D. S. Luther, L. K. Law, and A. White (1989), Observations of motional electromagnetic fields during EMSLAB, *J. Geophys. Res.*, *94*, 14,153–14,166.

Chave, A. D., D. S. Luther, and J. H. Filloux (1992), The Barotropic Electromagnetic and Pressure Experiment 1. barotropic current response to atmospheric forcing, *J. Geophys. Res.*, *97*(C6), 9565–9593.

Chave, A. D., D. S. Luther, and J. H. Filloux (1997), Observations of the boundary current system at 26.5°N in the Subtropical North Atlantic Ocean, *J. Phys. Ocean.*, *27*, 1827–1848.

Chen, S. S., J. F. Price, W. Zhao, M. A. Donelan, and E. J. Walsh (2007), The CBLAST-hurrican program and the next-generation fully coupled atmosphere-wave-ocean models for hurricane research and prediction, *B. Am. Meteorol. Soc.*, *88*, 311–317.

Churchill, J. H., and G. G. Gawarkiewicz (2008), Shelfbreak Frontal eddies over the continental slope north of Cape Hatteras, (in prep.).

Constable, S., and C. J. Weiss (2006), Mapping thin resistors and hydrocarbons with marine EM methods: insights from 1D modeling, *Geophysics*, *71*(2), G43–G51, doi: 10.1190/1.2187748.

Dillon, W. P., M. W. Lee, and D. F. Coleman (1994), Identification of marine hydrates *in situ* and their distribution off the Atlantic coast of the United States, in *International Converence on Natural Gas Hydrates*, *Annals of the New York Academy of Sciences*, vol. 715, edited by E. D. Sloan, Jr, J. Happel, and M. A. Hnatow, pp. 364–380, New York Academy of Sciences.

Dosso, H. W., and Z. W. Meng (1992), The coast effect response in geomagnetic field measurements, *Phys. Earth Planet. Int.*, *70*, 39–56.

Egbert, G. D., A. F. Bennet, and M. G. G. Foreman (1994), TOPEX/POSEIDON tides estimated using a global inverse model, *J. Geophys. Res.*, *99*, 24,821–24,852.

Evans, R. L. (2007), Using CSEM techniques to map the shallow section of seafloor: From the coastline to the edges of the continental slope, *Geophysics*, *72*(2), WA105–116, doi: 10.1190/1.2434798.

Everett, M. E., S. Constable, and C. Constable (1999), Modelling three-dimensional induction effects in satellite data, paper presented at the 2nd International Symposium on Three-Dimensional Electromagnetics, Univ. of Utah, Salt Lake City.

Filloux, J. H. (1967), Oceanic electric currents, geomagnetic variations, and the deep electrical consuctivity structure of the ocean-continent transition of central California, Ph.D. thesis, University of California, San Diego.

Filloux, J. H., D. S. Luther, and A. D. Chave (1991), Update on seafloor pressure and electric field observations from the North-Central and Northeastern Pacific: Tides, infratidal fluctuations, and barotropic flow, in *Tidal Hydrodynamics*, edited by B. B. Parker, chap. 31, John Wiley & Sons, Inc.

Filloux, J. H., et al. (1989), OFFSHORE EMSLAB: objectives, experimental phase and early results, *Phys. Earth Planet. Int.*, *53*, 422–431.

Flosadóttir, Á. H., J. C. Larsen, and J. T. Smith (1997), Motional induction in North Atlantic circulation models, *J. Geophys. Res.*, *102*(C5), 10,353–10,372.

Fristedt, T., and P. Sigray (2005), The motionally induced electric field from a two-layer channel-flow of rectangular or ellliptical cross-section; a possibility to resolve baroclinic flow features?, *Tech. rep.*, Department of Meteorology/Physical Oceanography, University of Stockholm, Stockholm, Sweden.

Gill, A. E. (1982), *Atmosphere-Ocean Dynamics*, *International Geophysics Series*, vol. 30, Academic Press, San Diego, CA, 666 pp.

Gille, S. T., K. Speer, J. R. Ledwell, and A. N.-G. Garabato (2007), Mixing and stirring in the Southern Ocean, *EOS Transactions, AGU*, *88*(39), 382.

Girton, J. B., T. B. Sanford, and R. H. Käse (2001), Synoptic sections of the Denmark Strait Overflow, *Geophys. Res. Lett.*, *28*(8), 1619–1622.

Glenn, S. M., and C. C. Ebbesmeyer (1994), Observations of Gulf Stream frontal eddies in the vicinity of Cape Hatteras, *J. Geophys. Res.*, *99*(C3), 5047–5055.

Griffiths, D. J. (1999), *Introduction to Electrodynamics*, 3rd ed., Prentice Hall, Upper Saddle River, New Jersey, 576 pp.

Grow, J. A., and R. G. Markl (1977), IPOD-USGS multichannel seismic reflection profile from Cape Hatteras to the Mid-Atlantic Ridge, *Geology*, *5*, 625–630.

Hautala, S. L., J. Sprintall, J. T. Potemra, C. C. Jackson, W. Pandoe, N. Bray, and A. G. Ilahude (2001), Velocity structure and transport of the Indonesian Throughflow in the major straits restricting flow into the Indian Ocean, *J. Geophys. Res.*, *106*(C9), 19,527–19,546.

Heinson, G., and S. Constable (1992), The electrical conductivity of the oceanic upper mantle, *Geophys. J. Int.*, *110*, 159–179.

Hornbach, M. J., C. Ruppel, D. M. Saffer, C. L. Van Dover, and W. S. Holbrook (2005), Coupled geophysical constraints on heat flow and fluid flux at a salt diapir, *Geophys. Res. Lett.*, *32*(24), L24,617, doi:10.1029/2005GL024862.

Hughes, P. (1969), Submarine cable measurements of tidal currents in the irish sea, *Limnol. Oceanogr.*, *14*, 269–278.

Hutchinson, D. R., C. W. Poag, and P. Popenoe (1995), Geophysical database of the east coast of the United States: Southern Atlantic margin — stratigraphy and velocity from multichannel seismic profiles, *Tech. Rep. 95–27*, U.S. Geological Survey.

Hutchinson, D. R., C. W. Poag, A. Johnson, P. Popenoe, and C. Wright (1996), Geophysical database of the east coast of the United States: Southern Atlantic margin — stratigraphy and velocity in map grids, *Tech. Rep. 96–55*, U.S. Geological Survey.

Johns, W. E., T. J. Shay, J. M. Bane, and D. R. Watts (1995), Gulf Stream structure, transport, and recirculation near 68°W, *J. Geophys. Res.*, *100*(C1), 817–838.

Jolley, L. (Ed.) (1961), *Summation of Series*, pp. 251 pp., Dover Publications, Inc., New York, NY.

Jones, A. G., A. D. Chave, G. D. Egbert, D. Auld, and K. Bahr (1989), A comparison of techniques for magnetotelluric response function estimation, *J. Geophys. Res.*, *94*, 14,201–14,214.

Kanzow, T., et al. (2007), Observed flow compensation associated with the MOC at 26.5 degrees N in the Atlantic, *Science*, *317*(5840), 938–941, doi:10.1126/science.1141293.

Kennelly, M. A., P. A. McKeown, and T. B. Sanford (1986), XCP performance near the geomagnetic equator, *Tech. Rep. 8607*, Applied Physics Lab, Seattle, WA.

Kim, K., S. J. Lyu, Y.-G. Kim, B. H. Choi, and K. Taira (2004), Monitoring volume transport through measurements of cable voltage across the Korea Strait, *J. Atmos. Ocean. Tech.*, *21*(4), 671–682.

Korn, G. A., and T. M. Korn (1961), *Mathematical Handbook for Scientists and Engineers*, second ed., pp. 1130 pp., McGraw-Hill Book Company, New York, NY.

Kuvshinov, A., and N. Olsen (2006), A global model of mantle conductivity derived from 5 years of CHAMP, ørsted, and SAC-C magnetic data, *Geophys. Res. Lett.*, *33*, L18,301.

Kuvshinov, A. V., N. Olsen, D. B. Avdeev, and O. V. Pankratov (2002), Electromagnetic induction in the oceans and the anomalous behaviour of coastal C-responses for periods up to 20 days, *Geophys. Res. Lett.*, *29*(12), doi:10.1029/2001GL014409.

Larsen, J. C. (1968), Electric and magnetic fields induced by deep sea tides, *Geophys. J. Int.*, *16*, 40–70.

Larsen, J. C. (1971), The electromagnetic field of long and intermediate water waves, *J. Mar. Res.*, *29*(1), 28–45.

Larsen, J. C., and T. B. Sanford (1985), Florida Current volume transport from voltage measurements, *Science*, *227*(4684), 302–304.

Laske, G., and G. Masters (1997), A global digital map of sediment thickness, *EOS Transactions, AGU*, *78*(F483).

Lee, H. A., et al. (2007), Submarine mass movements on continental margins, in *Continental Margin Sedimentation: From Sediment Transport to Sequence Stratigraphy*, edited by C. A. Nittrouer, J. A. Austin, M. E. Field, J. H. Kravitz, J. P. M. Syvitski,

and P. L. Wiberg, Special publication number 37 of the International Association of Sedimentologists, chap. 5, pp. 213–274, Blackwell Publishing, Malden, MA, USA.

Longuet-Higgins, M. S., M. E. Stern, and H. Stommel (1954), The electrical fields induces by ocean currents and waves, with applications to the method of towed electrodes, *Papers in Physical Oceanography and Meteorology* *13(1)*, Woods Hole Oceanographic Institution/Massachusetts Institute of Technology, 37 pp.

Luther, D. S., and A. D. Chave (1993), Observing integrating variables in the ocean, in *Proceedings of the 7th Annual 'Aha Huliko'a Hawai'ian Winter Workshop on Statistical Methods in Physical Oceanography*, pp. 103–129, University of Hawai'i.

Luther, D. S., J. H. Filloux, and A. D. Chave (1991), Low-frequency, motionally induced electromagnetic fields in the ocean: 2. Electric field and eulerian current comparison, *J. Geophys. Res.*, *96*(C7), 12,797–12,814.

Macmillan, S., et al. (2003), Ninth generation International Geomagnetic Reference Field released, *Geophys. J. Int.*, *155*, 1051–1056.

Manoj, C., A. Kuvshinov, S. Maus, and H. Lühr (2006), Ocean circulation generated magnetic signals, *Earth Planets Space*, *58*, 429–437.

Mattick, R. E., and J. Libby-French (1988), Petroleum geology of the United States Atlantic continental margin, in *The Geology of North America*, vol. I-2, The Atlantic Continental Margin: U.S., edited by R. E. Sheridan and J. A. Grow, chap. 22, pp. 445–462, The Geologic Society of America.

Maus, S., M. Rother, K. Hemant, C. Stolle, H. Lühr, Hermannr, A. Kuvshinov, and N. Olsen (2006), Earth's lithospheric magnetic field determined to spherical harmonic degree 90 from CHAMP satellite measurements, *Geophys. J. Int.*, *164*, 319–330, doi: 10.1111/j.1365-246X.2005.02833.x.

Meinen, C. S., D. S. Luther, D. R. Watts, K. L. Tracey, A. D. Chave, and J. Richman (2002), Combining inverted echo sounder and horizontal electric field recorder measurements to obtain absolute velocity profiles, *J. Atmos. Ocean. Tech.*, *19*(10), 1653–1664.

Meinen, C. S., D. S. Luther, D. R. Watts, A. D. Chave, and K. L. Tracey (2003), Mean stream coordinates structure of the Subantarctic Front: Temperature, salinity and absolute velocity, *J. Geophys. Res.*, *108*(C8), 3263, doi:10.1029/2002JC001545.

Meinen, C. S., D. S. Luther, and M. O. Baringer (2007), Structure and transport of the Gulf Stream at 68°w: Revisiting older data sets with new techniques, *J. Geophys. Res.*, *submitted*.

Miller, J. L. (1994), Fluctuations of Gulf Stream frontal position between Cape Hatteras and the Straits of Florida, *J. Geophys. Res.*, *99*, 5057–5064.

Montgomery, E., K. Polzin, R. Schmitt, and J. Toole ((in preparation)), Enhanced deep ocean vehicle for hydrography, velocity and turbulence measurements, *J. Atmos. Ocean. Tech.*

Nilsson, J. A. U., P. Sigray, and R. H. Tyler (2007), Geoelectric monitoring of wind-driven barotropic transports in the Baltic Sea, *J. Atmos. Ocean. Tech.*, *24*, 1655–1664.

Nittrouer, C. A., J. A. Austin, M. E. Field, J. H. Kravitz, J. P. M. Syvitski, and P. L. Wiberg (Eds.) (2007), *Continental Margin Sedimentation: From Sediment Transport to Sequence Stratigraphy*, Special publication number 37 of the International Association of Sedimentologists, Blackwell Publishing, Malden, MA, USA.

Ogawa, Y., A. G. Jones, M. J. Unsworth, J. R. Booker, X. Lu, J. Craven, B. Roberts, J. Parmelee, and C. Farquharson (1996), Deep electrical conductivity structures of the appalachian orogen in the southeasern U.S., *Geophys. Res. Lett.*, *23*(13), 1597–1600.

Olson, D. B., O. B. Brown, and S. R. Emmerson (1983), Gulf Stream frontal statistics from Florida Straits to Cape Hatteras derived from satellite and historical data, *J. Geophys. Res.*, *88*(C8), 4569–4577.

Pickart, R. S. (1994), Interaction of the Gulf Stream and Deep Western Boundary Current where they cross, *J. Geophys. Res.*, *99*(C12), 25,155–25,164.

Pickart, R. S., and W. M. Smethie (1993), How does the Deep Western Boundary Current cross the Gulf Stream, *J. Phys. Ocean.*, *23*, 2602–2616.

Poag, C. W., and L. W. Ward (1993), Allostratigraphy of the U.S. Middle Atlantic continental margin — characteristics, distribution, and depositional history of principal unconformity-bounded Upper Cretaceous and Cenozoic sedimentary units, *Professional Paper 1542*, U.S. Geological Survey.

Popenoe, P. (1985), Cenozoic depositional and structural history of the North Caroline margin from seismic-stratigraphic analyses, in *Geologic Evolution of the United States Atlantic Margin*, edited by C. W. Poag, chap. 4, pp. 125–188, Van Nostrand Reinhold, New York.

Pratson, L. F., and W. F. Haxby (1996), What is the slope of the U.S. continental slope?, *Geology*, *24*(1), 3–6.

Pratson, L. F., et al. (2007), Seascape evolution on clastic continental shelves and slopes, in *Continental Margin Sedimentation: From Sediment Transport to Sequence Stratigraphy*, edited by C. A. Nittrouer, J. A. Austin, M. E. Field, J. H. Kravitz, J. P. M. Syvitski, and P. L. Wiberg, Special publication number 37 of the International Association of Sedimentologists, chap. 7, pp. 339–380, Blackwell Publishing, Malden, MA, USA.

Robinson, I. S. (1976), A theoretical analysis of the use of submarine cables as electromagnetic oceanographic flowmeters, *Philos. Trans. Roy. Soc. Lond. A*, *280*(1297), 355–396.

Sabaka, T. J., N. Olsen, and M. E. Purucker (2004), Extending comprehensive models of the Earth's magnetic field with ørsted and CHAMP data, *Geophys. J. Int.*, *159*, 521–547.

Sanford, T. B. (1971), Motionally induced electric and magnetic fields in the sea, *J. Geophys. Res.*, *76*(15), 3476–3492.

Sanford, T. B., R. G. Drever, and J. H. Dunlap (1978), A velocity profiler based on the principles of geomagnetic induction, *Deep-Sea Res.*, *25*(2), 183–210.

Sanford, T. B., R. G. Drever, J. H. Dunlap, and E. A. D'Asaro (1982), Design, operation, and performance of an expendable temperature and velocity profiler (XTVP), *Technical Report APL-UW 8110*, Applied Physics Lab, University of Washington, Seattle.

Sanford, T. B., R. G. Drever, and J. H. Dunlap (1985), An acoustic doppler and electromagnetic velocity profiler, *J. Atmos. Ocean. Tech.*, *2*(2), 110–124.

Sanford, T. B., P. G. Black, J. R. Haustein, J. W. Feeney, G. Z. Forristall, and J. F. Price (1987), Ocean response to a hurricane. part I: Observations, *J. Phys. Ocean.*, *17*(11), 2065–2083.

Sanford, T. B., M. D. Allison, J. H. Dunlap, F. R. Stahr, and J. A. Verrall (1996), R/V *Endeavor* 239: Cruise report and preliminary results, *Tech. Rep. APL-UW 9603*, Applied Physics Lab, University of Washington.

Sanford, T. B., J. F. Price, J. B. Girton, and D. C. Webb (2007), Highly resolved observations and simulations of the ocean response to a hurricane, *Geophys. Res. Lett.*, *34*(13), L13,604.

Santos, F. A. M., M. Nolasco, E. P. Almeida, J. Pous, and L. A. Mendes-Victor (2001), Coast effects on magnetic and magnetotelluric transfer functions and their correction: application to MT soundings carried out in SW Iberia, *Earth Planet. Sci. Lett.*, *186*, 283–295.

Savidge, D. K. (2004), Gulf Stream meander propagation past Cape Hatteras, *J. Phys. Ocean.*, *34*, 2073–2085.

Savidge, D. K., C. Edwards, and M. Santana (2007), Baroclinic effects and tides on the Cape Hatteras continental shelf, *J. Geophys. Res.*, *112*(C09016), doi:10.1029/2006JC003832.

Scholle, P. A., H. L. Krivoy, and J. L. Hennessy (1978), Summary chart of geological data from the COST no. B-2 well, U.S. mid-Atlantic outer continental shelf, *Tech. Rep. OC-79*, U.S. Geological Survey.

Scholle, P. A., K. A. Schwab, and H. L. Krivoy (1981), Summary chart of geological data from the COST no. B-3 well, mid-Atlantic continental slope, *Tech. Rep. OC-106*, U.S. Geological Survey.

Schwiderski, E. W. (1979), *Global Ocean Tides*, vol. 79-414, technical report Part II: The semidiurnal principal lunar tide (M_2), Atlas of Tidal Charts and Maps, N.S.W.C., Dahlgren, VA.

Simpson, F., and K. Bahr (2005), *Practical Magnetotellurics*, pp. 251 pp., Cambridge University Press, Cambridge, United Kingdom.

Smith, W. H. F., and D. T. Sandwell (1997), Global seafloor topography from satellite altimetry and ship depth soundings, *Science*, *277*(5334), 1957–1962.

Stephenson, D., and K. Bryan (1992), Large scale electric and magnetic fields generated by the oceans, *J. Geophys. Res.*, *97*, 15,467–15,480.

Stommel, H. (1948), The theory of the electric field in deep ocean currents, *J. Mar. Res.*, *7*(3), 386–392.

Szuts, Z. (2004), Electric field floats in the North Atlantic Current: Validation and observations, *Tech. Rep. APL-UW 0405*, Applied Physics Lab, University of Washington.

Tracey, K. L., and D. R. Watts (1986), On Gulf Stream meander characteristics near Cape Hatteras, *J. Geophys. Res.*, *91*, 7587–7602.

Tucholke, B. E. (1986), Structure of basement and distribution of sediments in the western North Atlantic Ocean, in *The Western North Atlantic Region*, edited by P. R. Vogt and B. E. Tucholke, pp. 331–340, Geological Society of America, Inc.

Tyler, R. H., and L. A. Mysak (1995a), Motionally-induced electromagnetic fields generated by idealized ocean currents, *Geophys. Astro. Fluid*, *80*, 167–204.

Tyler, R. H., and L. A. Mysak (1995b), Electrodynamics in a rotating frame of reference with application to global ocean circulation, *Can. J. Phys.*, *73*, 393–402.

Tyler, R. H., L. A. Mysak, and J. M. Oberhuber (1997), Electromagnetic fields generated by a 3-D global ocean circulation, *J. Geophys. Res.*, *102*(C3), 5531–5551.

Tyler, R. H., S. Maus, and H. Lühr (2003), Satellite observations of magnetic fields due to ocean tidal flow, *Science*, *299*, 239–241.

Tyler, R. H., F. Vivier, and S. Li (2004), Three-dimensional modelling of ocean electrodynamics using gauged potentials, *Geophys. J. Int.*, *158*, 874–887.

Vivier, F., E. Maier-Feimer, and R. H. Tyler (2004), Simulations of magnetic fields generated by the Antarctic Circumpolar Current at satellite altitude: Can geomagnetic measurements be used to monitor the flow?, *Geophysical Research Letters*, *31*, l10306, doi:10.1029/2004GL019804.

von Arx, W. S. (1950), An electromagnetic method for measuring the velocities of ocean currents from a ship under way, *Papers in Physical Oceanography and Meteorology, MIT/WHOI*, *11*(3), 1–62.

Watts, D. R., K. L. Tracey, J. M. Bane, and T. J. Shay (1995), Gulf Stream path and thermocline structure near 74°W and 68°W, *J. Geophys. Res.*, *100*(C9), 18,291–18,312.

Wertheim, G. K. (1954), Studies of the electric potential between Key West, Florida and Havana, Cuba, *EOS T. Am. Geophy. Un.*, *35*, 872–882.

Wilson, D. W., and W. E. Johns (1997), Velocity structure and transport in the Windward Islands Passages, *Deep-Sea Res. I*, *44*(3), 487–520.

Appendix A

APPENDICES FOR CHAPTER 2

A.1 *Analytic Solution*

The electric field solution that is under consideration is time-invariant, electric currents flow but the magnetic field is constant. For this magnetostatic case, the only parameter that needs to be solved is the electric potential Φ. Other quantities can be calculated using standard electromagnetic equations

$$\boldsymbol{E} = -\nabla\Phi$$

$$\boldsymbol{J} = \sigma\left(\boldsymbol{v}\times\boldsymbol{F} - \boldsymbol{E}\right)$$

$$\nabla\times\boldsymbol{B} = \mu\boldsymbol{J} \quad .$$

The solution is

$$
\begin{aligned}
\Phi_1 = \;& \frac{v_0 F_z}{\alpha}\sin(\alpha x)\left[1 - \frac{\mathrm{scrcs}(\alpha(H - H'))}{\mathrm{scrcs}(\alpha H)}\cosh(\alpha z)\right]\dots \\
& + \frac{v_0 F_x}{\alpha}\cos(\alpha x)\left[\frac{\mathrm{ccrss}(\alpha(H - H')) - \mathrm{ccrss}(\alpha H)}{\mathrm{scrcs}(\alpha H)}\cosh(\alpha z) - \sinh(\alpha z)\right] \\
\Phi_2 = \;& \frac{v_0 F_z}{\alpha}\sin(\alpha x)\sinh(\alpha H')\left[\frac{\mathrm{ccrss}(\alpha(z + H))}{\mathrm{scrcs}(\alpha H)}\right]\dots \\
& + \frac{v_0 F_x}{\alpha}\cos(\alpha x)\left[\cosh(\alpha H') - 1\right]\frac{\mathrm{ccrss}(\alpha(z + H))}{\mathrm{scrcs}(\alpha H)} \\
\Phi_3 = \;& \frac{v_0 F_z}{\alpha}\sin(\alpha x)\sinh(\alpha H')\frac{\cosh(\alpha(z + H_s))}{\mathrm{scrcs}(\alpha H)}\dots \\
& + \frac{v_0 F_x}{\alpha}\cos(\alpha x)\left[\cosh(\alpha H') - 1\right]\frac{\cosh(\alpha(z + H_s))}{\mathrm{scrcs}(\alpha H)} \quad ,
\end{aligned}
\tag{A.1}
$$

where $\mathrm{scrcs}(x)$ and $\mathrm{ccrss}(x)$ are defined in section 2.3.1.

A.2 *Convergence of Finite Velocity Numerical Evaluation*

One problem with this discrete expansion is that there is a non-zero E_x outside of the jet that is uniform in x, as seen by the constant slope in electric potential (Figure A.1). This

is physically counter-intuitive, since with a finite forcing function $\boldsymbol{E}$ should also be finite and should decay to zero outside of the jet. Finite Fourier expansions always result in a repeating solution. Because the electric potential decreases across the jet, there must be non-zero gradient on either side of the jet for the potential to remain continuous. This is a numerical issue simply related to how many terms are used in the Fourier evaluation. A numerical model run with the same geometry (MOED, *Tyler et al.*, 2004) confirms that E_x does go to 0 far from the jet (appendix A.3). It was also verified that $\boldsymbol{J}$ is conserved in all solutions according to

$$\nabla \cdot \boldsymbol{J} = 0 \quad \Longrightarrow \quad \int (\nabla \cdot \boldsymbol{J}) \, \mathrm{d}V = \oint \boldsymbol{J} \cdot \mathrm{d}\boldsymbol{a} = 0 \quad ,$$

where, since this is a time-invariant problem there is no change in charge density $\partial \rho_c / \partial t = 0$.

The analytical solution is less computationally expensive to run than the numerical model and can be evaluated at arbitrary (x, z) locations without loss of accuracy, however, so it is preferred for calculating the solution over a wide parameter space.

The background E_x was found computationally to be dependent on the size of M, and tends towards 0 with increasing M (Figure A.1, right). To verify that this is the expected behavior of a finite numerical Fourier expansion, I performed the following calculations.

The Fourier coefficients $a_{n,M}$ are determined by

$$a_{n,M} = \int_{-\infty}^{\infty} v(x) \cos(k_{n,M} x) \, \mathrm{d}x \qquad , \tag{A.2}$$

where $v(x)$ is the chosen velocity form given in (2.9) and $k_{n,M}$ and $\nu_{n,M}$ are defined in section 2.3. The forcing function used can be considered the sum of a constant and a cosine multiplied by a rectangular function $\Pi(x/L)$

$$\Pi(x) = \begin{cases} 1 & |x| < 1/2 \\ 0 & |x| \geq 1/2 \end{cases} . \tag{A.3}$$

Thus the Fourier coefficients can be thought of the convolution (denoted by $*$) in the frequency domain of the Fourier transforms of $\frac{1}{2}[1 + \cos(2\pi x/L)]$ and of $\Pi(x/L)$. This
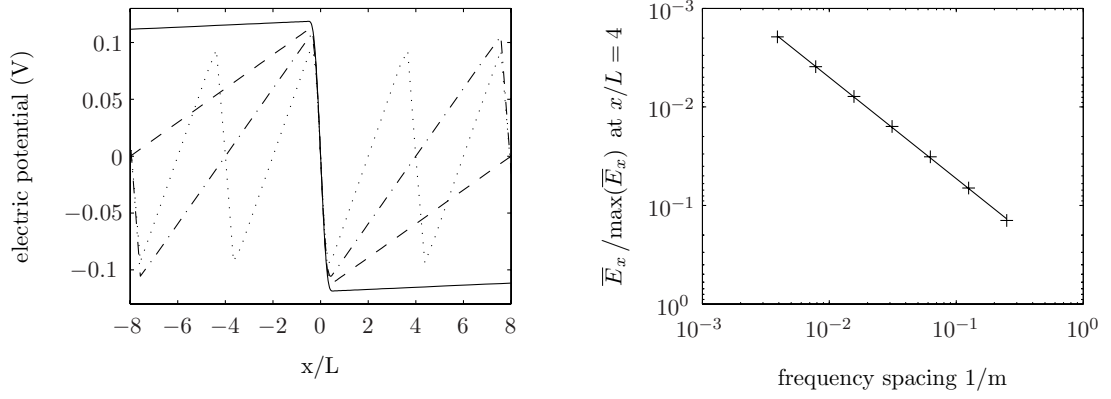
Figure A.1: (left) The electric potential Φ at $z = -H'/H$ for multiple values of m. The dotted line is for $m = 4$, the dashed-doted for $m = 8$, the dashed for $m = 16$, and the solid for $m = 256$. Note the a non-zero slope outside of the jet ($|x/L| < 1/2$) that corresponds to a non-zero horizontal electric field, and that for lower values of m the domain is small enough to show that the solution is periodic with period mx/L. The solution is under-resolved in x for $|x/L| > 1$. The offset of $\overline{E}_x / \max(\overline{E}_x)$ plotted against the frequency resolution $1/M$ (right). The slope of the best-fit line is -1.028 ± 0.007. The parameters used are: $H = 3000$, $H' = 500$, $H_s = 6000$ m, $L = 100$ km, and $\sigma_s/\sigma = 0.4$.

yields (*Korn and Korn*, 1961)

$$
\begin{aligned}
a_{n,M} &= \mathcal{F}\left\{\frac{1}{2}[1 + \cos(2\pi x/L)]\right\} * \mathcal{F}\left\{\Pi(x/L)\right\} \\
&= \left\{\frac{1}{2}\delta(k_{n,M}) + \frac{1}{4}\delta(k_{n,M} - 1/L) + \frac{1}{4}\delta(k_{n,M} + 1/L)\right\} * \left\{L \operatorname{sinc}(Lk_{n,M})\right\} \\
&= \frac{L}{2}\left[\operatorname{sinc}(\nu_{n,M}L) + \frac{1}{2}\operatorname{sinc}(\nu_{n,M}L - 1) + \frac{1}{2}\operatorname{sinc}(\nu_{n,M}L + 1)\right]
\end{aligned}
\tag{A.4}
$$

where $\operatorname{sinc}(c) = \sin(x)/x$. The continuous function $a(k)$ is shown in Figure A.2, with points indicating how it is discretized for $M = 8$. In practice The value of M is limited to powers of 2. Values of M that contain odd factors result in the positive and negative lobes of the continuous function $a(k)$ being divided unequally, with the result that the sum over two contiguous lobes of opposite sign is not close to 0. The resulting solution has large deviations from the true solution, much larger than solutions based on the nearest power of 2.
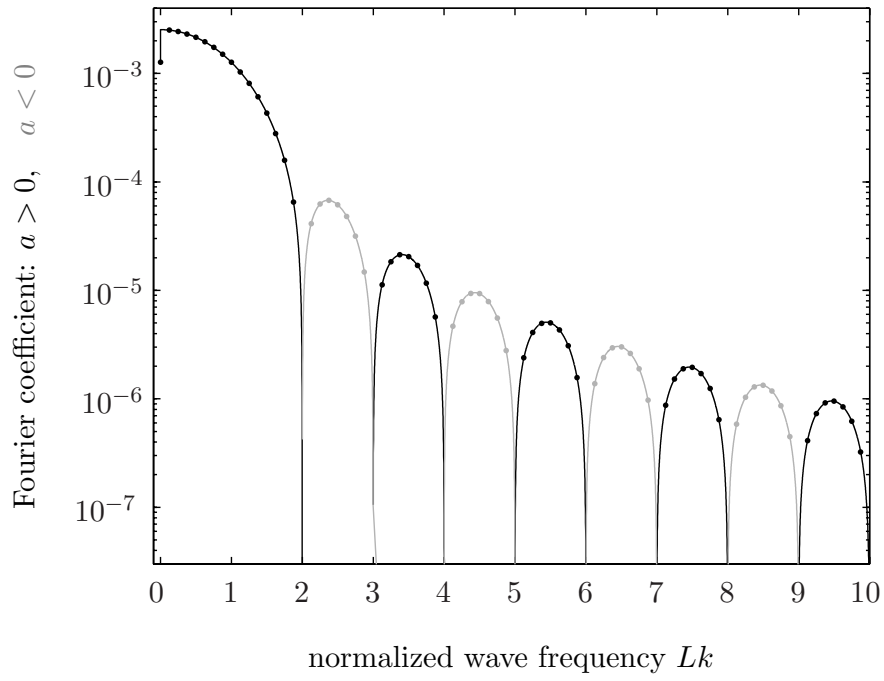
Figure A.2: The form of (A.4), with the solid line indicating the continuous function $a(k)$, and with the dots indicating $a_{n,M}$ where $M = 8$. Positive values are shown in black, and negative values in gray.

At any location x with fixed $z = z_0$, the solution can be written

$$E_{x,i:n,M}(x, z_0) = \frac{L}{2} \sum_{n=0}^{N} a_{n,M} \left[A_i(z_0) \cos(k_{n,M}x) + B_i(z_0) \sin(k_{n,M}x) \right] \quad . \tag{A.5}$$

for any region $i = 1, 2, 3$.

As $M \to \infty$ the sum converges to the exact solution. But in the case where M is finite, how is the error expressed? The positive and negative side lobes of $a_{n,M}$ for $k_{n,M} > 2$ are expected to largely cancel each other far from the jet, leaving the lowest frequencies $n/M < 2$ largely responsible for any error due to the discrete expansion.

The sinc functions that describe $a_{n,M}$ can be expanded with the following Taylor series

$$\cos(x) = 1 - \frac{x^2}{2!} + \frac{x^4}{4!} - \frac{x^6}{6!} + \cdots$$

$$\mathrm{sinc}(x) = 1 - \frac{x^2}{3!} + \frac{x^4}{5!} - \frac{x^6}{7!} + \cdots$$

$$\mathrm{sinc}(x-1) = 1 + \sum_{j=1}^{\infty} \left[\sum_{i=j}^{\infty} \frac{(-1)^{i+1}x^{2j-1}}{(2j-1)!(2i-2j+1)!(2i+1)} + \sum_{i=j}^{\infty} \frac{(-1)^i x^{2j}}{(2j)!(2i-2j)!(2i+1)} \right]$$

$$\mathrm{sinc}(x+1) = 1 + \sum_{j=1}^{\infty} \left[\sum_{i=j}^{\infty} \frac{(-1)^i x^{2j-1}}{(2j-1)!(2i-2j+1)!(2i+1)} + \sum_{i=j}^{\infty} \frac{(-1)^i x^{2j}}{(2j)!(2i-2j)!(2i+1)} \right] \quad .$$

When calculating the Taylor expansion of $a_{n,M}$, the odd exponents of $\nu_{n,M}L$ from $\mathrm{sinc}(\nu_{n,M}L - 1)$ and $\mathrm{sinc}(\nu_{n,M}L + 1)$ cancel, leaving

$$a_{n,M} = 2 + \sum_{j=1}^{\infty} (-1)^i (\nu_{n,M}L)^{2j} \left[\frac{1}{(j+1)!} + \sum_{i=j}^{\infty} \frac{1}{(2j)!(2i-2j)!(2i+1)} \right]$$

The inner sum is finite, since the terms converge as $1/i^2$, and it will be denoted C_{2j} for simplicity.

Using these we obtain an analytic form for how $E_{x,i:n,M}(x, z)$ behaves as $M \to \infty$. Let x_0 be outside of the jet, for instance at $x_0 = pL$ for any $p \geq 1$. Since $A_i(z)$ and $B_i(z)$ in (A.5) do not depend on M, the question of convergence becomes

$$\sum_{n=0}^{M-1} a_{n,M} \cos(2\pi np/ML)$$

$$= 2 \left\{ 1 + \left(\frac{n}{M}\right)^2 \left[\frac{-(2\pi p)^2}{2!} + C_2 \right] + \left(\frac{n}{M}\right)^4 \left[\frac{(2\pi p)^4}{4!} - \frac{(2\pi p)^2}{2!} C_2 + C_4 \right] + \ldots \right\} \quad . \tag{A.6}$$

 In this expression, it is important to note that for each term of $(n/M)^{2j}$ the first factor in square brackets, of the form $(2\pi p)^{2j}/(2j)!$, does converge, thus for $n/M < 1$ this series converges for any p and thus any x.

Over the interval $0 \leq n/M < 1$, the question has become how well does the discrete Fourier expansion for finite M

$$\frac{1}{M} \sum_{n=0}^{M-1} \nu_{n,M}^{2j} \Longrightarrow \frac{1}{M} \sum_{n=0}^{M-1} \left(\frac{n}{M}\right)^{2j} \tag{A.7}$$

differ from the exact result for $M \to \infty$

$$\int_0^1 f^{2j}\,\mathrm{d}f \quad ?$$

The finite sum of (A.7) can be expressed (*Jolley*, 1961)

$$\frac{1}{M^{2j+1}} \sum_{n=0}^{M-1} n^{2j} = \frac{1}{M^{2j+1}} \left[\frac{n^{2j+1}}{2j+1} + \frac{n^{2j}}{2} + \frac{1}{2} \begin{pmatrix} 2j \\ 1 \end{pmatrix} B_1 n^{2j-1} + \ldots \right]$$

For $j = 1$, the error of the discrete approximation is

$$\int_0^1 f^{2j}\,\mathrm{d}f - \frac{1}{M^3} \sum_{n=0}^{M-1} n^2 = \frac{1}{3} - \left(\frac{1}{3} - \frac{1}{2M} + \frac{1}{6M^2}\right) = \frac{1}{2M} + \frac{-1}{6M^2}$$

This error clearly goes to 0 with increasing M with a slope of -1, in agreement with the results of Figure A.1 right. The analysis above confirms that the uniform offset of E_x outside of the jet is due to numerical constraints with a slope of M^{-1}.

There are two ways to minimize the influence of this numerical issue: choose a very large M (> 100), or subtract a uniform E_x from the solution. The former is at the expense of computation time. Although the solution takes tens of minutes for $M = 128$ in Matlab on a Mac G4 desktop with 2 GB of RAM, this is still prohibitive if solutions over a wide parameter space are desired. The latter choice is physically sound, since the solutions of the magnetostatic equations (Laplace equations) are linearly independent and the addition of a constant E_x yields another valid solution. With this choice, M is chosen to make the offset in E_x outside of the jet much smaller than the forcing amplitude at $x = 0$.

In practice, the value of M does depend on the value of L/H used. For large values of L/H the electric field spreads horizontally for large multiples of L/H, roughly scaling as a few times H. The electric field does not go to a uniform value close to the jet edge. For small values of L/H, the electric field attains a uniform value within a few H. The repeating nature of the Fourier expansion thus requires a larger repeat length (smaller M) to properly resolve the uniform offset in E_x for large values of L/H. This is implemented first by defining an heuristic distance at which E_x becomes uniform as

$$M_{\text{heuristic}} = 12 \left(H + (H_s - H)\frac{\sigma_s}{\sigma} \right) /L + 1 = 12D/L + 1 \approx 2\alpha D + 1 \quad . \tag{A.8}$$

This formulation stresses that D is a key non-dimensional parameter for this problem. The value of M used is then calculated by $2\hat{\ }[\text{round}_{\text{up}}(M_{\text{heuristic}}) + 1]$. A minimum value of 8 is used for small $M_{\text{heuristic}}$, while the maximum used is 128 for large values.

A.3   Cross validation of the Analytic Solution and MOED

To cross-validate the Fourier-summed analytic technique (section 3.2) and the MOED model, the electric fields for the same geometry are calculated and compared here.

The different numerical techniques give rise to slight differences in the output. The analytic solution is calculated exactly at every location, with any error from the true solution resulting from the truncated and finite Fourier summation. The accuracy of the numerical model, however, depends on how well the grid resolves the step-changes in conductivity structure. For instance, even though there is a step change in velocity on either side of $z = -H'$, the model treats this as a linear change between the vertical grid-points that are on either side of this change. Thus the effective vertically integrated velocity forcing is slightly larger in MOED, which results in electromagnetic fields that are larger by 9%. The results from MOED are scaled by $1/1.09$ to correct for this numeric over-estimate.

Another feature of the numeric model is that it approximates the ocean-air interface as a linear decrease in conductivity from ocean conductivity at $z = 0$ to a zero conductivity at the next higher grid-point. This approximation also serves to increase the magnitude of the resulting electromagnetic solution.

In MOED the horizontal and vertical grid-spacings in the jet are $\Delta x = 10$ m and $\Delta z = 5$ m. In the analytic solution, the z-grid is resolved within $\epsilon = \pm 5 \times 10^{-8}$ m of $z = -Hp$ and $z = -H$ to allow for more accurate vertical integrals of the resulting output.

A small L and a small H' are chosen for the test parameter set so that the situation is fully 2D (Figures A.3 and A.4). The contours for E_x and E_z are every 1 μV m^{-1}, and the two techniques agree very well (left two panels in both figures). The difference between the models (ΔE_x and ΔE_z, right panels in both figures) are an order of magnitude smaller. The maximum magnitude of E_x is 12.4 μV m^{-1}, and the maximum, mean, and second moments of ΔE_x over the region $-1/2 \leq x/L \leq 1/2$ and $-H_s \leq z \leq 0$ are 0.11 μV m^{-1} (relative error of 0.9%), 0.012 μV m^{-1} (0.1%), and 0.05 μV m^{-1} (0.4%). The maximum magnitude of E_z is 7.5 μV m^{-1}, and the maximum, mean, and second moments of ΔE_z over the same region are 0.66 μV m^{-1} (9%), 0.0000014 μV m^{-1} (0.0002%), and 0.09 μV m^{-1} (1.2%). The differences between the electric fields are largest in the region of non-zero velocity, which suggests that the grid in MOED slightly effects the solution.
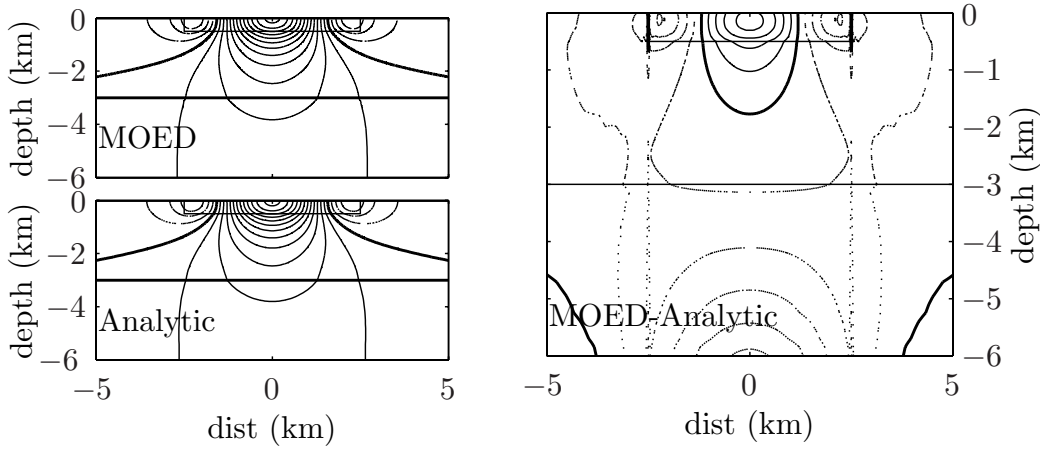
Figure A.3: The model result for E_x from MOED (top) and from the analytic case evaluated with a Fourier summation (bottom) for the parameters $L = 5$ km, $H' = 500$ m, $H = 3000$ m, $H_s = 6000$ m, and $\sigma_r = 0.4$, with contours every 1 μV m^{-1}. Positive contours are solid lines, negative are dotted, and 0 is shown as a thick line. At right is the difference between the two models as gridded to the MOED grid, with contours every 0.01 μV m^{-1}.
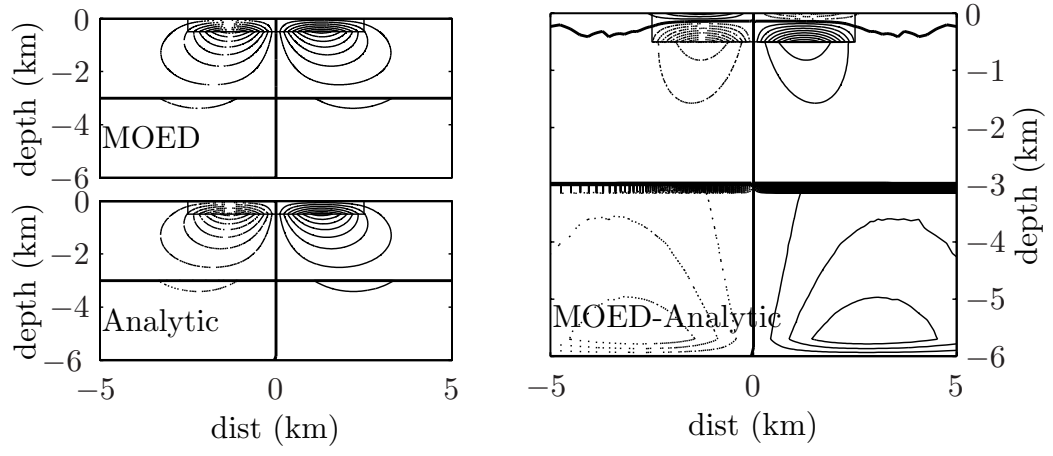
Figure A.4: The same as Figure A.3 except for E_z.

Appendix B

APPENDIX FOR CHAPTER 3

B.1 AVP data from R/V Endeavor cruise 329

The analysis in section 3.3 is based on data that have not yet been published. The locations, time, and quality of the data is listed in Table B.1, while the vertically averaged quantities used for the analysis are listed in Table B.2. Profiles of temperature, salinity, density, and velocity follow in Figures B.1 through B.27. Only the down profiles are shown, because these have high quality CTD sampling of undisturbed wtaer.

Table B.1: Station information for the AVP data

drop	station	date (1992)	time (UTC)	latitude (°N)	longitude (°W)	comments
avp403	35	Jul 15	16:56	34°33.950'	74°19.907'	good data
avp404	35	Jul 15	20:59	34°33.714'	74°20.108'	no data
avp405	5	Jul 16	10:45	35°3.975'	75°6.510'	good data
avp406	10	Jul 16	12:35	35°3.023'	75°4.028	good data
avp407	20	Jul 16	14:41	35°2.245	75°2.411	good data
avp408	10	Jul 16	17:25	35°3.082	75°4.036	good data
avp409	5	Jul 16	19:02	35°4.081	75°6.412	good data
avp410	10	Jul 16	20:22	35°3.336	75°3.755	good data
avp411	30	Jul 17	12:52	34°52.990	74°42.582	good data
avp412	20	Jul 17	17:24	35°2.485	75°2.339	good data
avp413	30	Jul 17	20:45	34°53.028	75°2.339	up-profile data lost
avp414	5	Jul 18	13:38	35°3.887	75°6.433	good data
avp415	10	Jul 18	15:05	35°2.933	75°3.817	good data

(continued on next page)

Table B.1: (continued)

drop	station	date (1992)	time (UTC)	latitude (°N)	longitude (°W)	comments
avp416	20	Jul 18	17:08	35°2.382	75°2.331	good data
avp417	10	Jul 18	19:44	35°3.073	75°3.964	good data
avp418	5	Jul 18	21:31	35°3.964	75°6.454	good data
avp419	5	Jul 18	22:34	35°5.571	75°4.911	good data
avp420	35	Jul 19	8:55	34°33.734	74°19.786	good data
avp421	30	Jul 19	13:55	34°52.846	74°42.486	good data
avp422	20	Jul 19	18:10	35°2.319	75°2.282	good data
avp423	20	Jul 19	20:26	35°2.921	75°1.924	good data
avp424	20	Jul 19	22:51	25°2.303	75°2.051	no trailer — OK
avp425	20	Jul 20	12:16	35°2.290	75°2.303	good data
avp426	10	Jul 20	14:52	35°3.067	75°3.961	good data
avp427	5	Jul 20	16:53	35°4.235	75°6.575	good data
avp428	10	Jul 20	18:22	35°3.031	75°4.085	good data
avp429	5	Jul 20	20:07	35°4.272	75°6.039	good data
avp430	10	Jul 20	21:43	35°3.588	75°3.604	good data
avp431	20	Jul 21	0:00	35°2.540	75°2.115	no data

Table B.2: A summary of the vertically integrated AVP data used in this analysis. The rotation angle θ is defined so that the cross-stream velocity u has the property $\overline{\sigma' u'} = 0$ (see section 3.3.2). There was no data for drops avp404, avp430, and profile avp413u.

drop	stn	H (m)	θ (°)	$\overline{\sigma}$ (S m^{-1})	$\overline{v}$ (m s^{-1})	$\overline{v}^*$ (m s^{-1})	γ
avp403d	35	3504	32.9	3.69	0.122	0.100	0.165
avp403u	35	3504	27.0	3.68	0.124	0.102	0.176
avp405d	5	594	44.3	4.18	0.417	0.289	0.173
avp405u	5	594	43.7	4.12	0.427	0.306	0.161
avp406d	10	1159	41.8	3.80	0.143	0.148	0.585
avp406u	10	1159	35.3	3.77	0.157	0.165	0.507
avp407d	20	2166	41.7	3.58	0.025	0.067	2.57
avp407u	20	2166	40.2	3.56	0.024	0.075	2.43
avp408d	10	1140	43.2	3.81	0.142	0.152	0.545
avp408u	10	1140	43.2	3.77	0.133	0.152	0.550
avp409d	5	592	46.7	4.17	0.300	0.229	0.218
avp409u	5	592	45.4	4.10	0.318	0.247	0.198
avp410d	10	1142	46.9	3.80	0.076	0.093	1.02
avp410u	10	1142	45.9	3.77	0.106	0.126	0.682
avp411d	30	2997	49.9	3.65	0.325	0.319	0.293
avp411u	30	2997	46.4	3.63	0.346	0.346	0.266
avp412d	20	2130	52.1	3.57	-0.005	0.043	-10.6
avp412u	20	2130	49.5	3.56	-0.011	0.038	-5.14
avp413d	30	2998	51.8	3.65	0.335	0.333	0.292
avp413u	30	2998		—			

Table B.2: (continued)

drop	stn	H (m)	θ (°)	$\overline{\sigma}$ (S m^{-1})	$\overline{v}$ (m s^{-1})	$\overline{v}^*$ (m s^{-1})	γ
avp414d	5	666	55.7	4.03	0.372	0.276	0.258
avp414u	5	666	52.5	3.99	0.391	0.302	0.238
avp415d	10	1345	54.3	3.71	0.142	0.183	0.720
avp415u	10	1345	52.9	3.69	0.111	0.151	0.899
avp416d	20	2099	53.4	3.59	0.041	0.104	2.21
avp416u	20	2099	50.8	3.57	0.047	0.105	1.91
avp417d	10	1232	51.9	3.77	0.165	0.187	0.731
avp417u	10	1232	49.5	3.74	0.173	0.187	0.666
avp418d	5	597	51.5	4.15	0.546	0.391	0.192
avp418u	5	597	49.7	4.09	0.548	0.391	0.182
avp419d	5	550	50.3	4.21	0.587	0.393	0.175
avp419u	5	550	48.4	4.14	0.584	0.390	0.169
avp420d	35	3525	44.2	3.68	0.068	0.060	0.255
avp420u	35	3525	39.7	3.68	0.062	0.055	0.284
avp421d	30	2987	51.6	3.67	0.307	0.296	0.277
avp421u	30	2987	46.8	3.66	0.303	0.298	0.275
avp422d	20	2115	52.3	3.59	0.064	0.114	1.29
avp422u	20	2115	50.1	3.57	0.074	0.124	1.08
avp423d	20	2072	53.4	3.60	0.104	0.149	0.806
avp423u	20	2072	52.7	3.58	0.093	0.138	0.852
avp425d	20	2100	54.3	3.59	0.155	0.179	0.594
avp425u	20	2100	52.5	3.57	0.161	0.189	0.553
avp426d	10	1209	54.1	3.76	0.362	0.315	0.289
avp426u	10	1209	50.9	3.74	0.354	0.311	0.284
avp427d	5	502	54.1	4.27	0.731	0.421	0.121

(continued on next page)

Table B.2: (continued)

drop	stn	H (m)	θ (°)	$\overline{\sigma}$ (S m^{-1})	$\overline{v}$ (m s^{-1})	$\overline{v}^*$ (m s^{-1})	γ
avp427u	5	502	52	4.22	0.73	0.413	0.119
avp428d	10	1173	54.7	3.79	0.397	0.358	0.269
avp428u	10	1173	53.2	3.76	0.408	0.36	0.261
avp429d	5	578	53.2	4.20	0.759	0.485	0.139
avp429u	5	578	50.8	4.14	0.758	0.481	0.136
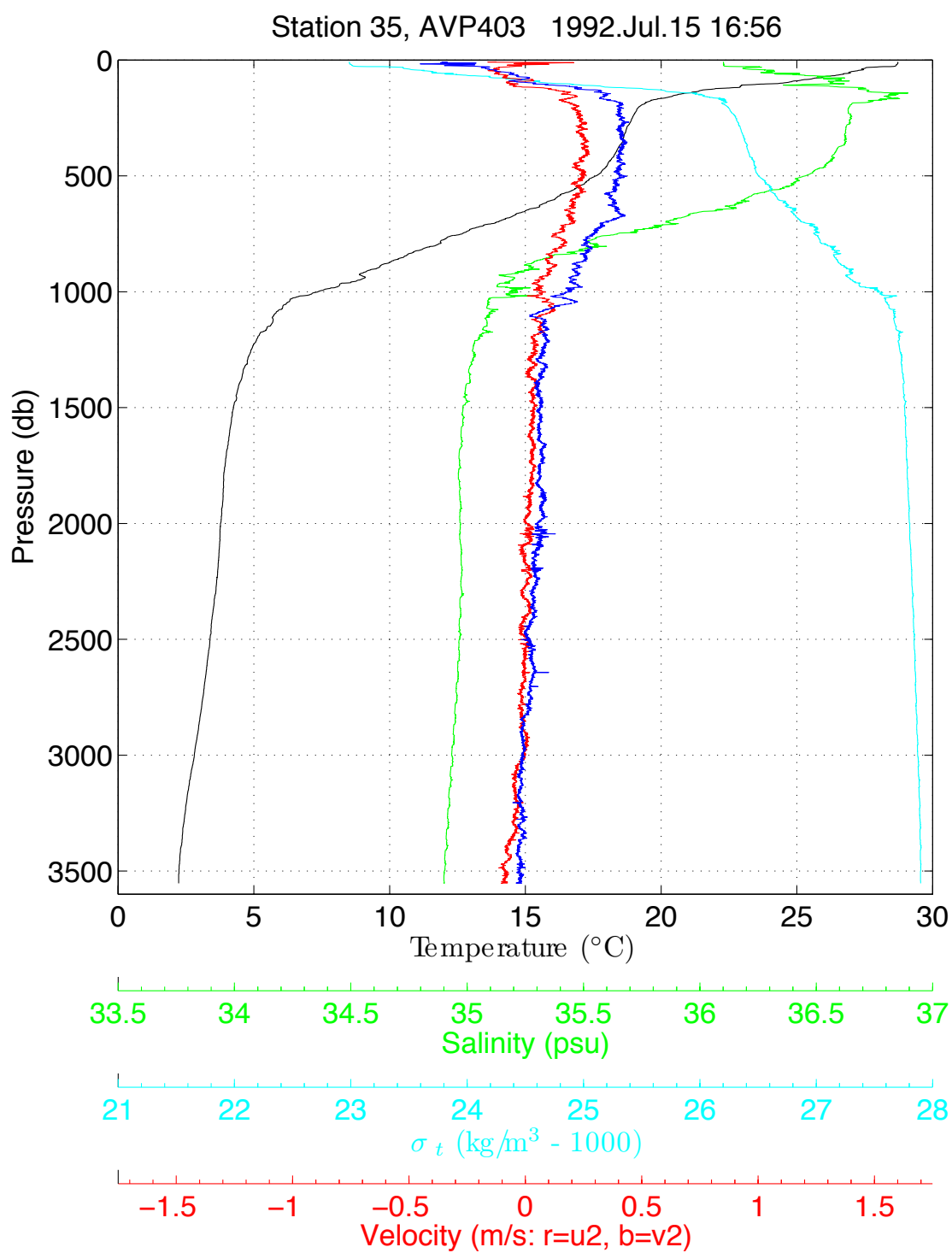
Figure B.1: Profile data from avp403d.

144
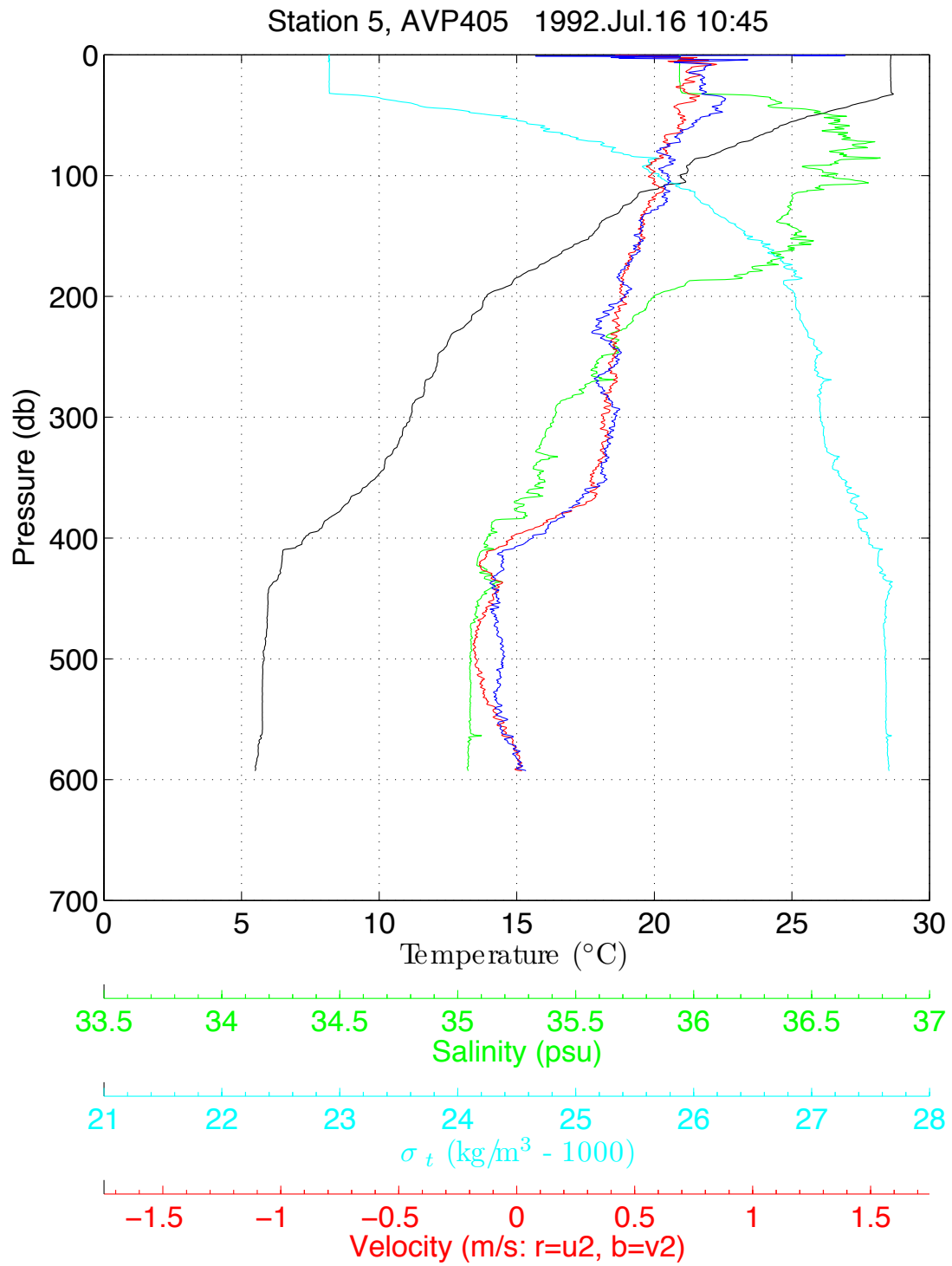
Figure B.2: Profile data from avp405d.
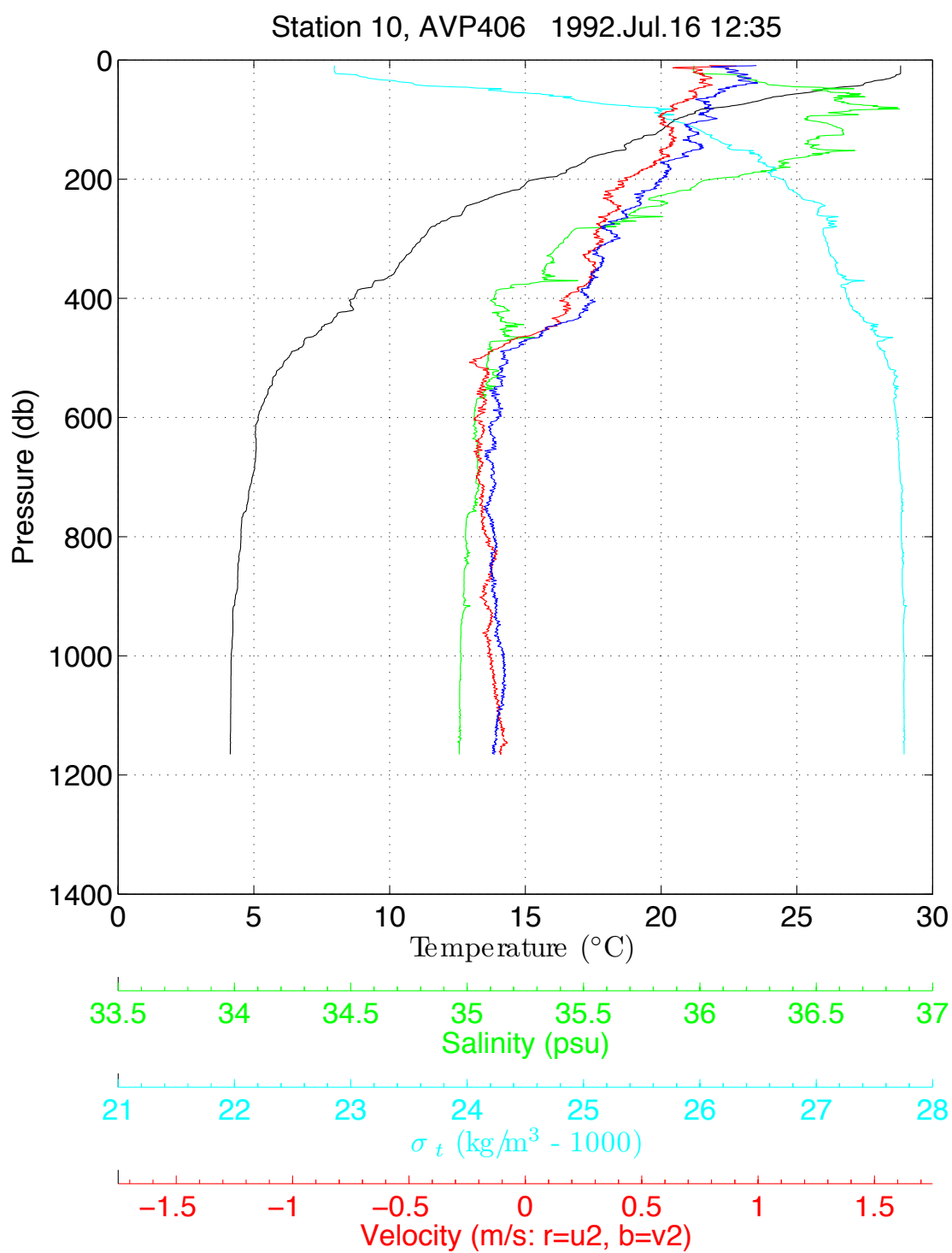
Figure B.3: Profile data from avp406d.
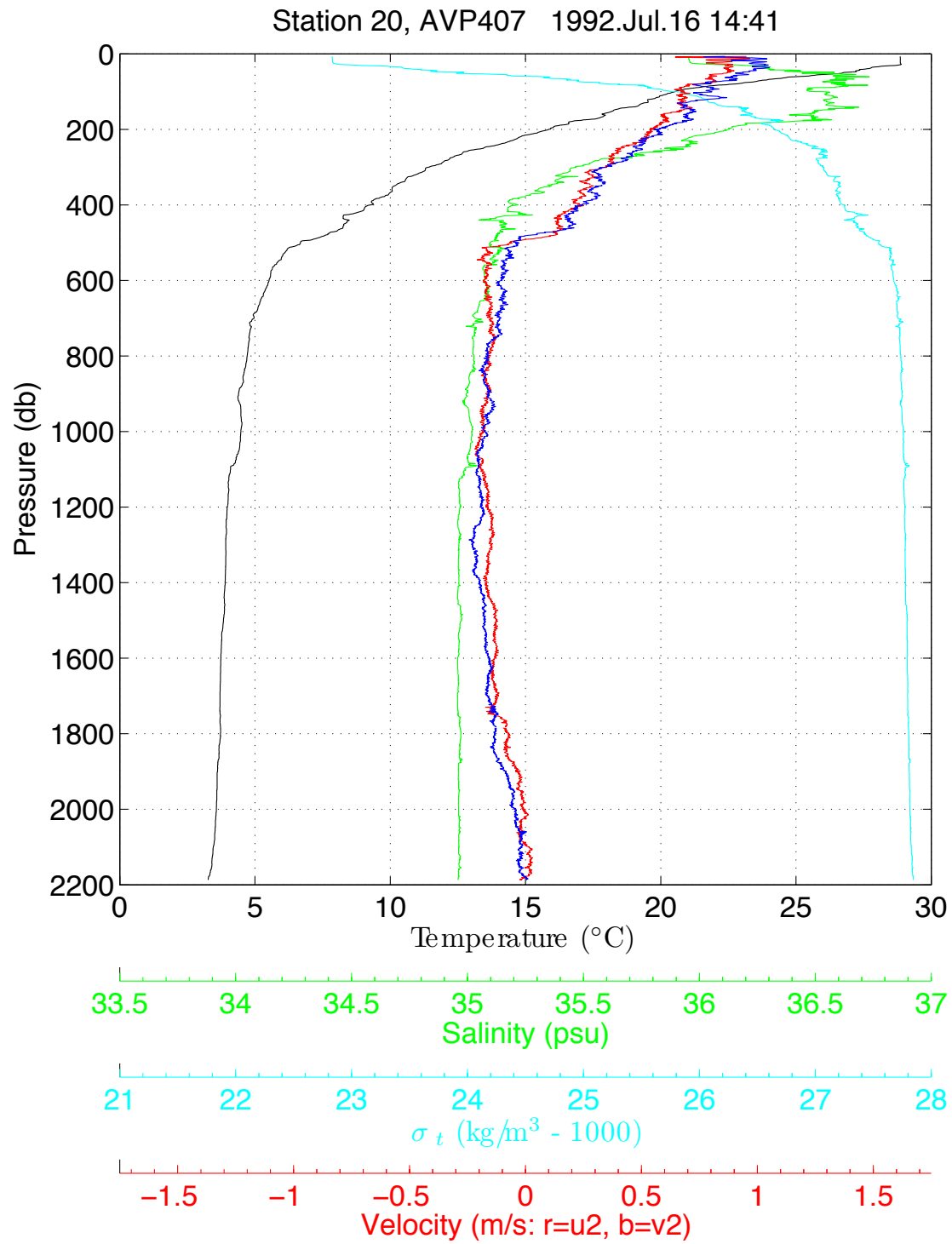
Figure B.4: Profile data from avp407d.
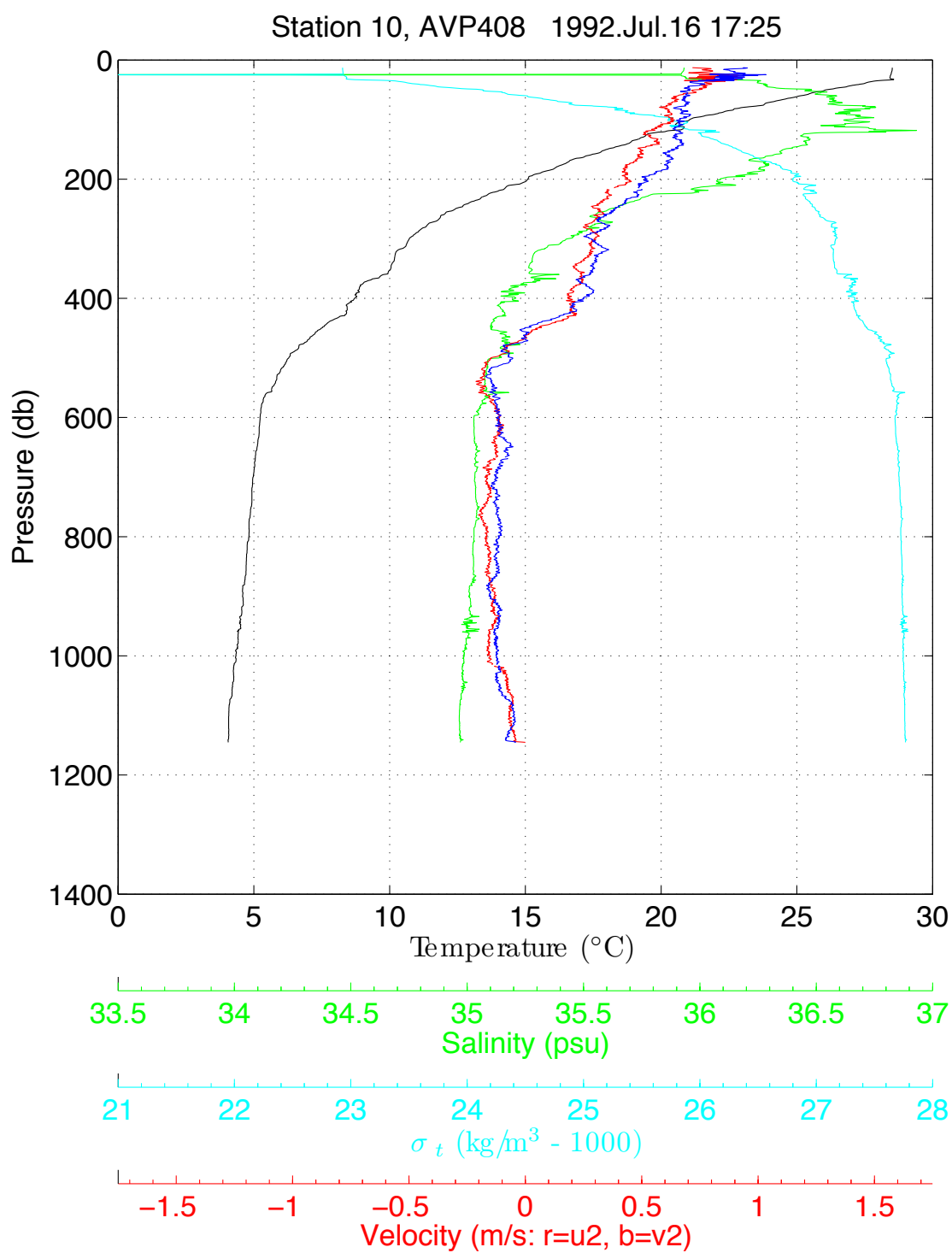
Figure B.5: Profile data from avp408d.
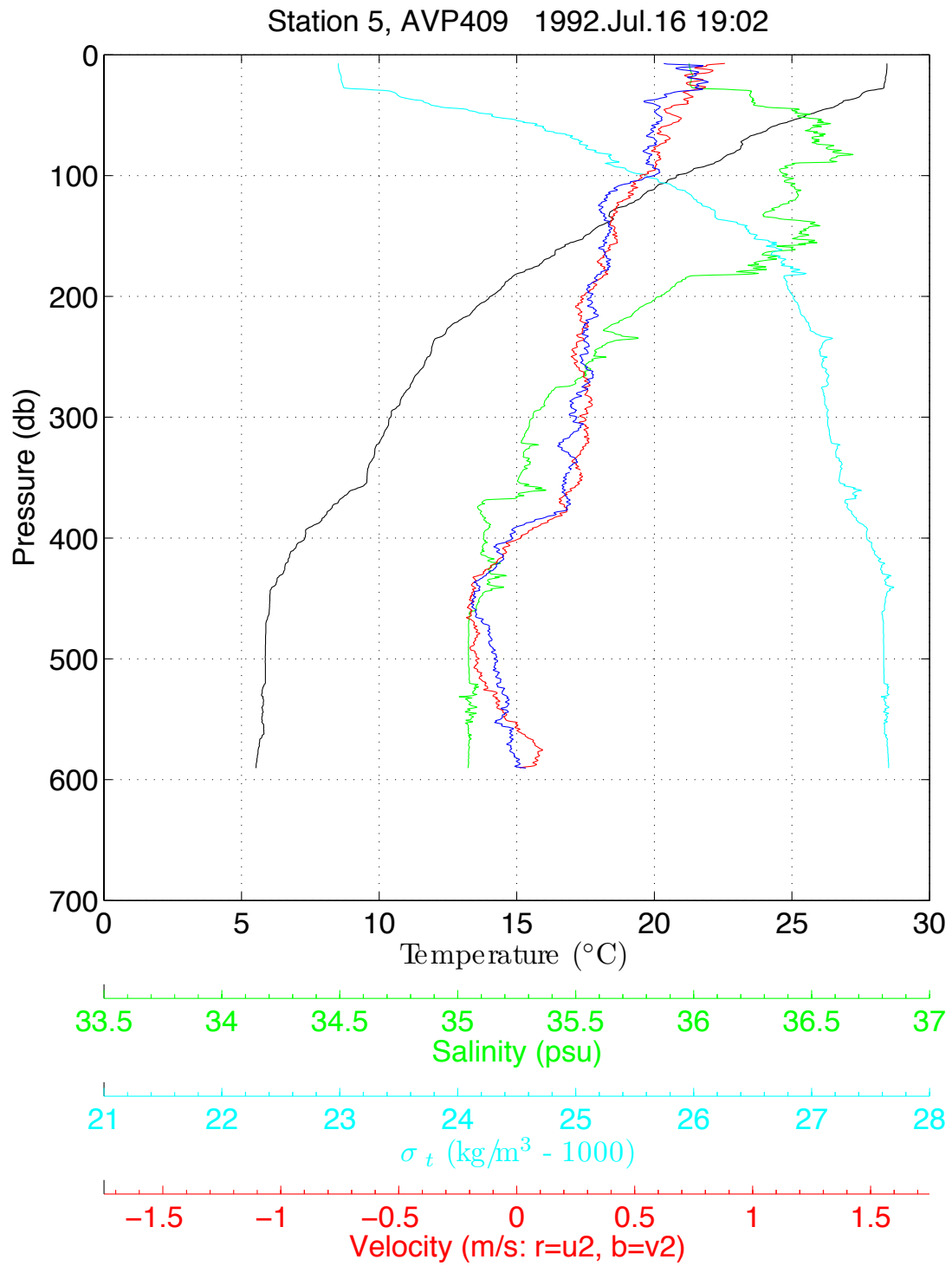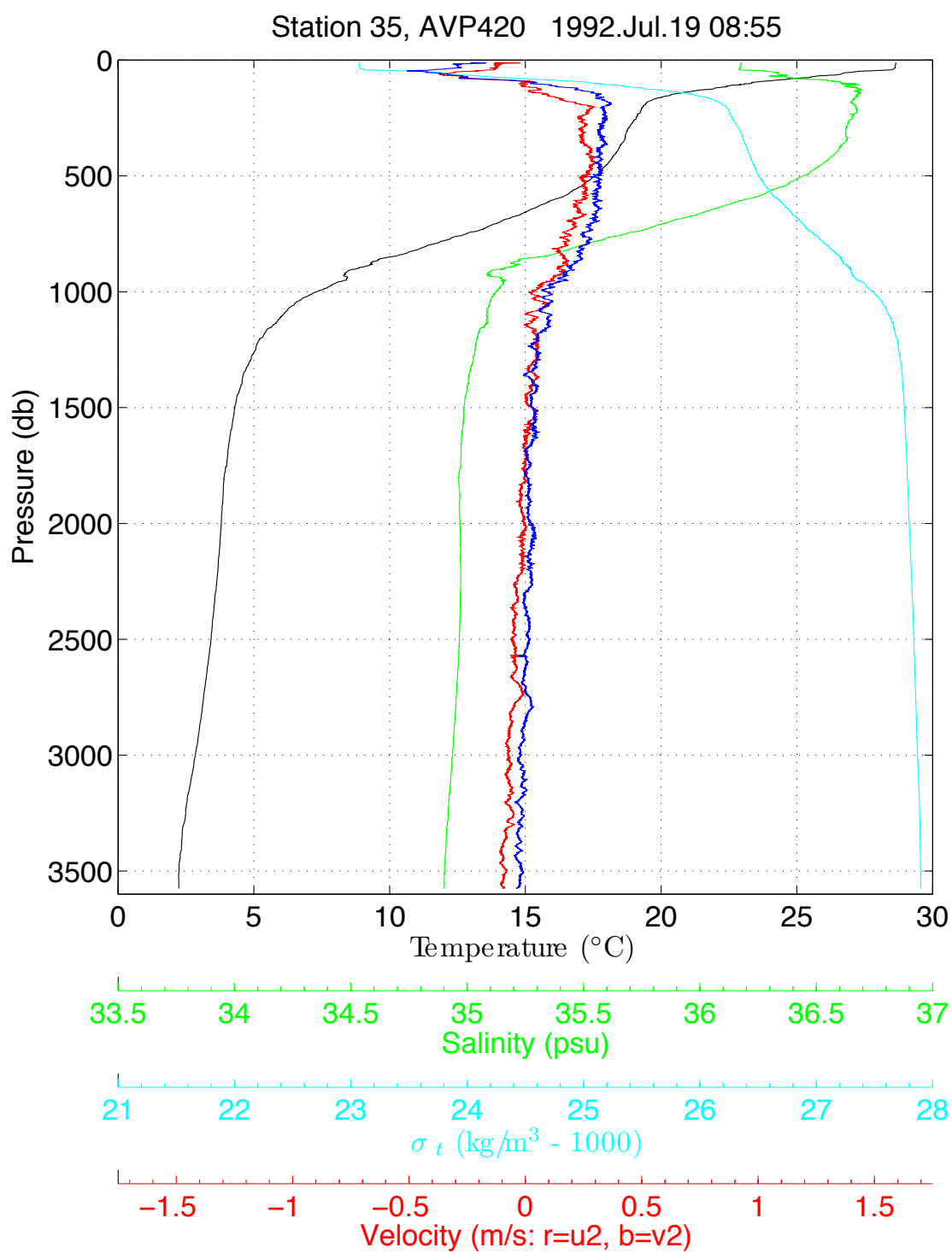
Figure B.6: Profile data from avp409d.
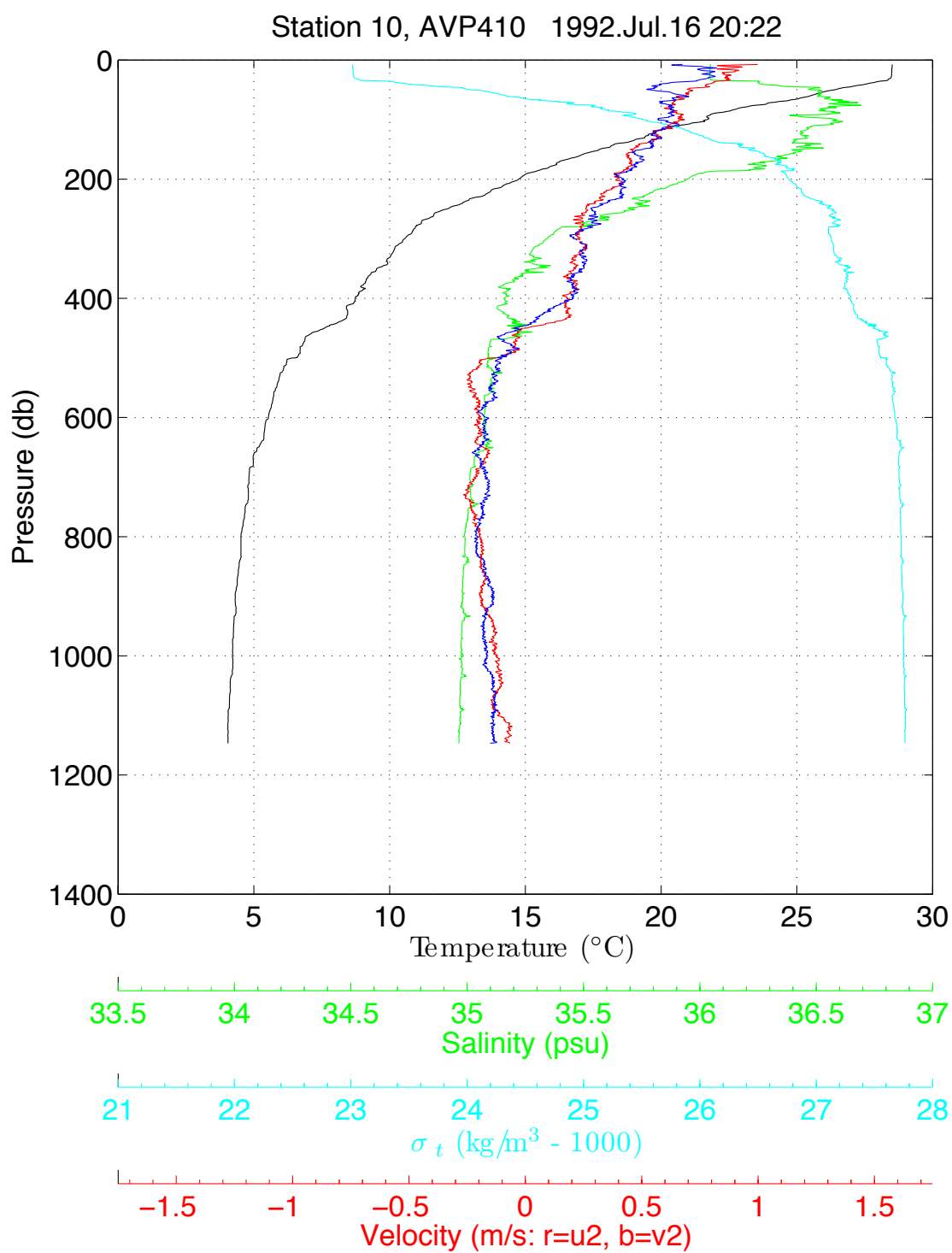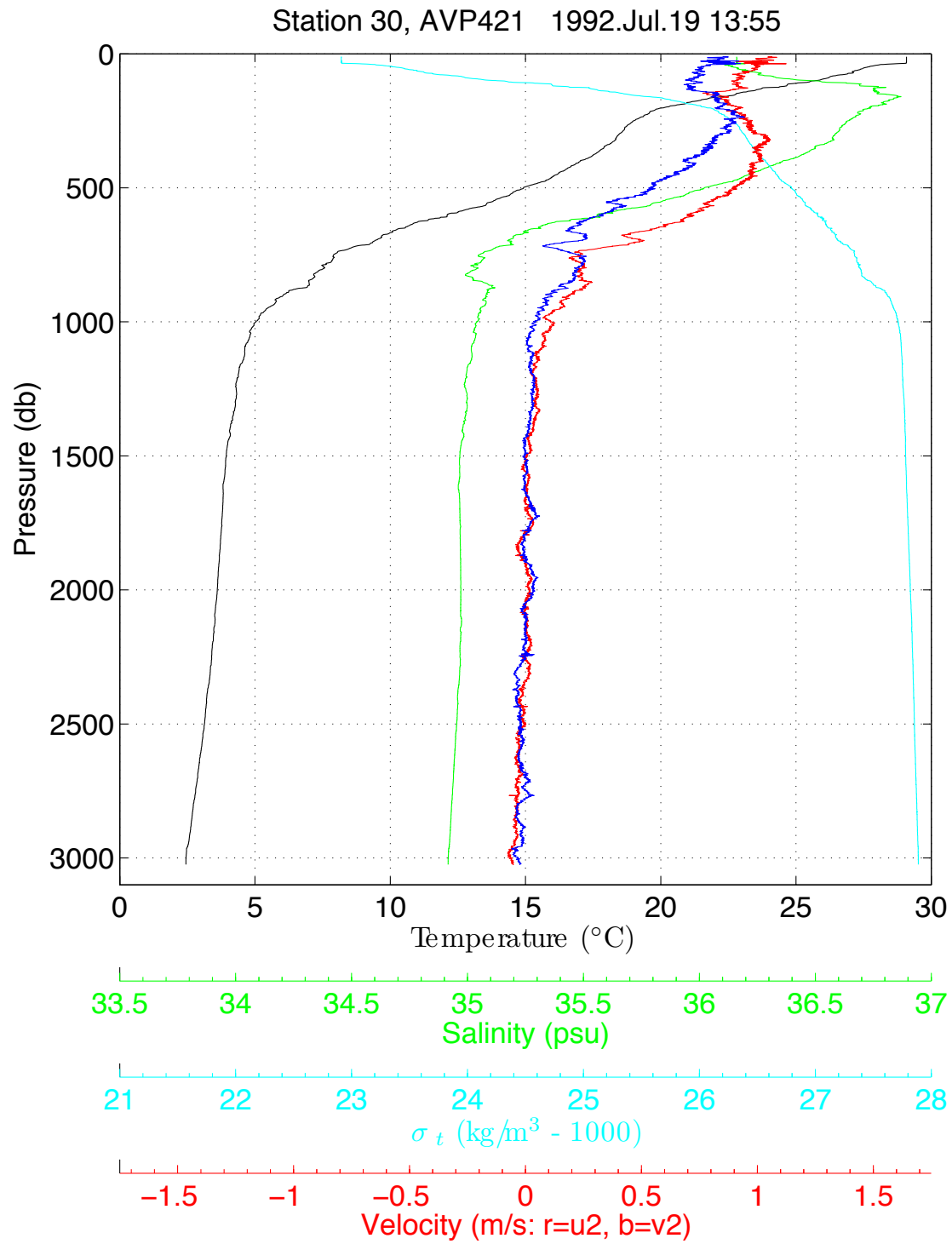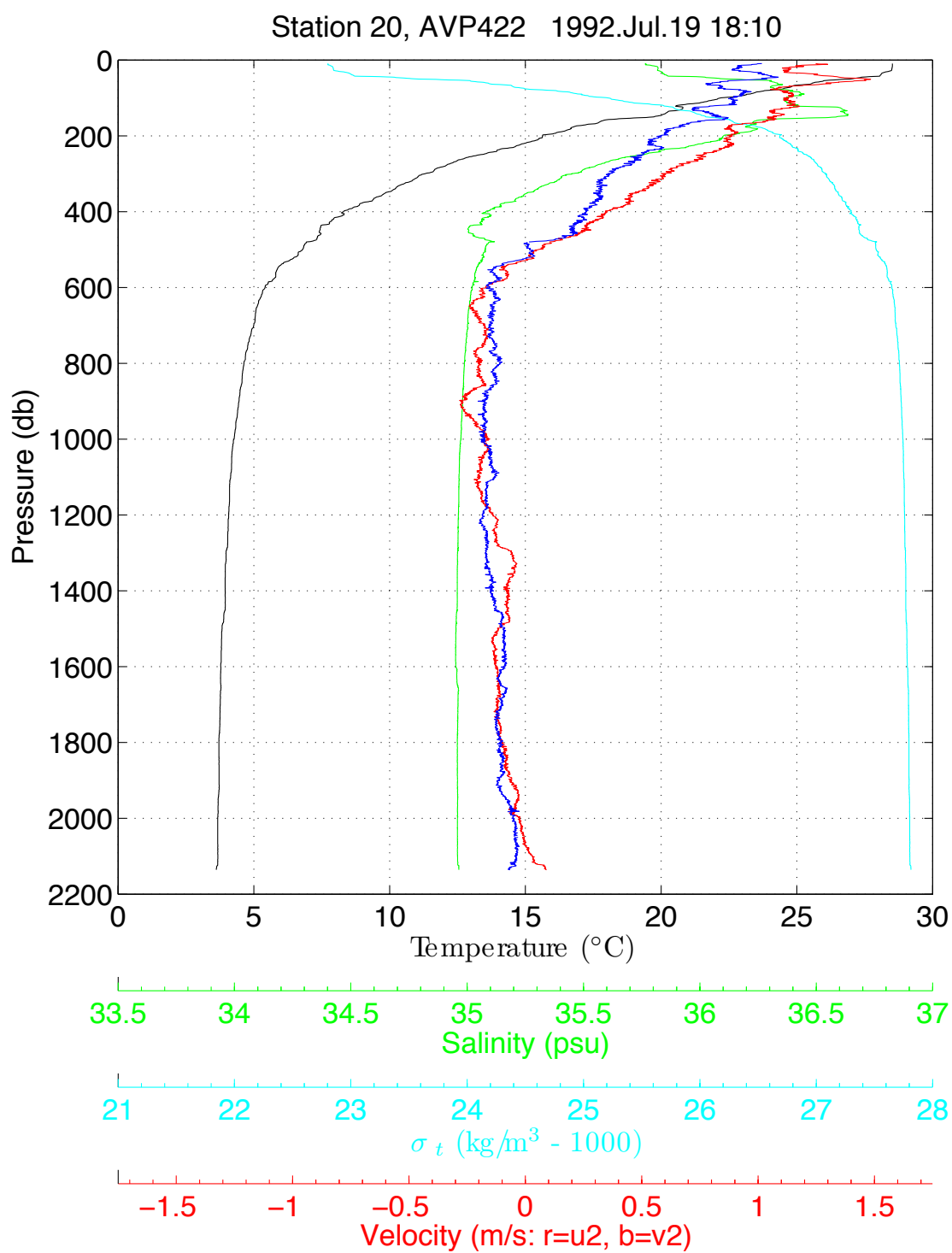
Figure B.7: Profile data from avp410d.
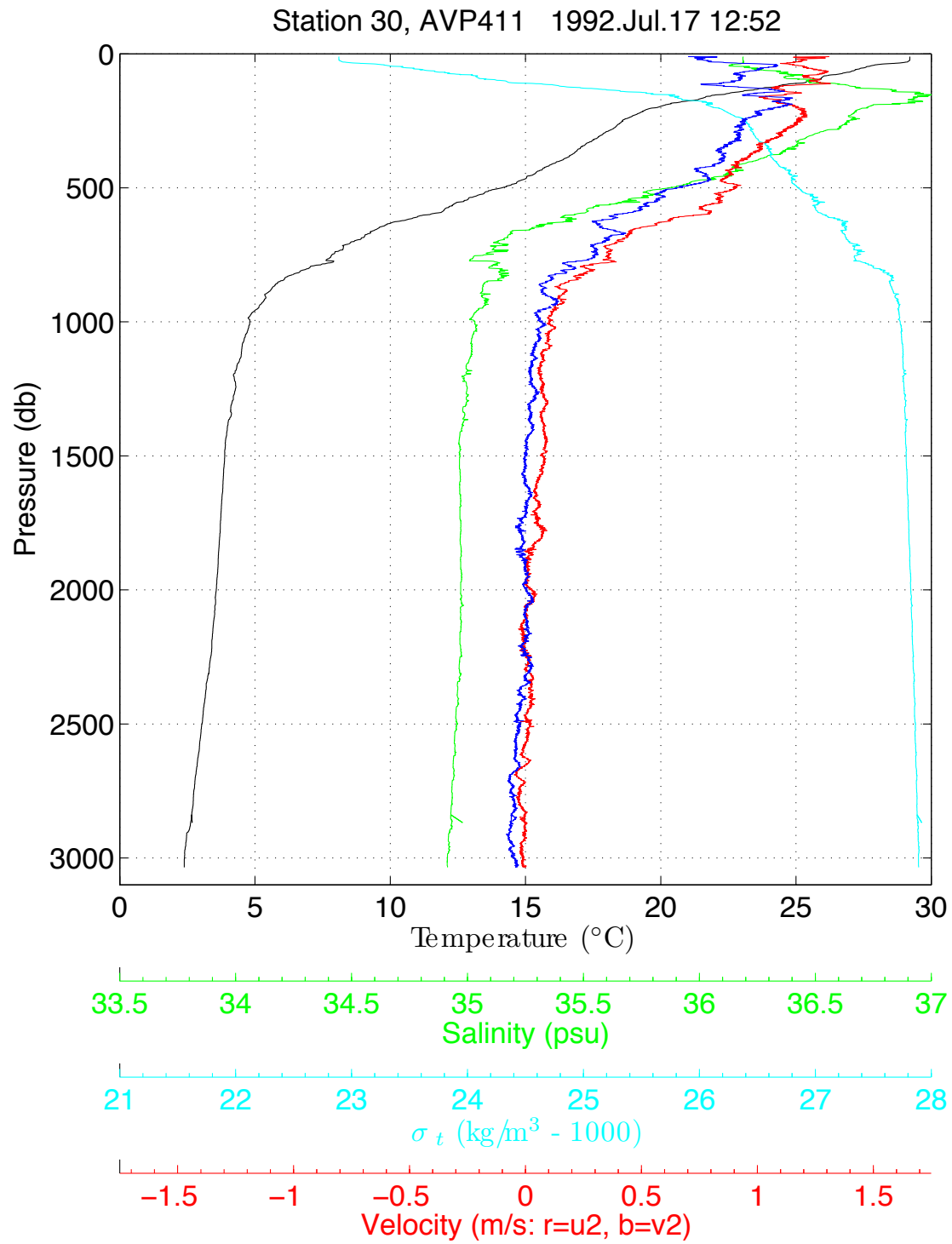
Figure B.8: Profile data from avp411d.
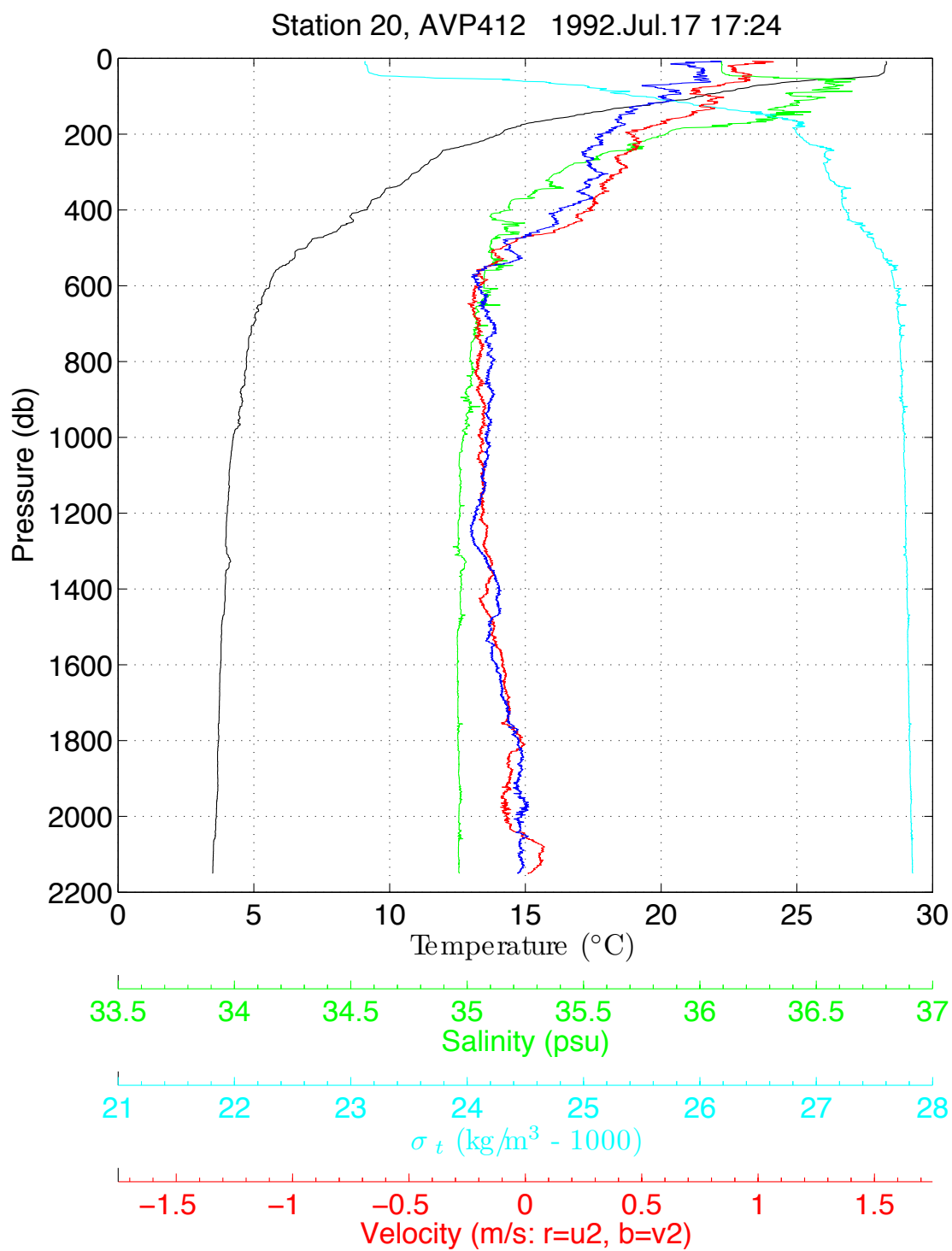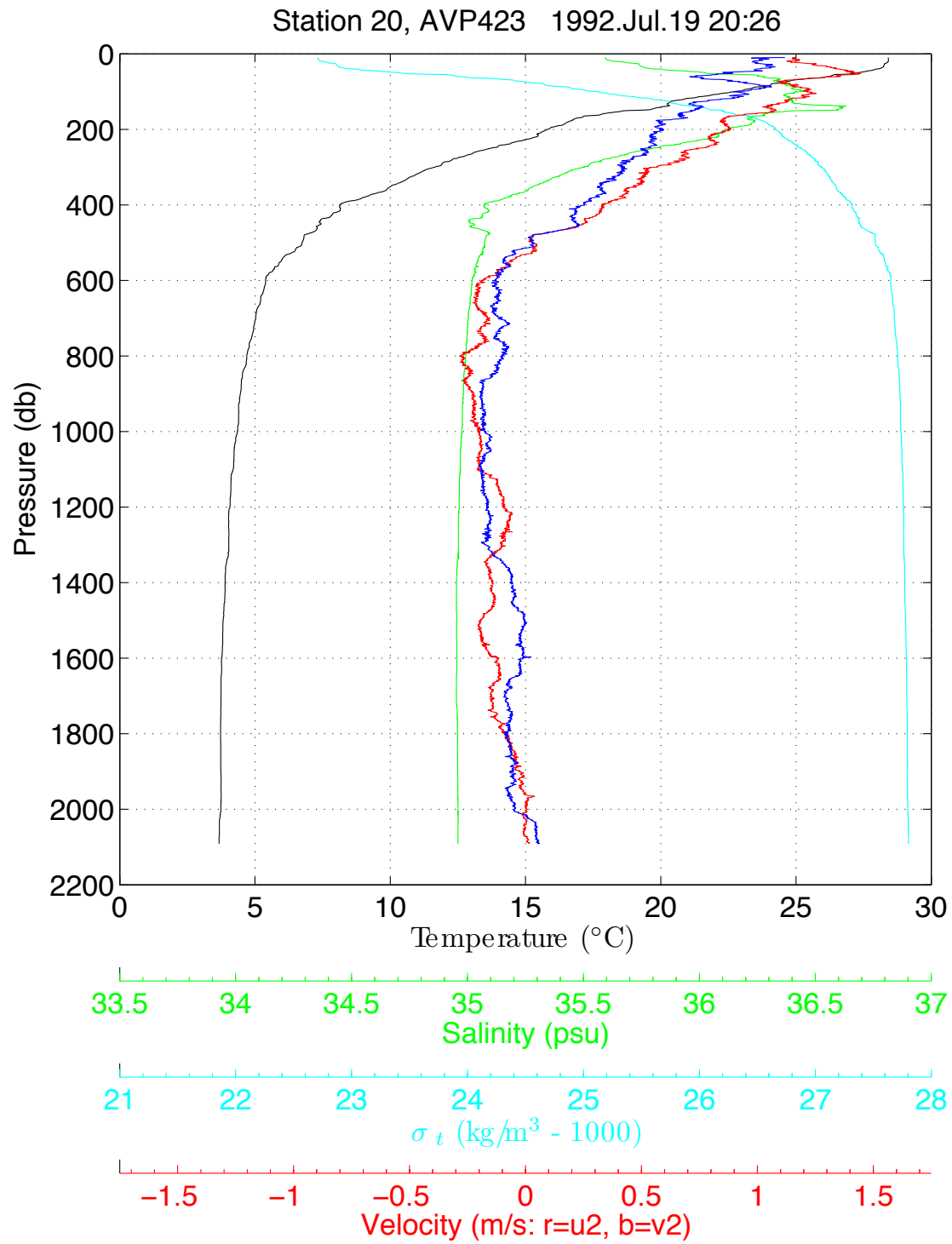
Figure B.9: Profile data from avp412d.
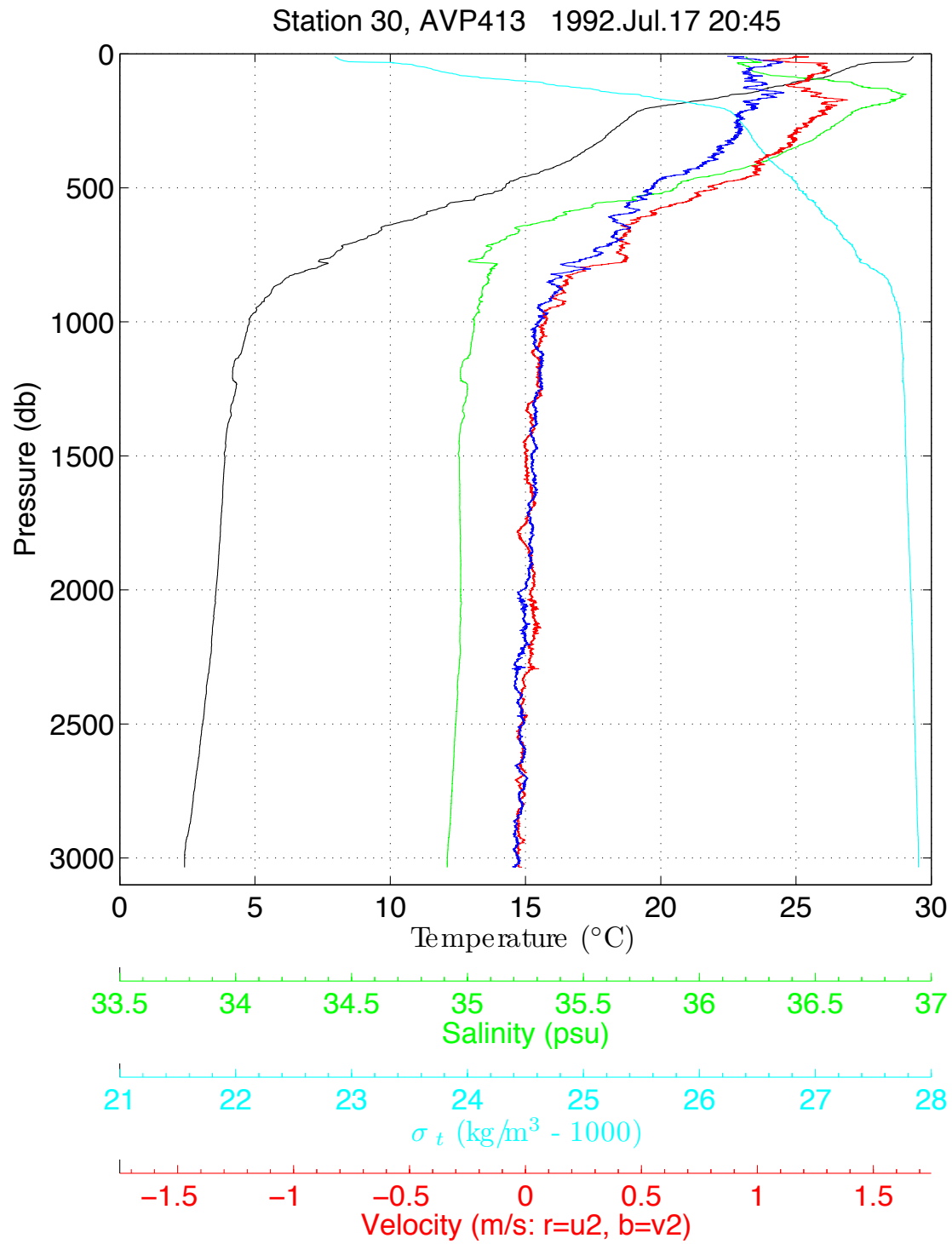
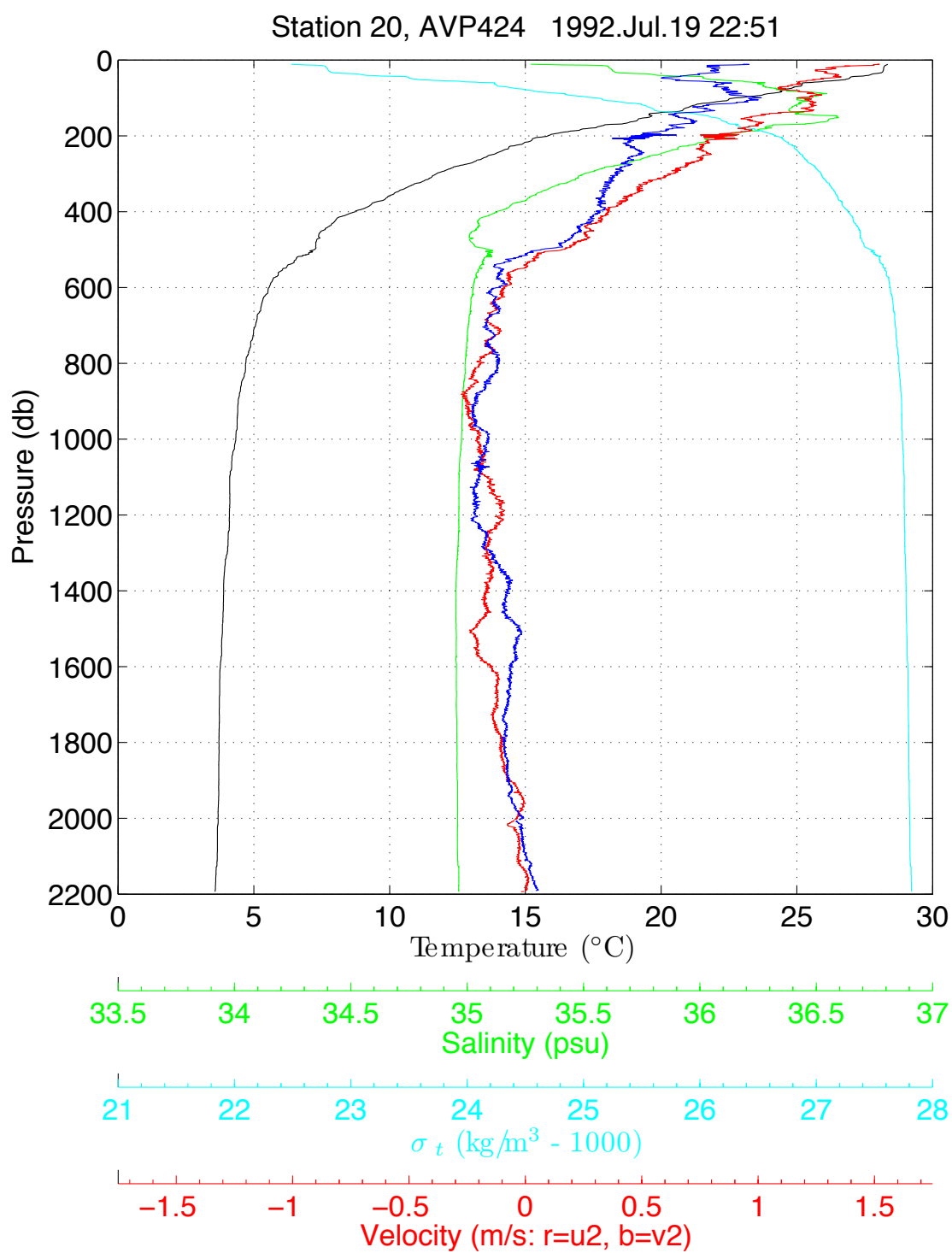Figure B.10: Profile data from avp413d.
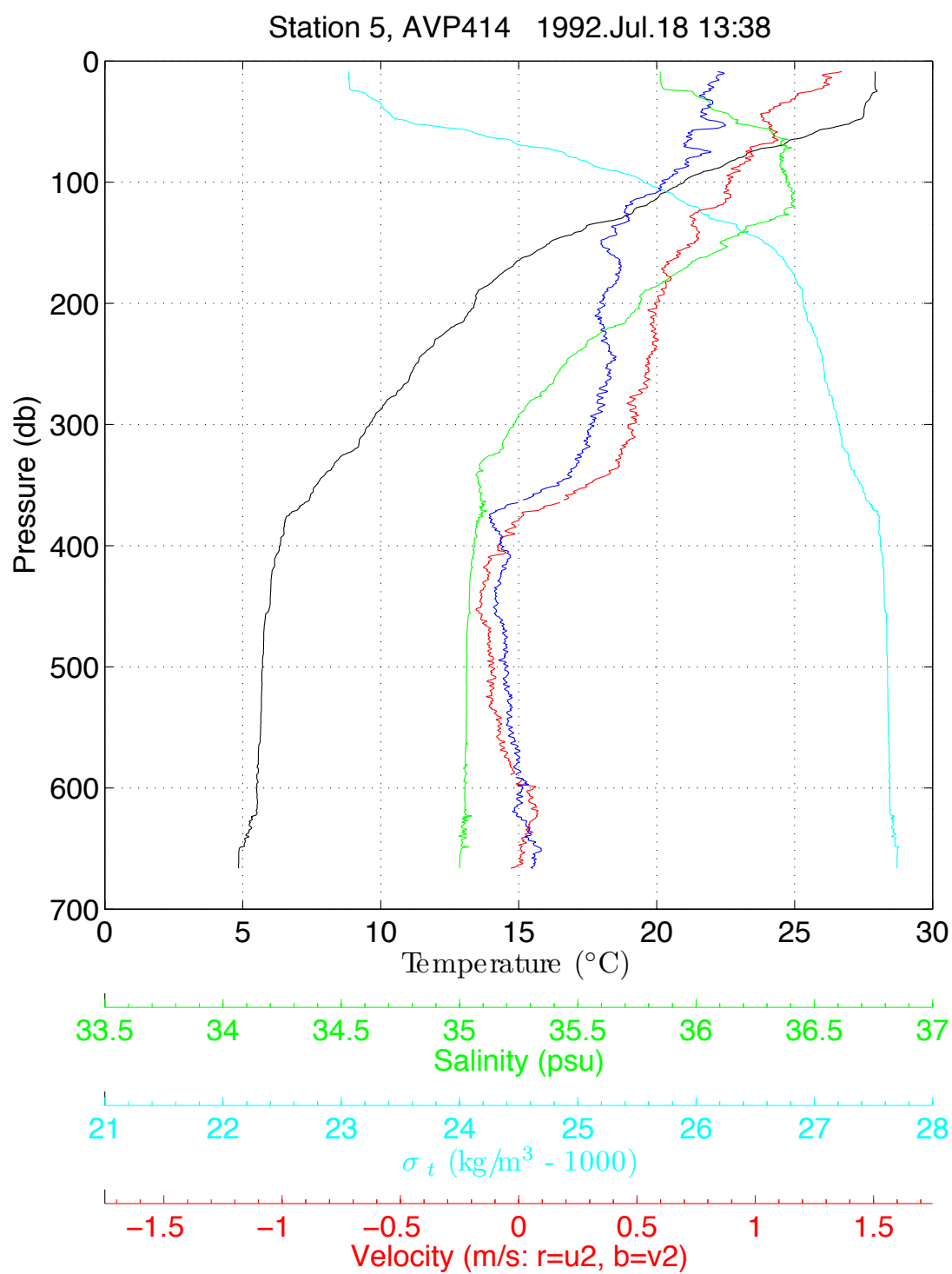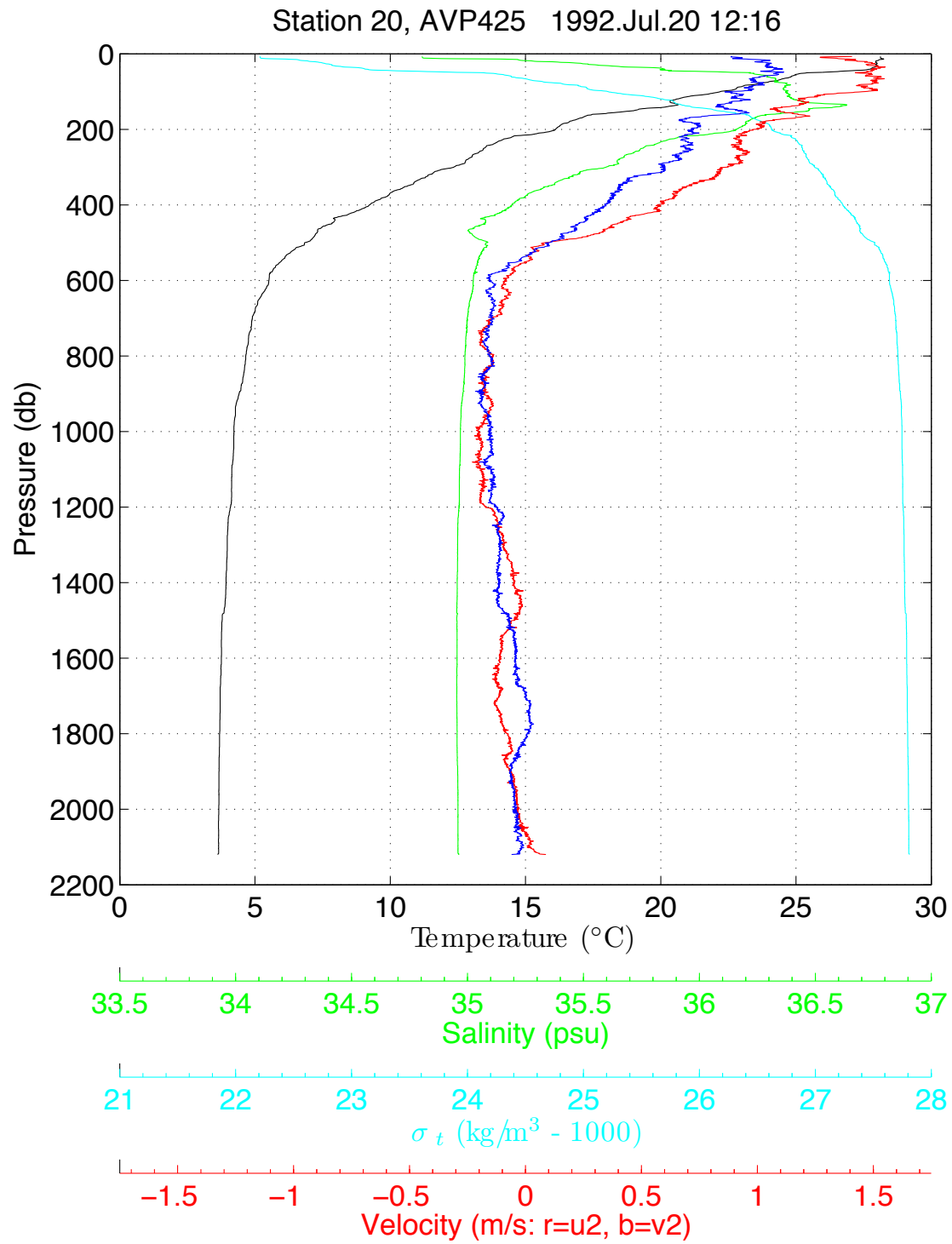
Figure B.11: Profile data from avp414d.
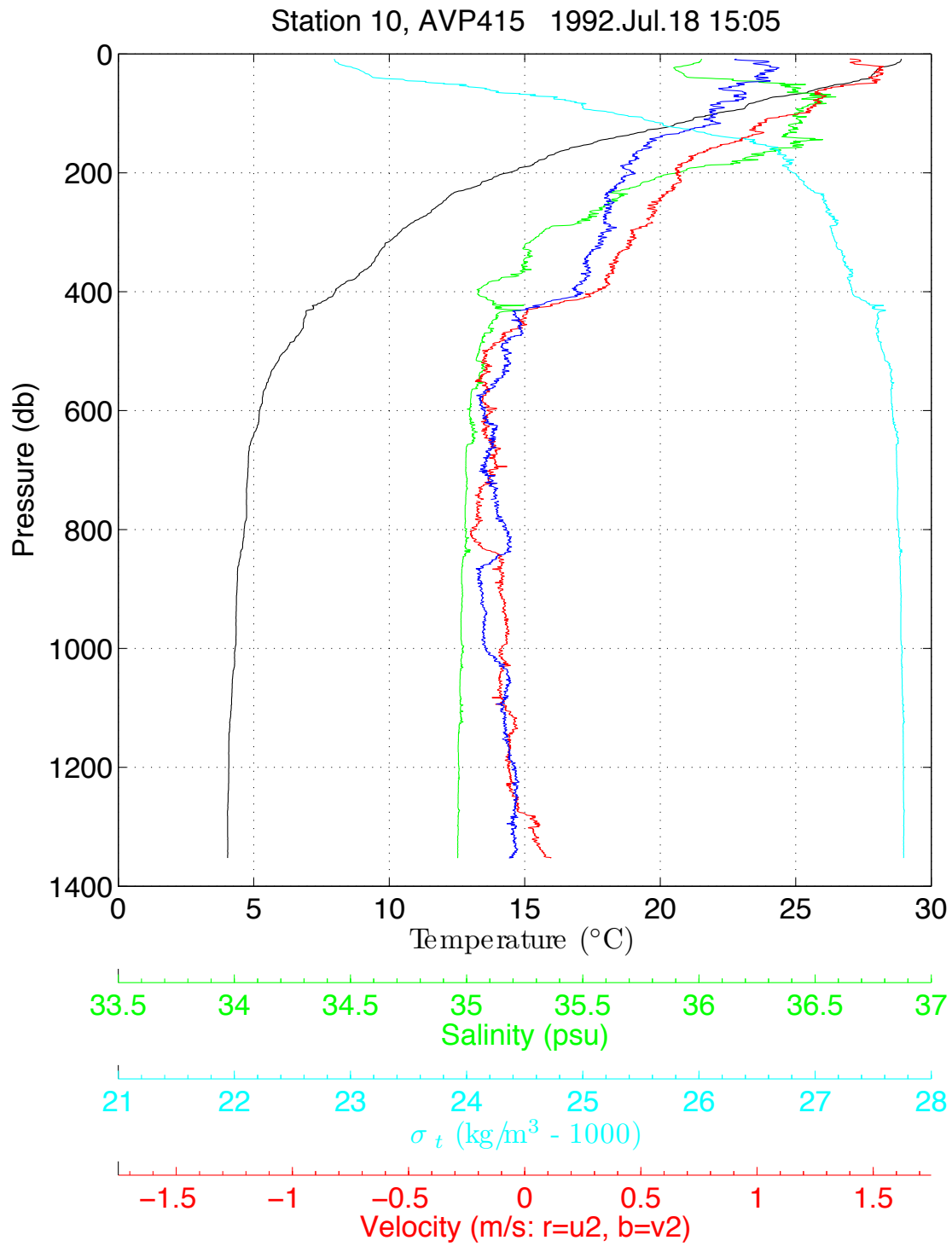
Figure B.12: Profile data from avp415d.
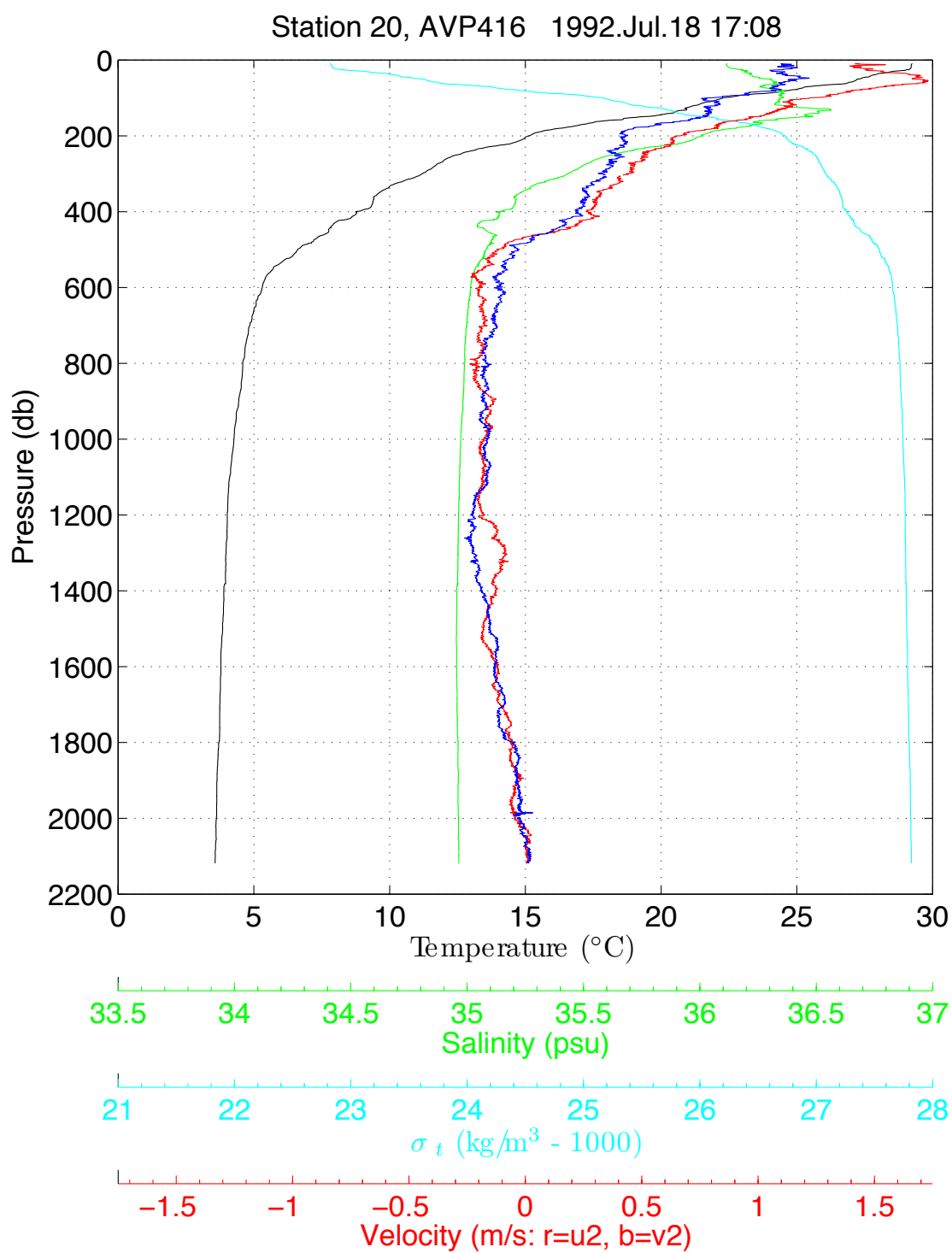
Figure B.13: Profile data from avp416d.
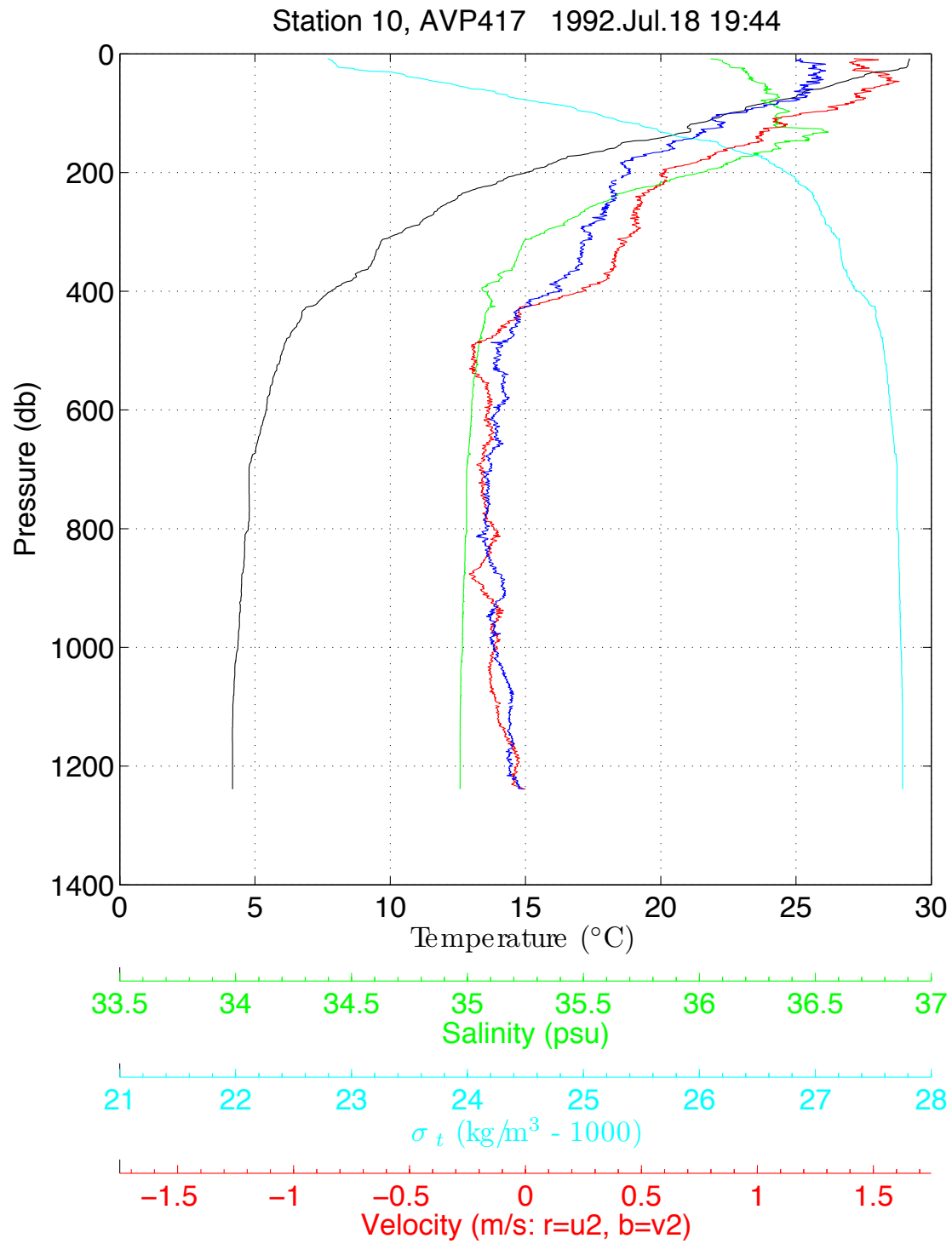
Figure B.14: Profile data from avp417d.
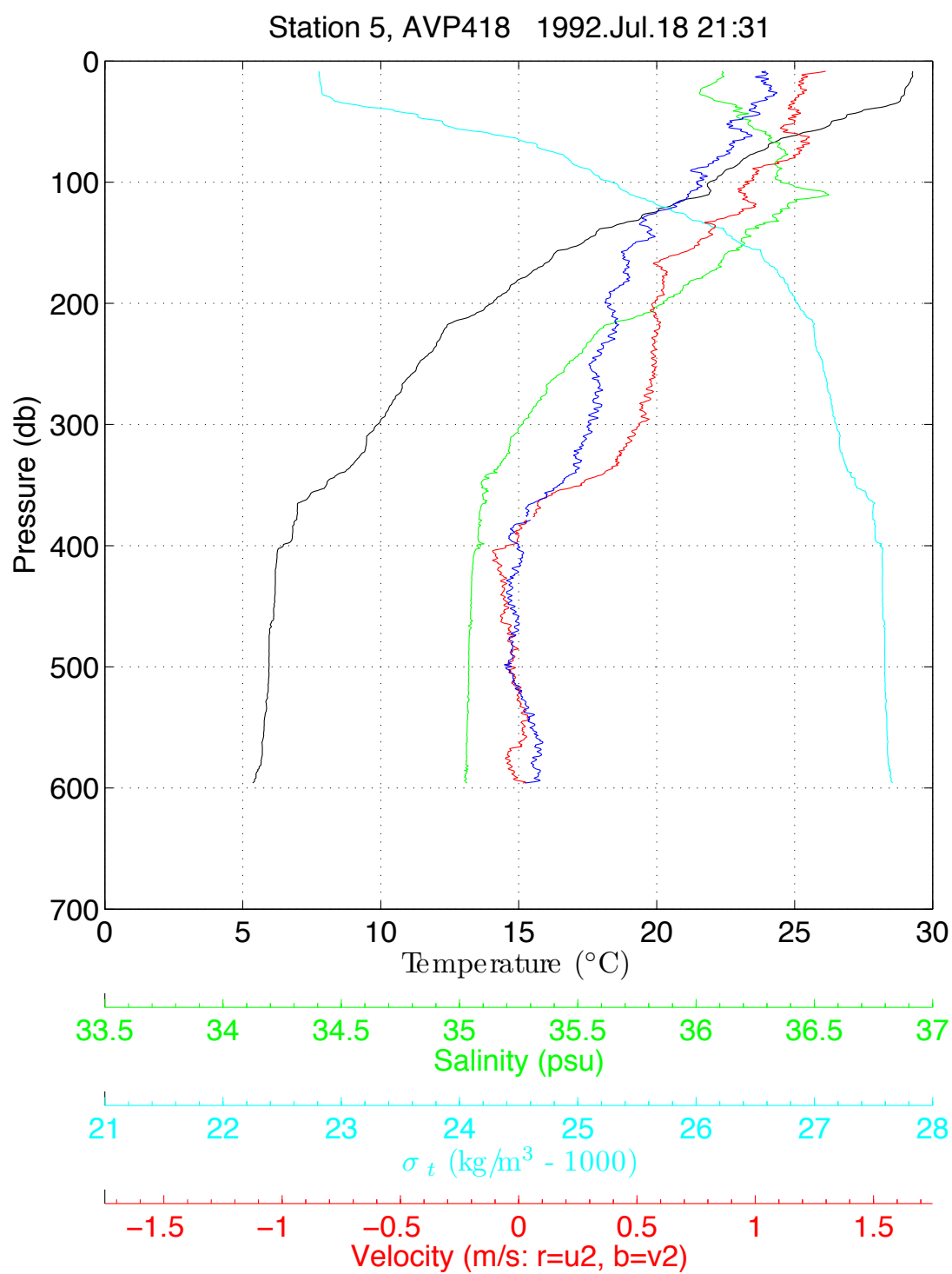
Figure B.15: Profile data from avp418d.
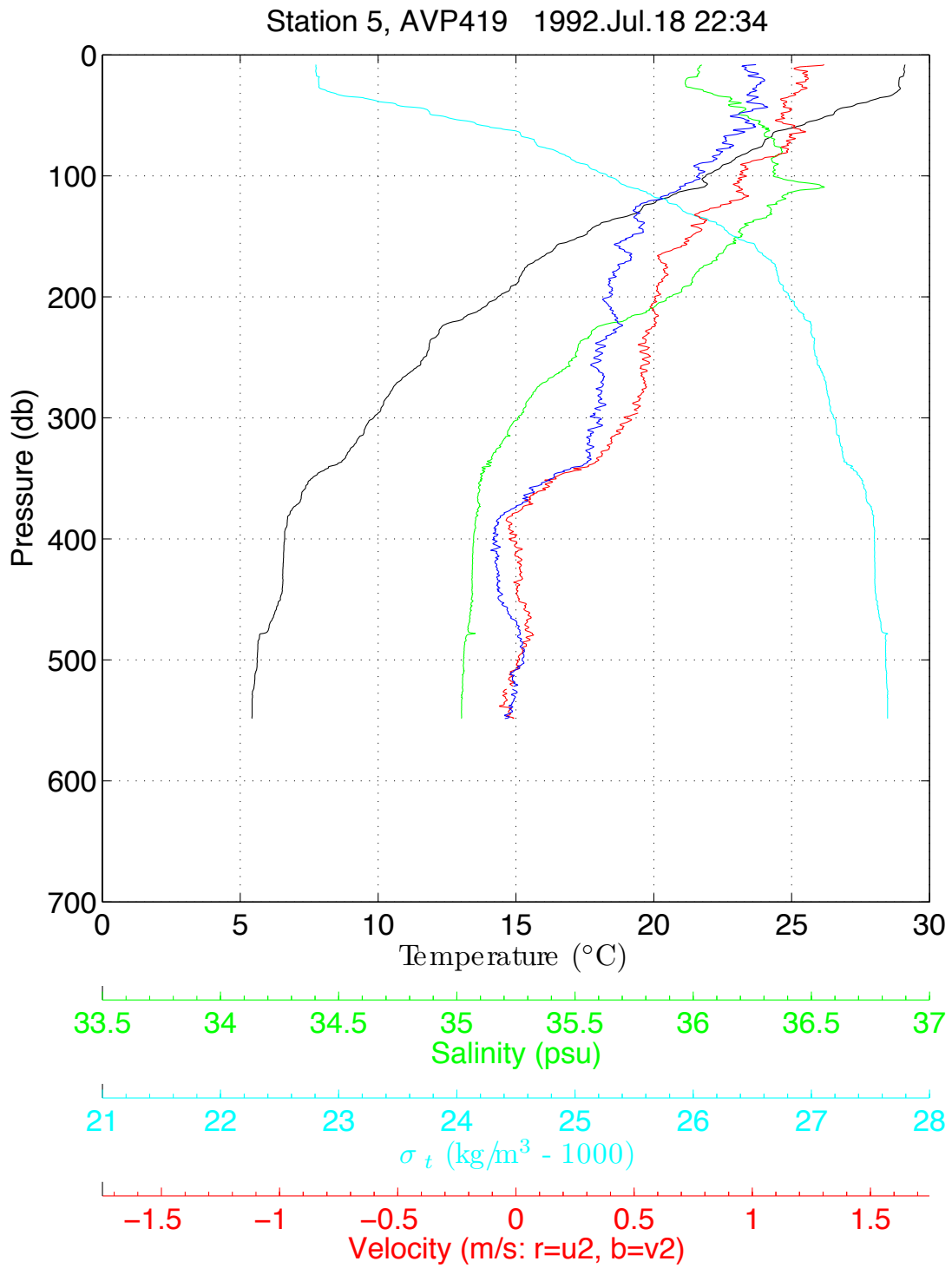
Figure B.16: Profile data from avp419d.

Figure B.17: Profile data from avp420d.

Figure B.18: Profile data from avp421d.

Figure B.19: Profile data from avp422d.

162

Figure B.20: Profile data from avp423d.

Figure B.21: Profile data from avp424d.

164

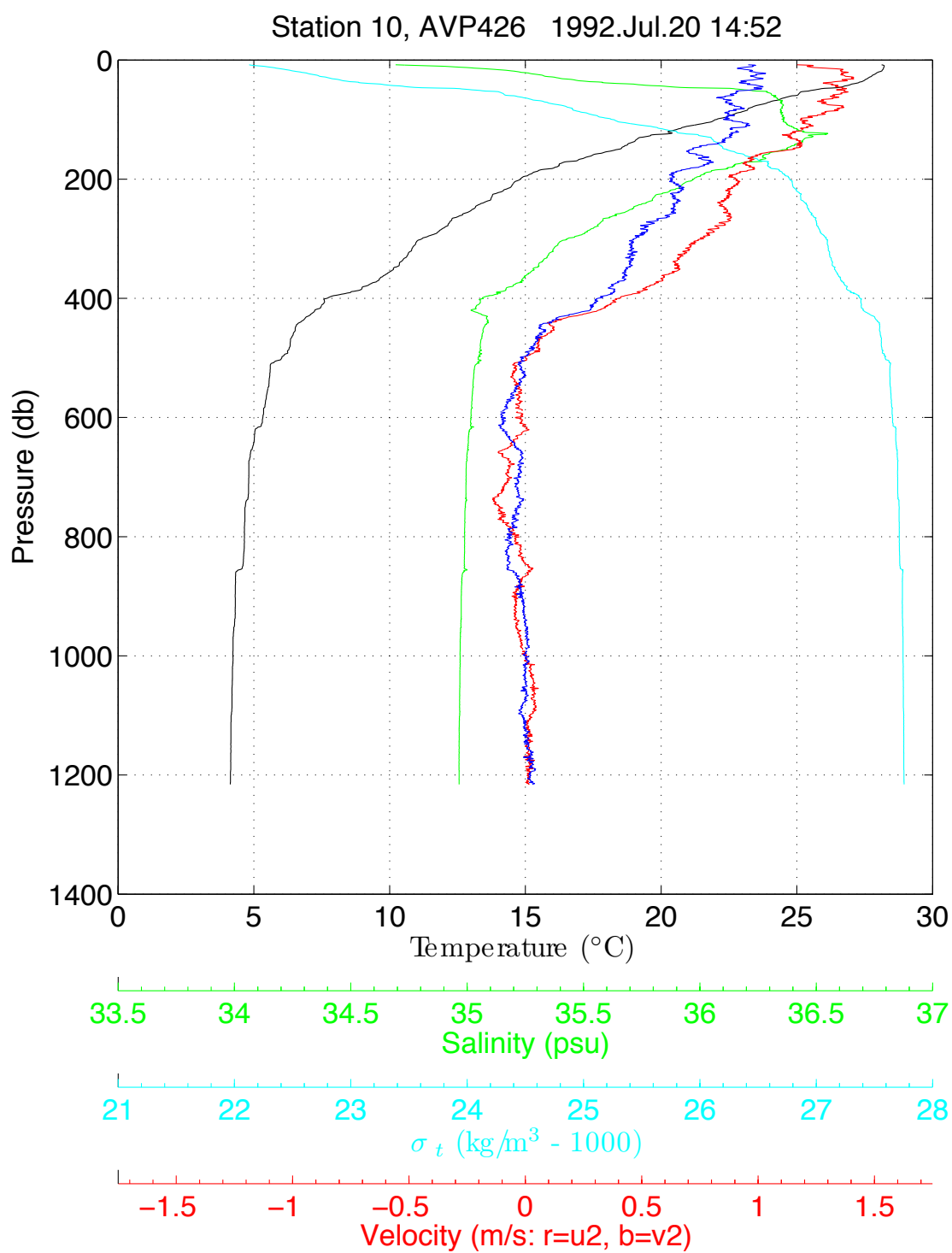Figure B.22: Profile data from avp425d.
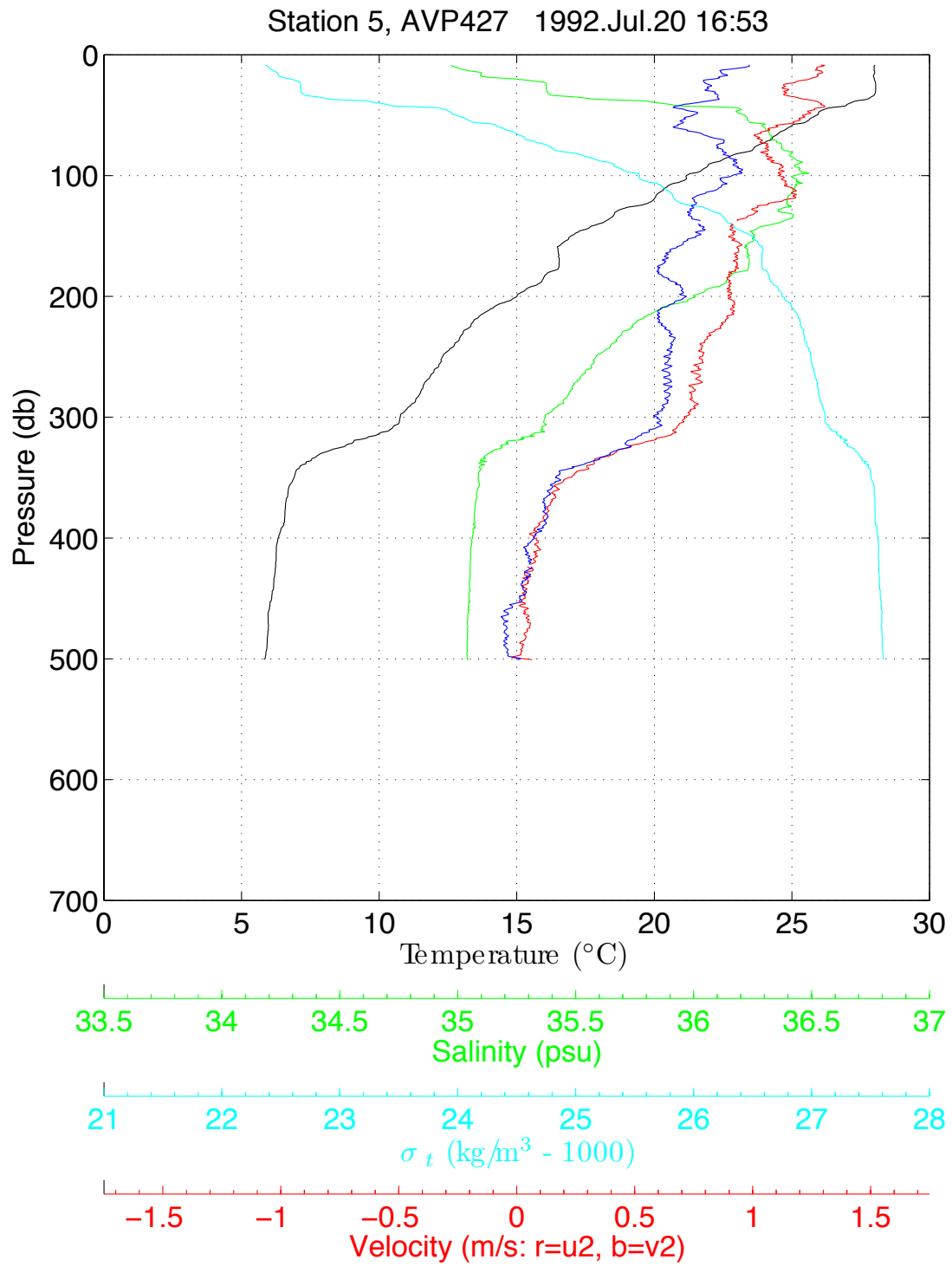
Figure B.23: Profile data from avp426d.

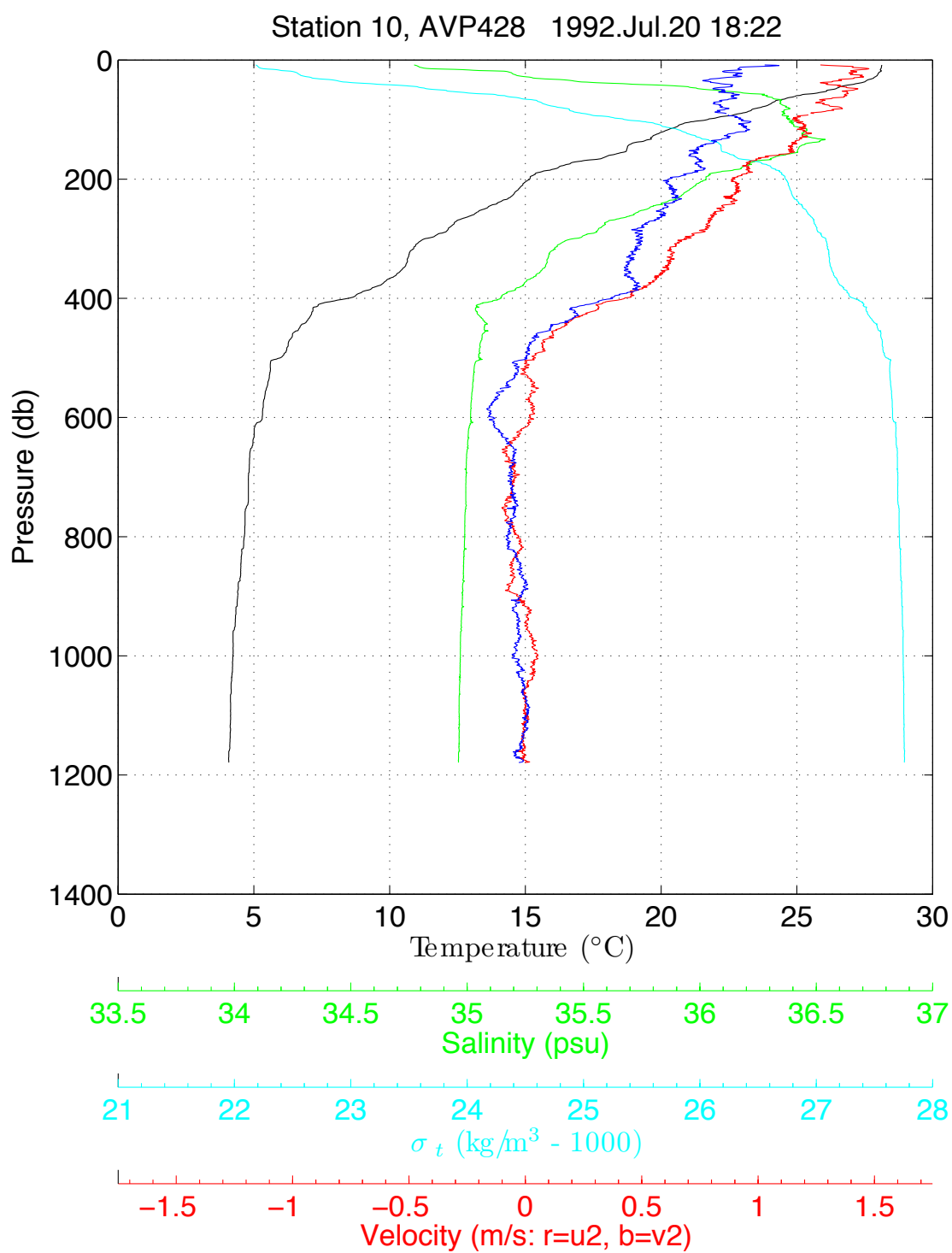Figure B.24: Profile data from avp427d.

Figure B.25: Profile data from avp428d.

Figure B.26: Profile data from avp429d.
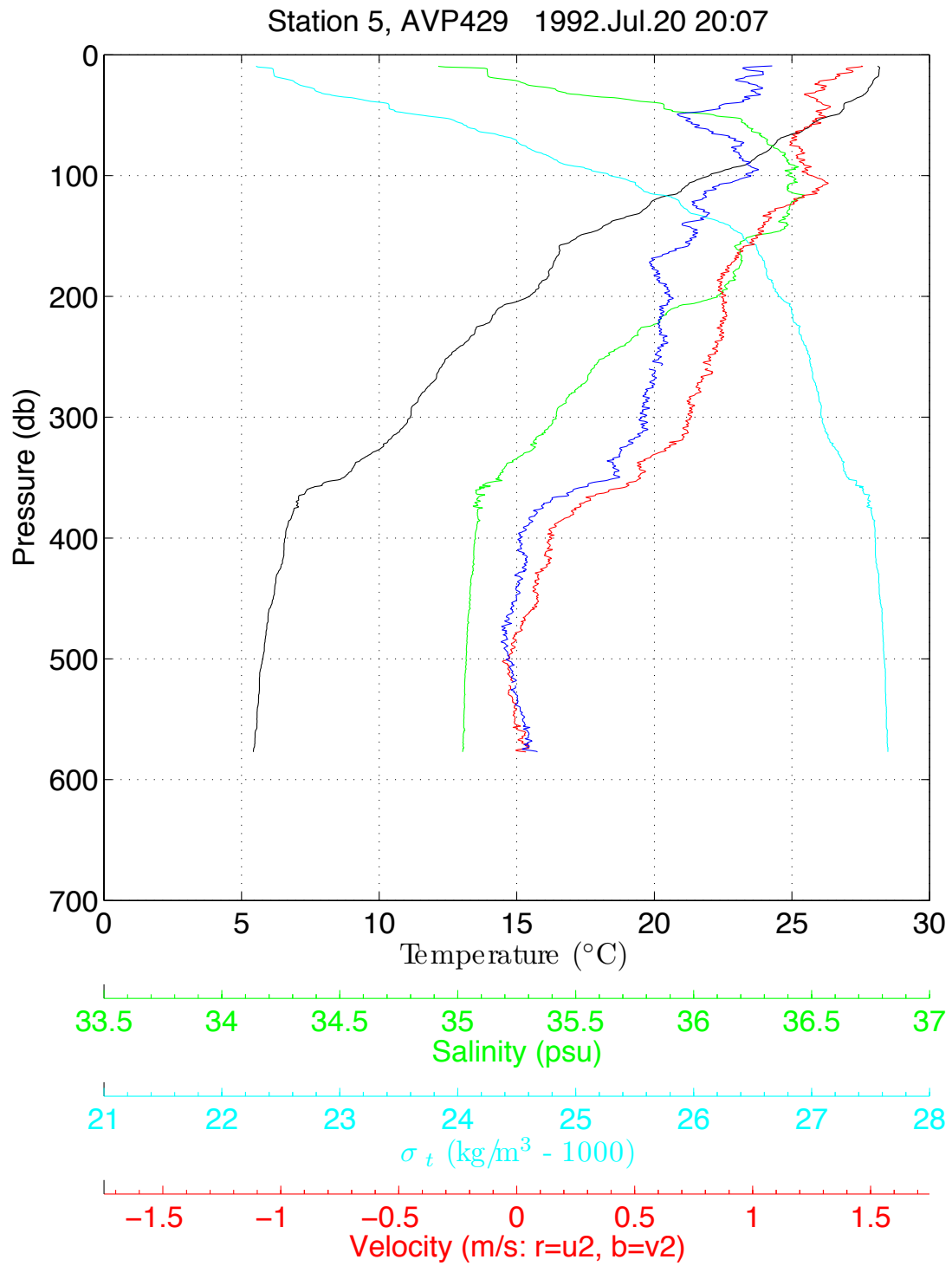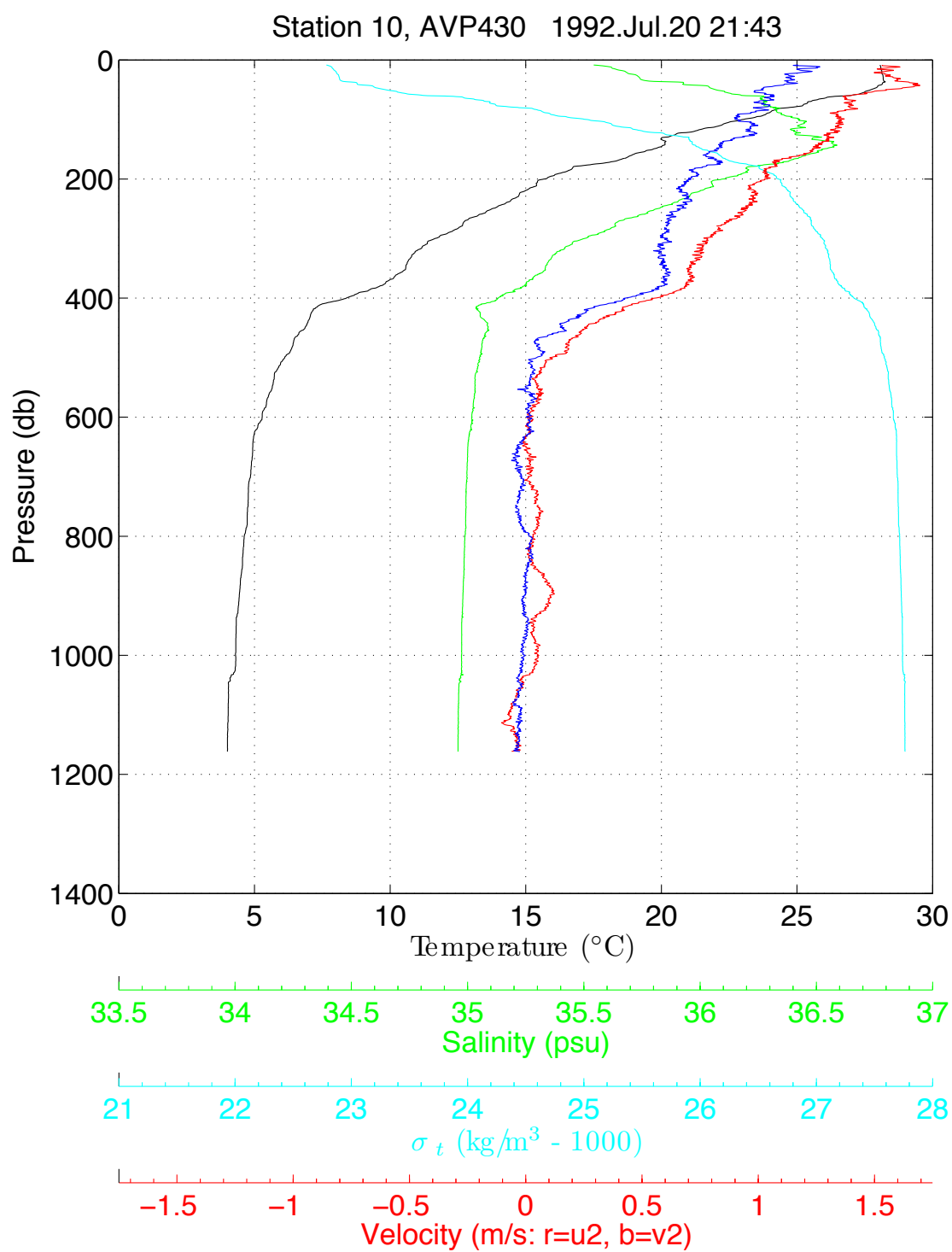
Figure B.27: Profile data from avp430d.

CURRICULUM VITAE

Education

June 2008	Ph. D.: *Interpretation of Motionally Induced Electric Fields in Oceans of Complex Geometry*, advisor: Dr. Tom Sanford.
June 2005	Master of Science, *Electric Field Floats in the North Atlantic Current: Validation and Observations*, advisor: Dr. T. Sanford.
Jan 2002 – present	Research Assistant, Applied Physics Lab, University of Washington, Seattle, WA.
Sep 1997 – Dec 2000	Bachelor of Arts, Oberlin College, Oberlin, OH. Major in Biology
Aug 1996 – June 1997	Foreign exchange year in Fribourg, Switzerland. attended Collège Saint-Michel.
June 1996	Graduated from Governor Dummer Academy, Byfield, MA.

Research Experience

Fall 2000	Research project in physics under Dr. Stephen Fitzgerald, Oberlin College, Oberlin, OH.
Summer 2000	Summer Student Fellowship at the Woods Hole Oceanographic Institution supervised by Dr. Glen Gawarkiewicz, Woods Hole, MA.
Summer 1999	Sea Education Association, Woods Hole, MA: an interdisciplinary 8-week program on oceanography, sailing, and maritime studies, half on land and half on a research sailing vessel.
Summers 1998, 1999	Research assistant in a neurophysiology lab under Dr. Eve Marder, Brandeis University, Waltham, MA.

Awards and Grants

Apr 2006 – Sep 2008	NSF Grant received titled "Interpretation of Motionally Induced Electric Fields in Oceans of Complex Geometry," written by me, with Dr. T. Sanford as PI.
Sep 2002 – Aug 2005	National Defense Science and Engineering Graduate Fellowship, 3 years of support for graduate studies.
Spring 1999	Millar Award, awarded by Oberlin College Biology Department, Oberlin, OH.

Teaching Experience

2006 – 2008	Volunteer and question writer for the regional competition of the National Ocean Sciences Bowl, a marine-based quiz competition for high school students.
Fall 2005	Teaching Assistant for *Introduction to Oceanography* (Oceanography 101), University of Washington, Seattle, WA. Prepared and taught a weekly lab, graded homework.
2002 – present	Volunteer Instructor for Ocean Inquiry Project, an experiential oceanography program that teaches high school and college students about oceanography through a hands-on oceanographic day cruise.

Publications

Szuts, Z.B., 2004. Electric Field Floats in the North Atlantic Current: Validation and observations. Technical Report 0405. Applied Physics Lab, University of Washington, Seattle, WA. 76 pp.

Birmingham, J.T., Z.B. Szuts, L.F. Abbott, and E. Marder, 1999. Encoding of muscle movement on two time scales by a sensory neuron that switches between spiking and bursting modes. Journal of Neurophysiology, 82: 2786–2797.

Presentations and Posters

Szuts, Z.B. Oceanic electric fields and the water velocities that generate them: from measurements to the limitations of first order theory. presentations at: the Institut Français de Recherche pour l'Exploitation de la Mer (IFREMER), Brest, France on Sep 4, 2007; the Laboratoire d'Océanographie et du Climat: Expérimentation et Approches Numérique (LOCEAN), Paris, France on Sep 6, 2007; and the National Oceanography Centre, Southampton (NOCS), Southampton, England on Sep 10, 2007.

Szuts, Z.B. The generation of oceanic electric fields: Steep topography, thick and variable sedimentary layers, and oceanic flow across topography. presentation at the American Geophysical Union (AGU) 2006 Fall General Assembly on Dec 14, 2006, San Francisco, CA.

Szuts, Z.B. Motionally induced oceanic electric fields near complex topography. presentations at the Swedish Defense Research Agency (FOI) on Apr 24, 2006 and at the Department of Meteorology at Stockholm University (MISU) on Apr 26, 2006, both located in Stockholm, Sweden.

Szuts, Z.B. Motionally induced oceanic electric fields near complex topography. presentation at Marine Electrodynamics (Marelec) Conference on Apr 19, 2006, Amsterdam, the Netherlands.

Szuts, Z.B. and T.B. Sanford. Barotropic velocities in the North Atlantic Current from motional induction methods on a RAFOS tracked float. presentation at the American Geophysical Union (AGU) 2004 Ocean Sciences conference on Jan 27, 2004, Portland, OR.

Szuts, Z.B. and G.G. Gawarkiewicz. Variability of thermohaline structure in the shelf-break front in the southern Middle Atlantic Bight. poster at the American Society of Limnology and Oceanography (ASLO) Aquatic Sciences 2001 Conference on Feb 13, 2001, Albuquerque, NM.

Field Experience

Aug 10–19, 2006, AESOP cruise in Monterey Canyon to measure the generation of internal waves from barotropic tides.

Aug 25–30, 2006, PLUSNet recovery leg, recovery and technical support of bottom-mounted EF sensors.

Sep 4–23, 2002, Hawaiian Ocean Mixing Experiment (HOME), Nearfield cruise, measuring the transfer of barotropic tidal energy to internal waves along the Hawaiian Ridge.

Sep 10–17, 2001, Port Townsend, WA, investigating Langmuir circulation in Puget Sound with an electromagnetic vorticity meter.

Aug, 2001, Puget Sound, WA, 4 day-cruises to develop and test the electromagnetic vorticity meter.

Other Services

Reviewer for *Geophysical Research Letters* and *Journal of Atmospheric and Oceanic Technology.*

Graduate student representative for the Physical Oceanography Department at faculty meetings, 2006–2008, School of Oceanography, University of Washington, Seattle, WA.

Computer Programs

Matlab	Linux
LaTeX	Adobe Photoshop and Illustrator
Mac OS X	Microsoft Word and Excel

Languages

English (native), French (conversant), Hungarian (intermediate), German (basic), Italian (basic)

Personal Info

Zoltan Bela Szuts
born on May 9, 1979 in Plymouth, MA, USA
US and Hungarian Citizen

REPORT DOCUMENTATION PAGE

Public reporting burden for this collection of information is estimated to average 1 hour per response, including the time for reviewing instructions, searching existing data sources, gathering and maintaining the data needed, and reviewing the collection of information. Send comments regarding this burden estimate or any other aspect of this collection of information, including suggestions for reducing this burden, to Washington Headquarters Services, Directorate for Information Operations and Reports, 1215 Jefferson Davis Highway, Suite 1204, Arlington, VA 22202-4302, and to the Office of Information and Regulatory Affairs, Office of Management and Budget, Washington, DC 20503.

1. AGENCY USE ONLY	2. REPORT DATE October 2008	3. REPORT TYPE AND DATES COVERED Technical Report

4. TITLE AND SUBTITLE

The Interpretation of Motionally Induced Electric Fields in Oceans of Complex Geometry

5. FUNDING NUMBERS

OCE0552139

6. AUTHOR(S)

Zoltan B. Szuts

7. PERFORMING ORGANIZATION NAME(S) AND ADDRESS(ES)

Applied Physics Laboratory
University of Washington
1013 NE 40th Street
Seattle, WA 98105-6698

8. PERFORMING ORGANIZATION REPORT NUMBER

APL-UW TR 0803

9. SPONSORING / MONITORING AGENCY NAME(S) AND ADDRESS(ES)

Eric Istweire
Physical Oceanography Program, Division of Ocean Sciences, Room 725
National Science Foundation
4201 Wilson Boulevard
Arlington, VA 22230

10. SPONSORING / MONITORING AGENCY REPORT NUMBER

11. SUPPLEMENTARY NOTES

12a. DISTRIBUTION / AVAILABILITY STATEMENT

Approved for public release; distribution is unlimited.

12b. DISTRIBUTION CODE

13. ABSTRACT *(Maximum 200 words)*

Sea water moving through the earth's magnetic field induces electric currents in the ocean, and in general their distribution depends on the 3D structure of the ocean and its surroundings. Although velocity is traditionally calculated from measurements of the electric field with a one-dimensional relationship in the vertical, higher dimension processes are expected near steep topography or in energetic and variable flows. The observational capabilities of recently developed electric field instruments highlight the need for a qualitative and quantitative assessment of higher dimensional processes.

The first part of this dissertation analyzes electric field solutions for 2D effects caused by horizontal gradients of either velocity or topography. Magnetostatic solutions are calculated for simple geometries that are described by a few non-dimensional spatial scales.

The second part analyzes measurements collected across the Gulf Stream where it separates from the continental margin, where the oceanic flow is fast and meandering, topography is steep, and sediment is thick. Geophysical data are compiled to estimate the sediment electrical properties.

14. SUBJECT TERMS

ocean electric fields, motional induction, Absolute Velocity Profiler (AVP), Cape Hatteras, Gulf Stream

15. NUMBER OF PAGES

190

16. PRICE CODE

17. SECURITY CLASSIFICATION OF REPORT	18. SECURITY CLASSIFICATION OF THIS PAGE	19. SECURITY CLASSIFICATION OF ABSTRACT	20. LIMITATION OF ABSTRACT
Unclassified	Unclassified	Unclassified	SAR